THE EFFECT OF HEAT TRANSFER ON TEMPERATURE MEASUREMENT AND IT'S APPLICATIONS TO STUDY MICROCHANNEL HEAT SINKS

A Thesis Submitted for the Degree

of

Doctor of Philosophy

in the

School of Engineering

of the

University of Glasgow

By

Ahmed Al-Waaly
BSc. MSc.

System, Power & Energy Research Division
School of Engineering
University of Glasgow
Glasgow, UK

August 2015

This work is dedicated to

My parents and especially to the Soul of my mother

My beloved wife

Maysaa Al-Zubaidi

My Sons and girl

Jaafar, Rafel and Yousif

Decleration

This dissertation is the result of my own work. No part of this dissertation has already been, or is being concurrently submitted for any other degree, diploma or qualification.

.....
Ahmed Al-Waaly

August , 2015

Abstract

Analytical, numerical and experimental analyses have been performed to investigate the effects of thermocouple wire electrical insulation on the temperature measurement of a reference surface. Two diameters of K-type thermocouple, 80μm and 200μm, with different exposed stripped wire lengths (0 mm, 5mm, 10mm, 15mm and 20mm) were used to measure various surface temperatures (4°C, 8°C, 15°C, 25°C and 35°C). Measurements were made when the thermocouple probe is in direct contact with the surface and the wires are extended vertically and exposed to natural convection from outside environment. Experimental results confirmed that the thermal effect from the electrical insulation on temperature measurement was within -0.5°C and therefore it can be neglected. Moreover, the experimental results agree well with those obtained by both the analytical and numerical methods and further confirm that the diameter of the thermocouple has an impact on the temperature measurement. Analytical results of the thermocouple wire with insulation confirm that there is no specific value for the critical radius and the rate of heat flux around the thermocouple wire continuously increases with the wire radius even when this is larger than the critical radius.

Experimental and numerical analyses have been performed to investigate the heating impact of using thermocouples for the temperature measurement of small volumes of cold water. Two sizes of K-type thermocouple have been used: 80μm and 315μm to measure the temperature of the cold water inside a small chamber while the thermocouple wires were extended vertically in the outside environment. For this study, the chamber temperature was adjusted to 4°C. The results show that the heating effect of the thermocouple decreases for the greater depth measurements and this effect is eliminated when the thermocouple junction is close to the chamber bottom surface. The increase in the thermal resistance between the bottom surface and the thermocouple junction raises the heating effect of the thermocouple impact. Moreover, the exposed length of thermocouple wires to the environment has no effect over a specific length where the wire end temperature is equal to that of the environment.

Experimental and numerical analyses have been carried out to study the effect of using subchannels in heat sink to minimise the effect of hotspots generated on a chip circuit. Two devices of heat sink – with and without subchannels – were fabricated in order to investigate this effect. The first device was manufactured with a normal parallel channel while the second one was designed to extract more heat by dividing the main channels above the hotspot into two subchannels. A hotspot heat flux (16.7×10^4 [W/m^2]) was applied at the centre of the channels while a uniform heat flux (4.45×10^4 [W/m^2]) was applied at upstream and downstream of the channels. Five mass flow rates have generated under gravity force to investigate the performance of devices under different operating conditions. The results showed the maximum surface temperature was reduced by 4°C the temperature uniformity was improved. Moreover, thermal resistance was reduced by 25% but the pumping power was increased as a result of the presence of the subchannels.

Acknowledgements

All the praises be to Allah, the Most Beneficent, the Most Merciful. I would like to express my gratitude to my supervisors, Dr Manosh C. Paul and Dr Phillip S. Dobson for all their guidance, support and encouragement during this research. His stimulating comments and suggestions have been of immense benefit to me.

Iraqi Government, Ministry of Higher Education and Scientific Research/Iraq and Iraqi Cultural Attache/London for the financial support.

School of Engineering of the University of Glasgow for this study is gratefully appreciated. Grateful thanks are due to the members of IT Support Team of School of Engineering, CAD technician Mr Ewan Russell, and Mr Ken McColl for their constant effort to keep the system always running and help in fixing any problems in the computer systems.

I would like to express my sincere thanks to all the friends and colleagues, Mr Manaf Al-Taleb, Mr Hussein Al-Bugharbee, Dr Blaid Alganash, and Dr Najeeb Yahya, for their spirited support and encouragement has been of great help to me throughout the relentless endurance test of my PhD.

I am deeply indebted to my beloved parents, wife, sons and girl, siblings, and mother-in-law. I owe you all much more than I can possibly express. I am also grateful to all of my well-wishers for their invaluable advice and support that has
helped me greatly to make it this far.

Contents

List of table captions

List of figures captions

List of symboles

Symbol	Description
A	Cross-sectional area [m^2]
C_p	Specific heat capacity [J/kg K]
D	Diameter [m]
g	Gravitational acceleration [m/s^2]
H	Thin cylinder height [m]
h	Heat transfer coefficient of free convection [W/m^2 K]
h_j	Thermal joint conductivity[W/m^2 K]
k	Thermal conductivity [W/m K]
p	Perimeter [m].
q	Heat flux [W/m^2].
r_{cr}	Critical radius [m].
R	Thermal resistance resistance[K/W]

t	Thickness [m].
T	Temperature [K].
T_{dif}	$T\_{measured}$-$T\_{peltier}$ [K].
Greek symboles	
θ	T -T_{inf} [K].
v	Kinematic viscosity [m^2/s]
α	Thermal diffusivity [m^2/s]
β	Thermal expansion coefficient $[1/K]$
μ	Dynamic viscosity [$kg/m\,s$].
α	A_w/A_p.
Subscripts	
a	Air.
b	Bottom of the probe.
c	Contact thermal resistance.
dif	$T\_{measured}$-$T\_{peltier}$.
eqins	Equivalent insulation thickness.
inf	Environmental.
ins	Thermocouple metal wire with insulation.
L	Top of the probe.
m	Modified surface.
w	Thermocouple metal wire.
w	Water.
p	Thermocouple probe.
s	Undisturbed surface temperature.
w1	Thermocouple metal wire 1.

w2	Thermocouple metal wire 2.
weq	Equivalent single wire model.

Chapter 1
Introduction

1.1 Thermocouple impact

Thermocouples are one of the most prevalent temperature sensors that are used in the real experiments. The probe and wires of the thermocouple interface with a system during temperature measurement, altering the temperature field at the attachment point. Consequently, the sensor disturbs the medium and records a different value than expected from the measurement at the point of contact. This type of effect was classified by Moffat as *system/sensors interaction error* [2].

The principal reason for this effect on measurement is the presence of a temperature gradient along the wires. If the wires are passing through a medium with a temperature higher than that of the probe, heating impact occurs and the reading is higher than expected. Moreover, a cooling impact takes place when temperature of the wires is lower than that of the probe and the reading is lower than expected. Therefore, in order to minimise the impact of the thermocouple, both probe and wires should be at the same isothermal plane.

The impact of the thermocouple depends on several parameters such as the attachment method, wire size, probe size, fixing glue, insulation material and thickness, temperature gradient along the wires, etc.[3-6]. Moreover, the increase in the difference between the thermal conductivity of thermocouple wires and that of the system leads to an increase in the effect of the thermocouple.

Various attachment methods can be used to measure surface temperatures, depending on the physical application. Furthermore, the attachment methods specify the route along which the wires and the probe can be placed to measure surface temperature. Fig. 1.1 shows three typical positions of the thermocouple during surface temperature measurement. Fig. 1.1a shows the vertical thermocouple position, in which the probe in contact with the surface and the wires are exposed to natural convection from the outside environment. A thermocouple consists of two dissimilar wires which have different thermal conductivities. Therefore, the impact is a combination of conduction

heat transfer through both wires. The greater the temperature difference between environment and surface temperature, the larger the effect of the thermocouple.

The cooling effect takes place when the thermocouple wires are in an environment of temperature lower than surface temperature. Heat transfer is conducted through the probe and then along the wires out of the surface when T_s is higher than $T_{inf.}$ (See Fig. 1.1). Consequently, the surface temperature at the contact area will be lower and the thermocouple measures a lower temperature than expected. Conversely, a heating impact occurs when T_s is lower than $T_{inf.}$ due to heat transfer by conduction through the wires to the surface. Therefore, the surface at contact area will therefore have a higher temperature and the temperature measured will be higher than expected.

Fig. 1.1b shows the parallel position, in which the wires are in contact with the surface while simultaneously encountering convection from the environment. Consequently, the probe and the wires will be at different temperatures, and error in measurement occurs due to the heat transfer by conduction through the wires. As discussed in the preceding paragraph, heating or cooling effects occur when T_s is lower than T_{inf} or T_s is greater than T_{inf}, respectively. Moreover, the error in temperature will be more complex when surface temperature T_s varies along the wires.

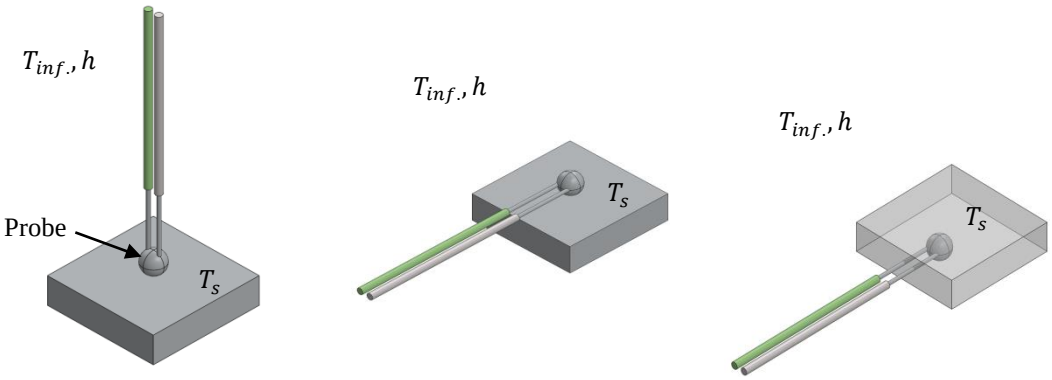

(a) vertical position (b) parallel position (c) inside the body

Fig. 1.1: Three-dimensional models of thermocouple in contact with surface in different directions.

Fig. 1.1c shows the insertion of the thermocouple inside the body near the surface to measure the temperature. If the surface temperature varies along the wires, a temperature gradient will be present and error in measurement is expected.

The error in thermocouple reading becomes larger with the increase in thermocouple wire diameter in all cases shown in Fig. 1.1. Furthermore, Fig. 1.1(a-b) shows that when no fixing glue is used; adding material to attach the probe to the surface may cause some error [4, 6-8]. Inserting the thermocouple inside the body requires a hole to be made, as shown in Fig. 1.1c. The temperature field will be changed due to the existence of the hole and thus will affect the thermocouple reading.

Conduction heat transfer through thermocouples wires is enhanced when the thermal conductivity is greater. Consequently, a thermocouple with lower thermal conductivity produces less effect on the measurement process [9-12]. Moreover, the type of electrical insulation can affect temperature measurement. Increased insulation thickness enhances heat flux to the thermocouple up to the size at which heat transfer begins to drop [8]. A small diameter bare thermocouple wire is highly recommended to minimise the error [13].

Thermocouple interaction with liquids is different than with solids. Inserting a thermocouple inside fluid flow to measure temperature will obstruct the flow and generate fluid boundary layers around the probe, increasing convection heat transfer and causing reading error [14]. Moreover, the presence of the probe can change the flow direction and behaviour [15].

Generally, the most important points to be considered is the placing of thermocouple wires and probe in the same isothermal plane in order to eliminate temperature gradient and thus reading error. If there is no possibility to avoid this, the following should be considered:

1. Using a small size thermocouple.
2. Using as small a difference in thermal conductivity between thermocouple material properties and measured medium as possible

3. Removing the electrical insulation, can reduce error depending on the physical application.
4. Minimise the size of attachment fixing glue.

During temperature measurement, the error produced by the interaction of the thermocouple should be considered and the reading must be corrected. However, if the impact of the thermocouple is smaller than experimental error (e.g. fixed and random errors), this correction can be neglected.

1.2 Non-uniform heat flux generation liquid cooling

Recent developments in technology and industry require treating huge quantities of information and data efficiently and with optimum time management. Dealing with a high volume of information requires high-efficiency microprocessors and rapid computational time [16]. Consequently, the cooling system should be designed to permit high heat dissipation from the processor. Microprocessor heat flux generation is non-uniform due to the performance of different operations on each part of the chip [17]. Maximum chip temperature should be kept below the endurable limit of the material and avoid any sharp changes in temperature distribution between the chip components [16]. The parallel microchannel is the normal method for cooling of high-density heat flux generated from a small-scale system [18]. However, using parallel microchannels for the cooling process generates non-uniform temperature distribution, regardless of whether the heat generated is uniform or non-uniform from chip circuits [19]. Therefore, alternative methods should be used to reduce heat generated on the hotspot of the chip circuit.

There is no specific cooling method for removing heat generation from hotspots generated above chip circuits. Parallel microchannels can be used after rearranging the distribution of the hotspots above the circuit [16, 20]. Changing the inlet flow direction in order to increase the mass flow rate of the liquid above the hotspot can mitigate a raised temperature [17, 21]. A two-phase flow is a possible method of cooling a chip circuit with a variable density of heat flux [22, 23]. The width of the microchannel(s) can be varied to target the hotspots by using narrow channels and wide channels for the other parts [16]. Extra generated heat can also be extracted by using a superlattice

hybrid system as a solid-state cooler which can be placed above the hotspot [24, 25]. Each application needs a special design of the microchannels and inlet manifold in order to achieve a uniform temperature distribution above the surface.

The main parameters to be considered in the design of a liquid cooling system for a chip circuit with hotspot heat dissipation are: maximum surface temperature; uniformity of temperature at the surface; thermal resistance; and pumping power. The primary target is a reduction of maximum surface temperature, but at the same time uniform temperature distribution and lower thermal resistance are necessary. Minimising the pumping power is also important. An increase in cooling system complexity can reduce the surface temperature, but this will occur at the expense of pumping power; a compromise between these parameters should therefore be considered.

1.3 Objective

1.3.1 Thermocouple conduction error

1.3.1.1 Thermocouple electrical insulation effect

In the present study, two different diameters (80μm and 200 μm) of Type K thermocouple were used to measure a surface temperature with direct contact between the junction and the surface without any fixing glue, as shown in Fig. 1.2. During the experiments thermocouple wires were extended vertically and exposed to a natural convection from outside environment. Because of the environment temperature is different than the surface temperature, heat flux then will be conducted through the thermocouple wires and the probe to (or from) the surface and therefore the surface temperature will be altered. A cooling effect is happening when the surface temperature is higher than environment temperature and therefore the thermocouple will measure a temperature lower than expected value. Whereas, heating impact is taking place when the environment temperature is higher than surface temperature and the thermocouple will measure a higher temperature than the expected.

The study examined the impacts of different lengths of wire stripped of electrical insulation on surface temperature measurement using a thermocouple. The electrical

insulation was stripped for different lengths: 0mm, 5mm, 10mm, 15mm, and 25mm for both thermocouple sizes. A Peltier element was used as the target surface for generating different surface temperatures (4°C, 8°C, 15°C, 25°C, and 35°C). Experimental results were compared to analytical and numerical calculations in order to fully understand the various heat transfer mechanisms in play.

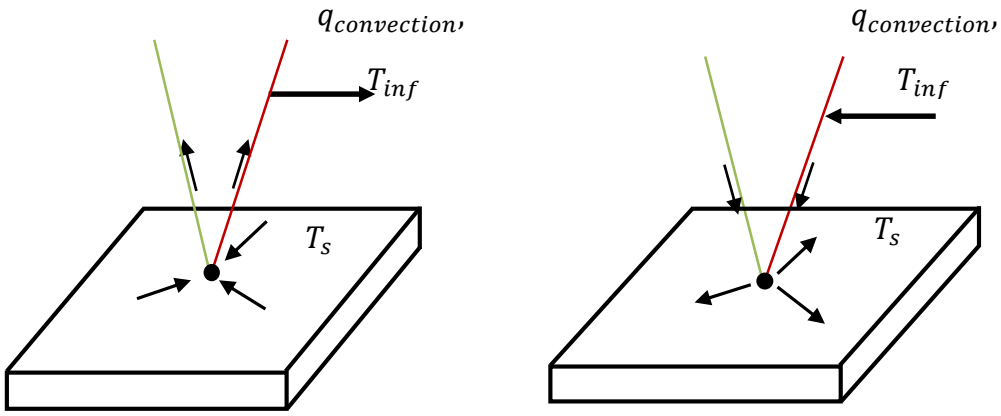

a) cooling effect when $T_s > T_{inf}$ b) heating effect when $T_{inf} > T_s$

Fig. 1.2: Effect of thermocouple conduction error on surface temperature measurement: a) cooling effect, b) heating effect.

1.3.1.2 Thermocouple conduction effect on small volume of cold water

The objective is to studying the heating impact of a thermocouple(s) on the temperature measurement of a small volume of water in a cooling system. The small volume of water is inside a chamber in the first row of TG40 cooling system. TG40 system consists of 5 rows with 8 chambers in each row, see Fig. 1.3 [26]. Two lids are covering all chambers and separating them from outside environment. There are two main parts in each row: plastic insert and copper block, the plastic insert is placed inside the copper block. The water inside the plastic insert was cooled by the copper block which its temperature is controlled by TG40 system. There are two wells in each chamber inside the plastic insert, a small well (with volume about $4mm^3$) and a large well (with volume about $32mm^3$), both of them are filled with water, see Fig. 1.4.

The first set of experiments was performed to measure the water temperature distribution inside the large well of the plastic insert without lids by using a thermocouple. The second set was to measure water temperature distribution inside

the copper block to confirm the block temperature. Two different sizes of thermocouple (80μm and 315μm) were used to measure the temperature.

During the experiments, thermocouple wires were extended vertically and exposed to natural convection from the outside environment while the probe was immersed inside the water. Because the environmental temperature was higher than that of the water inside the chamber, the heat transfer was therefore conducted to the water through the thermocouple wires and the probe. This caused a heating impact on the water around the probe and the water temperature will be altered. Consequently, thermocouple will measure the affected water temperature which is higher than the actual value.

Experimental and numerical analyses have been adopted to investigate the heating impact effect of the thermocouple. Depending on this validation, numerical results of the full chamber geometry were considered solely to examine the temperature distribution inside the large and small wells without the effect of the thermocouple.

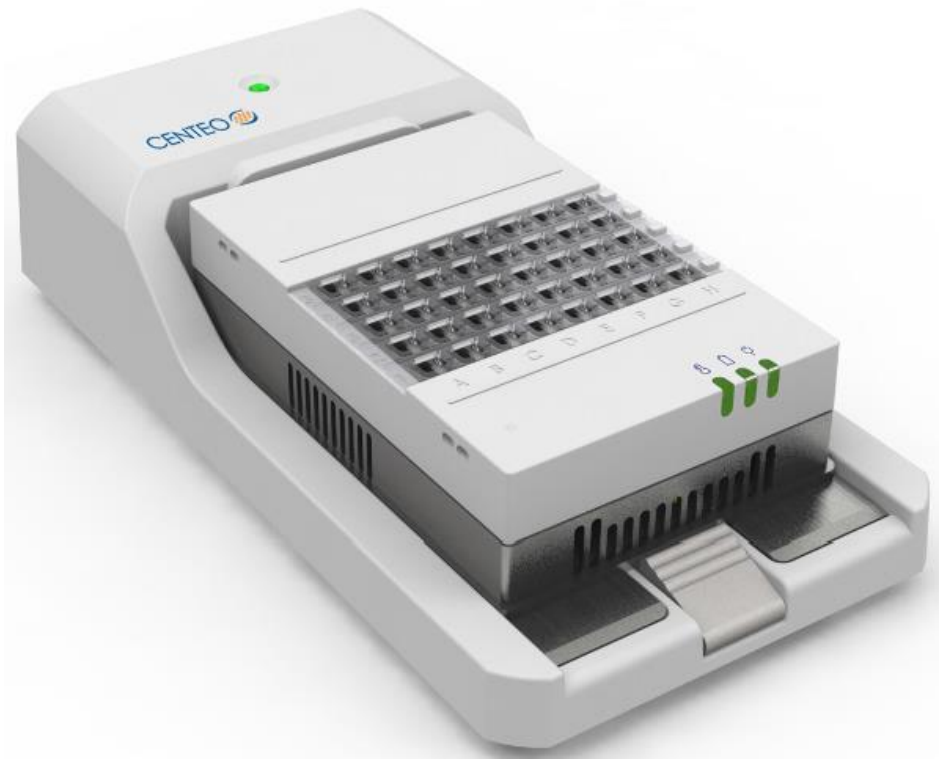

Fig. 1.3: CENTEO's TG40 cooling system.

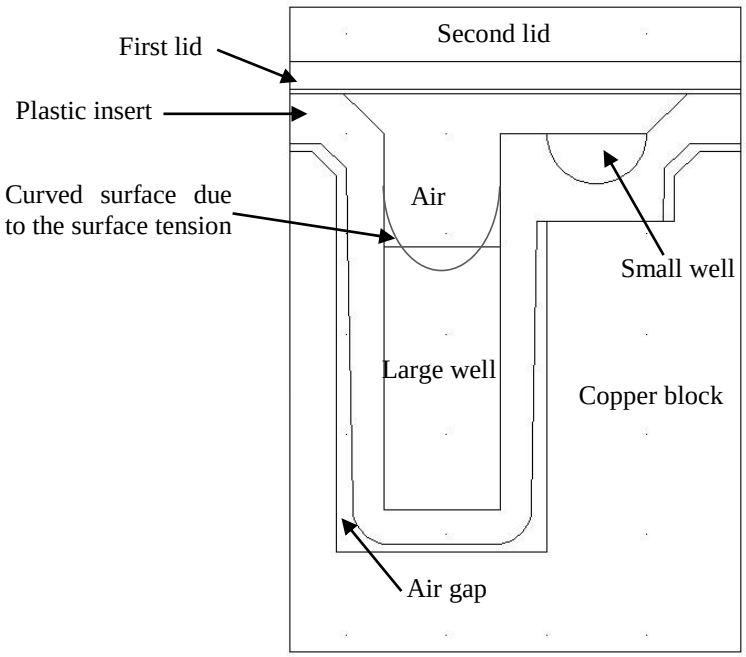

Fig. 1.4: Two-dimensional cross-sectional view of the chamber. (Note: this figure is Fig. 5.2 re-inserted here).

1.3.2 Cooling of non-uniform heat flux

The expected results from the section 1.3.1 will give us a good understanding of the effect of thermocouple on temperature measurements. Depending on this results, the appropriate locations of the thermocouple wires and the probe attachment methods will be chosen in this part of the research to minimize the impact of the thermocouple. Consequently, the temperature measurement(s) will be more accurate obtained and better understanding of the system behaviour is obtained.

In the present study, the increase of the liquid-solid interaction area has been adopted to remove the extra heat flux generated on the hotspot to reduce the maximum surface temperature above the chip circuit. Heat generated above the chip circuit is non-uniform due to the effect of different operations performed by the circuit. Consequently, the temperature distribution will be non-uniform above the surface and hotspots are created.

Two heat sinks were fabricated: the first one with parallel channels and the second with subchannels by dividing the main channels into two subchannels above the

hotspot. Twelve microheaters were used to generate the hotspot at the middle position and uniform heat fluxes upstream and downstream of the flow.

Experimental and numerical results were adopted to investigate the effect of adding subchannels above the hotspot and to predict the thermal and hydraulic performance of the new design.

1.4 Thesis outline

In **Chapter 2**, a literature review has been presented about the available techniques for reducing the high temperature of the hotspot in non-uniform heat flux generated on a chip circuit.

In **Chapter 3**, a brief description is given of the governing equations for flow and thermal fields with the applied boundary conditions. In addition, the finite element method used for the formulation of the partial differential equations and the solving method are briefly discussed. COMSOL Multiphysics software was used to solve two benchmark cases based on the FEM method in order to investigate the validity of using FEM to solve the flow through microchannels.

Chapter 4 outlines the effect of thermocouple electrical insulation on a surface temperature measurement. Two sizes of thermocouple were used to examine the cooling and heating effects on temperature measurement. Furthermore, the insulation was stripped off in order to study its influence on the measurement process. During temperature recording, the thermocouple was held in a vertical position, while the probe was in direct contact with the surface without the use of any glue. Analytical, numerical and experimental results have been conducted to analyse the effect of the thermocouple(s).

The heating effect impact of using different sizes on a small quantity of cold water was investigated in **Chapter 5.** Two sizes of thermocouple were used to investigate the heating impact of a thermocouple on a small cold volume of water. The water boundary temperature was kept at 4^{o}C and the thermocouple probe was immersed in the cold water during the measurement process, while the wires were held vertically into the environmental temperature. Heat transfer by conduction occurred through the

wire into the water as the environmental temperature was higher than that of the water. The measurement from the thermocouple was higher than expected due to the heat transfer to the water. Experimental and numerical methods have been adopted using COMSOL Multiphysics software.

In **Chapter 6**, two models of parallel channels with and without subchannels were designed to investigate the effect of adding subchannels. Experimental and numerical analyses have been considered. The model(s) was fabricated using copper material and the manifold was made from low thermal conductivity material to minimize heat losses. Twelve microheaters were used to generate a hotspot at the middle of the channels and uniform heat fluxes at upstream and downstream positions. Therefore, a wide parallel channel was used to cool the uniform heat dissipation, while narrow channels were involved on the hotspots.

The conclusions used to target the results' chapters have been included in **Chapter 7**. Moreover, recommendations and suggestion for the future works were listed as well.

Chapter 2
Literature Review

2.1 Thermocouple conduction error

When thermocouple wires are exposed to an environment with a temperature different to that of the object being measured, heat transfer occurs through the wires, which disturbs the system, alters the thermocouple junction temperature and causes an impact on the temperature measurement.

Boelter and Lockhart [8] conducted experimental work to measure the temperature of a thick stainless steel plate. The plate was kept at constant temperature(s) by heating one side and cooling the other side, using hot and cold air flow respectively. Two types of thermocouple were tested (iron-constantan and Chromel-Alumel) with different wire sizes; the thermocouples were attached to the cold air side during the measurement process. They also investigated the influence of vertical and horizontal thermocouple attachment methods on the surface temperature measurement. They suggested that the impact of the thermocouple on measurement can potentially be minimised by using an inter-thermocouple wire inside a plate or by extending the wires along the surface being measured for a length more than 50 times the wire diameter.

Tarnopolsky and Seginer [11] performed an experimental analysis to study the effects of wire diameter and electrical insulation on error due to the conduction through thermocouple wires during temperature measurement of vegetable leaves. Small wire(s) size (AWG40) Type T thermocouples were placed parallel to the surface, while the probe was attached using special glue and the surface was exposed to cold (or hot) air flow. Different surface contact lengths of insulated and uninsulated thermocouple wires were tested. They verified that the glued length of the thermocouple wire (size AWG40) of the Type T with Teflon insulation was reduced from 22mm to 14mm when the insulation is removed to achieve a uniform temperature between the junction and the measured surface. Moreover, the glued length is reduced to 10mm when thermocouple Type K was used. He et al. [6] conducted a CFD analysis and compared results between the effects of vertical and parallel positions of thermocouples on

surface temperature measurement. Thermocouple(s) were attached to a uniform heat-generating surface that was cooled by air flow at different speeds. They showed that placing wires parallel to the surface can reduce the impact of the thermocouple on measurement by more than half as compared with a vertical position. He et al. [6] showed that the relative errors (with respect to the difference between the undisturbed surface temperature and the ambient temperature) were 11.8% and 27.1% for the horizontal and vertical position respectively.

Various thermocouple arrangements inside low-conductivity materials exposed to high heat transfer were examined experimentally by Brewer [27] and Dow [28]. They proved that a relatively high error due to thermocouple impact was produced when thermocouple wires passed through a low-conductivity material parallel to the heat flow. They therefore recommended placing the wires at the same isothermal surface of the junction for several diameters to minimise the error. Singh and Dybbs [3] measured temperature variation inside the body by inserting thermocouples at different depths, parallel as well as normal, to temperature variation through the body. They reported that the thermocouple wires and the junction should be at the same isothermal plane in order to reduce error. Consequently, if experiment conditions do not permit this, the temperature reading should be corrected. However, the correction is not appropriate if the experimental error of the thermocouple is larger than the error due to the impact of the heat conduction through the wires.

Another strategy was adopted by Li and Wells [5] to measure surface temperature by pushing a thermocouple through a hole opposite the surface. The surface temperature was measured during the quenching process by a Type K thermocouple which was inserted into the hole near the surface. Experimental and numerical studies confirmed that when the thermal conductivity of the hole is less than the surrounding material, heat transferred to the thermocouple junction will be less and the measured temperature is lower than expected. Therefore, the effect of both hole and thermocouple wires should be considered during the temperature measurement. Furthermore, Li and Wells [5] proved that an increase in the hole diameter caused a larger effect on the temperature measurement. Two-dimensional analysis by Bartkus

et al. [29] predicted that most of the error in thermocouple measurement within the body comes from the increase in thermal resistance between the thermocouple insulation and the surrounding materials. Experimental and numerical results by Atia et al. [9] consolidated the conclusions of Li and Wells [5] and Bartkus et al. [29]. Moreover, Attia et al. [9] studied the effects of different thermocouple material properties (E, J and T) and the surrounding material on temperature measurement inside the body. They showed that an increase in thermocouple thermal conductivity augmented heat transfer and thus underestimated temperature readings. Furthermore, the existence of a thermocouple hole altered the temperature field around the thermocouple and caused a reading error [9].

Tarnopolsky and Seginer [11] observed that a thermocouple with lower thermal conductivity (Type K) requires 60% less contact length than one with a higher conductivity (Type T). Dow [28] pointed out that because of its high thermal conductivity, alumina tubes produce a greater impact on measurement by 277 [K] higher than resin-glass insulation when used as an insulation material for thermocouple wires. Numerical results of Kidd [10] used skin-technique to confirm that pairing chromel-constantan wires gave a lower conduction error than other materials used for thermocouple wires. Experimental results of Boelter and Lockhart [8] showed that iron-constantan gives a higher error in temperature measurement than Chromel-Alumel. Shaukatullah and Claassen [4] performed experimental results for the temperature measurement of a chip surface with different thermocouple sizes and attachment methods. They attached number of thermocouples radially (where there is a temperature gradient along the wires) and axially along the isothermal plane. They reported that the error due to heat conduction through the wires was 5.5% of the actual reading while the experimental error was 1.5%.

Boelter and Lockhart [8] confirmed that for the same size of the thermocouple there is a small effect from electrical insulation on temperature measurement when the thermocouple diameter (including the insulation) is equal to the critical radius. Mohun [30] discussed analytically the effect of electrical insulation for temperature measurement inside a solid wall. Mohun showed that the presence of electrical insulation over a critical length can only affect the thermocouple reading if the wires

pass through a variable environmental temperature. Tszeng and Zhou [31] used the finite element method to analyse conduction error through thermocouple wires when the probe was in direct contact with the surface of a body. They showed that when the body temperature is 1000^{o}C, the insulated wire can cause an impact of 25^{o}C temperature drop while the uninsulated wires has negligible impact (about 0^{o}C). Moreover, the increase in the wire diameter 0.02mm to 0.15mm leads 30^{o}C temperature measurement difference. Tszeng and Zhou [31] recommended using bare wire with a small diameter rather than a larger diameter thermocouple with insulation. Woolley [12] confirmed that alumina oxide Al_2O_3 insulation causes higher measurement error than glass braid insulation during temperature measurement at the interface between aluminium and sand during a metal casting process. These results have been demonstrated for different sizes of thermocouples (AWG[1]24, AWG30, AWG36, and AWG44) and for very high temperature differences (~1500K). Similarly, Tszeng and Saraf [13] showed that a thermocouple of small size has less impact on measurement.

Experimental results presented by Perera et al. [7] studied the effect of different fixing methods of the thermocouple on an LED lens for surface temperature measurement. They indicated that using thermal adhesive tape or silicone elastomer have an identical effect on the measurement. Furthermore, fixing the thermocouple junction with a spot weld gave better results than soldering or condenser-discharge welding (Boelter and Lockhart [8]). Shaukatullah and Claassen [4] showed that using silver epoxy, either alone or with insulating epoxy, to fix the thermocouple to the surface gave a good contact and consequently lower error in temperature measurement. Attaching the thermocouple to the surface with polyimide or aluminium tapes produced higher errors due to poor contact. He et al. [6] state that an increase of the epoxy drop diameter from 2.5mm to 7.5mm led to reduced measurement error, but that this increased again for a diameter of 10mm. Their results confirmed that the thermocouple error can be

[1] AWG is abbreviation of American Wire Gage. The sizes AWG24, AWG30, AWG36, and AWG44 are equivalent to 0.511mm, 0.255mm, 0.127mm, and 0.05mm respectively.

minimized when using high thermal conductivity silver filled epoxy instead of classic epoxy of low conductivity.

Another approach was taken by Robertson and Sterbutzel [32], who used two thermocouples and a heater which were attached to a probe. The first thermocouple was in direct contact with the surface and measured the disturbed temperature, while the second, away from the surface, measured the temperature of the probe itself. Both thermocouple outputs were fed into a power controller which supplied a heater current proportional to the temperature difference. Consequently, the heater reduced the temperature difference between the thermocouples. When both thermocouples were at the same temperature there was no heat flux along the thermocouple wires and the first thermocouple accurately recorded surface temperature.

Numerical results of Kulkarni et al. [14] verified that the flow around a thermocouple probe generates an increased amount of heat transfer coefficient, and that this consequently causes an error in the temperature measurement. They demonstrated that when a thermocouple probe is placed close to the wall, the measurement error is increased due to the rapid acceleration and convection flow developing over the boundary. However, this error is minimised when the flow Reynolds number is relatively low. Heitor and Moreira [15] showed that the existence of an object changed the direction and behaviour of flow, particularly during preparing flow for combustion. Moreover, the thermal interaction between the probe and surrounding fluids generates more perturbation. Rabin [33] proved that the behaviour of flow inside a measured system affects measurement error; in particular, laminar flow around the thermocouple produced a greater measurement error than that of the turbulent flow.

Experimental analysis of Hindmarsh et al. [34] showed that the presence of a thermocouple junction affects a water droplet freezing when it is suspended by a thermocouple to measure its freezing stages. Conduction through the wires forced the freezing to begin from the centre toward the outer surface of the water droplet. Xu and Gadala [35] demonstrated that the high thermal conductivity of fluid surrounding a thermocouple wire increases the error in measurement due to conduction through the wires. During surface cooling by water, the error is larger than that of the air cooling

due to the difference in high heat transfer coefficient. However, analytical results of Rabin [33] showed that an increase in the length of the immersed thermocouple wires inside the flowing fluid leads to a reduction in the error due to the conduction of heat through the wires. Moreover, Rabin confirmed that the effect of the conduction can be minimised when the size of the thermocouple is small.

Fang and Ward [36] used two sizes of thermocouple to measure the temperature at the interface between liquid water and its vapour. Two Type K thermocouples, 25.4 μm and 80.3 μm, have been used. The wires of 24.5μm were extended horizontally within the measured medium to a length that equalled 20 times the junction diameter to avoid any possible conduction error. However, the wires of the larger size thermocouple (80.3μm) were extended to 110 times the junction size.

Kobus [37] compared single-wire and two-wire thermocouple models and found that the two-wire model is more accurate than the single-wire because the thermal conductivity is very different.

2.2 Liquid cooling of non-uniform heat flux

The principal purpose of using microchannels is to remove the maximum amount of heat generated from a limited space [18]. This technology is used to remove uniform heat generated from integrated circuits [18, 38, 39]. Due to non-uniform heat dissipation from electronic circuits, however, hotspots are generated [20, 40]. Parallel microchannels have been used to cool uniform and non-uniform heat flux distribution but, due to unequal flow rate distribution through microchannels, non-uniform temperature distributions have been generated [18, 21]. Different design approaches have therefore been developed to extract greater heat flux from the hotspots.

Different technologies are available to minimise the effect of hotspots on the performance of a non-uniform heat flux generation chip circuit. Two-phase flow boiling through parallel microchannels for cooling hotspots has been studied by several authors [41-50]. A superlattice can be employed as a solid-state cooler which can be placed above the hotspot to extract the extra heat generated [24, 25]. Single- and two-phase porous media with microchannels have been studied numerically [22]

and experimentally for cooling hotspots [23]. Another type of two-phase flow of spray cooling by breaking the flow into small droplets to generate a small layer of vapour can cool the heat generated at hotspots [51, 52].

A single-phase liquid is the primary target of microchannel cooling of chip circuits [18]. Therefore, the present study exploits the benefit of increasing solid-liquid interaction area by adding subchannels above the hotspot to extract the extra heat generated for a single-phase flow.

Locations and amounts of heat generated at the hotspot on the chip surface determine the type of microchannel design in order to achieve uniform temperature distributions. Hegde et al. [53] attached a two-layer heat sink to the chip surface which generates various heat flux scenarios: ascending and descending along the microchannels, upstream, middle, and downstream heat dissipation. Numerical results of Hegde confirmed that the parallel fluid flow through the channels gives lower surface temperature with the descending heat flux generation. Furthermore, counter flow showed a similar surface temperature for ascending and descending heat dissipation. Hedge and Seetharamu [53] numerical results showed that the parallel flow with partial heat at the downstream gave lower temperature in comparison with counter flow case. The last observation of Hedge and Seetharamu [53] validates the experimental results of Wei [1] who confirmed that lower surface temperature has been obtained for the parallel flow with downstream heating.

Another approach is to redistribute the hotspot locations to obtain a uniform heat flux above the chip circuit. Chauhan et al. [17, 20] numerical results showed that the changing in the flow direction where the cold fluid met the hotspot at the entrance or in opposite direction. In addition, Chauhan [20] used a counter flow between two adjacent microchannels; the results showed that placing hotspots at the inlet gave more cooling action. The numerical analysis of Zhang [40] et al. and Li et al. [16] used the same method of rearranging the hotspots on the chip circuit, but, they increased the channels density above the hotspots. Xie et al. [54] numerically analysed a combination between two and three different manifolds and two hotspot locations (in-line and diagonal arrangements perpendicular to the flow direction). Xie showed that

a lower and more uniform temperature was achieved when the inlet and outlet ports were located at the middle and perpendicular to the heat sink surface, but a greater pressure was also produced. Analytical analysis by Biswal et al. [55] showed the effect of the size of the heat source on thermal resistance. When a heat source is 25% of the size of the heat sink, thermal resistance is reduced by 16% for fully developed flow (14% for not fully developed flow) when the hotspot is moved from inlet to the middle position. Biswal et al. [55]showed that an increase in the size of the heat source in comparison with heat sink area led to a reduction in base thickness.

The cooling effect of the cross-linked microchannel on different locations and density of the hotspot were studied by Ling [56]. Placing the hotspot upstream led to a lower temperature than downstream because of lower water temperature coming into contact with the hotspot. Moving the cross-linked microchannel after the hotspot showed better improvement in comparison with the position above the hotspot. Microchannels with two passes along the chip circuit were investigated by Liu et al. [57]. Three separate heaters were attached to the back of a heat sink to get non-uniform heating. Two designs of manifold were studied experimentally: the first made the flow perpendicular to, and second parallel to, the flow in the microchannels. The authors found that placing the hotspot at the inlet created a higher temperature than middle and downstream positions. The presence of the hotspots at the inlet raise the liquid temperature and therefore the cooling capacity is reduced when liquid comes in contact with the other parts of the surface. Moreover, if the hotspot was upstream or downstream the liquid temperature will be lower when the flow approaches the hotspot and the cooling capacity will be higher.

The using of the parallel channels for cooling a unifrom heat flux generation above the chip circuit, produces a non-uniform surface temperature distribution. Therefore, variable channel widths have been investigated by several authors for cooling uniform heat flux generation in order to improve the temperature uniformity. A reduced channel width gives better thermal performance, as confirmed by Saad et al. [58]. An experimental comparison between flat plate heat and five heat sinks of different channel widths (0.2mm, 0.5mm, 1mm, and 1.5mm) was investigated. There was a

greater reduction in surface temperature when using fins compared with a flat heat sink. Moreover, an increase in the flow rate led to a rapid decrease in surface temperature of the flat heat sink, unlike the case with minichannels [58]. Barrau et al. [59] experimentally investigated the effect of varying channel widths with flow direction for a uniform heat flux heat sink. The manifold was designed to supply liquid water at the middle section through a slot and deflected 90^o to enter the channel section. The channel(s) height and wall thickness were 2.5mm and 0.5mm respectively. Channel(s) width varied from 3.5mm at the middle section (flow upstream) to 0.5mm at downstream. Various values of uniform heat flux and mass flow rates were applied at the back of the channels and inlet ports respectively. Uniform temperature distribution was achieved, with a small effect on pressure loss compared with conventional microchannels. Riera [60] experimentally and numerically confirmed the results of the previous investigation [59]. Riera [60] repeated the same design configuration as above but with the smaller size. Channel(s) width varied in five stages: 1.528mm below the flow inlet at the middle location of the channels and 0.136mm downstream of the flow. Channel height of 0.3mm and wall thickness of 0.1mm remained constant along the channels.

The same designs of variable channel widths have been applied for cooling of non-uniform heat flux generation. The placing of narrow channels above the hotspot increases the solid-liquid interaction area and then reduces surface temperature. Hotspot with heat flux of 1250 W/m^2 can be cooled by using a different design of microchannels, reducing the channel width above the chip circuit (Prasher and Chang [61]). Experimental results of Prasher and Chang demonstrated lower thermal resistance has been achieved with narrow channel cooling. Numerical analysis of Minliang [62] and Wang [63] followed the same procedure by narrowing the width of microchannels above the hotspot to increase the fluid-solid interaction area. Optimum design by Göker [64] confirms that reducing microchannel width at the hot spot increases heat transfer and consequently increases pressure drop. Zhang et al. [40] and Li et al. [16] divided a chip into low and high heat flux areas and reduced the width of the microchannels above the hotspots to minimise the temperature in comparison with

uniform heating. Their numerical results showed a good improvement in surface temperature.

Optimum manifold and microchannel designs have achieved a minimisation of the effect of the hotspot on temperature uniformity (Sharma et al. [65]). Sharma designed a manifold to direct water flow inlets on the hotspot and an outlet above the uniform background heat dissipation. In addition, small-width microchannels were placed on hotspots, while larger widths were used above the uniform flux. Lower thermal resistance and smoother temperature distribution were obtained, but higher pumping power was required. An experimental study conducted by Sharma [66], using the a similar design of Sharma et al. [65], by directing water flow above the hotspots locations on which the channels widths is less than the widths above the uniform heat flux. Sharma et al. [66] used a special design of manifold by throttling the flow above the channels whether these were placed above the hotspots or uniform heat flux. Two models of have been investigated with different heat flux generation: first model was 150 W/cm^2, and 20 W/cm^2 and the second model was 300W/cm^2, 40W/cm^2, and 20 W/cm^2. The design proposed by the author improves the temperature uniformity by 4^{o}C and 15^{o}C for the first and second model respectively. Instead of reducing the channel width(s) above the hotspot(s), varying the channel depth(s) was investigated by Dias [67]. Dias [67]suggested variable depth microchannels to reduce the high temperature at the hotspot. Above the hotspot, the channel will be deeper than the background heat flux; a deeper channel means more heat transfer interaction area between fluid and solid.

Another technique can be selected to increase the solid-liquid interaction area. The effect of using oblique fins was investigated numerically by Lee [68] and experimentally by Lee [69], in studies comparing conventional microchannels with two different configurations of oblique fins. Numerical [68] and experimental [69] analyses confirmed that the use of oblique fins led to a decrease both in chip temperature and temperature difference above the chip surface. Varying the fin density according to the heat dissipated at the hotspot can improve temperature uniformity [69], but at the cost of pressure increase. Lee [70] added a fin pins array to the hot

spots in order to extract the high heat flux and obtain uniform temperature with a higher pressure drop. The number of fin pins on downstream hot spots was greater than upstream in order to compensate for the rise in temperature of water that had passed through upstream hotspots. Goodson [71] suggested a complex manifold design to control volume flow rate by supplying a high flow rate to the hotspot, thereby reducing its temperature, while reducing the flow rate provided to the lower heat flux area. This can be achieved by controlling the flow by supplying the cooling fluid directly to the hotspot through short passages at a greater pumping power. Goodson [71] used different microchannel sizes and fins of different heights to obtain a uniform temperature above the chip surface but the pressure drop was increased.

Another study for cooling the hotspot is injecting cold water directly above the hotspot to reduce the temperature and obtain a more uniform temperature distribution Fan and Hassan [72]. A numerical analysis was performed for flow through a single microchannel heat sink crossing a jet of cold water flow(s) from a spiral inlet above the hotspot(s). Fan and Hassan [72] show that the increase of flow velocity through the microchannel led to a decrease in temperature when jet flow velocity was constant. Moreover, for a constant microchannel inlet velocity, the increase in jet velocity led to a decreased hotspot temperature. Fan suggested the addition of pins inside the channel to increase the solid/liquid interaction area. Furthermore, the density of the fin pins was increased downstream of the channels due to fluid's high temperature.

Four separated blocks generating differing heat fluxes were cooled by separated parallel microchannels in a study by Xu [73]. Water was used as the cooling liquid; it was supplied to the system through a single inlet port and collected through two or four outlet ports. The four microchannel sets were each linked together by a unique channel. Each microchannel set had a specific number of channels with variable space width between the neighbours channels depending on the heat generated at each block. The flow rate(s) through the heat sink was controlled by using a computer controlled pump to get different flow rates. The system of 5ports (one inlet and four outlet) gave a better performance than the 3-port system (one inlet and two outlets). A lower pressure drop and thermal resistance were obtained from 5-ports.

Chapter 3
Governing Equations and Numerical Methods

3.1 Governing differential equations

Heat transfer analysis of the interaction between solid and liquid includes solving a system of equations through solid and liquid simultaneously. Continuity and Navier-Stokes equations of incompressible steady-state flow behaviour can be written as follows [74]:

Continuity equation:

$$\frac{\partial u}{\partial x}+\frac{\partial v}{\partial y}+\frac{\partial w}{\partial z}=0 \tag{3.1}$$

Navier-Stokes equations:

$$\rho\left(u\frac{\partial u}{\partial x}+v\frac{\partial u}{\partial y}+w\frac{\partial u}{\partial z}\right)=-\frac{\partial p}{\partial x}+\mu\left(\frac{\partial^2 u}{\partial x^2}+\frac{\partial^2 u}{\partial y^2}+\frac{\partial^2 u}{\partial z^2}\right)+F_x \tag{3.2}$$

$$\rho\left(u\frac{\partial v}{\partial x}+v\frac{\partial v}{\partial y}+w\frac{\partial v}{\partial z}\right)=-\frac{\partial p}{\partial y}+\mu\left(\frac{\partial^2 v}{\partial x^2}+\frac{\partial^2 v}{\partial y^2}+\frac{\partial^2 v}{\partial z^2}\right)+F_y \tag{3.3}$$

$$\rho\left(u\frac{\partial w}{\partial x}+v\frac{\partial w}{\partial y}+w\frac{\partial w}{\partial z}\right)=\mu\left(\frac{\partial^2 w}{\partial x^2}+\frac{\partial^2 w}{\partial y^2}+\frac{\partial^2 w}{\partial z^2}\right)+F_z \tag{3.4}$$

where u, v and w are the velocity components [m/s] in the x-, y- and z-directions respectively, ρ is the density [kg/m^3], ν is the kinematic viscosity [m^2/s], and p is the pressure [Pa]. F_x, F_y, and F_z are body force [N] in the x-, y-, z- directions respectively.

The energy equation describes the heat flow through the liquid and solid by considering convection terms in the equation as follows:

$$\rho\, Cp\left(u\frac{\partial T}{\partial x}+v\frac{\partial T}{\partial y}+w\frac{\partial T}{\partial x}\right)=k\left(\frac{\partial^2 T}{\partial x^2}+\frac{\partial^2 T}{\partial y^2}+\frac{\partial^2 T}{\partial z^2}\right) \tag{3.5}$$

where C_p is the specific heat capacity [J/kg K], and k is the thermal conductivity [W/m K].

Analytical solution(s) of Eqs.(3.1) and (3.5) is applicable for a simple physical system, such as one-dimensional and in some cases simple two-dimensional. However, flow through heat exchanging systems is more complex and it is impossible to find an analytical solution for the velocity and temperature distributions. A numerical solution should therefore be considered for the above differential equations. Many numerical methods are available, such as finite difference, finite volume or finite element methods. In the present analysis, the finite element method (FEM) is the numerical method that has been used to solve the three-dimensional equations (3.1)-(3.5).

3.2 Finite element method

The finite elements method (FEM) is a numerical method which discretises the geometry of a model into sub-geometries. The smallest sub-geometry is called the *element* which consists of a number of nodes. Combination of all the elements within the full geometry results in *mesh elements* (See Fig. 3.1). The shape of this element can be 1D, 2D or 3D, depending on the model dimensions and complexity (See Fig. 3.2 and Fig. 3.3[75-77]). The relationship between the variable within each element is called the *shape function* (or *interpolation function*) [77]. Shape function is a polynomial function which is defined on each node. The number of nodes determines the degree of the shape function within each element.

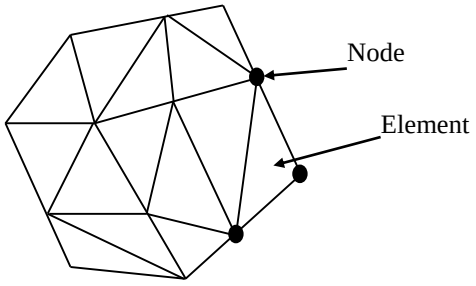

Fig. 3.1: Demonstration of mesh elements.

The number of unknown variables specifies the *degree of freedom* within an individual element and through the full system.

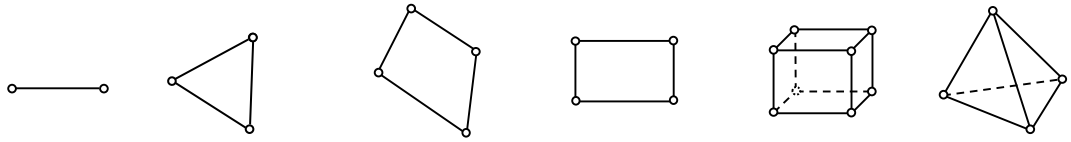

a)1D element | b) 2D triangular element | c) 2D quadrilateral element | d) 2D rectangular element | e) 3D hexahedron element | f) 3D tetrahedron element

Fig. 3.2: Types of linear one-, two- or three-dimensional elements.

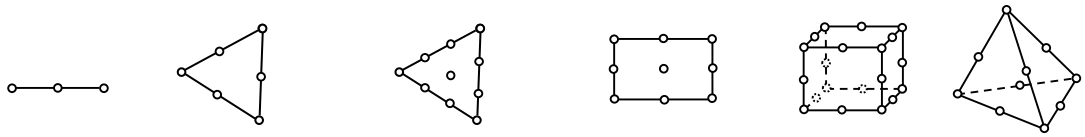

a)1D element | b) 2D 6 nodes triangular element | c) 2D 10 nodes triangular element | d) 2D 9 nodes rectangular element | e) 3D hexahedral element | f) 3D tetrahedral element

Fig. 3.3: Types of quadratic one-, two- or three-dimensional elements.

The accuracy of the numerical solution is usually improved by increasing the degree of the shape function [75]. However, this leads to an increase computational time and memory required due to the increase number of the degree of freedom.

The shape function should have the following properties to satisfy solution of the PDEs:

1. No discontinuity within the elements.
2. Compatibility of each element to its neighbors. This means the degree and the number of nodes should be the same at the element boundaries.
3. The behavior of the shape function should be continuous at the element boundaries and within all the elements of the model.
4. Geometric isotropy: the shape function should have the same properties in the transformation from one coordinate system to another.

The general form of the shape function is written as follows [78]:

$$T_n(x) = \sum_{k}^{n+1} \alpha_k x^{k-1} \tag{3.6}$$

where T is the polynomial shape function (temperature as an example), n is the polynomial degree, α is a constant, x is the coordinate along the element. Therefore,

for the 0th, 1st, and 2nd degrees the shape functions can be written respectively as follows in one-dimensional system:

$$\begin{aligned} T_0(x) &= \alpha_1 \\ T_1(x) &= \alpha_1 + \alpha_2 x \\ T_2(x) &= \alpha_1 + \alpha_2 x + \alpha_3 x^2 \end{aligned} \tag{3.7}$$

A higher degree of the shape function (for one- and two dimensional problems) can also be predicted from a Pascal's triangle, as shown in Fig. 3.4.

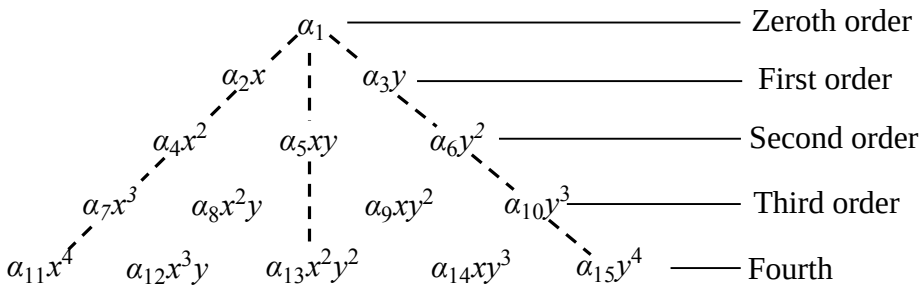

Fig. 3.4: Pascal's triangle for higher order of shape function [78].

In order to understand the behaviour and properties of the function over the element, a linear first order shape can be considered (See Fig. 3.5). The linear shape is written as follows (from (3.7)):

$$T(x) = \alpha_1 + \alpha_2 x \tag{3.8}$$

where T represents the temperature variation along the element. Let T_i and T_j represent the temperature at nodes i and j respectively. These values are then substituted into Eq.(3.8).

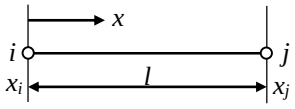

Fig. 3.5: 1D linear element.

Then:

$$T_i(x)=\alpha_1+\alpha_2 x_i$$
$$T_j(x)=\alpha_1+\alpha_2 x_j \tag{3.9}$$

Consequently:

$$\alpha_1=\frac{T_i x_j - T_j x_i}{x_j - x_i}$$

and (3.10)

$$\alpha_2=\frac{T_j - T_i}{x_j - x_i}$$

α_1 and α_2 are substituted back into Eq.(3.8), then:

$$T(x) = \left[\frac{x_j - x}{x_j - x_i}\right] T_i + \left[\frac{x - x_i}{x_j - x_i}\right] T_j \tag{3.11}$$

or:

$$T(x) = N_i T_i + N_j T_j = \begin{bmatrix} N_i N_j \end{bmatrix} \begin{bmatrix} T_i \\ T_j \end{bmatrix} \tag{3.12}$$

where N_i and N_j are the shape functions written as

$$N_i = \left[\frac{x_j - x}{x_j - x_i}\right],\ N_j = \left[\frac{x - x_i}{x_j - x_i}\right] \tag{3.13}$$

Eq. (3.12) can now be written in the matrix form:

$$T=[N][T] \tag{3.14}$$

where

$$[N]=\begin{bmatrix} N_i N_j \end{bmatrix},\ \ [T]=\begin{bmatrix} T_i \\ T_j \end{bmatrix} \tag{3.15}$$

Here $[T]$ is the matrix of a variable that should be calculated and represents *degrees of freedom* of the element. Degrees of freedom in the model are the total number of unknown variables on each node(s).

Shape function(s) are equal to one at the specific node and zero at the other node(s). Moreover, the derivative is constant along the element, as shown in Fig. 3.6**.** The characteristics of other shape functions of different degrees and dimensions are found in detail in [76, 79].

The partial differential equation(s) (PDE) is transformed into integral form in order to be solved by FEM [77]. The outcome equations of FEM area, system of linear or nonlinear matrices which can be solved in order to find the final solution. Several different approaches which can be used to convert PDEs into FEM form. One of the most important forms is the *Method of Weighted Residual (MWR)*.

a) shape function variation b) shape function derivative

Fig. 3.6: Shape function properties

The governing differential equations for any system is as follows:

$$L(T) = 0 \ in \ \Omega \tag{3.16}$$

It is assumed that the trial function approximates the solution of Eq.(3.16):

$$T \approx \overline{T} = \sum_{i=1}^{n} a_i N_i(x) \tag{3.17}$$

Eq.(3.17) is substituted into Eq.(3.16)

$$L(\overline{T}) \neq 0$$

or (3.18)

$$L(\overline{T}) \neq R(residual)$$

The residual is multiplied by a proper function and integrated over the entire domain in order to specify the parameters $a_1, a_2, \ldots\ldots a_n$. Then:

$$\int_{\Omega} w_i(\boldsymbol{x}) R dx = 0 \tag{3.19}$$

where $w_i(x)$ is called the *weighting function*. Different methods are available to determine the weighting function which can satisfy Eq.(3.19). One of the most popular methods is the *Galerkin approximation* [77].

According to Eq.(3.19), a proper weighting function should be specified in order to convert continuity, Navier-Stokes and energy equations(3.1)-(3.5) into the FEM integral form as follows:

First choose the proper shape functions for velocity, pressure and temperature field as shown in Eq.(3.20)

$$\begin{aligned} u &= \sum N_i(x, y, z)u_i \\ v &= \sum N_i(x, y, z)v_i \\ w &= \sum N_i(x, y, z)w_i \\ p &= \sum N_{pi}(x, y, z)P_i \\ T &= \sum N_i(x, y, z)T_i \end{aligned} \tag{3.20}$$

where N_i and N_{pi} are the shape functions; N_{pi} is the function for the pressure and its degree is less than N_i [80]. Substitute Eqs.(3.1) to (3.5) and Eq.(3.19) into Eq.(3.19). The results are as follows:

Continuity equation:

$$\int_{\Omega} \left(\frac{\partial u}{\partial x} + \frac{\partial v}{\partial y} + \frac{\partial w}{\partial z}\right) N_{pi}\, d\Omega = 0 \tag{3.21}$$

Navier-Stokes equations:

$$\int_{\Omega} \left(u\frac{\partial u}{\partial x} + v\frac{\partial u}{\partial y} + w\frac{\partial u}{\partial z} + \frac{1}{\rho}\frac{\partial p}{\partial x} - \nu\left(\frac{\partial^2 u}{\partial x^2} + \frac{\partial^2 u}{\partial y^2} + \frac{\partial^2 u}{\partial z^2}\right) - F_x\right) N_i\, d\Omega = 0 \tag{3.22}$$

$$\int_{\Omega} \left(u\frac{\partial v}{\partial x} + v\frac{\partial v}{\partial y} + w\frac{\partial v}{\partial z} + \frac{1}{\rho}\frac{\partial p}{\partial y} - \nu\left(\frac{\partial^2 v}{\partial x^2} + \frac{\partial^2 v}{\partial y^2} + \frac{\partial^2 v}{\partial z^2}\right) - F_y\right) N_i\, d\Omega = 0 \tag{3.23}$$

$$\int_{\Omega} \left(u\frac{\partial w}{\partial x} + v\frac{\partial w}{\partial y} + w\frac{\partial w}{\partial z} + \frac{1}{\rho}\frac{\partial p}{\partial z} - v\left(\frac{\partial^2 w}{\partial x^2} + \frac{\partial^2 w}{\partial y^2} + \frac{\partial^2 w}{\partial z^2}\right) - F_z \right) N_i d\Omega = 0 \qquad (3.24)$$

Energy equation:

$$\int_{\Omega} \left(\rho Cp\left(u\frac{\partial T}{\partial x} + v\frac{\partial T}{\partial y} + w\frac{\partial T}{\partial x}\right) - k\left(\frac{\partial^2 T}{\partial x^2} + \frac{\partial^2 T}{\partial y^2} + \frac{\partial^2 T}{\partial z^2}\right) \right) N_i d\Omega = 0 \qquad (3.25)$$

The elements equations are combined and the boundary conditions (See sections 3.3.1-3.3.2) are applied; the results are written in matrix form [80] for both the velocity and temperature fields:

$$\begin{aligned} [K][U] &= [f] \\ [K][T] &= [f] \end{aligned} \qquad (3.26)$$

where $[K]$, $[U]$, $[T]$, and $[f]$ are the stiffness matrix, the vector of unknown velocity, the unknown temperature, and the force vector respectively.

Eq.(3.26) represents a system of linear (or nonlinear) equations which can be solved to determine the unknown variables. Where fluid properties are temperature-independent, hydraulic and energy equations can be solved separately. Moreover, both fluid and thermal equations are solved simultaneously when temperature-dependent properties are considered.

Generally, the finite element method can solve PDEs of the system of single, two or more materials systems. The density of the mesh elements should be increased if there is a sharp change in the variables through the boundaries. For example, if fluid flow in the microchannels experiences sharp velocity change near the walls then the density of the elements must be increased to capture this change.

3.3 COMSOL Multiphysics software

COMSOL Multiphysics (COMSOL for abbreviation in the consecutive sections) is commercial software that is based on the finite element method as a numerical technique. COMSOL uses Galerkin method to convert PDEs into FEM integral form [81]. COMSOL can also solve a single- or multi-physics problem, steady or transient

models with different boundary conditions and materials are built-in in the software library. The software also provides a facility for defining more material or the boundary conditions which are not available in the library.

Navier-Stokes Eqs.(3.1) and (3.4) and energy equation (3.5) are already available in COMSOL for steady and transient state simulations with different boundary conditions. Consequently, both physics can be imported into the COMSOL working environment and solved for different models. The present analysis compares the experimental with the numerical results of solving Navier-Stokes and energy equations for different systems.

3.3.1 Hydraulic boundary conditions

The following boundary conditions are adopted for Navier-Stokes [75]:

1. Non-slip boundary conditions for the solid-liquid interaction wall(s):

$$\boldsymbol{u}=0 \tag{3.27}$$

2. Inlet (or outlet) velocity boundary conditions:
   - The first inlet velocity boundary condition can be defined as a velocity vector with three-dimensional components along x-, y-, and z-axis as follows:

$$\boldsymbol{u}_o=U\boldsymbol{i}+V\boldsymbol{j}+W\boldsymbol{k} \tag{3.28}$$

   - The second inlet (or outlet) velocity boundary condition is defined as a normal inlet velocity:

$$\boldsymbol{u}=-\boldsymbol{n}U_o \tag{3.29}$$

The normal vector $\boldsymbol{n}$ pointed to the outlet of the boundary.

3. Outlet (or inlet) boundary condition

$$p=p_o \tag{3.30}$$

representing imposed pressure on the outlet boundary.

4. Simulating large models in FEM consumes time and computer memory. Therefore, it is recommended to exploit the benefit of symmetry in geometry to cut the size to half or even a quarter. Consequently, the following symmetry boundary condition can be applied at the cut plane:

$$\begin{aligned} \boldsymbol{u}\cdot\boldsymbol{n}&=0 \\ \boldsymbol{t}\cdot\left(-p\boldsymbol{I}+\mu(\nabla\boldsymbol{u}+(\nabla\boldsymbol{u})^{T})\right)\boldsymbol{n}&=0 \end{aligned} \tag{3.31}$$

there $\boldsymbol{t}$ is the tangential vector to the boundary. Eq.(3.31) shows that there is no motion through the symmetry boundary and shear stress equals to zero.

5. Open boundary is considered when the system is open to large volume and no constraints are applied:

$$\begin{aligned} \boldsymbol{u}\cdot\boldsymbol{n}&=0 \\ \mu(\nabla\boldsymbol{u}+(\nabla\boldsymbol{u})^{T})\boldsymbol{n}&=0 \end{aligned} \tag{3.32}$$

3.3.2 Thermal boundary conditions

Convection-conduction boundary conditions are as follows:

1. General heat flux applied to the boundary:

$$\boldsymbol{n}\cdot(k\nabla T)=q_o+h\left(T_{inf}-T_o\right) \tag{3.33}$$

where q_o represents the heat flux normal to the boundary, which could be heat generated from the electric heater. COMSOL has a direct option to apply q_o[W/m^2] at the specified boundary. The second term represents the heat transfer by convection for the surfaces that are exposed to free or forced convection imposed by fluid flow. Convection heat transfer coefficient h can be defined as a numeric value or as a function of geometry dimensions. Standard functions of h are installed in COMSOL library, such as vertical and horizontal surface. T_{inf} [^{o}C] is the environment temperature.

2. Absolute temperature T_o can be defined at any inlet, outlet or external boundary.
3. The contact boundary between different surfaces can be represented by "Thin Thermally Resistive Layer", which is defined as [75]:

$$-\boldsymbol{n}(-k_d \nabla T_d) = -\frac{k_{res}}{d_{res}}(T_u - T_d)$$
$$-\mathbf{n}\ (-k_u \nabla T_u) = -\frac{k_{res}}{d_{res}}(T_d - T_u) \quad (3.34)$$

where k_d and k_u are the thermal conductivities of the contacted surfaces [W/m K]. k_{res} [W/m K] and d_{res} [m] are thermal conductivity and thickness of the thin layer between surfaces. T_u and T_d represent the contact surface temperatures [K]. This boundary condition is adopted when *pair* is assumed between the surfaces.

4. COMSOL assumes that the boundary between two different materials is a continuous boundary:

$$-\boldsymbol{n}_1\boldsymbol{q}_1 - \boldsymbol{n}_2\boldsymbol{q}_2 = 0 \quad (3.35)$$

This condition is applicable for solid-liquid interaction surfaces where heat transfer by conduction is equal to convective heat flux.

5. Convective boundary which is normally applied at exit boundary defined as

$$\boldsymbol{q}_{cond} \cdot \boldsymbol{n} = -k \nabla T \cdot \boldsymbol{n} = 0,\ \boldsymbol{q}_{conv} \cdot \boldsymbol{n} = \rho\ Cp\ \nabla T\ \boldsymbol{u} \cdot \boldsymbol{n} \quad (3.36)$$

Eq.(3.36) assumes an adiabatic condition at solid exit boundaries and that all heat is totally extracted by convection.

6. Another important boundary condition is the *periodic boundary conditions.* This type of boundary is applicable when the model consists of multiple similar small cells. Studying one cell reveals the behaviour of the full model. The model in Centeo TG40 in Chapter 5 consists of many small similar chambers in each row, so studying one single chamber is sufficient to understand the performance of the full system. Boundary conditions of a single chamber with neighbours are periodic.

Other boundary conditions which are available on COMSOL as a direct input value or function can be defined by inserting the proper function at the specific boundary.

3.3.3 Material properties

Water has been chosen as a working liquid for the numerical analysis of Chapter 5 and Chapter 6. The properties of water are available in the COMSOL library.

Therefore, the water properties built-in to COMSOL have been compared with available data in the literature, as shown in Fig. 3.7-Fig. 3.9.

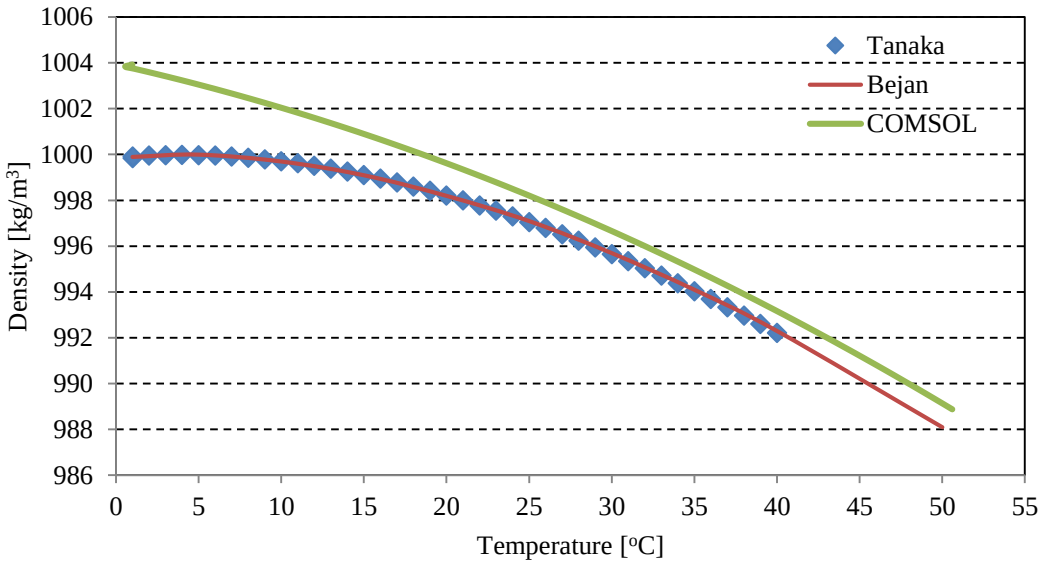

Fig. 3.7: Density of water with temperature according to the equation built in COMSOL library and the data in Bejan [74] and Tanaka [82].

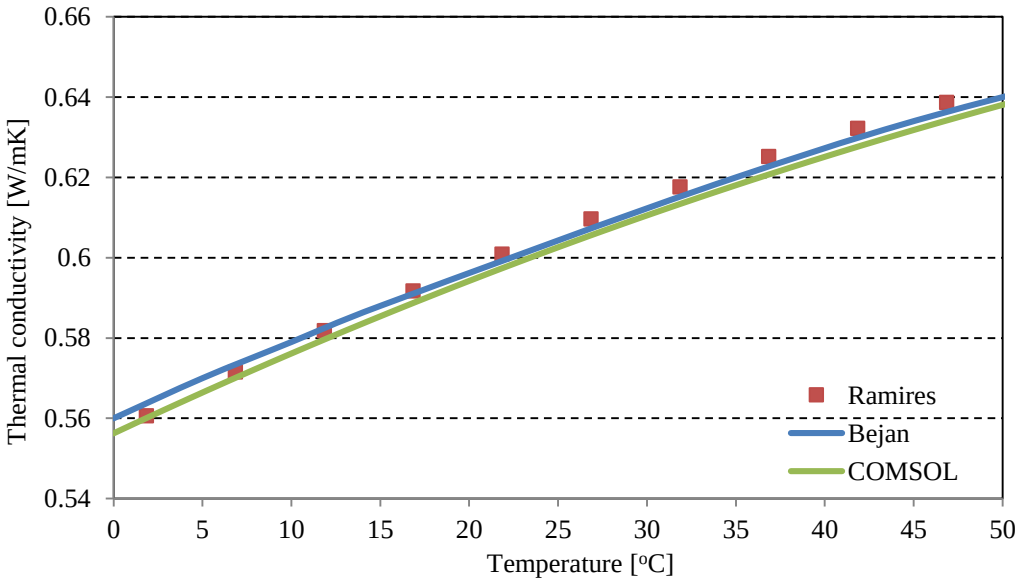

Fig. 3.8: Thermal conductivity of water with temperature according to the equation built in COMSOL library and the data in Bejan [74] and Ramires [83].

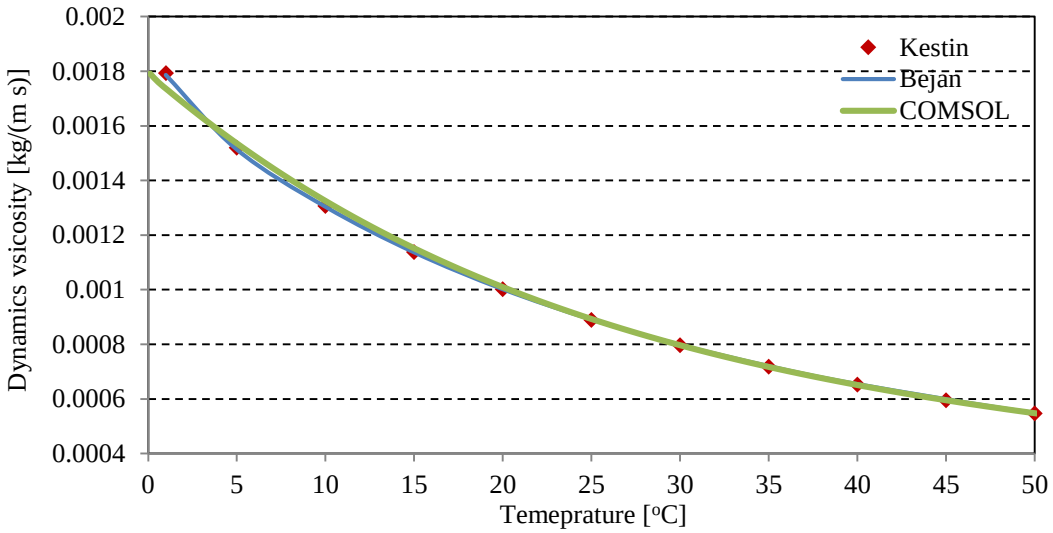

Fig. 3.9: Dynamic viscosity of water with temperature according to the equation in COMSOL library and the data in Bejan [74] and Kestin [84].

A good match is observed between the thermal conductivity and viscosity of water extracted from the COMSOL built-in equations and that of the references mentioned in Fig. 3.8 and Fig. 3.9. However, COMSOL overestimates water density in comparison with the references mentioned in Fig. 3.7. For this reason, the water properties of Bejan [74] have been selected for the subsequent analysis. The there is no major change in the specific heat capacity of water within the temperature range in the consecutive chapters, then its value is taken to be equal to 4178[J/kg K] [74].

3.3.4 Meshing process, element and shape function

The meshing process may be performed on a specific point, edge, boundary, or subdomain, or for full geometry. The tetrahedral element is the default element for the free mesh process. The tetrahedral element is chosen for irregular geometry such as curved surfaces or the existence of small objects. The shape function in COMSOL is called *Lagrange shape*. Lagrange quadratic function P2-P1 is the default function in COMSOL. The Lagrange quadratic function P2-P1 is mixed between the second and first order degrees of the shape function. It is recommended for the Navier-Stokes equation to choose a second order polynomial for the velocity distribution and first order pressure [75]. Quadratic shape function is also used for solving energy equations.

Different solvers are available in COMSOL, depending on selected physics and linearity, model dimensions, the number of degrees of freedom and the available computer memory. COMSOL solvers check the PDEs linearity and split it into several groups of linear equations in order to solve the equations [85].

3.4 Solved examples by COMSOLv3.5a

Two benchmark cases have been initially studied using COMSOL in order to assess the applicability of COMSOL and to be familiar with the working environment of the software.

3.4.1 Two-layers stacked microchannel

The following case is considered by Wei [1]; both experimental and numerical solutions are used to solve flow, convection and conduction process for a two-layer heat sink. The finite volume method (FVM) has been used as a numerical method to solve model equations. Silicon and water were used as the substrate material and cooling liquid respectively. Fig. 3.10 to Fig. 3.12 represent the boundary conditions and dimensions of the tested model; Table 3.1gives the details of the model dimensions.

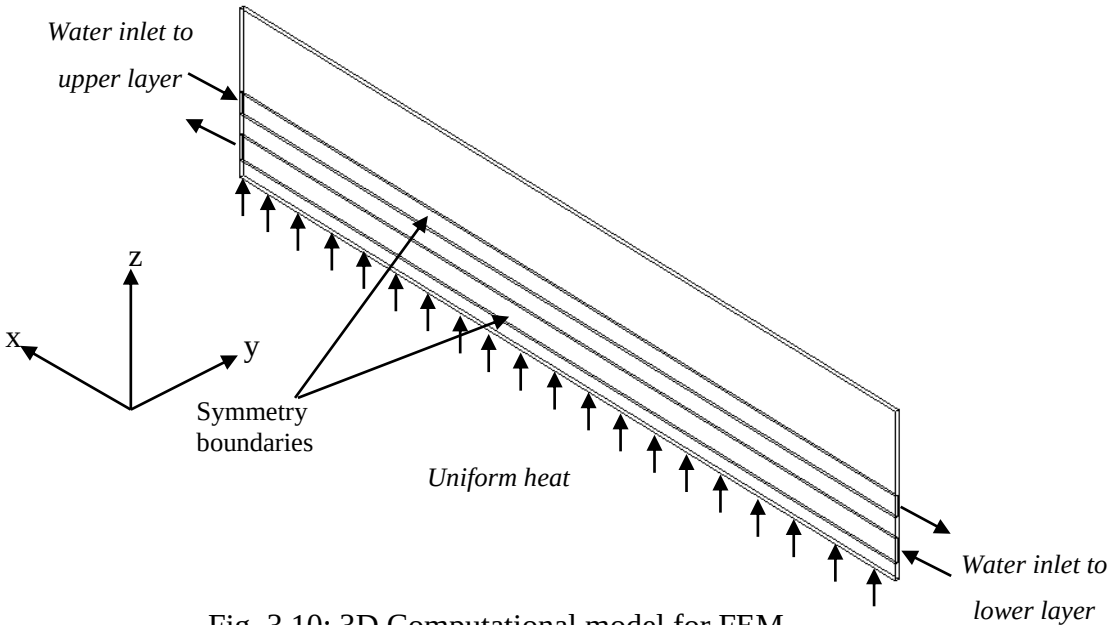

Fig. 3.10: 3D Computational model for FEM.

Heat is supplied at the lower boundary of the model. The counter flow was studied where hot fluid enters at the lower channel while the cold fluid passes through the upper channel.

Table 3.1 Micro channel dimensions (mm) of the model [1].

Channel Length	H_{c1}	H_{c2}	H_1	H_2
10	0.284	0.243	0.48	0.48
W_{c4}	W_u	W_{c1}	W_{c2}	W_{c3}
0.053	0.1	0.056	0.054	0.061

The flow is assumed to be laminar and steady-state for both heat transfer and incompressible fluid. The following boundary conditions are considered:

Lower layer:
Inlet conditions: Inlet temperature = 295.55 [K], Uniform inlet velocity = 0.4421[m/s].

Outlet conditions: Pressure = 0 (atmospheric), convective heat transfer.

Upper water:
Inlet conditions: Inlet temperature = 295.67 [K], Uniform inlet velocity = 0.5127 [m/s].

Outlet conditions: Pressure = 0 (atmospheric pressure), Convective heat transfer.

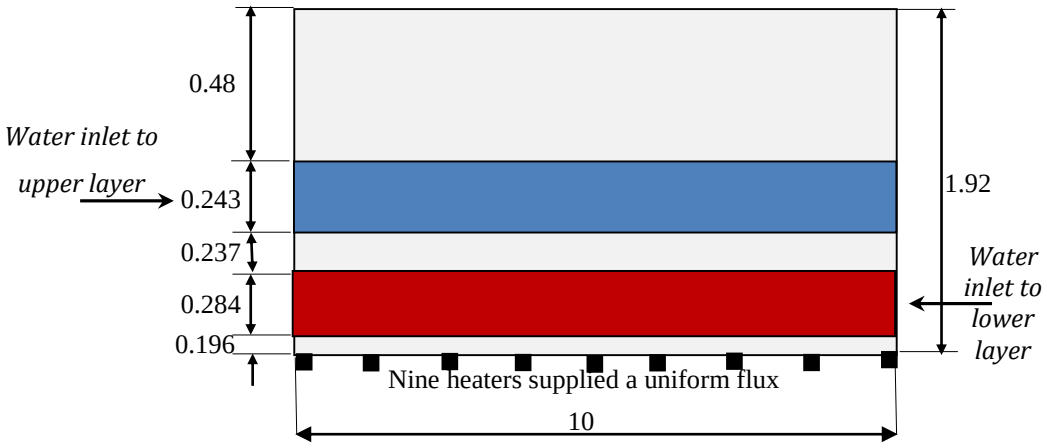

Fig. 3.11: 2D cross section about z-x plane of the computational model for FEM. All dimensions are in mm.

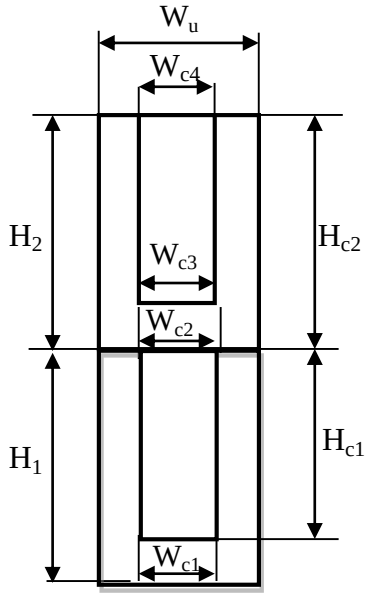

Fig. 3.12: Dimensions of stacked micro channels [1].

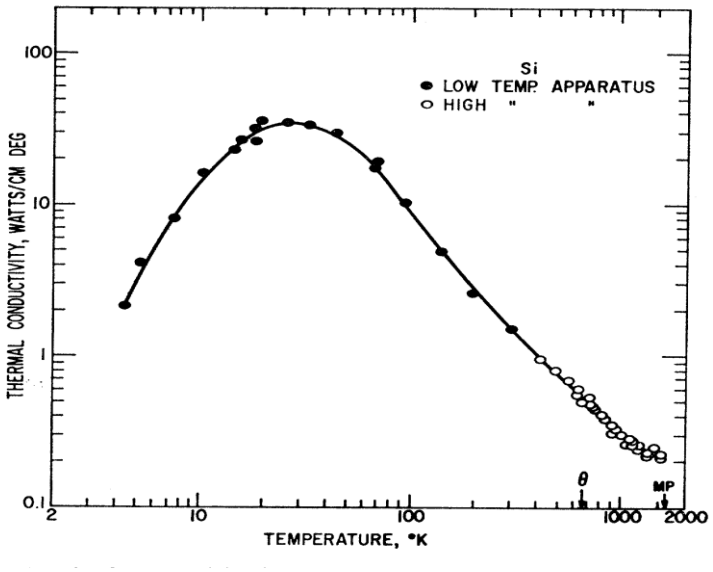

Fig. 3.13: Silicon thermal conductivity [86].

A constant heat flux of 70 W/cm^2 (5% of the heat input is lost as radiation to the environment) is applied at the lower boundary. The other boundaries are considered as non-slip wall and insulated boundaries for fluid flow and heat transfer respectively. According to these boundary conditions, the flow is laminar for both fluids. Temperature-dependent properties for water and silicone are considered for numerical

analysis. Water properties vary according to the temperature, as shown in Fig. 3.7 to Fig. 3.9, while heat capacity is considered as a constant value (4178 [J/kg K]) [74]. Silicon thermal conductivity is extracted from Glassbrenner and Slack [86] as shown in Fig. 3.13. The other properties of the silicon are constant ρ = 2330 [kg/m^3] and Cp=712 [J/kg K] [87].

3.4.1.1 Numerical analysis and results

A half geometry has been investigated due to symmetry about the *z-x* plane, as shown in Fig. 3.10. A symmetry boundary condition is applied to the model *z-x* section. A tetrahedral element with the Lagrange quadratic shape function is considered for the model. Lagrange quadratic shape function is recommended for the flow problem by COMSOL [75], and was also adopted by Parsa [88] and Adrover [89]. COMSOL automatically checks the mesh element quality, which may affect the solution results. A good mesh quality is obtained for the present model, as shown in Fig. 3.14. COMSOL calculates mesh quality for the tetrahedral element as follows:

$$Q = \frac{72\sqrt{3}V}{(h_1^2+h_2^2+h_3^2+h_4^2+h_5^2+h_6^2)^{3/2}} \tag{3.37}$$

where V is the volume and h_1, h_2, h_3, h_4, h_5, and h_6 are the edge lengths of the element [75]. Mesh quality should be $Q>0.1$ in order to avoid the effect of low quality on the solution.

Fig. 3.15 shows a good agreement between the COMSOL results and numerical and experimental results of Wei [1] for the heat sink bottom surface temperature. Moreover, Fig. 3.15 demonstrate also the mesh independent solution of the model when COMSOL is used with different number of mesh element. Another model validation is shown in Fig. 3.16 and Fig. 3.17, which demonstrate temperature distribution at different cross-sections along the channel axis for two mass flow rates. As shown from these figures, a good agreement is found between the results of the present numerical investigation performed by COMSOL and those of [1].

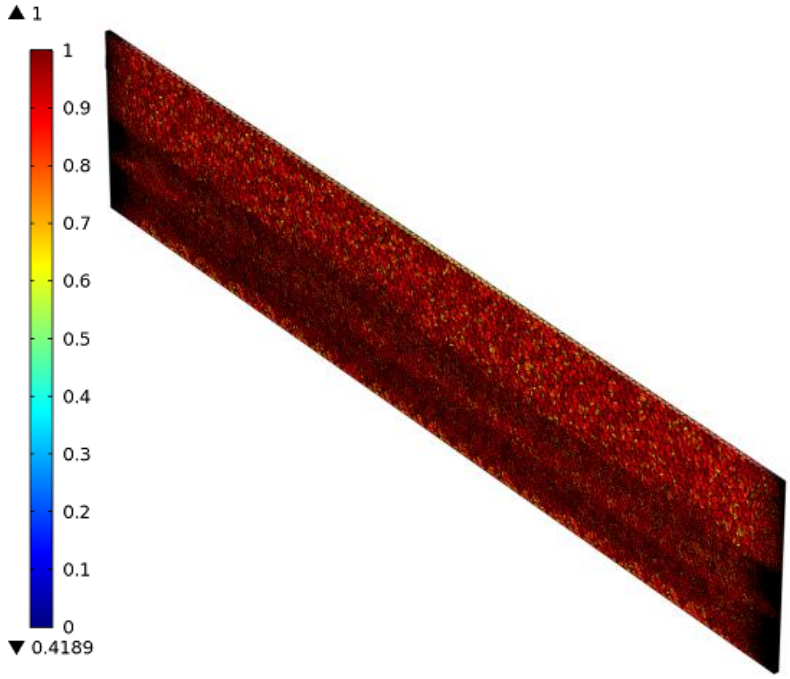

Fig. 3.14: Two-layers model mesh quality.

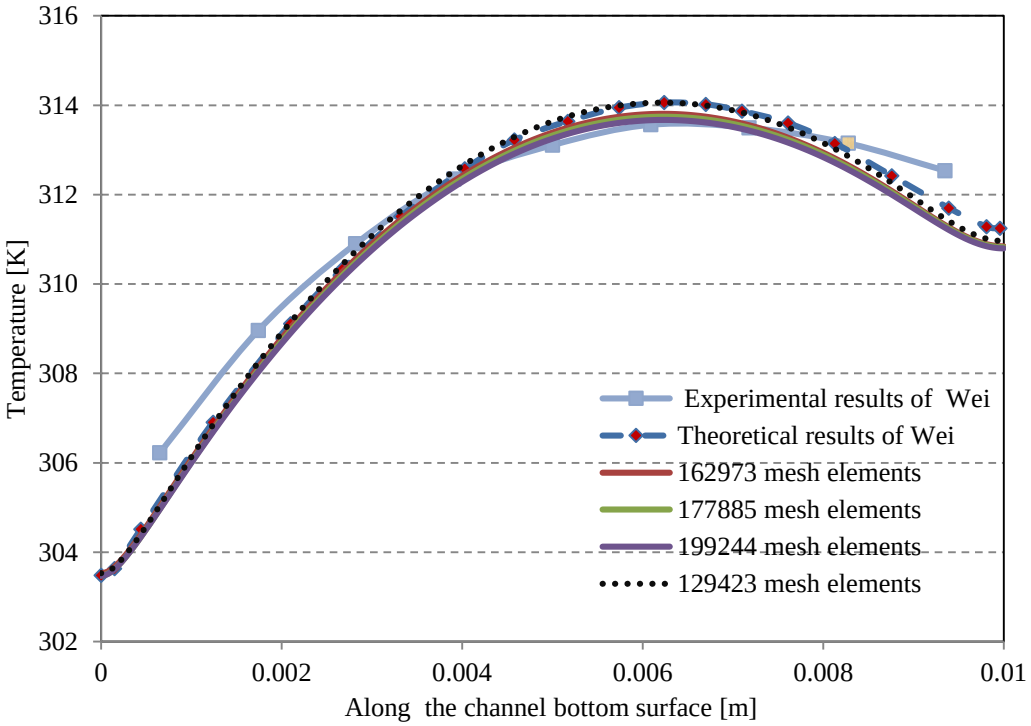

Fig. 3.15: A comparison between the temperature along the channel between the present numerical model and results of Wei [1] for amass flow rate of 83ml/min.

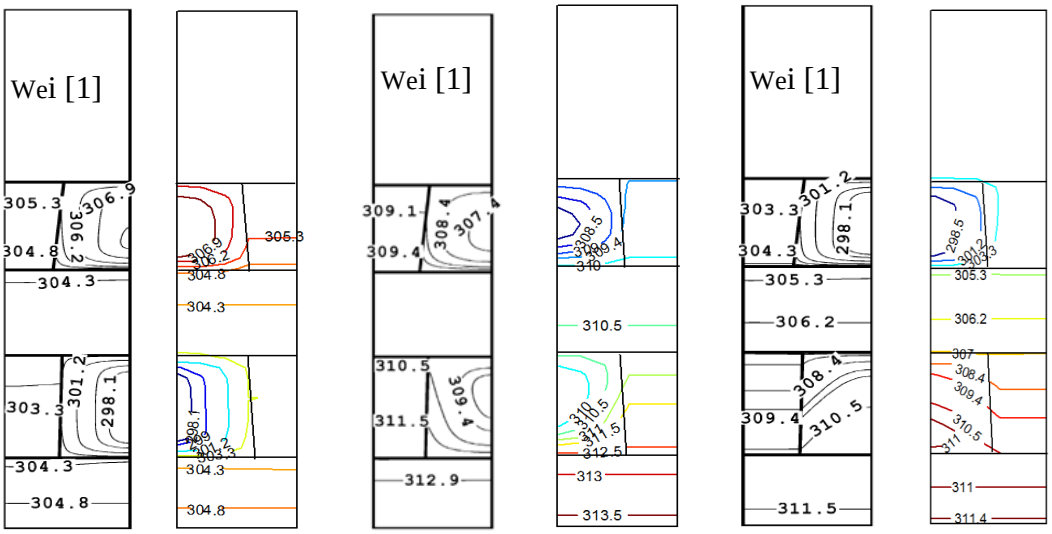

x= 0.65mm x=5mm x=9.35mm

Fig. 3.16: A comparison between the present model and Wei [1] for temperature contours for cross-section at different axial locations for a mass flow rate of 83ml/min.

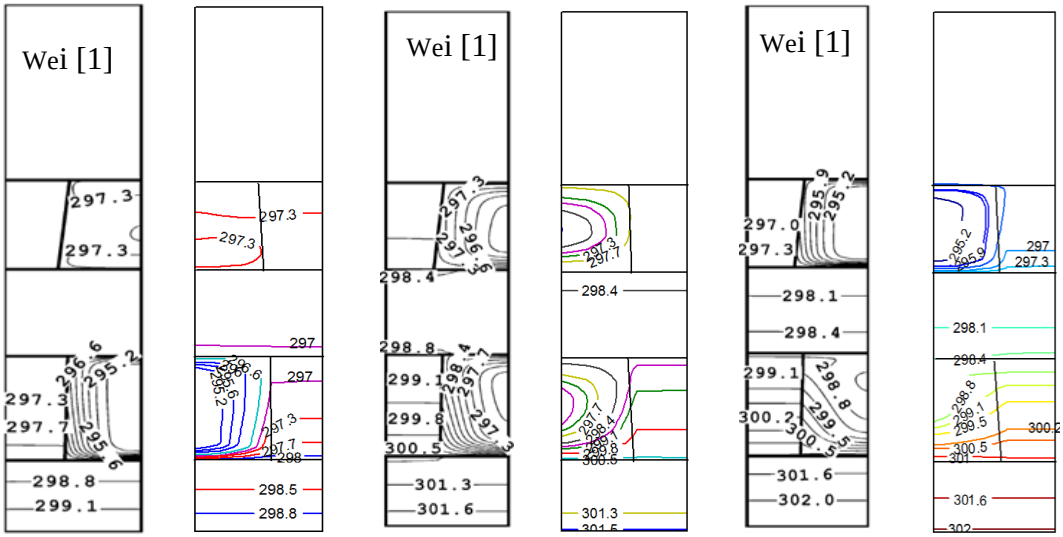

x= 0.65mm x=5mm x=9.35mm

Fig. 3.17: A comparison between the present model and Wei [1]for temperature contours for cross-section at different axial locations for amass flow rate of 300 ml/min.

3.4.2 Three-dimensional microchannel

The second case represents a single microchannel used for cooling a chip. A constant heat flux is supplied at the upper boundary, as shown in Fig. 3.18. This case was adopted and investigated by the finite difference numerical method by Qu and Mudawar [90]. Fig. 3.19 shows a cross-section of the channel with all dimensions. Single phase, steady state, incompressible, laminar, and fixed properties are given for both water and silicon, which is used as a substrate material with no radiative heat losses. The thermal properties of water and silicon are chosen from sections 3.3.3 and 3.4.1.

Boundary conditions

Inlet boundary conditions are: Reynolds number 140, temperature 20^{o}C, uniform heat flux is 90W/cm^2 on the top heat sink surface, and all other surfaces are assumed to be adiabatic (See Fig. 3.18 and Fig. 3.19).

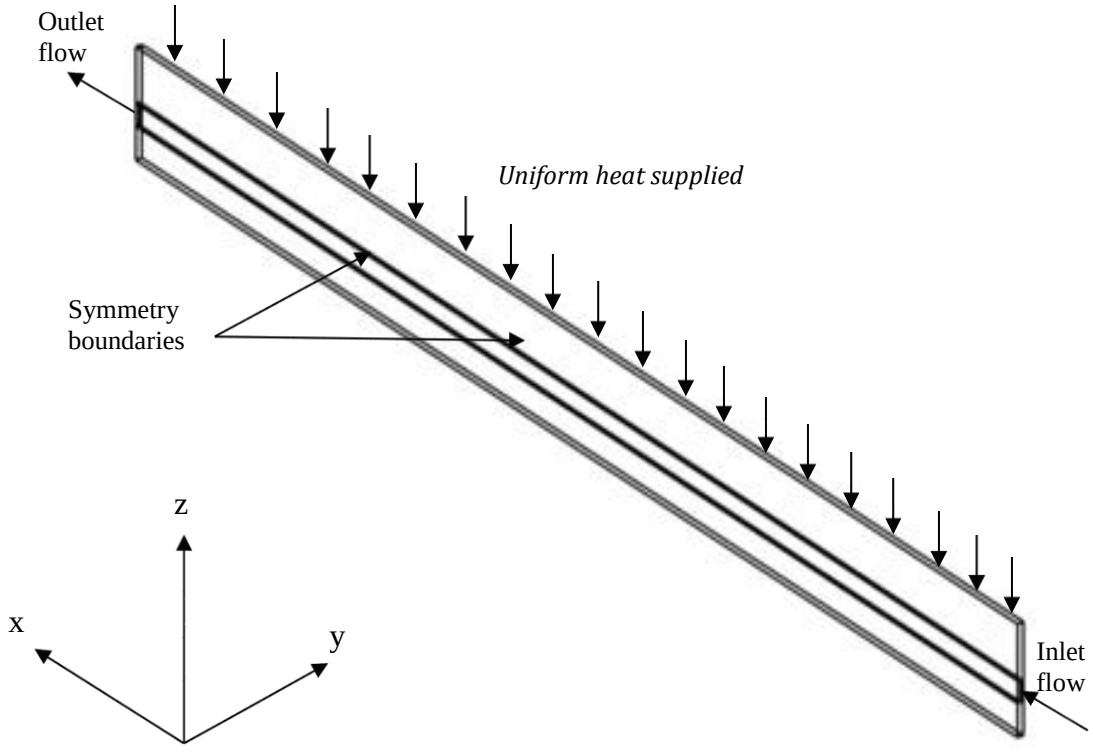

Fig. 3.18: Three-dimensional geometry of the heat sink, 10 mm in length.

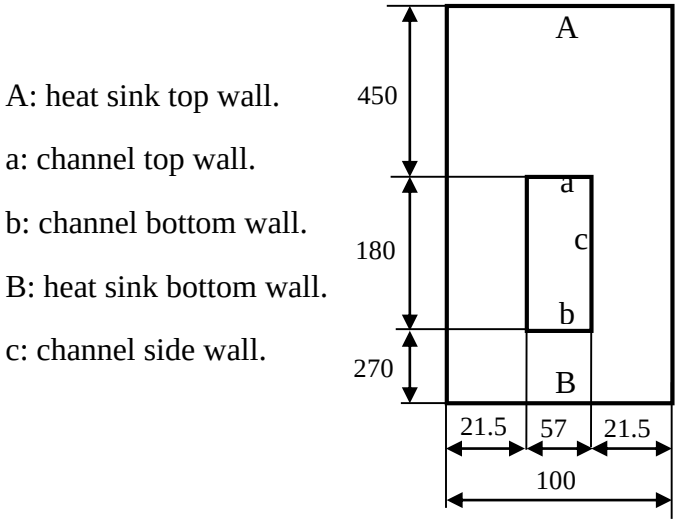

Fig. 3.19: Cross-section of the channel; all dimensions are in µm.

3.4.2.1 Numerical analysis and results

A tetrahedral element with Lagrange quadratic shape function is chosen to analyse the model with COMSOL. A mesh-independent solution is confirmed by comparison of the bottom channel surface temperature with a different number of mesh elements, as shown in Fig. 3.20. A good mesh quality is achieved for this model, as shown in Fig. 3.21. Convergence criterion for the relative error is set at 10^{-6}.

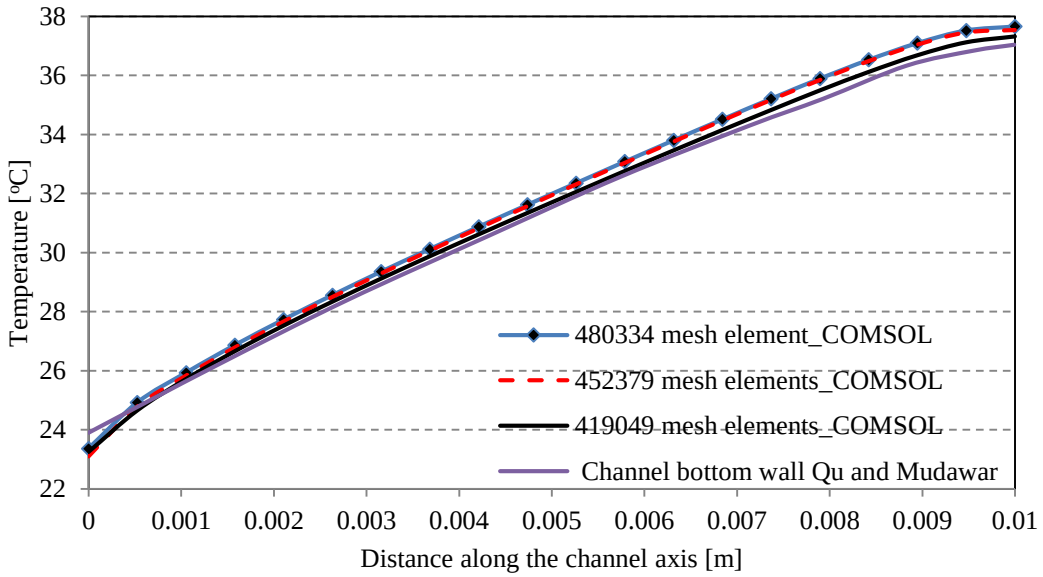

Fig. 3.20: Mesh-independent solution for the channel bottom wall temperature result of Qu and Mudawar [90].

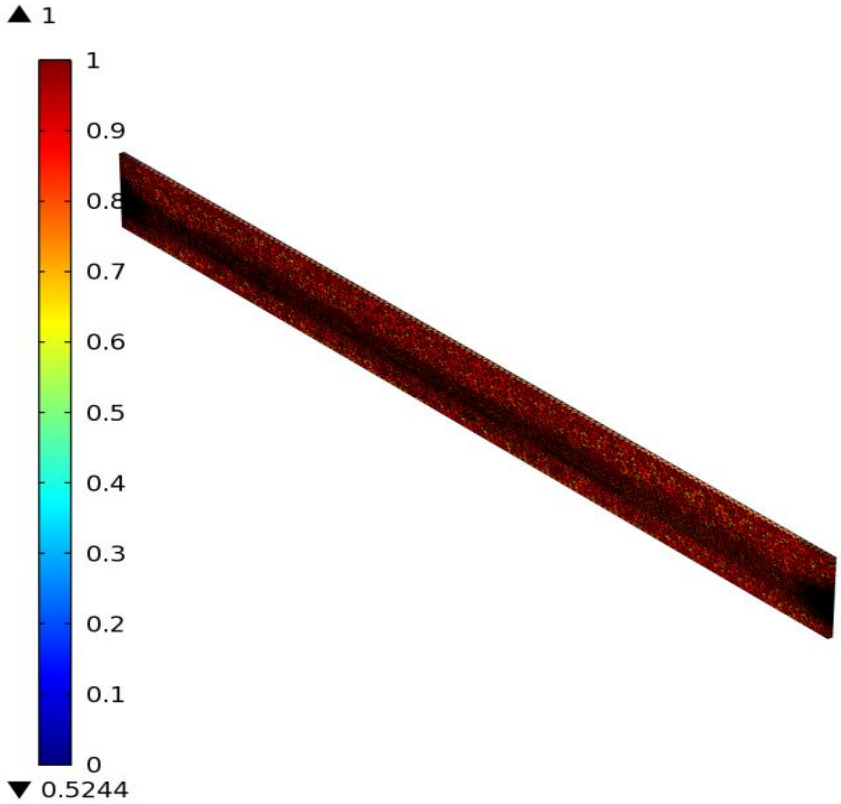

Fig. 3.21: Single channel model mesh quality.

The average temperatures of the walls along the axial distance for both top, side and bottom walls are calculated from:

$$T_{w,avg(x)} = \frac{1}{L}\int_{L} T_w dl \tag{3.38}$$

where $T_{w,avg(x)}$ [K] represents the average temperature at a specific axial distance *x*, *L* (for side, top, bottom channel walls) wall width, and T_w [K] temperature distribution along the wall's perimeter at a specific x-axis location.

Fluid bulk temperature is calculated from:

$$T_{b,avg} = \frac{\int \rho T u dA}{\int \rho u dA} \tag{3.39}$$

As can be seen in Fig. 3.22 and Fig. 3.23 that a good match is achieved between the results of the present study and those of [90] for the average temperature distribution

for the top and bottom walls of the channel and the heat sink. Furthermore, there is a good agreement for the fluid bulk temperature results, as shown in Fig. 3.24.

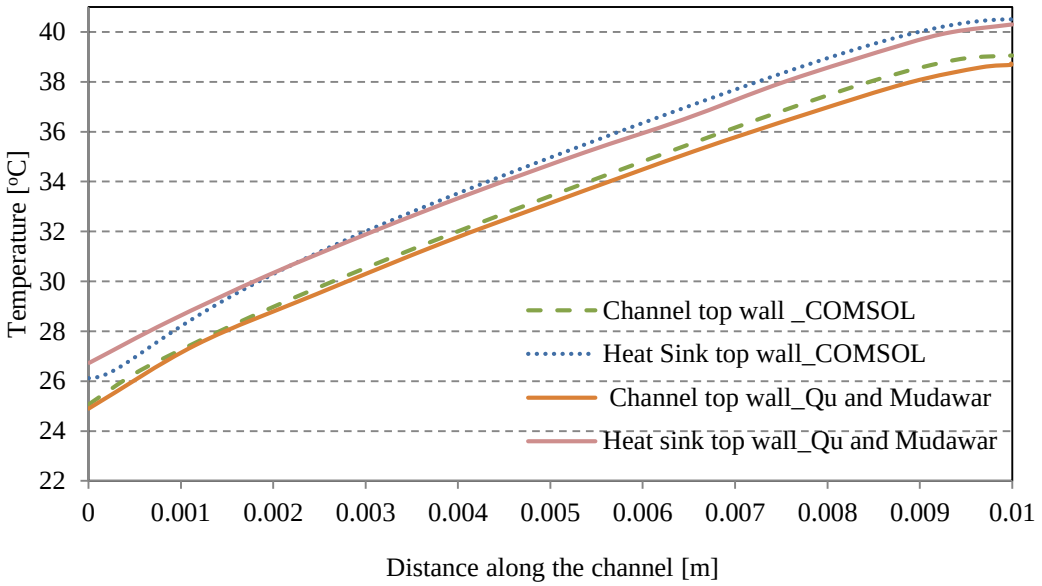

Fig. 3.22: Comparison between the COMSOL (dashed lines) and Qu and Mudawar [90] (solid lines) results for the temperature distribution along the axial axis of the channel and heat sink to top walls.

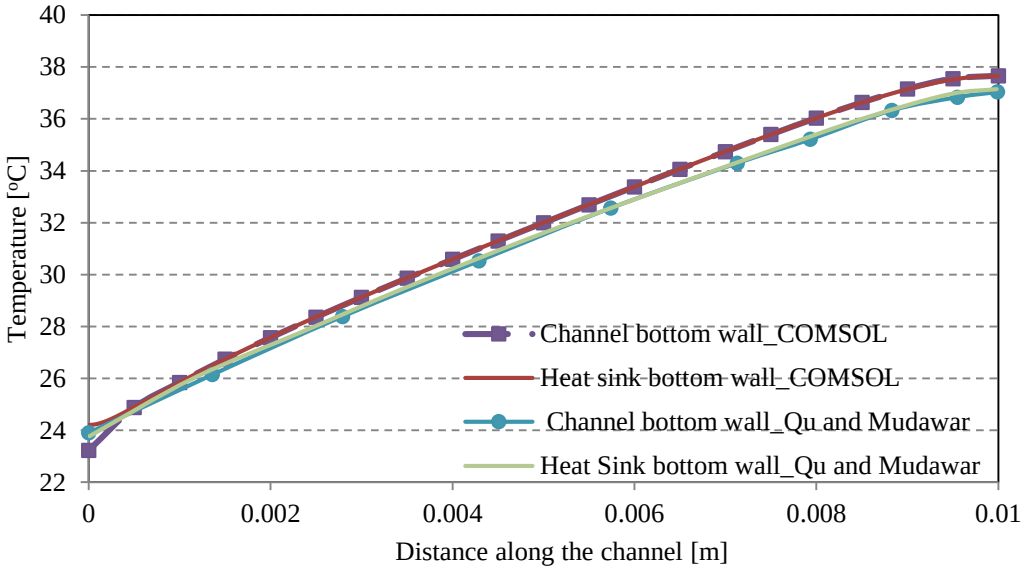

Fig. 3.23: Comparison between the COMSOL (dashed lines) and Qu and Mudawar [90] (solid lines) results for temperature distribution along the channel axial axis of the channel and heat sink bottom walls.

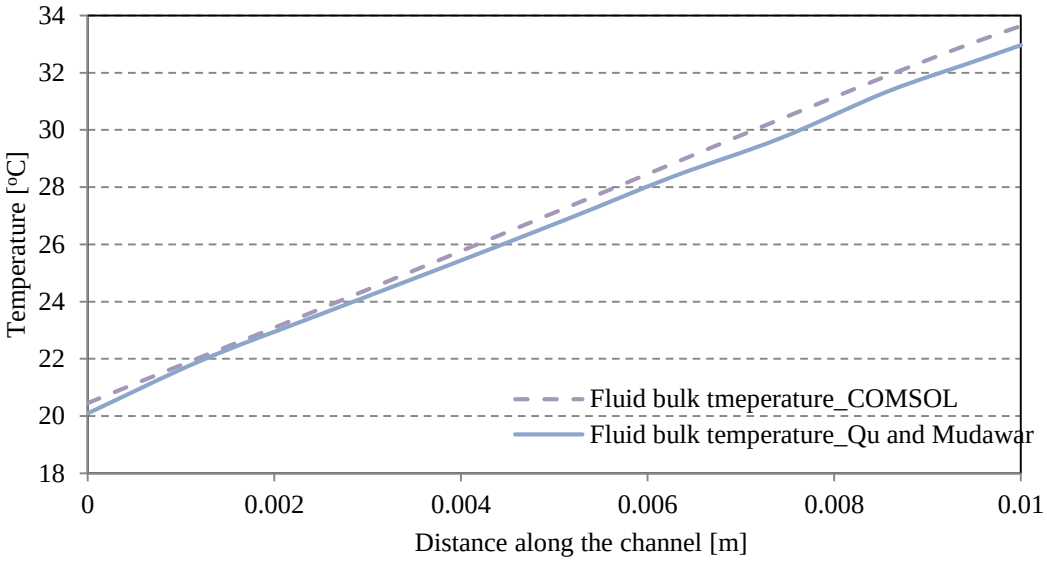

Fig. 3.24: Comparison between the COMSOL (dashed line) and Qu and Mudawar [90] (solid line) results for bulk temperature distribution along the channel axial axis.

Heat flux results to the liquid water of Qu and Mudawar [90] from top, side, and bottom channel walls confirm the validity of the COMSOL model, as shown in Fig. 3.25 to Fig. 3.27.

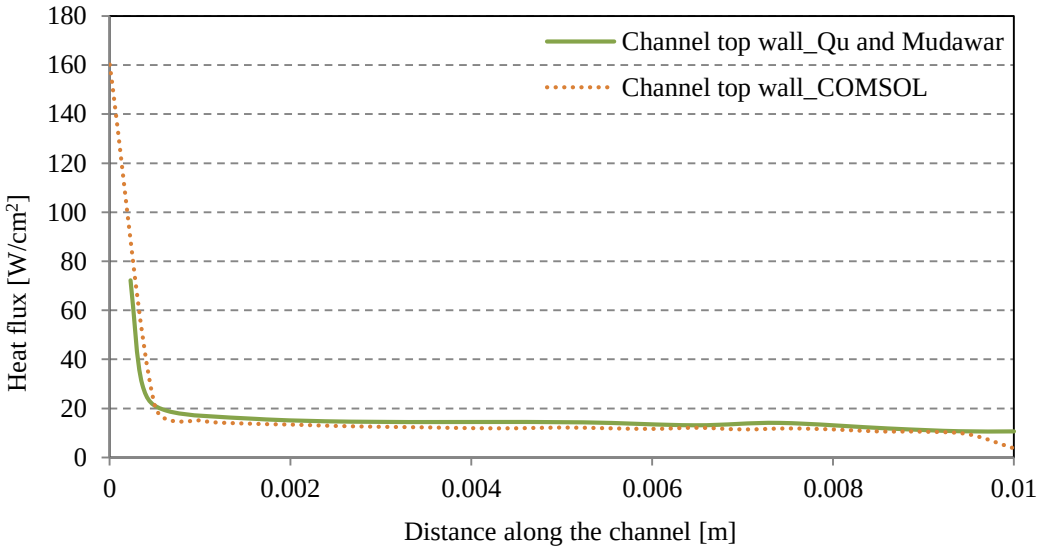

Fig. 3.25: Comparison between the COMSOL (dashed line) and Qu and Mudawar [90] (solid line) results for heat flux distribution along channel top wall.

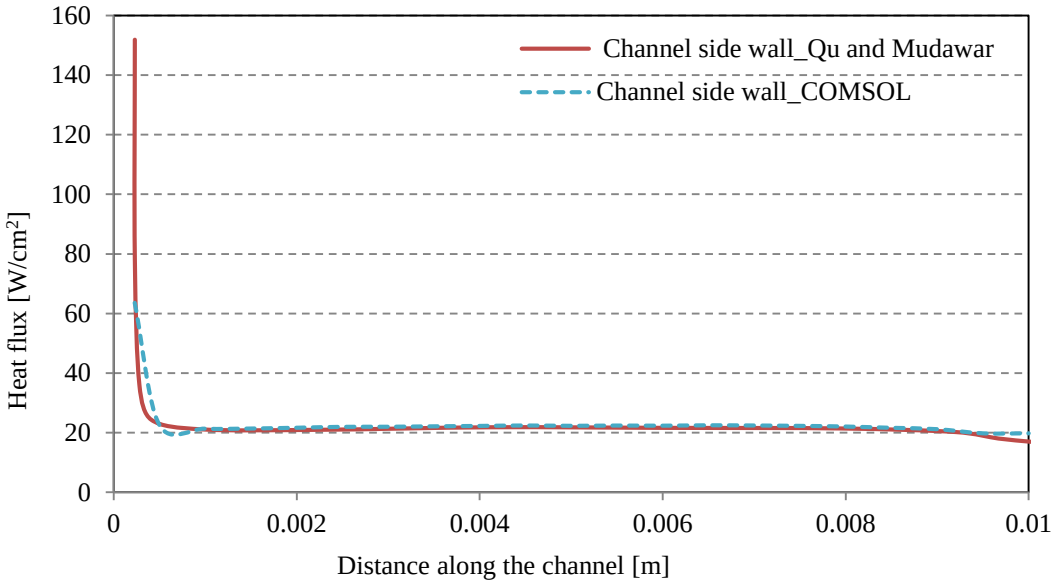

Fig. 3.26: Comparison between the COMSOL (dashed line) and Qu and Mudawar [90] (solid line) results for heat flux distribution along channel side wall.

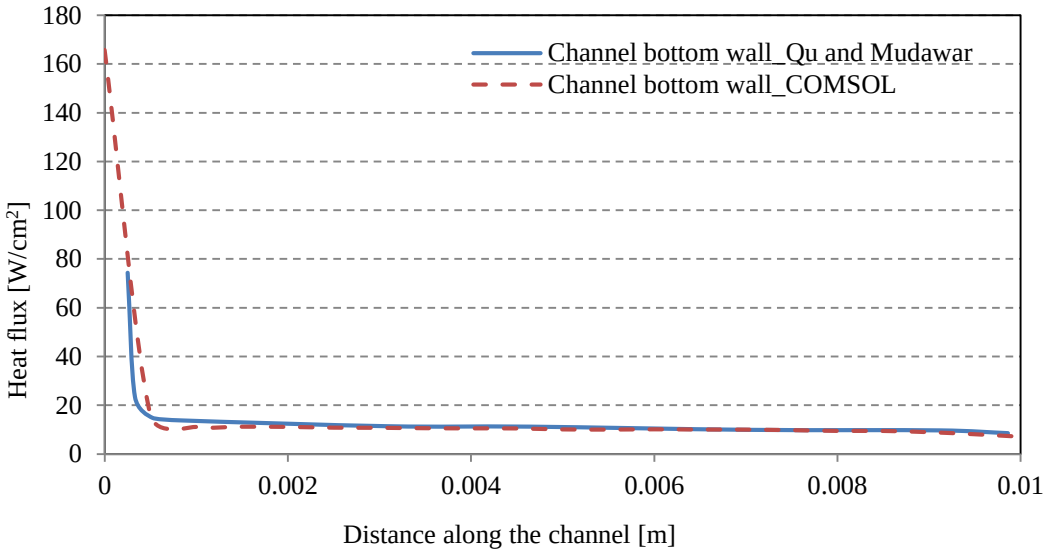

Fig. 3.27: Comparison between the COMSOL (dashed line) and Qu and Mudawar [90] (solid line)(dashed lines) results for heat flux distribution along channel bottom wall.

The results of Fig. 3.22 to Fig. 3.27 are substituted into Eq.(3.40) to calculate the average heat flux and average Nusselt number [90] :

$$Nu = \frac{D_h}{k_f} \frac{q''}{T_{w,avg} - T_{b,avg}} \tag{3.40}$$

where D_h[m] is the hydraulic diameter, q''[W/m^2] is the average perpherial heat flux at a specific axial location, k_f [W/mK] fluid thermal conductivity. Results for Nu_{ave} are shown in Fig. 3.28 to Fig. 3.30. There is a good agreement with the present study.

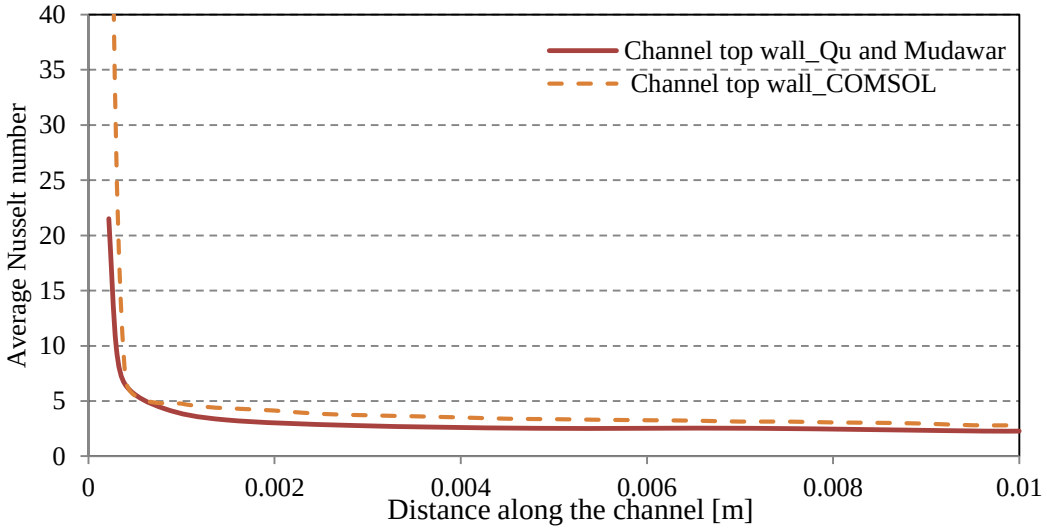

Fig. 3.28: Comparison between the COMSOL (dashed line) and Qu and Mudawar [90] (solid line) results for average Nusselt number along the channel top wall.

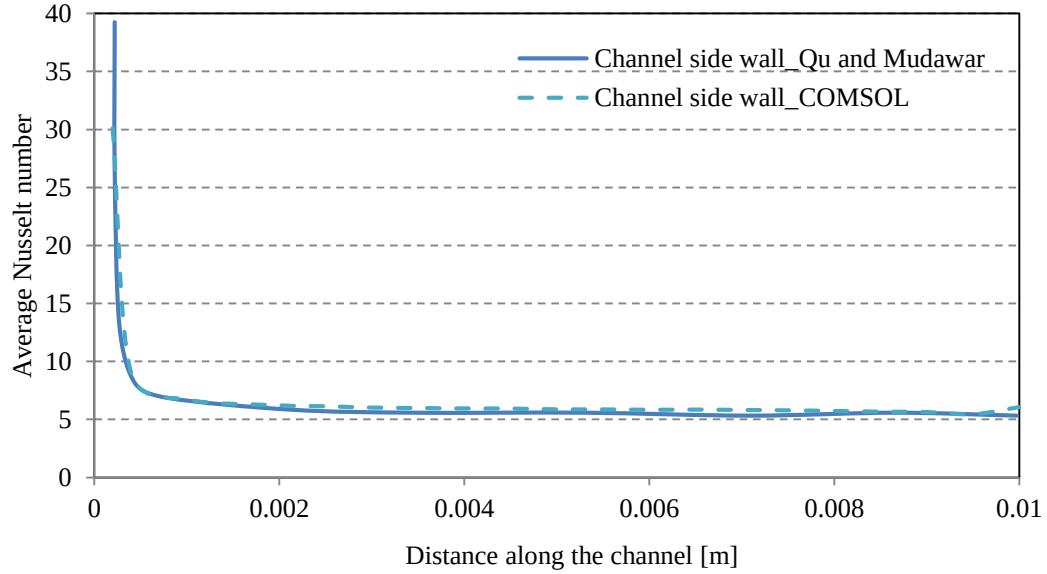

Fig. 3.29: Comparison between the COMSOL (dashed line) and Qu and Mudawar [90] (solid line) results for average Nusselt number along the channel side wall.

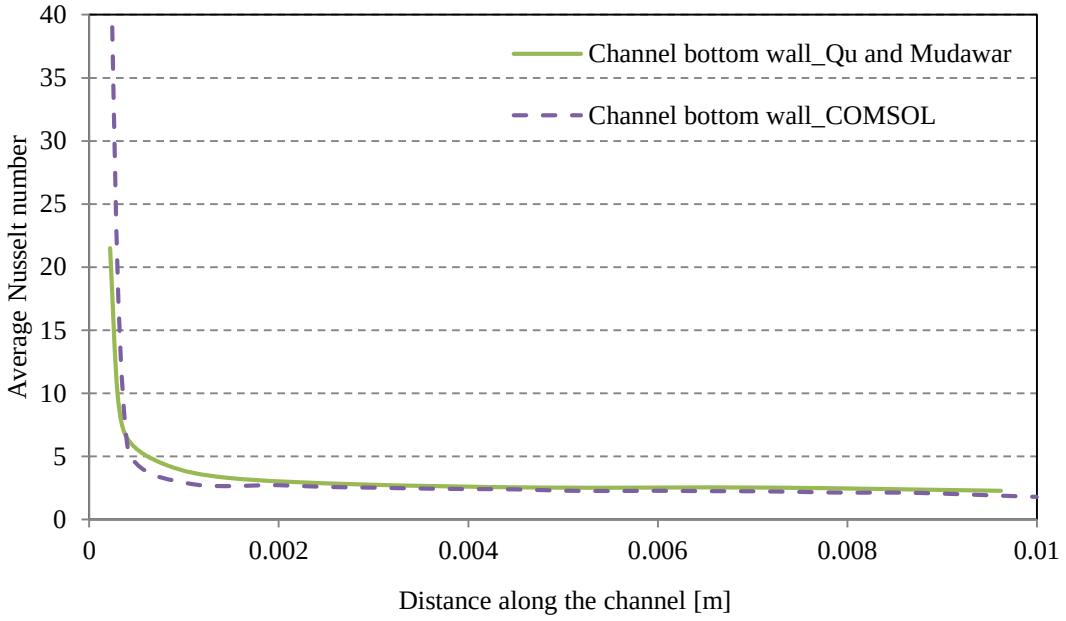

Fig. 3.30: Comparison between the COMSOL (dashed line) and Qu and Mudawar [90] (solid line) results for average Nusselt number along the channel bottom wall.

3.5 Conclusions

Two cases of the microchannel with uniform heat flux supplied have been studied [1, 90]. The first microchannel model has been analysed numerically using FVM [1], while the finite difference method is adopted by Qu and Mudawar [90] to study the second model. Both cases studied the thermal and hydraulic performances of the flow through microchannels. Similar cases will be discussed through the preceding chapters. similar Multiphysics software based on the finite element method was adopted to analyse the models numerically. According to the comparison of the numerical and experimental results, COMSOL is appropriate software to solve conjugate heat transfer problems with a high degree of accuracy.

Chapter 4

Effects of Thermocouple Electrical Insualtion on the Measurement of Surface Temperature

The objective of this work is determine the effect of stripping thermocouple electrical insulation on surface measurement. Analytical, numerical, and experimental analyses have been performed to investigate the effect of different stripped lengths on temperature measurement of surface.

Two sizes of thermocouple type K, 80μm and 200μm,with different stripped lengths (0 mm, 5mm, 10mm, 15mm and 20mm)were used to measure different Peltier surface temperatures of 4ºC, 8ºC, 15ºC, 25ºC and 35ºC. The thermocouple wires were extended vertically and exposed to natural convection from the external environment. A thermocouple was attached to a micrometer and pressed against the surface to measure the temperature without fixing the probe with any additional material. The thermocouple was connected to a TC08 pico log data acquisition system to convert the readings using computer software.

A model of equivalent single wire was chosen instead of a two-wire model of the thermocouple to simplify the analytical analysis. Analytical modelling of thermocouple wires assumed that each wire is similar to a vertical very long fin, with its end temperature equal to the environmental temperature.

Analytical study proved that 20mm of totally bare or totally insulated wires has a negligible effect on heat flux rate due to convection to (or from) thermocouple wires.

Maximum heat flux rate around the insulated cylindrical cross-section occurs where the diameter including insulation reaches a value is called *critical radius.* Critical radius depends on the cylinder thermal conductivity and heat transfer coefficient with the outside environment [91]. However, the heat transfer coefficient of natural convection around the thermocouple wire (including insulation) varies with diameter [74]. As a consequence of these analytical results of thermocouple wire with insulation confirmed that there is no specific value of the critical radius. Heat flux rate around

thermocouple wires continuously increases with wire diameter, even where this is larger than the critical radius (or diameter).

Numerical simulation was performed on a two wires model by using COMSOL Multiphysics software with finite element method. The results also confirmed that there is a negligible effect from the electrical insulation. Moreover, experimental results supported the analytical and numerical results and revealed that the size of the thermocouple causes an impact on temperature measurement.

4.1 Experimental techniques

4.1.1 Experimental set up

The Peltier effect was found by Peltier in 1834 [92]. When an electric current passes through two connected dissimilar materials, heating or cooling effects are generated, depending on the current direction. A basic operating circuit is shown in Fig. 4.1(a-b), consisting of two semiconductor materials, n-type and p-type, connected together.

The cooling effect occurs when the current flows from n-type to p-type, while heating effect occurs when the current flows back from p-type to n-type. Peltier effect is related to a *Peltier coefficient* which controls heating or cooling effect.

The temperature-controlled surface consisted of a conventional Peltier device, with one side attached to a large heat sink and the other side exposed to the environment with a small PT100 thermometer adhered using high thermal conductivity glue, as shown in Fig. 4.2. The temperature working range of PT100[2] is between -50ºC-500ºC and the full dimensions are shown in Fig. 4.3. Fig. 4.4 shows the electrical connections made to the Peltier plate, consisting of two power supplies, a Peltier plate, a switch (to reverse the current) and a PT100 signal conditioning circuit feeding into a voltmeter.

The temperature of the Peltier plate was controlled by changing the current supplied (magnitude and current direction). The PT100 thermometer was connected to the

[2] The model number of PT100 is F4050B which was supplied by OMEGA, the tolerances in temperature and resistance (at 0ºC) are ±(0.3+0.005t)[ºC] and ±0.12[Ω] respectively. See website for details: http://www.omega.co.uk/pptst/F1500_F2000_F4000.html.

voltmeter and a TC08 pico log data acquisition system in order to independently record the Peltier surface temperature.

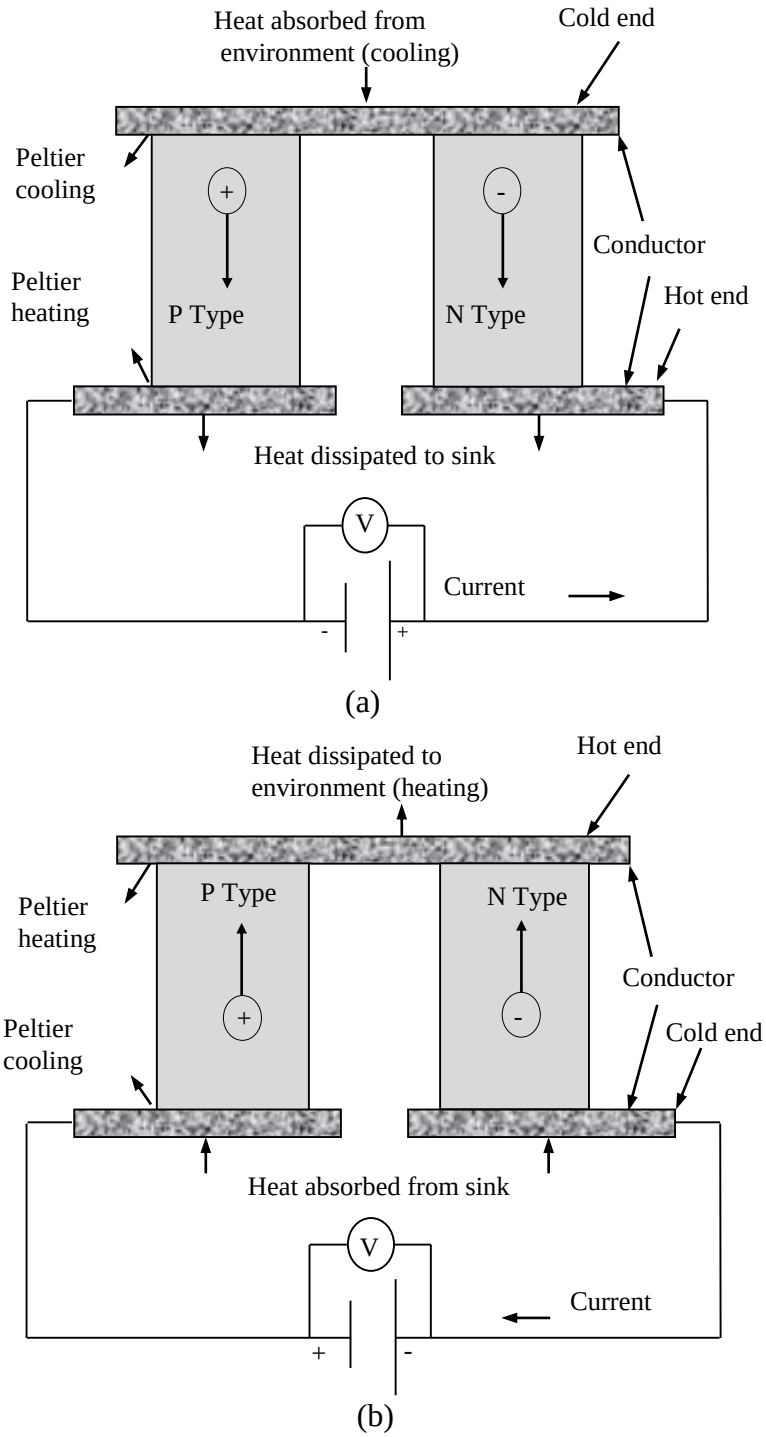

Fig. 4.1: Diagram showing the Peltier effects: (a) cooling effect and (b) heating effect [92].

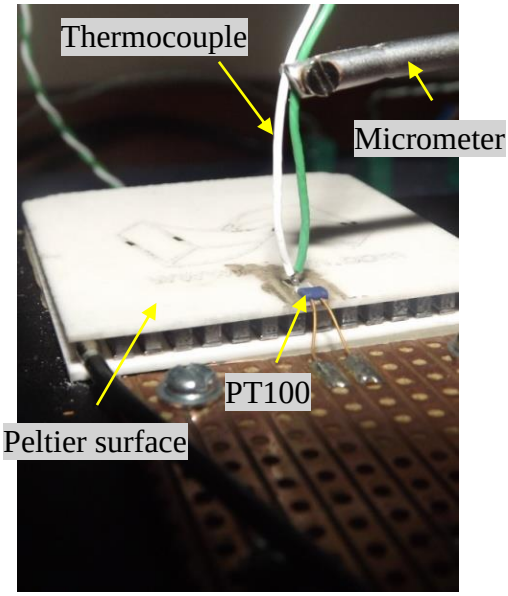

Fig. 4.2: Thermocouple probe in contact with Peltier surface.

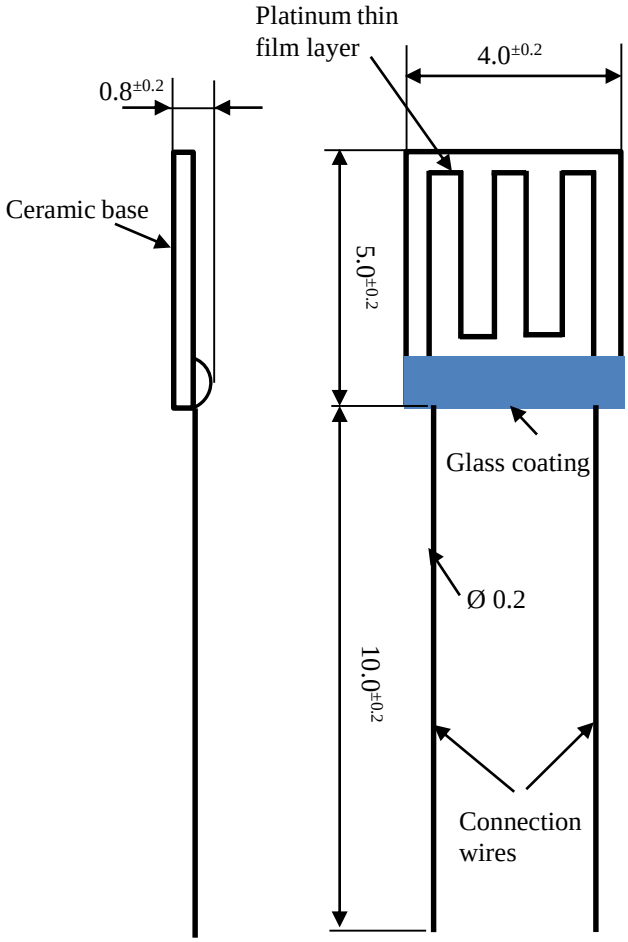

Fig. 4.3: PT100 temperature sensor dimensions. All dimensions are in mm.

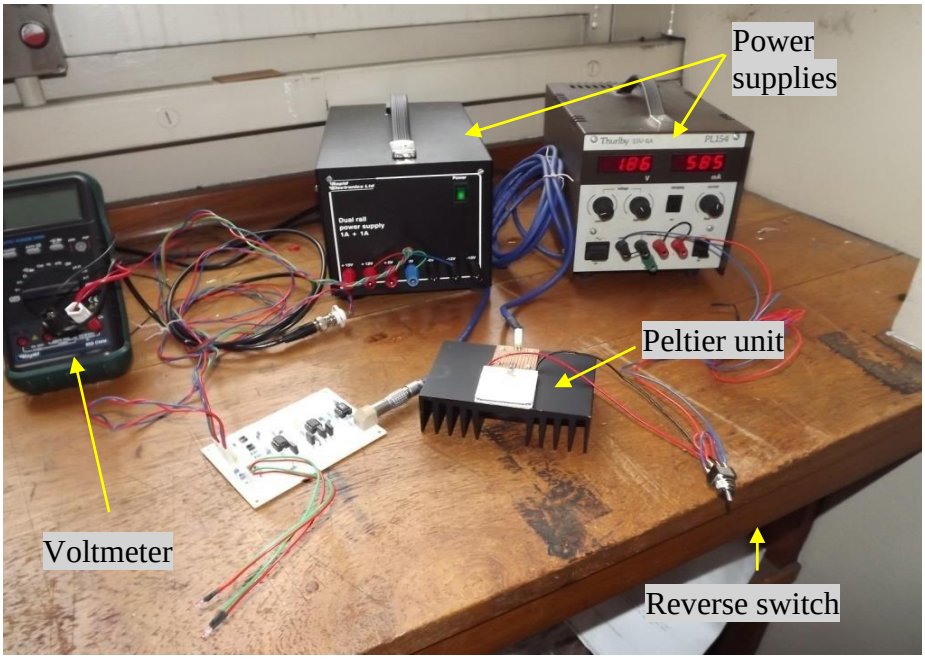

Fig. 4.4: Electrical connections to the Peltier plate.

4.1.2 Measurement procedure

Each thermocouple was fixed to a Z-positioning micrometer stage and pressed down against the Peltier surface until the thermocouple reading became steady-state (See Fig. 4.2). The two thermocouples used were type-K with bare wire diameters of 80µm (250µm including PFA insulation) and 200µm (500µm including PTFE insulation); see Table 4.1 and Table 4.2 (See section 4.4).

The aim of this study is to investigate the effect of thermocouple impact on temperature measurement. Therefore, two specific sizes and types of thermocouple were used. Any type or size of thermocouple may also be used, but their effect will vary depending on the size and properties of the wires as well as their insulation.

The average environmental temperature was recorded while the Peltier surface temperature (as measured using the PT100) was set to 4°C, 8°C, 15°C, 25°C, and 35°C as the surface temperature (measured by the thermocouple) was recorded. The insulation on the thermocouple wires was stripped off to various lengths from the probe: 5mm, 10mm, 15mm, and 20mm, to investigate the effect on the temperature measurement. Five runs were performed for each stripped length to confirm the reproducibility in each of the experiments. The position of PT100 is in same level of

Peltier surface, therefore it was assumed that PT100 has no impact on temperature measurement of the surface.

Table 4.1 Thermocouple type K material properties.

Thermocouple wire components	Thermocouple wires properties		Thermocouple insulation properties	
	Chromel [93]	Alumel [93]	80µm [PFA][94]* part no. Z2-K-2 X 5	200µm [PTFE][95]* part no. ZO-PFA-K-1 X 5
Thermal conductivity [W/(m K)]	19.2 (k_{w1} or k_{w2})	29.77(k_{w1} or k_{w2})	0.3 (k_{ins})	0.25 (k_{ins})
Density [kg/m^3]	8730	8600	7900	2130-2230
Heat capacity [J/(kg K)]	447.7	523.34	500	1000

*manufacturer Labfacility.

The uniformity of the Peltier surface temperature was confirmed by a photograph using a thermal image camera FLIR A325 setup shown in Fig. 4.5. Fig. 4.6 shows the approximate uniform temperature distribution for the Peltier surface.

The temperature at spots ‘1’ and ‘2’ was 33.2^{o}C and 33.8^{o}C respectively. The thermal imaging camera detects thermal radiation from a surface and then converts it to an image that can be seen by eye [96]. However, thermal radiation depends on the emissivity of the surface, which in turn depends on the surface temperature, material and characteristics [91]. The radiation from the surface can be influenced by the reflection from the surroundings, which can be detected by a thermal camera. Therefore, a slight difference in surface temperature can be seen in Fig. 4.6.

Fig. 4.5: Thermal imaging picture for the Pltier device using FLIRA325 camera.

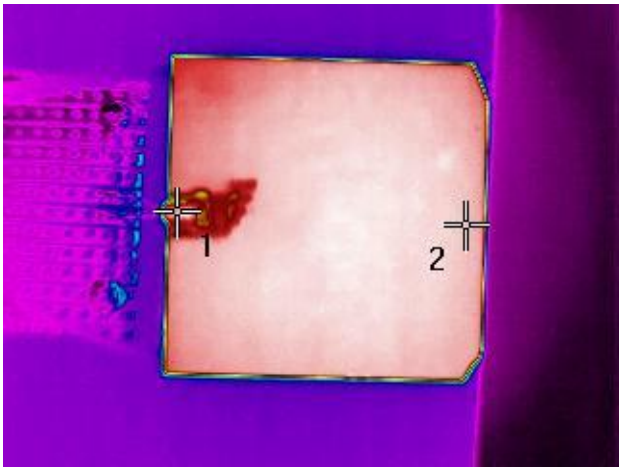

Fig. 4.6: Temperature distribution of Peltier surface of spots 1 and 2 temperature was 33.2^{o}C and 33.8^{o}C respectively.

4.1.3 Thermocouple calibration

A thermocouple calibration process was performed by comparing the thermocouple reading when fully submerged in crushed ice and boiling water with the standard water freezing and boiling temperature respectively, as shown in Fig. 4.7 (a-b) [93]. A Pyrex beaker of two litres was filled with crushed ice, and the thermocouple probe was immersed for a sufficient length of time to avoid any effect of outside temperature on the reading. Additionally, during the calibration process a proper distance was left

between the thermocouple probe and the bottom of the beaker to prevent the effect of heat transfer with the beaker standing base. Freezing or water boiling standard temperature was considered (to 2 d.p.) to be those at standard atmospheric conditions (e.g. 1 atm) where water boils at 99.98^{o}C[3] and freezes at 0^{o}C[97].

(a) (b)

Fig. 4.7: Thermocouple calibration: (a) Comparison with water boiling point, (b) Comparison with water freezing point .

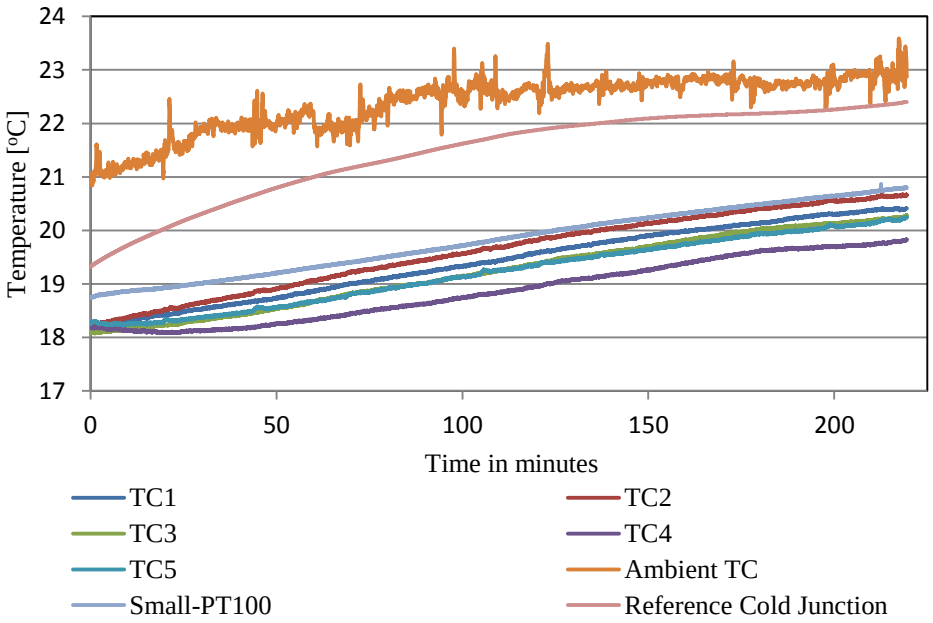

Fig. 4.8: PICO log data acquisition cold junction compensation.

[3]The boiling point of 99.98°C was used in accordance with the strict two-point calibration of Vienna Standard Mean Ocean Water (VSMOW) and as used elsewhere in the literature, see e.g. R. Tillner-Roth and D. G. Friend, J. Phys. Chem. Ref. Data, 1997, vol. 27, No. 1, 199.

The TC08 was connected to a laptop via a USB cable to record the readings. It was recommended by Pico Technology Technical Support to unplug the laptop from its power supply to avoid incorrect earthing that may impact on the TC08, resulting in inaccurate measurement [98]. One advantage of the TC08 is that it incorporates cold junction compensation, eliminating measurement variations caused by fluctuations in environmental temperature during the experiments, as shown in Fig. 4.8 [99].

4.2 Experimental results

Fig. 4.9 (a-b) to Fig. 4.13(a-b) show the results of different exposed wire lengths for both sizes of thermocouple, 80µm and 200µm. The vertical axis indicates the difference between the thermocouple measured temperature and the Peltier surface temperature (PT100 measured), while the horizontal axis represents the Peltier surface temperature. The maximum temperature drop is equal to 2^{o}C and 4^{o}C for 80µm and 200µm respectively, with an environmental temperature of 13^{o}C and Peltier surface temperature of 35^{o}C.

Experimental working conditions (atmospheric: 13^{o}C and 1 bar) were essentially constant for each of the thermocouple sizes and every exposed wire length. During the experiments and due to the temperature difference between Peltier surface (4^{o}C-35^{o}C) and the environment (13^{o}C), heat was conducted along the thermocouple wires. Fig. 4.9 to Fig. 4.13 show the impact of thermocouple on temperature measurement versus actual Peltier temperature. The plots in Fig. 4.9 to Fig. 4.13 should have zero slopes if there is no impact of thermocouple; however, this is clearly not the case. It can also be seen that the 200µm thermocouple has a higher conduction effect than the size 80µm for different stripped lengths, as shown in Fig. 4.14. The reason for this is that the larger diameter provides a larger heat transfer area and consequently the heat flux to or from the thermocouple is higher. During the experiment the thermocouple probe was pressed against the Peltier surface in order to increase the contact area with the surface and minimise the thermal contact error [91]. The probability of getting the same contact area in each experiment for the size 200µm is greater than for the size 80µm because of the probe size. Therefore, it can be seen in Fig. 4.9 to Fig. 4.13 that the experimental error of the 80µm is larger than for the 200µm, and consequently the

error bar is larger. Moreover, change in the Peltier surface temperature leads to a change in the air circulation around the thermocouple probe. Consequently, the combined effect of the air circulation (due to the varying surface temperature) and the effect of the probe contact area with the surface cause a different experimental error, resulting in a different error bar length, as shown in Fig. 4.9 to Fig. 4.13.

Generally, we can conclude from these results that the effect of the stripped insulation of any length on the temperature measurement is small enough to be neglected (within 0.5^{o}C), or, more accurately, the experimental error for a typical system is higher than the effect of the stripped insulation [3]; see Fig. 4.15. In addition, the temperature difference between the environment and the working range of the Peltier surface (4^{o}C-35^{o}C) is not great enough to have a strong effect on the temperature measurement (See Fig. 4.33).

4.3 Thermocouple impact versus experimental errors

The precision of any experimental measurement is minimizing the total difference between the real value and measured value. There are two types of the experimental errors: the first is a *systematic (or bias) error* and the second is a *random (or precision) error* [100, 101]. The systematic error represents approximately a constant value during all the runs of the experiments. This error can be predicted by calibrate the device with standard reference point. The random error can be caused by several reasons such as human fluctuations, device fluctuations, and other unknown sources. The random error can be called sometimes by *repeatability error* or *precision error.* The precision of any experimental results is evaluated by the degree of scattering of the experimental data around the mean value in the *normal* (or *Gaussian*) *error distribution* [100]. The normal error distribution gives the probability of the *repeated* experimental data to be within a certain interval. The width of the interval can be determined the value of the standard deviation. The probability of experimental data falling within one, two and three standard deviation are 68.27%, 95.45% and 99.73% respectively [100].

According to above discussion, the calibration process was performed to predict the bias error, see in section 4.1.3. Whereas, the error bars in Fig. 4.9 to Fig. 4.13 represent

the scattering of the experimental data within ±one standard deviation (i.e. the probability was 68.27%). The impact of the thermocouple on temperature measurement can't be classified as a bias or random error because it depends of the physical application and experimental conditions. In the present study, the impact of the thermocouple can be specified by the difference between thermocouple measurement temperature and PT100 temperature record. The Y-axis in Fig. 4.9 to Fig. 4.13 represents the impact of the thermocouple on measurement. Different case is shown in Chapter 5 where the actual value of the temperature can't be measured directly without disturbing the system. Therefore, a comparison has been made between the experimental and numerical results to predict the heating impact of the thermocouple.

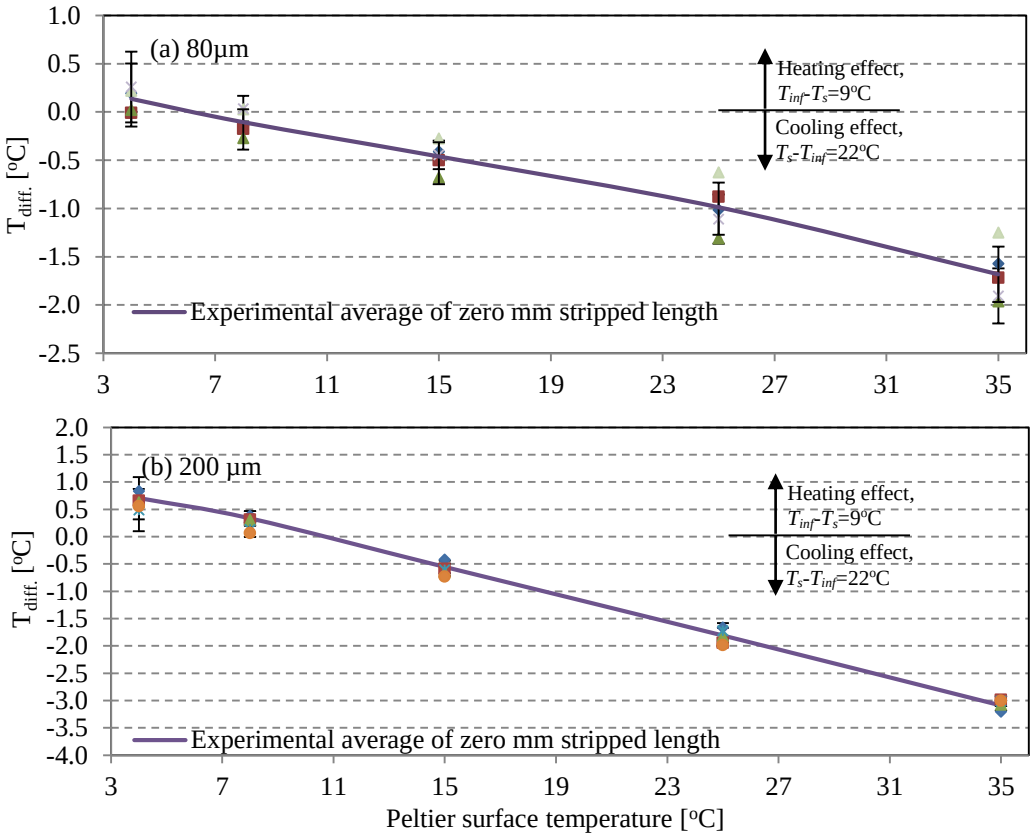

Fig. 4.9: Effect of non-stripped length distance of stripped electrical insulation of thermocouple on temperature measurement for the sizes: (a) 80µm and (b) 200µm.

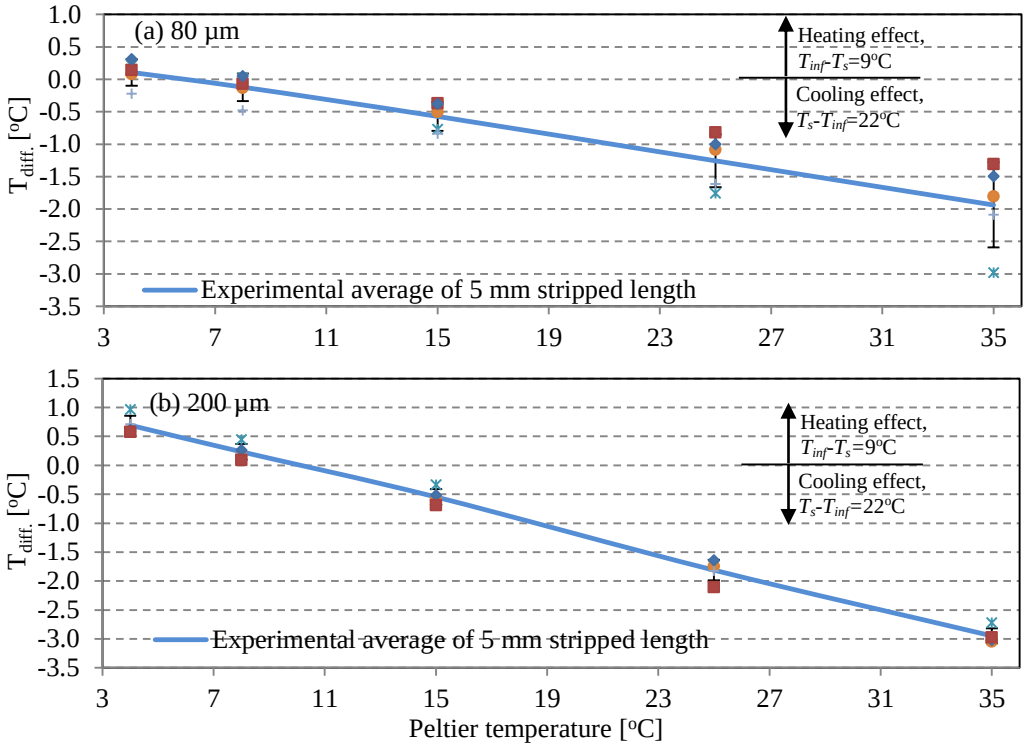

Fig. 4.10: Effect of 5mm distance of stripped electrical insulation of thermocouple on temperature measurement for the sizes: (a) 80µm and (b) 200µm.

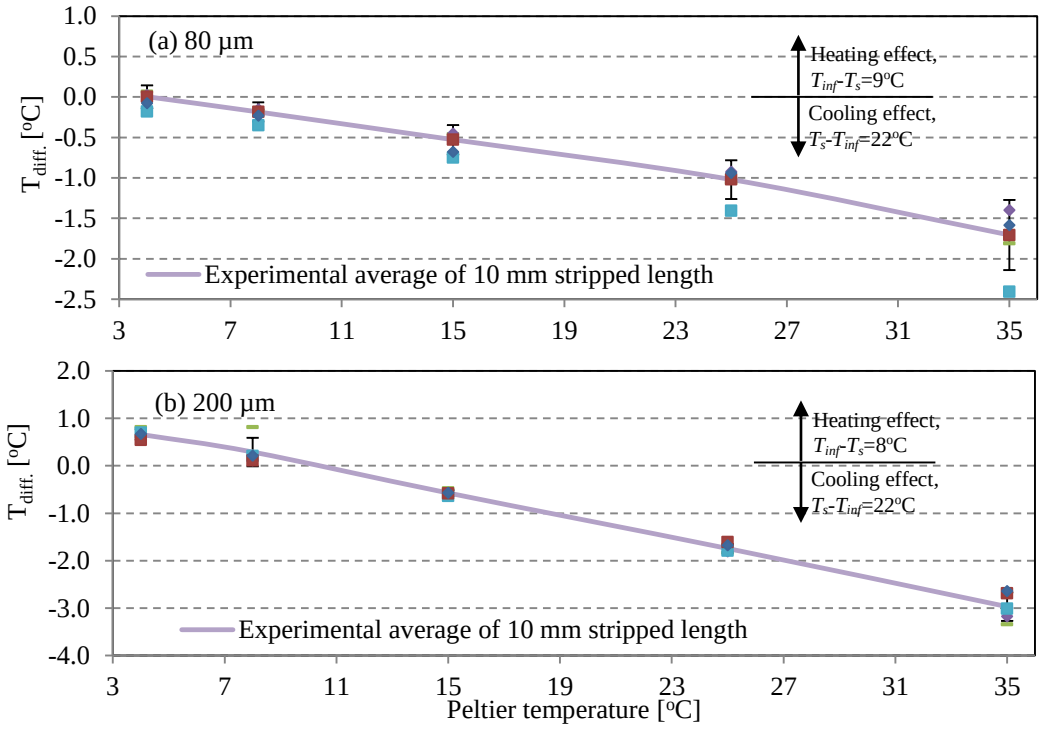

Fig. 4.11: Effect of 10mm distance of stripped electrical insulation of thermocouple on temperature measurement for the sizes: (a) 80µm and (b) 200µm.

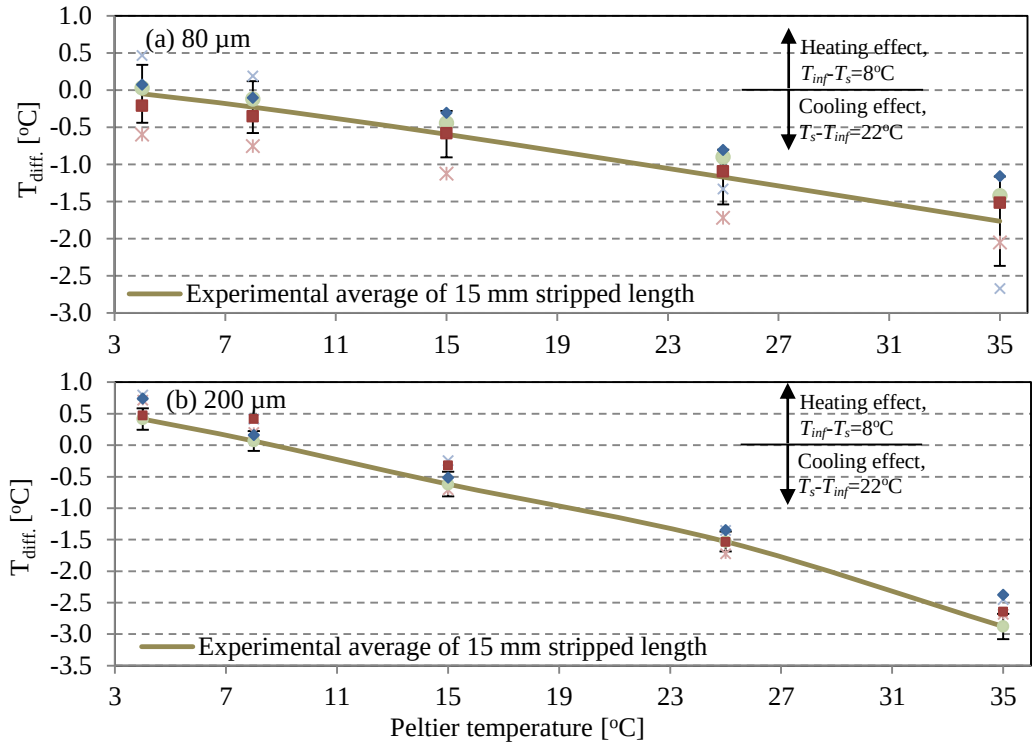

Fig. 4.12: Effect of 15mm distance of stripped electrical insulation of thermocouple on temperature measurement for the sizes: (a) 80µm and (b) 200µm.

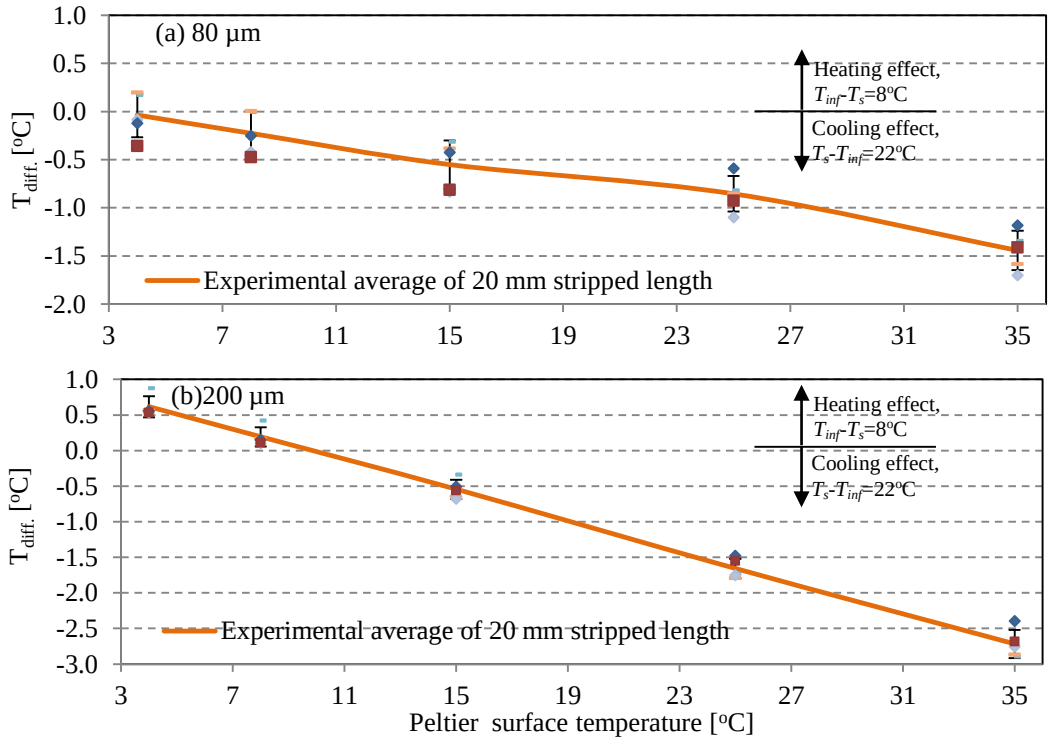

Fig. 4.13: Effect of 20mm distance of stripped electrical insulation of thermocouple on temperature measurement for the sizes: (a) 80µm and (b) 200µm.

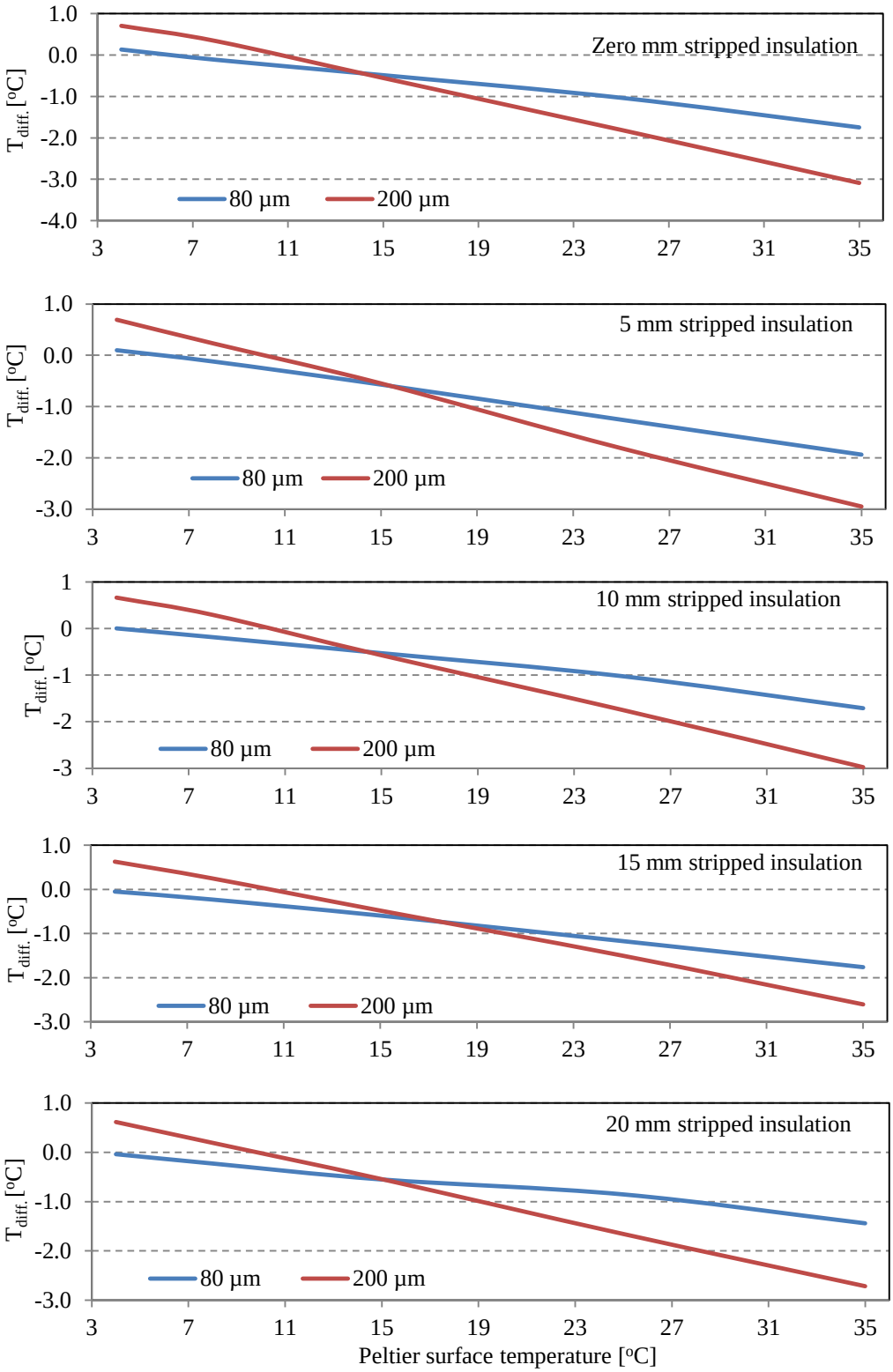

Fig. 4.14: Comparison between mean experimental data of variable distance of stripped electrical insulation with average environmental temperature of 13ºC.

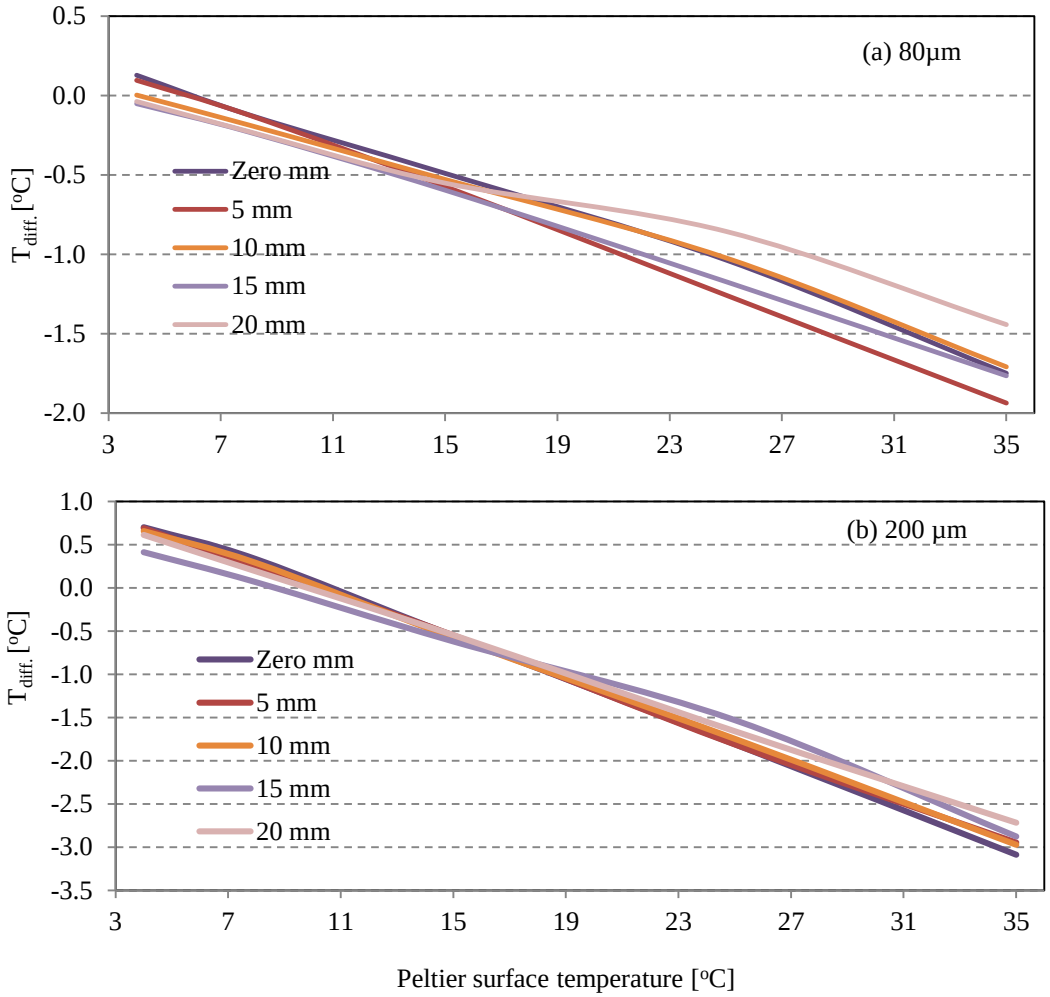

Fig. 4.15: Comparison between mean experimental data of variable distance of stripped electrical insulation with average environmental temperature of 13° C.

4.4 Mathematical modelling

4.4.1 Thermocouple wire length

It can be assumed that each strand of thermocouple wire behaves as a very long one-dimensional fin exposed to free convection from the outside environment (See Fig. 4.16). In this case, the following analysis can be used to provide an analytical prediction of the wire length over which the temperature becomes equal to that of the environment. Fin analysis considers heat transfer by conduction occurring along the thermocouple wire due to its high thermal conductivity in comparison with the

surrounding insulation; as such it assumes that there is no radial temperature gradient across the metal wire [3] (See Fig. 4.16).

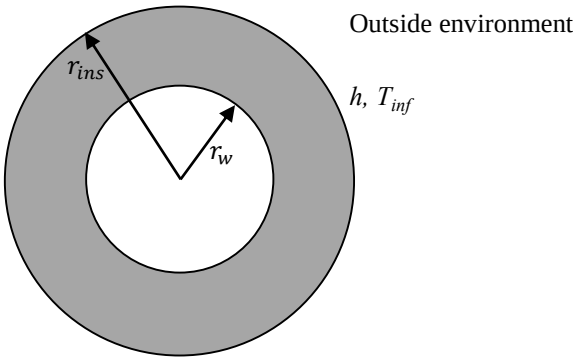

Fig. 4.16: Cylindrical cross-section of thermocouple wire with insulation.

It must be considered that a thermocouple consists of contact between two dissimilar metals. Both wires have different physical and thermal properties and should therefore be considered to each have a different effect on the thermocouple junction temperature. To simplify this, a single equivalent wire model was adopted rather than a two-wire model (See Fig. 4.17) [9, 102]. The equivalent bare wire diameter is calculated:

$$D_{weq}=\sqrt{2}D_w \tag{4.1}$$

where D_w is the metal wire diameter (See Table 4.2).

Fig. 4.17 shows that the total insulation thickness of both wires in horizontal direction equal to the average difference between the diameter of both wires with and without insulation. Moreover, the insulation thickness in vertical direction equal to the difference between wire diameter with and without insulation. Therefore, the equivalent insulation outer diameter is calculated by considering the average thickness around each wire (See Fig. 4.17) [102], which becomes:

$$t_{eqins}=\frac{1}{2}\times\left[\frac{2\times D_{ins}-2\times D_w}{3}+\frac{D_{ins}-D_w}{2}\right] \tag{4.2}$$

where D_{ins} is the wire diameter with insulation (See Table 4.2). Therefore, the equivalent insulation thickness is:

$$t_{eqins}=\frac{1}{2}\times\left[\frac{4\times t_{ins}}{3}+\frac{2\times t_{ins}}{2}\right]=\frac{7}{6}t_{ins} \tag{4.3}$$

Therefore, the equivalent insulation diameter is:

$$D_{eqins}=D_{weq}+2\times t_{eqins}=D_{weq}+\frac{7}{3}t_{ins} \tag{4.4}$$

Equivalent thermal conductivity k_{weq} for a single wire model is calculated from [3, 103]:

$$k_{weq}=\frac{k_{w1}+k_{w2}}{2} \tag{4.5}$$

where k_{w1} and k_{w2} are the thermal conductivities of the thermocouple wires given in Table 4.1.

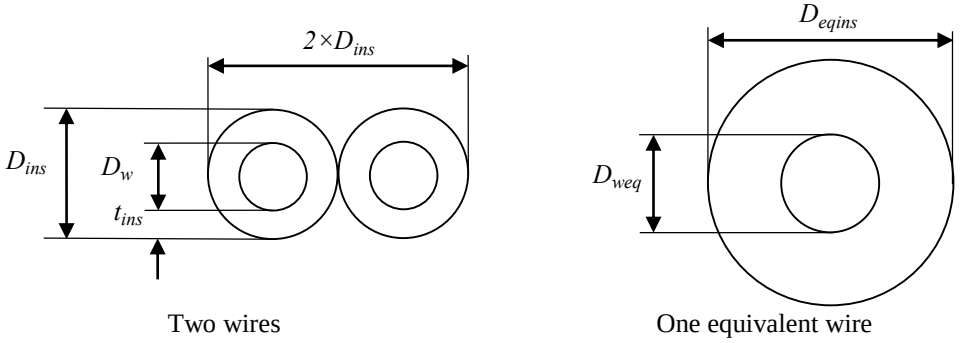

Fig. 4.17: Cross-sectional area of two wires and one equivalent wire.

Heat balance for the fin elemental cross section of width dx with heat lost by convection is calculated using Eq. (4.6) (See Fig. 4.18) [91]:

$$dq_{conv}=\frac{2\pi(T-T_{inf})dx}{\frac{ln\left(\frac{D_{eqins}}{D_{weq}}\right)}{k_{ins}}+\frac{2}{D_{eqins}\,h}} \tag{4.6}$$

where T is the temperature along the centreline of the metal wire by assuming no radial temperature gradient, h is the heat transfer coefficient of the free convection, T_{inf} is the environmental temperature, D_{eqins} is the thermocouple insulation equivalent

diameter, D_{weq} is the bare wire equivalent diameter as shown in Fig. 4.17, and k_{ins} insulation thermal conductivity. The values of D_{eqins}, and D_{weq} are listed in Table 4.2.

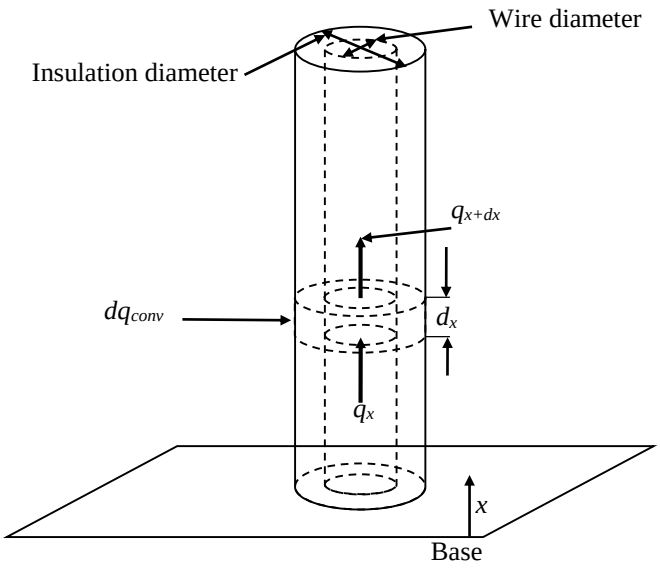

Fig. 4.18: One-dimensional conduction and convection through fin with insulation.

According to the Fourier Law, through heat input the elemental area is calculated:

$$q_x = -k_{weq} A_w \frac{dT}{dx} \tag{4.7}$$

Heat output from the element is:

$$q_{x+dx} = -k_w A_w \left(\frac{dT}{dx} + \frac{d^2T}{dx^2} dx \right) \tag{4.8}$$

where $A_w = \pi r_w^2$ is the metal wire cross-section area.

Combining Eqs.(4.6), (4.7) and (4.8), we obtain:

$$\frac{d^2T}{dx^2} - m^2 \left(T - T_{inf} \right) = 0 \tag{4.9}$$

Eq.(4.9) represents the differential equations of a fin exposed to natural convection. m is a constant which is calculated from:

$$m=\sqrt{\frac{4}{k_{weq}D_w^2}\frac{2}{\frac{ln\left(\frac{D_{eqins}}{D_{weq}}\right)}{k_{ins}}+\frac{2}{D_{eqins}\,h}}} \tag{4.10}$$

h is considered to be a constant along the fin to simplify the differential equation. Applying the following boundary conditions for a very long fin with outside boundary conditions as shown in Fig. 4.16 and Fig. 4.18:

$$T=T_0 \text{ at } x=0, \text{ and} \tag{4.11}$$

$$T=T_{inf} \text{ when } x\rightarrow\infty \tag{4.12}$$

The following solution for the temperature is obtained:

$$T=T_{inf}+(T_0-T_{inf})\, e^{-mx} \tag{4.13}$$

where T_0 is the fin's base temperature.

Table 4.2 Thermocouple wire diameter with measured insulation thickness.

Bare wire radius [μm]*, $r_w=D_w/2$	40	100
Wire diameter with insulation [μm]* $r_{ins}=D_{ins}/2$	125	250
Insulation thickness [μm], t_{ins}	85	150
$r_{weq}=D_{weq}/2$ [μm], Eq.(4.1)	56.57	141.5
t_{eqins}[μm] Eq.(4.3)	99.2	175
$r_{eqins}=D_{eqins}/2$[μm], Eq.(4.4)	155.75	316.5
h [W/m^2 K], Eq.(4.15)	124	53.3
r_{cr}[μm], Eq.(4.16)	2419.4	5464.5

* measured by accurate micrometer.

The best approximation is to consider the thermocouple wire as a vertical thin cylinder so that the Nusselt number Nu_H can be calculated [74]:

$$Nu_H = \frac{4}{3}\left[\frac{7Ra_H Pr_a}{5(20+21Pr_a)}\right]^{1/4} + \frac{4(272+315Pr_a)H}{35(64+63Pr_a)D} \quad (4.14)$$

where $Nu_H = hH/k_a$; Rayleigh number; $Ra_H = g\beta_a \Delta T H^3 / \alpha_a v_a$; Prandtl number, $Pr_a = v_a/\alpha_a$; H [m] is the cylinder height, D is diameter, and k_a is air thermal conductivity. v_a; α_a; β_a; μ_a; and C_{pa} are the kinematics viscosity, thermal diffusivity, thermal expansion coefficient, dynamic viscosity, and specific heat capacity respectively; see Table 5.2 (section 5.2 in Chapter 5).

The calculation of Nu_H from Eq.(4.14) assumed that thermocouple wires are similar to thin cylinder with constant average heat transfer coefficient h along the wire(s). Moreover, the temperature difference between the wire surface and the environment was assumed to be fixed along the wire(s). Therefore, Eq.(4.14) gives us an indication on the variation of h with curvature of the wires not the exact value.

The heat transfer coefficient (h) is then derived as:

$$h = \frac{4k_a}{3H}\left[\frac{7Ra_H Pr_a}{5(20+21Pr_a)}\right]^{1/4} + \frac{4(272+315Pr_a)k_a}{35(64+63Pr_a)D} \quad (4.15)$$

The maximum temperature difference between the environment and surface in the present experiments was observed to be equal to ($\Delta T = 22^{o}$C) (See section 0). Substituting this temperature difference, a value of H is assumed in Eq.(4.15) to calculate h. These values are then substituted in Eqs.(4.10) and (4.13) to calculate a new value of H. The calculation above is repeated until H reaches a constant value which represents the calculated length of the thermocouple wire where it's temperature reaches the environmental temperature. Fig. 4.19 shows the variation of h with the wire diameter for different values of H, which has a negligible effect of the value of h. According to the Eq.(4.15) and due to the large order difference in value between the wire length H and wire diameter (wire length in centimetre while the diameter in micrometre), the variation in diameter will be dominant. Therefore, the second term in Eq.(4.15) is dominant on the calculation of h. Moreover, Fig. 4.19 shows that h starts

to become independent on the wire diameter at larger values while a small effect of *H* becomes obvious.

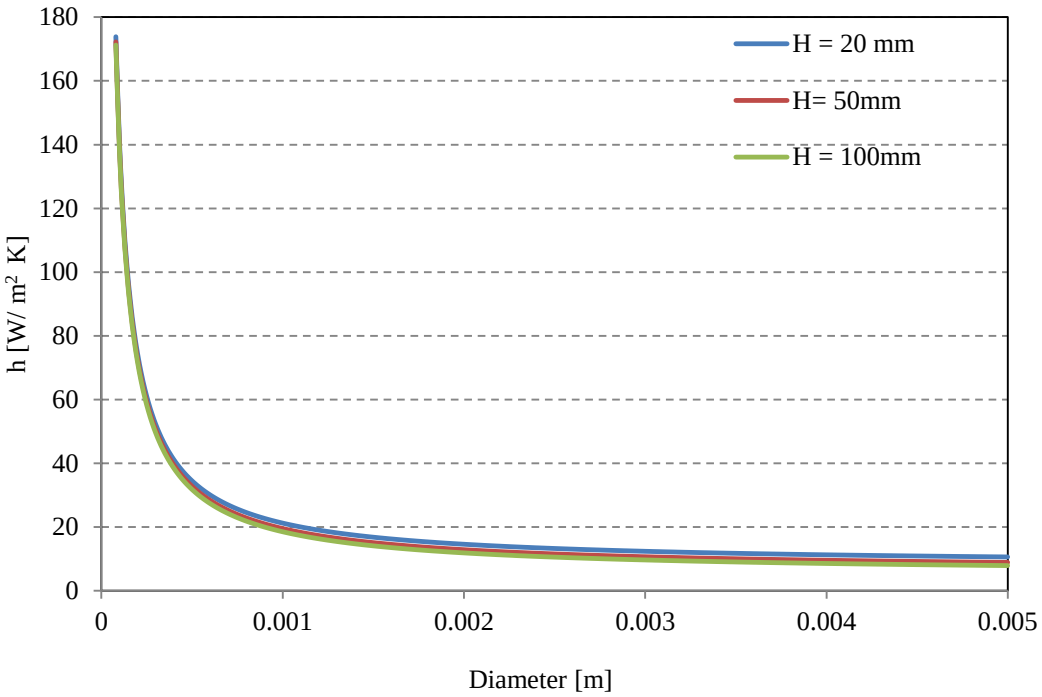

Fig. 4.19: Variation of heat transfer coefficient with diameter.

Fig. 4.20 and Fig. 4.21 show the required length for the wire end temperature to equal to that of the environment for each diameter of thermocouple with and without insulation. The increase in the diameter of the thermocouple leads to an increase in the area that is exposed to convective heat transfer with the outside environment. Moreover, a larger wire diameter means an increase in the cross-sectional area, which allows more heat to be conducted through the wires. Consequently, a greater length is required for the 200µm diameter to reach the environmental temperature in comparison to the 80µm diameter wires. It is also shown that there is no effect from the length of electrical insulation for these two thermocouples.

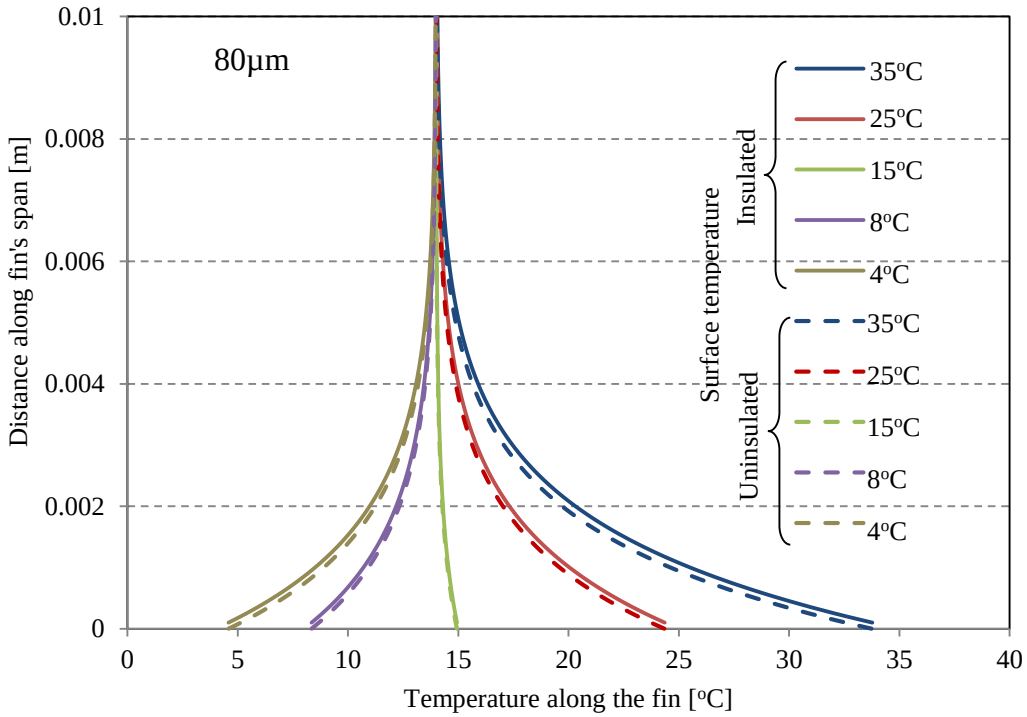

Fig. 4.20: Fin length required to reach the environmental temperature where each curve starts with the Peltier surface temperature for the size 80µm.

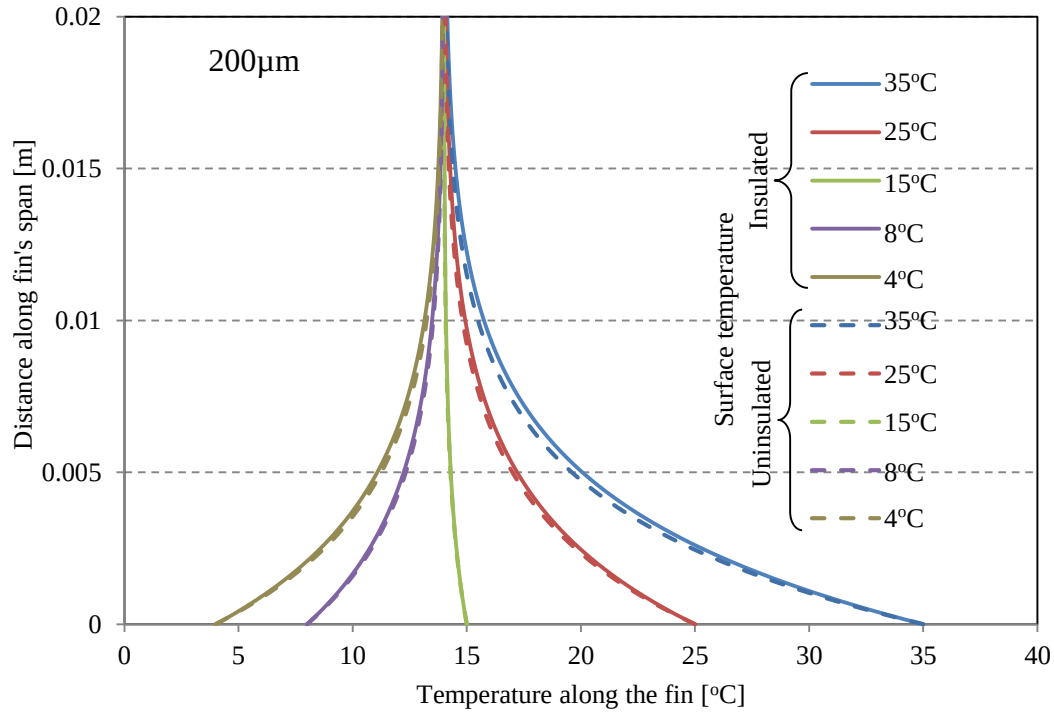

Fig. 4.21: Fin length required to reach the environmental temperature where each curve starts with the Peltier surface temperature.

4.4.2 Thermocouple insulation

Heat transfer to a cylindrical shape with insulation around it depends on the ratio between the insulation thermal conductivity and the heat transfer coefficient with the outside environment [91]. This ratio is called critical radius (r_{cr}), and is equal to:

$$r_{cr} = \frac{k_{ins}}{h} \tag{4.16}$$

As insulation thickness increases, the heat transfer area with the outside environment increases (see Fig. 4.16). The Convection heat transfer rate with the outside environment will also increase. A continuous increase in insulation thickness leads to an increase in cylinder outer diameter and consequently heat transfer rate, until maximum heat transfer rate is achieved where the cylinder outer diameter with insulation is equal to r_{cr}.

Continuous increase in insulation thickness means cylinder outer diameter becomes larger than r_{cr} and heat transfer will begin to decrease [91]. This criterion is valid when the heat transfer coefficient with the environment is constant but for this study *h* is varying with wire diameter (See Eq.(4.15) and Fig. 4.19).

The following two cases study the effect of *h* on heat flux exchange between the cylinder and outside environment. The first ***Case 1*** assumed that *h* is constant and its value is calculated from Eq.(4.14) based on the values of the equivalent radius in Table 4.2. The second ***Case 2*** considered the variation of *h* with diameter according to the Eq.(4.14) and the calculation starts with values in Table 4.2.

Case 1: Assuming constant *h* as calculated using Eq.(4.14) and solving Eq.(4.6), the results shown in Fig. 4.22 can be generated. Heat flux continuously increases until the wire diameter becomes equal to the critical radius, at which point the heat flux begins to decrease. Table 4.2 shows the critical radius for each of the thermocouple sizes. This behaviour of heat flux is explained by the fact that the thermal resistance to convection heat transfer is minimal when the cylinder outer diameter is equal to r_{cr}, as shown in Fig. 4.23.

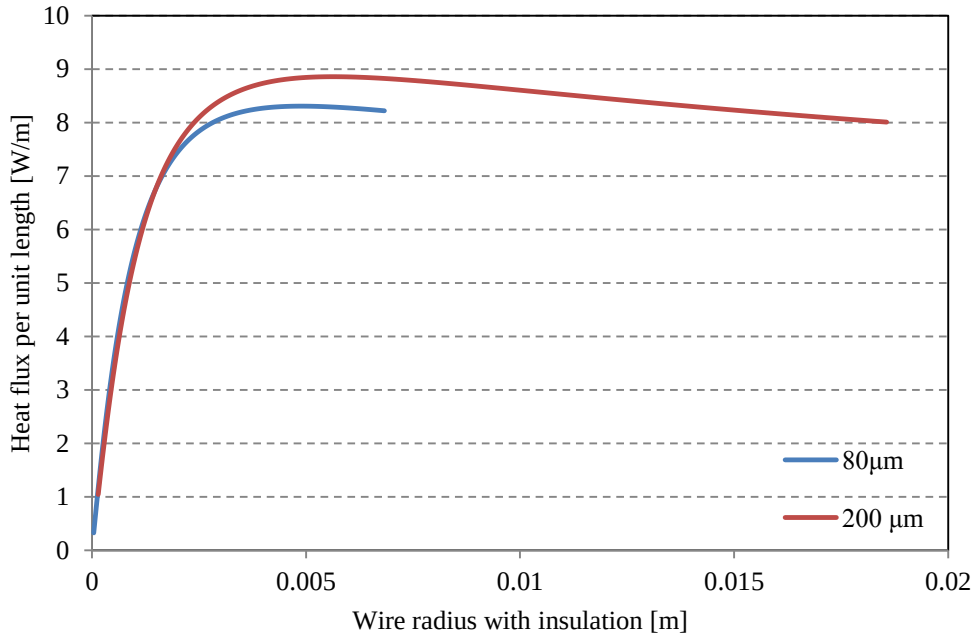

Fig. 4.22: Variation of heat flux with wire radius of constant *h*.

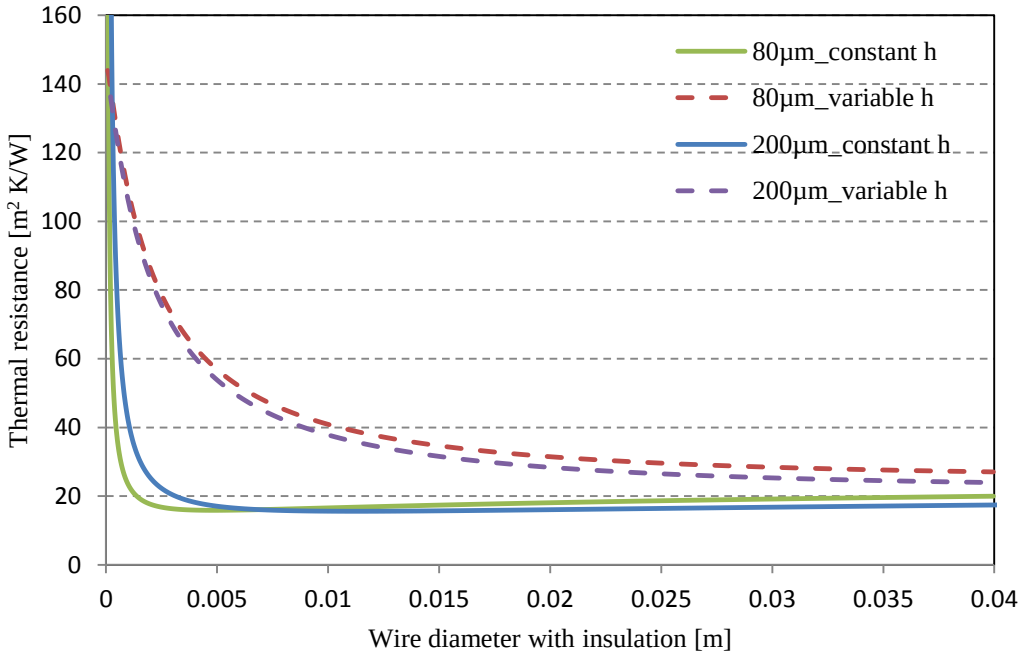

Fig. 4.23: Variation of thermal resistance of the thermocouple wires with insulation of size 80 µm with constant and variable *h*.

However, due to the small size of the thermocouple wire, the effect of wire curvature on the convection heat coefficient *h* around the wires should be considered [74]. This case has been discussed in detail in ***Case 2*** below**.**

Case 2: The same calculation procedure as in ***Case 1*** is repeated. However, this time the effect of wire curvature on *h* is also considered [74]. The variation of *h* with the wire diameter can be calculated using Eq.(4.15). In this case there is no minimum value of thermal resistance, as shown in Fig. 4.23. Therefore, a constant increase in heat flux with no apparent critical radius is observed, as shown in Fig. 4.24.

Fig. 4.24 shows that there is no critical diameter for the wire and the heat flux continues to increase with the wire diameter. In this case there is no a specific critical diameter as *h* varies inversely with the wire diameter (Eq.(4.15)). Increasing in diameter leads to decrease in *h*, and at the same time thermal resistance to heat convection decreases, see Eq.(4.6). The dominator of Eq.(4.6) represents the thermal resistance which decreases with increasing in wire diameter (See Fig. 4.23) while the nominator remains constant. Therefore, heat flux continues to increase.

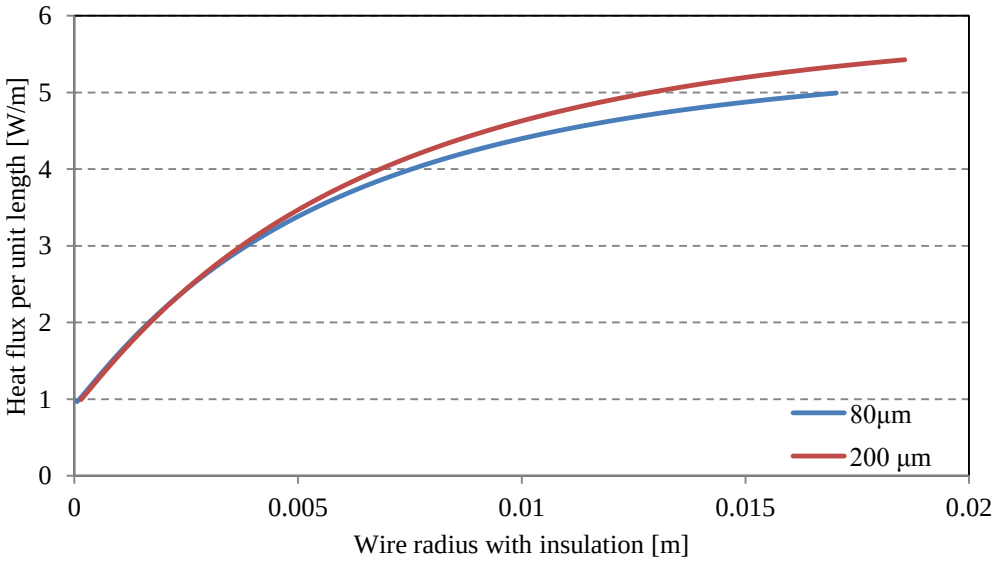

Fig. 4.24 Variation of heat flux with wire radius and variable *h.*

Heat flux through the thermocouple wire is now calculated by substituting Eq.(4.13) into Eq.(4.7):

$$q_x = k_w m \frac{\pi}{4} D_{weq}^2 (T_o - T_{inf}) e^{-mx} \tag{4.17}$$

where m is calculated using Eq.(4.10). Fig. 4.25 shows the variation of the heat flux along the thermocouple wire. Environmental temperature is $T_{inf}=13^oC$, and $T_o=35^oC$ represents the base temperature, i.e. $T_o-T_{inf}=22^oC$. Therefore, heat transfer occurs from the thermocouple wire to the environment (cooling effect), which is considered as positive heat flux. It is shown in Fig. 4.25 that heat flux is higher for a larger diameter, and that the distance required to reach zero heat flux is greater. There is also a negligible effect of thermocouple electrical insulation on the heat flow through the wires for all sizes. Environmental temperature is considered as a constant along the wire; therefore, the effect of the insulation is negligible [30].

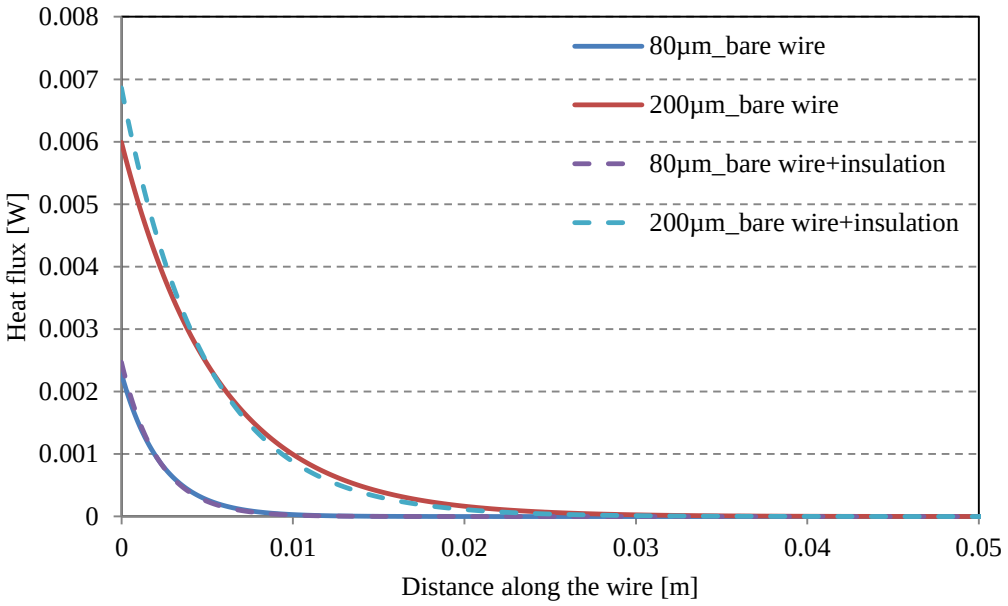

Fig. 4.25: Variation of heat flux along thermocouple wire for both thermocouple sizes.

4.4.3 Thermocouple probe temperature distribution

4.4.3.1 Stepped fin analysis

The thermocouple probe is the active component which measures the surface temperature. Thermocouple wires interact with the environment; they transfer heat to

(or from) a surface and alter the measured temperature [104]. The probe therefore measures the disturbed temperature rather than the actual surface temperature. Consequently, the temperature distribution along the thermocouple junction and wire can be analysed by considering them as a stepped fin [105, 106] (See Fig. 4.26). The thermocouple wires represented by the single wire model (See section 4.4.1) were considered to be a very long fin, while the thermocouple junction was considered to be a fin with a prescribed end temperature [91]. Therefore, the junction temperature distribution can be calculated using Eq.(4.18) for the length $0 \leq x \leq D_p$:

$$\frac{\theta_p}{\theta_b} = \frac{\left(\frac{\theta_L}{\theta_b}\right) sinhm_p x + sinhm_p(D_p - x)}{sinhm_p D_p} \tag{4.18}$$

where $m_p = \sqrt{h_p p_p / k_p A_p}$, $k_p = k_{weq}$ is calculated using Eq.(4.5). $\theta_p = T_p - T_{inf}$, $\theta_L = T_L - T_{inf}$, $\theta_b = T_b - T_{inf}$, T_p temperature variable of the probe [K], T_L probe temperature at top [K], T_b bottom's temperature at bottom [K], and D_p probe diameter.

Thermocouple wire temperature can be calculated using Eq.(4.13) for the length ($D_p \leq x \leq L_w$):

$$\frac{\theta_w}{\theta_L} = e^{-m_w(x - D_p)} \tag{4.19}$$

where m_w is calculated using Eq.(4.10), $\theta_w = T_w - T_{inf}$; T_w temperature variable of the thermocouple wire [K]. At $x = D_p$: $T_L = T_w$, and at the joint between the probe and the wires the following boundary condition is applied [105, 106]:

$$-A_p k_p \frac{dT_p}{dx} = -A_{weq} k_{weq} \frac{dT_w}{dx} + h(A_p - A_{weq})(T_L - T_{inf}) \tag{4.20}$$

where $A_p = (\pi/4) D_p^2$ and $A_{weq} = (\pi/4) D_{weq}^2$.

Substituting Eqs.(4.18) and (4.19) into Eq.(4.20):

$$\theta_L = \frac{\frac{m_p}{sinhm_p D_p}}{\frac{m_p\, coshm_p\, D_p}{sinhm_p\, D_p} + \alpha m_w + \frac{(1-\alpha)h_p}{k_p}}\theta_b \tag{4.21}$$

where, $\alpha = A_{weq}/A_p$.

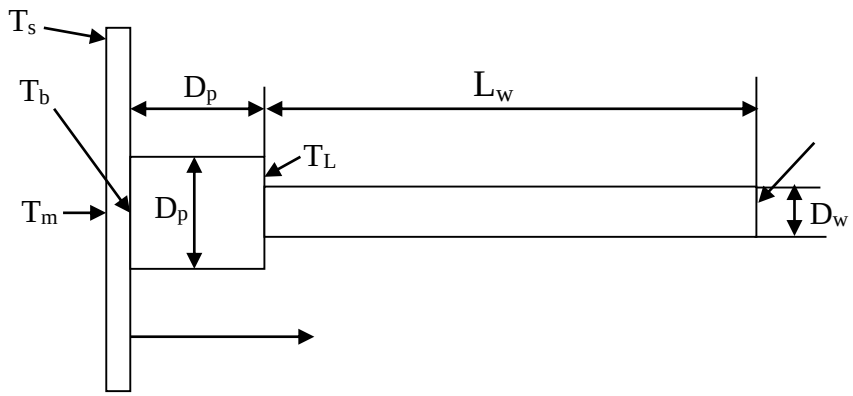

Fig. 4.26 Analogy of thermocouple with probe geometry as a stepped fin.

4.4.3.2 Electrical resistance analogy

An electrical resistance analogy of the thermal interaction of the thermocouple with the environment and surface is shown in Fig. 4.27. The thermocouple measures the average temperature of T_L and T_b, which represent the top and bottom temperatures of the junction (See Fig. 4.26). Fig. 4.26 can be redrawn as electrical resistance, as shown in Fig. 4.27. Assuming a very low value for R_m, meaning that it can be neglected [104]:

$$q = \frac{T_s - T_b}{R_c} = \frac{T_b - T_L}{R_p} = \frac{T_L - T_{inf}}{R_w} \tag{4.22}$$

where R_m is constriction thermal resistance [m^2 K/W], R_c contact thermal resistance [m^2 K/W], R_p probe thermal resistance [m^2 K/W], and R_w wire thermal resistance [m^2 K/W].

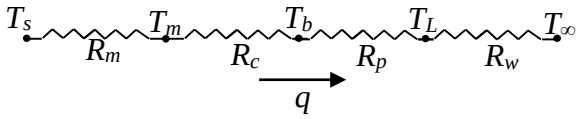

Fig. 4.27 Electrical resistance analogy of thermocouple thermal resistance.

Heat flux transfers through all resistance are equal to the heat flux transferred to the probe q_p plus the wires q_w. Therefore:

$$q=q_p+q_w \tag{4.23}$$

Fin analysis for both the thermocouple wire and junction heat fluxes is calculated using Eqs.(4.18) and (4.19):

$$q_p=\frac{coshm_pD_p-\frac{\theta_L}{\theta_b}}{sinhm_pD_p}\sqrt{h_pp_pk_pA_p}\theta_b \tag{4.24}$$

$$q_w=k_{weq}m_w\frac{\pi}{4}D_{weq}^2\theta_L \tag{4.25}$$

Eqs.(4.24) and (4.25) are substituted into Eqs.(4.22) and (4.23):

$$\theta_b=\frac{\theta_s-R_c\theta_L(Z_w-Z_p)}{1+Z_pR_c\ coshm_p\ D_p} \tag{4.26}$$

Eq.(4.26)is substituted into Eq.(4.21):

$$\theta_L=\frac{\theta_s\ A_1}{1+R_c\ Z_p\ coshm_p\ D_p+A_1R_c(Z_w-Z_p)} \tag{4.27}$$

where:

$$Z_w=k_wm_w\frac{\pi}{4}D_{weq}^2 \tag{4.28}$$

$$Z_p=\sqrt{h_pp_pk_pA_p}/sinhm_pD_p \tag{4.29}$$

$$A_1 = \frac{\frac{m_p}{sinhm_p D_p}}{\frac{m_p\, coshm_p\, D_p}{sinhm_p\, D_p} + \alpha m_w + \frac{(1-\alpha)h_p}{k_p}} \tag{4.30}$$

θ_L is calculated using Eq.(4.27) and the results substituted into Eq. (4.26) to compute θ_b while θ_s is taken to be the value measured using the PT100 device (See section4.1).

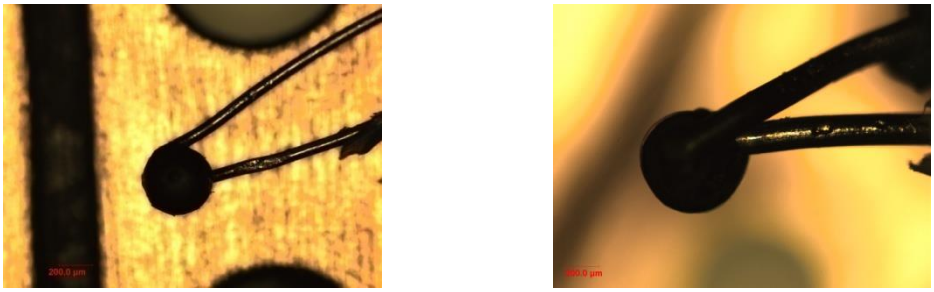

(a) 449μm (b) 635μm

Fig. 4.28 Thermocouple probe size shown in microscope pictures: a) 80μm, b) 200μm and c) 315μm.

Thermocouple tip sizes on the 80μm and 200μm diameter thermocouples were measured using a microscope and were found to be 449μm and 635μm respectively, as shown in Fig. 4.28. These values were used with values of R_c of 0.000025, 0.00035, and 0.000045m^2 K/W for the size 80μm and between 0.000045, 0.0005, and 0.000055m^2 K/W for the size 200μm have been substitute into Eqs.(4.26) and (4.27) to calculate the results of Fig. 4.29 (a-b).

The experimental data of stripped insulation with length 0mm and 20mm were chosen for comparison with analytical results. Fig. 4.30 and Fig. 4.31 shows good agreement with the experimental results to within 0.5°C for the values of R_c: 0.00035 m^2 K/W for the size 80μm and 0.000055m^2 K/W for the size 200μm. Furthermore, analytical results show that the effect of the insulation is negligible for totally insulated and uninsulated wire of length 20mm for zero thermal contact resistance ($R_c = 0$). Consequently, the other stripped lengths (5mm, 10mm, and 15mm) should also have negligible effect. The analysis presented above is one-dimensional and assumes the contact area between the probe and the surface is equal to the probe diameter. Thermal contact resistance depends on the shared area between the probe and the surface; in

reality the probe geometry is irregular, making it too complex to specify an actual contact area. It is therefore difficult to specify the actual value of R_c.

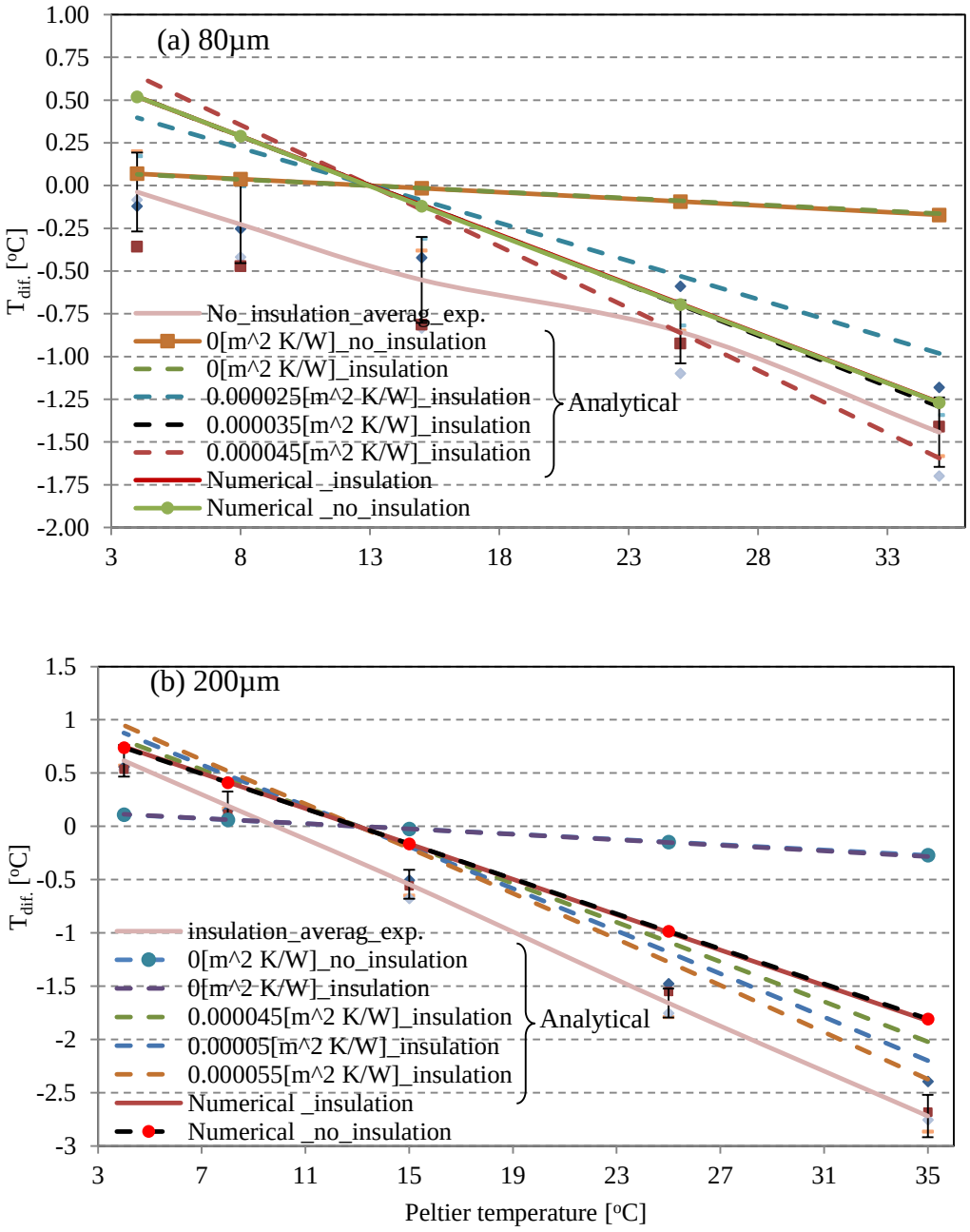

Fig. 4.29 Comparison between experimental, analytical and numerical results for different values of thermal contact resistance between probe of and Peltier surface for thermocouple sizes: (a) 80µm and (b) 200µm. 20mm stripped insulation of the experimental results is chosen for comparison.

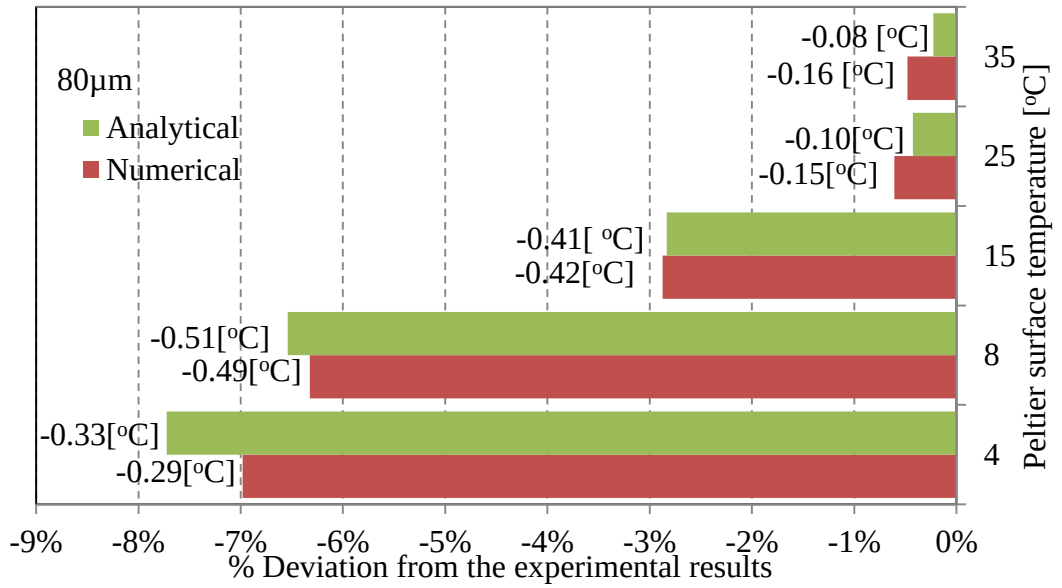

Fig. 4.30 Comparison between analytical and numerical results of the values of R_c equal 0.00035 m^2K/W for size 80µm. Bars lengths and labels represent percentage deviation and temperature difference from experimental results respectively. 20mm stripped insulation is chosen for comparison.

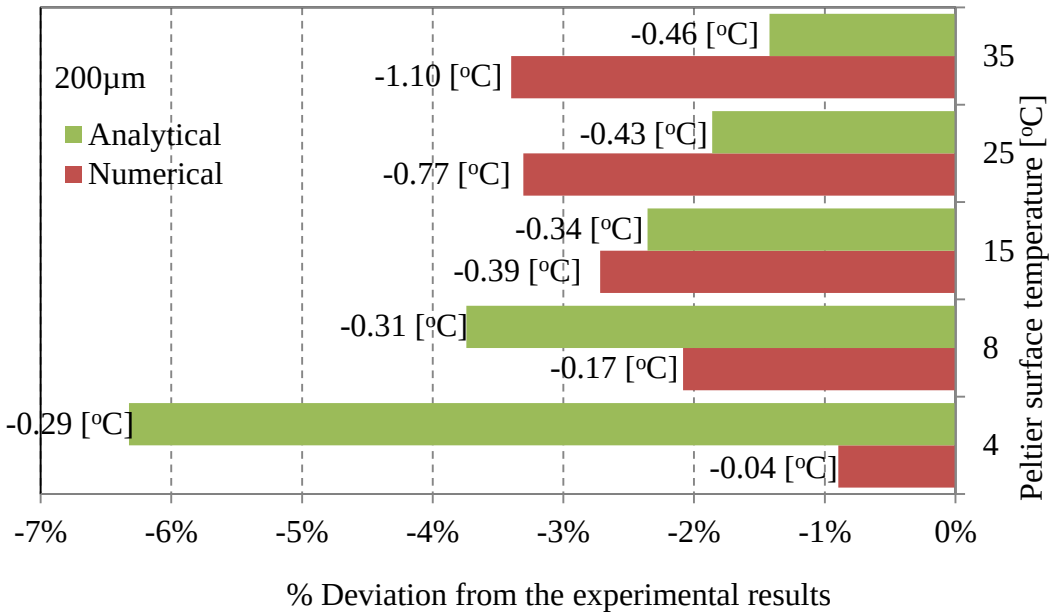

Fig. 4.31 Comparison between experimental, analytical and numerical results of the values of R_c equal to 0.000055m^2K/W for size 200µm. Bars lengths and labels represent percentage deviation and temperature difference from experimental results respectively. 20mm stripped insulation is chosen for comparison.

4.4.4 Numerical modelling

A three-dimensional model of the actual geometry of a thermocouple was created as shown in Fig. 4.32. This model considered the actual size of the thermocouple wires and insulation, but the geometry of the junction was represented as a cube with side length equal to the junction diameter. Consequently, the contact area is the bottom surface of this cube.

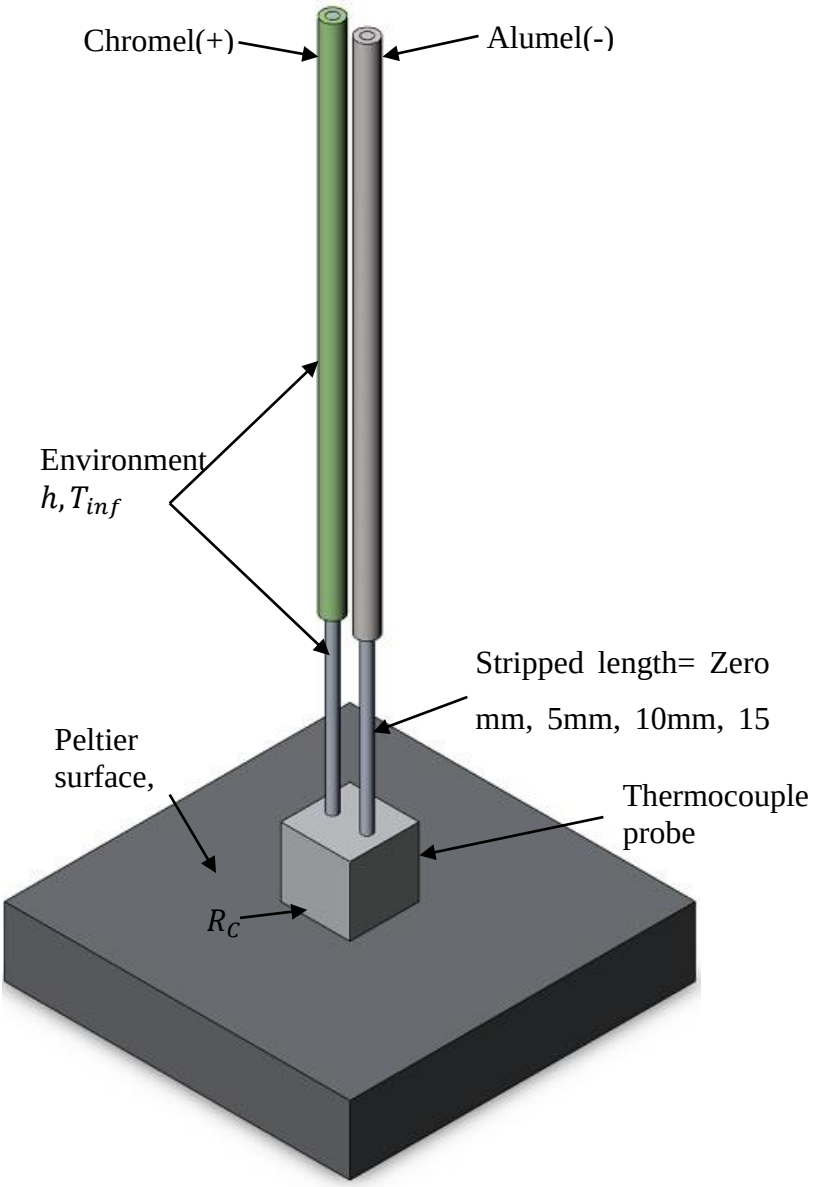

Fig. 4.32: Demonstration graph of thermocouple three-dimensional model for numerical analysis.

In order to model thermal contact resistance in COMSOL, it is necessary to define thermal joint conductivity h_j[107] from Fourier's law (Eq.(4.7)):

$$q=h_j\Delta T\ [W/m^2] \tag{4.31}$$

where:

$$h_j=\frac{k_{res}}{d_{res}}\left[\frac{W}{m^2K}\right] \tag{4.32}$$

where k_{res} and d_{res} represent thermal conductivity of the contact layer between the surface and the junction and its thickness respectively. It is seen that h_j is the reverse of R_c.

COMSOL applies a *slit boundary condition* [107] (See Eq.(3.34) section 3.3.2 Chapter 3) to include the effect of contact resistance:

$$\begin{aligned} -\boldsymbol{n}(-k_d\nabla T_d)&=-\frac{k_{res}}{d_{res}}(T_u-T_d)\\ -\boldsymbol{n}\ (-k_u\nabla T_u)&=-\frac{k_{res}}{d_{res}}(T_d-T_u)\end{aligned} \tag{3.34}$$

where subscript d and u refer to the downside and upside of the slit.

Boundary conditions of Eq.(3.34) can be defined in COMSOL by creating a *contact pair* between the thermocouple junction and the Peltier surface. The ratio k_{res}/d_{res} is equivalent to *thermal joint conductivity* h_j[107], which is equal to the inverse of R_c. The values of R_c0.000035m^2 K/W for 80µm size and 0.000055m^2 K/W for 200µm were selected from analytical analysis to substitute for h_j in the numerical analysis. These values were chosen as they gave good agreement with experimental results to within 0.5^{o}C (See section 4.4.3.2). This model was used to investigate the effects of the two different exposed wire lengths (0mm and 20mm) on the junction temperature. Fig. 4.29(a-b) shows a comparison between experimental and numerical results for the 80µm and 200 µm thermocouples. There is a good agreement between the

experimental and numerical analysis for size 80µm, as shown in Fig. 4.29a and Fig. 4.30.

Fig. 4.30 shows the maximum divergence of approximately 7% between the numerical and experimental results for the size 80, while the greatest temperature difference in comparison with the experimental results is 0.49ºC. The size 200µm deviates from the experimental results by 3.5%, with a temperature difference of approximately 1.1ºC when the surface temperature is higher than that of the environment as shown in Fig. 4.31. Furthermore, numerical results showed that the effect of insulation is negligible for totally insulated and uninsulated wire of length 20mm for zero thermal contact resistance $R_c = 0$.

In the case of one-dimensional analysis, the contact area was assumed to be equal to the probe(s) diameter (See section4.4.3 and Fig. 4.26). In the three-dimensional numerical model, a squared shape contact area with side length equal to the probe diameter was used (See Fig. 4.32). Both analyses assumed that the contact area was larger than actual value seen in experiments due to the spherical geometry of the actual probe. Moreover, surface roughness leads to increased thermal resistance in experiments, an effect that was not considered in the analyses above. Accordingly, the analytical and numerical analyses underestimate thermal resistance and consequently the calculated temperature drop is lower than the true value.

The percentage deviation of theory from experiment for both the numerical and analytical results is dissimilar, as shown in Fig. 4.30 and Fig. 4.31. The analytical analysis is a one-dimensional approach where both thermocouple wires are assumed to act as a single equivalent wire (See section 4.4.1). Consequently, the effect of ambient temperature is considered on a single wire with an equivalent diameter and thermal conductivity; this differs from the actual thermocouple wire properties and size (See Table 4.1and Table 4.2). Conversely, in the numerical analysis the model is three-dimensional and the actual size and properties were used (see Fig. 4.32).

Experimental working conditions were approximately the same for both sizes of thermocouple. By comparing experimental, analytical and numerical results, it can be

concluded that the thermal contact resistance of the thermocouple is in the order of 1×10^{-5} m^2 K/W and 1×10^{-4} m^2 K/W for 80µm and 200µm respectively.

Fig. 4.33 shows a calculation of the effect of the electrical insulation when the Peltier temperature is above the range considered in the present experiments. The insulation has a negligible effect for the 80µm thermocouple even when surface temperature reaches 800°C. However, there is a noticeable effect (about 2°C) of insulation for the 200µm thermocouple when the temperature reaches 250°C. Therefore, for larger thermocouples the effect of insulation should be taken into consideration at elevated surface temperatures.

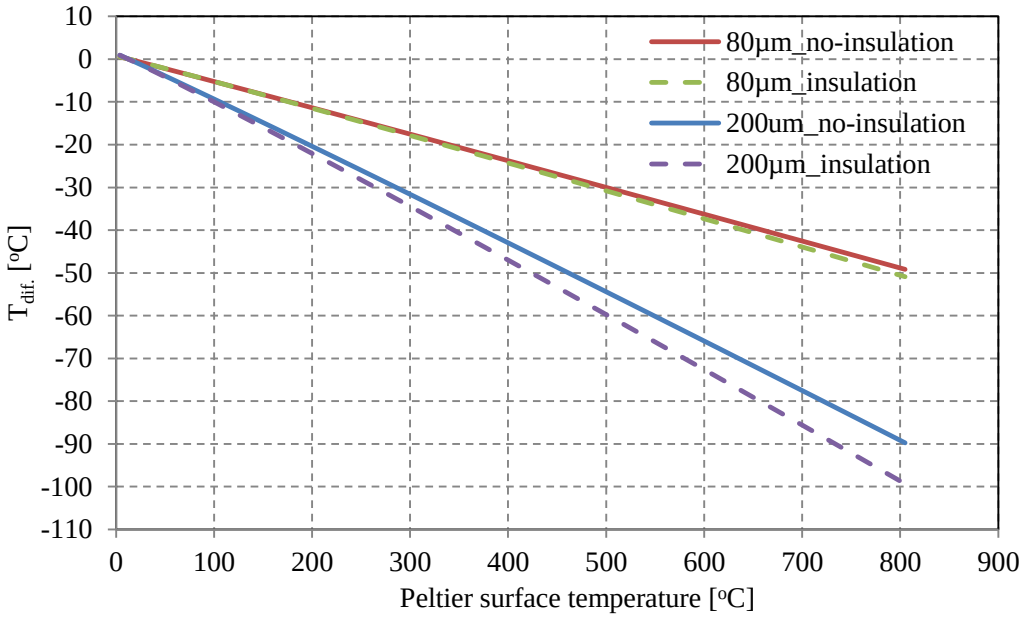

Fig. 4.33 Analytical results for the thermocouple error measurement for Peltier surface temperature up to 800°C beyond the experimental working range.

4.5 Conclusions

Analytical, numerical and experimental analyses have been performed to investigate the effects of different insulation lengths on thermocouple measurements of surface temperature. During the experimental work, the thermocouple probe was in direct contact with the surface while the wires were exposed to natural convection from the outside environment. Two sizes of thermocouple (80µm and 200µm) were used to measure a surface temperature. A satisfactory agreement was found between

experimental, analytical, and numerical results within the range of surface temperatures measured (4°C-35°C) and an average environmental temperature of 13°C. From this, the following can be concluded:

1. Stripping different lengths (0mm, 5mm, 10mm, 15, and 20mm) of insulation has a negligible effect on the heat transfer along the thermocouple wire and consequently on surface temperature measurement.
2. Both sizes of thermocouples considered, 80μm and 200μm, have different insulation thickness; however, stripping different lengths has no impact on either measurement. Therefore, the effect of the stripped insulation is independent of thermocouple size within the temperature measured range (4°C-35°C).
3. The effect of stripped insulation on the thermocouples with a wire diameter of 200μm becomes relevant when the Peltier surface temperature reaches 250°C, while for 80μm diameter wires insulation has negligible effect even for surfaces above 800°C.
4. Regardless of the stripped length of insulation, a larger diameter of thermocouple wire has a greater impact on surface temperature measurement than a smaller thermocouple wire.
5. The effect of the wire's curvature on heat transfer has been considered due to the small size of the wire. The impact of this curvature means that there is no specific critical diameter of the thermocouple wire(s) over which heat transfer to the wires decreases (See Fig. 4.22 and Fig. 4.24 and Eq.(4.16)).
6. If the experimental error in temperature measurement is higher than the impact of using the thermocouple (with or without insulation), the error is negligible. Therefore, any stripped length of electrical insulation can be said to have no impact on measurement accuracy.
7. The effect of the electrical insulation can be neglected until the surface temperature reaches 800°C for 80μm thermocouples, while for the 200μm thermocouples the effect of the insulation must be considered when the surface temperature reaches 250°C.

Chapter 5
Thermocouple Heating Impact on the Temperature Measurement of Small Volumes of Water in a Cooling System

Two different sizes of thermocouple (80μm and 315μm) were used to measure the temperature of a small volume of water inside a chamber in the first row of a micro-well thermostatically controlled system (TG40).This system consists of 5 rows with 8 chambers in each row, as shown in Fig. 5.1. The temperature of the first row was maintained at 4^{o}C, while that of the last row was at 20^{o}C. The thermocouple was placed vertically and its movement was controlled by a micrometre to measure the temperature of the large well in a single chamber of the first row. The large well (shown in Fig. 5.2) contained a small volume of water with an average height of approximately 6 mm and a cross-sectional area of 4mm^{2}.

The thermocouple was connected to a PICO log data acquisition (TC08) system to record the measured data onto a computer and saved to an Excel file. The zero position of the thermocouple began when the thermocouple probe was in contact with the water surface, and the measurement continued at incremental step of 0.25mm below the water surface until the depth of 5mm was reached, at which point the temperature variation observed was negligible.

The first set of experiments was performed to measure the temperature distribution inside the large well of the plastic insert without lids (See Fig. 5.2). The second set was to measure the temperature distribution inside the copper block. Five runs for each experiment were performed for each depth and for each thermocouple size.

The thermocouple wire was extended vertically and exposed to natural convection from the outside environment during the temperature measurement. Because the environmental temperature was higher than that of the water inside the chamber, the heat transfer was therefore conducted to the water through the thermocouple wires and

the probe. This caused a heating impact on the water temperature around the probe which was inserted inside the large well. Consequently, the thermocouple will measure the affected water temperature not the actual value.

The natural convection heat transfer model was considered in the numerical analysis with an option of the variable fluid density acting as a driving force. Density change occurs because of the temperature difference between the outside atmosphere and working water. Moreover, a laminar single-phase air-water system heated from above was considered in the simulation.

Finite element methods (FEM) are adopted as the numerical method to solve the governing differential equations of motion and heat transfer. This numerical method was built on COMSOL Multiphysics software.

The results show that the larger size of thermocouple has a greater impact on the temperature measurement. The presence of the plastic insert between the water inside the large well and the copper block leads to an increase in thermal resistance. Therefore, inserting the thermocouple inside the water led to a rise in the heating impact of the thermocouple. However, the difference in the heating impacts was eliminated in the copper block experiments when the thermocouple probe was very close to the copper surface.

A strong agreement has been obtained between the numerical and experimental results of the temperature distribution inside the large well of the plastic insert and inside the copper block. Depending on this validation, numerical results of the full chamber geometry are considered solely to examine the temperature distribution inside the large and small wells without the effect of thermocouple.

Thermocouple wires stretched vertically through the environment have a specific length over which their temperature becomes equal to that of the environment. Above this length there will not be an effect of the length of the wire on the temperature measurement.

5.1 Experimental techniques

5.1.1 TG40 model description

Centeo's TG40 is a mobile device, temperature-controlled microplate in SBS (Society for Biomolecular Screening) design that permits to the researchers to monitor the temperature during the experimental process. TG40 keeps the samples against sudden temperature variation while is being transported through the lab during the experiment. The maximum operation of TG40 during transportation is 30 minutes by using the built-in battery [26]. TG40 microplate is connected to external power supply through the dock station for recharging the built-in battery as shown in Fig. 5.1. Moreover, TG40 device can be connected to external computer in order to control the temperature of each row.

The TG40 system consists of five rows of rectangular copper blocks with eight chambers per row (See Fig. 5.1). The maximum working range of temperature of the copper block was usually between 4ºC and 60ºC. However, in this study the temperature of the first row was adjusted to 4ºC, while the last one was set to 20ºC with a temperature difference of 4ºC maintained between every two consecutive rows.

Fig. 5.1: CENTEO's TG40 cooling device.

Each chamber in the plastic insert has two wells containing aqueous liquid (with different NaCl concentrations) as shown in Fig. 5.2. However, to simplify the analysis, the small and large wells were filled with tap water in the experiments. The base part

Table 5.1 Properties of cyclic olefin copolymer and polystyrene.

Material types	Density [kg/m^3]	Thermal conductivity [W/(m K)]	Heat capacity [J/(kg K)]
Cyclic olefin copolymer	1020[108]	0.15 [109]	1340-1466[110]
Polystyrene	1065[111]	0.14[111]	1340-1466[110]

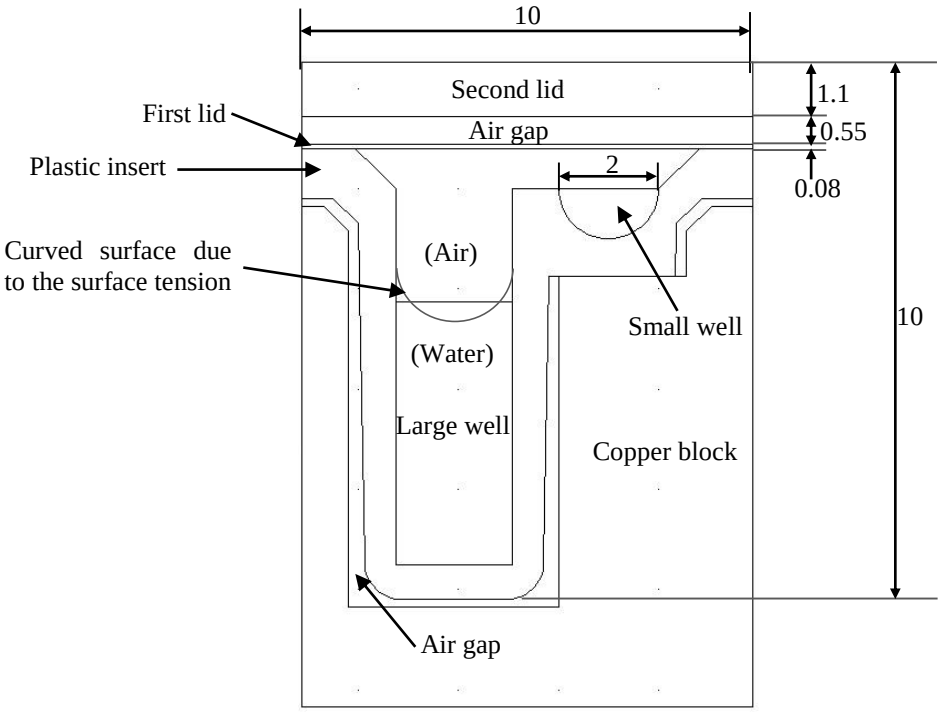

Fig. 5.2 Two dimensional cross-sectional of the chamber. All dimensions in mm.

of the chamber was made of copper, while the material of the plastic insert was cyclic olefin copolymer (COC) and the first and second lids were made from polystyrene (Table 5.1). Note that the upper lid covered all 40 chambers and left an air gap of

0.55m thickness above the chambers. The other air gap, generated due to manufacturing tolerances, was confined between the plastic insert and copper (Fig. 5.2).

The thicknesses of the first lid, second lid, and the air gap between them were 0.08mm, 1.1mm, and 0.55mm respectively. The depth of the small well was 1mm; the outer dimensions of the chamber were approximately (10×10×10) mm^3, including the lids.

5.1.2 Experimental setup

Fig. 5.3 shows the experimental setup, which consisted of three main parts: the base holding the TG40 cooling device, micrometer movement, and PICO log data acquisition TC08, which converted the thermocouple signal into data read by computer.

The plastic base was fabricated to align the TG40 dock station with micrometer in order to measure the temperature of the middle chamber in the first row as shown in Fig. 5.3. TG40 dock station was connected to external power supply for continuous operation during the experiments. A special Centeo's TG40 software was installed in a laptop and the micoplate TG40 was linked to a laptop through USB cable in order to control the temperature of each row.

Two thermocouples used were type-K with bare wire diameters of 80µm (250µm including PFA insulation) and 315µm (600µm including PFA insulation)[4], (See Table 4.1 in section 4.1.2 in Chapter 4) for thermocouple materials properties) to measure the temperature inside the large well in order to study their heat impact effect on the measurement. During the measurement process, the thermocouple(s) were held vertically by a micrometre while the wires were extended into the outside environment. Another two thermocouples of size were used to record ambient temperature. All thermocouples were connected to PICO log data acquisition TC08 which was liked to the laptop for recoding the temperatures.

[4] The manufacturer of both thermocouple is Labfacility with codes Z2-K-2 X 5 and Z2-K-5.0-C81-MP for 80µm and 315µm respectively.

Fig. 5.3 Experimental setup for theTG40 cooling system with micrometre tool movement.

5.1.3 Measurement procedure

The experimental work has concentrated only on measurement of the temperature of the large well. Upon obtaining a satisfactory agreement between the experimental and simulation results, the prediction of the temperature inside the small well will be solely based on the numerical methods described in section 5.3. This is due to the small size of the small well, meaning that using the thermocouple will have a large impact on the well temperature measurement.

During the plastic insert experiments the large well was filled with 42µl of water in order to achieve a water height of 5mm. Water volume (42µl) was calculated from the CAD file of a single chamber. A micro pipette of 20µl size was used to measure water quantity during the experiments. Moreover, due to manufacturing tolerances and the irregular geometry of the water surface (See Fig. 5.18 and Fig. 5.19 in section 5.3.2.1) the calculated water height from the CAD file was different to the actual value. The actual water height was therefore measured by using the thermocouple tip and micrometer while taking the bottom surface of the large well as a reference point (See Fig. 5.3). The average water height was found to be approximately equal to 6mm.The following steps were followed through each run of the experiment:

1. Connect the dock station to an external power supply and the TG40 cooling device to a laptop. Login to the TG40 software and set the first row temperature equal to 4^{o}C and the last row equal to 20^{o}C with 4^{o}C temperature step between two consecutive rows. Wait for enough time in order to reach each row in the TG40 the specified steady state temperature.
2. Plug-in the thermocouples into PICO log data acquisition TC08 to recod the temperature. Attach the required size of the thermocouple to the micrometre and then position the probe at centre line of the large well in the plastic insert.
3. The starting point for the thermocouple measurement was when the probe came into contact the water surface, noticeable by the sudden drop in the temperature recording or by viewing the probe with a digital microscope. Thermocouple measurement was recorded at each 0.25mm step below the surface; this movement was controlled by a micrometre. Wait for seconds after each step till thermocouple reading reaches steady state and then record the temperature with an average sixty-second duration at each step.
4. Temperature of twenty step below the water surface were recorded till the thermocouple reading records no change in the measurement.
5. Repeat the steps 1-5 for each thermocouple size and for five times.

An identical set of experiments was repeated by filling the copper block with an amount of water to obtain the equivalent height of the water inside the plastic insert. Consequently, the copper block contained 116µl of water in order to obtain the same height of water inside the plastic insert. The copper block experiments were performed to predict the copper block temperature which will be used as a boundary condition for the numerical method (See section 5.3.2.4).

Thermocouple calibration was then performed by comparing the reading to the freezing or boiling point of water, as explained in section 4.1.3 Chapter 3. The calibration process is to predict the bias error of the instrument that has been used in the measurement .Whereas, the error bars in Fig. 5.4-Fig. 5.5 and in Fig. 5.7-Fig. 5.8 represents the precision error of the repeated run of the experiments (See section 4.3 inChapter 4.

5.1.4 Geometry uncertainty

Due to manufacturing tolerances, there is a difference in the dimensions between the CAD drawing of TG40 and the real system. These tolerances will affect the size of the plastic insert and the copper block and, consequently, the air gap between them (See Fig. 5.2). For the CAD drawing of TG40, it was assumed that the plastic insert is in direct contact under the small well. This was not the actual case, where there was an air gap between the plastic insert and copper block under the small well. The gap was therefore measured and was found to be within the order of $+10^{-1}$mm.

5.1.5 Experimental results

5.1.5.1 Copper-water experimental results

Fig. 5.4 and Fig. 5.5 show the experimental results of the water temperature distribution inside the copper block measured by the thermocouple of sizes 80µm and 315µm respectively. Fig. 5.4 and Fig. 5.7 show that the error bars are larger for the measurement of the thermocouple of the size 80µm. The probe size of the thermocouple 80µm is smaller than that of the thermocouple 315µm (See Fig. 5.28 in

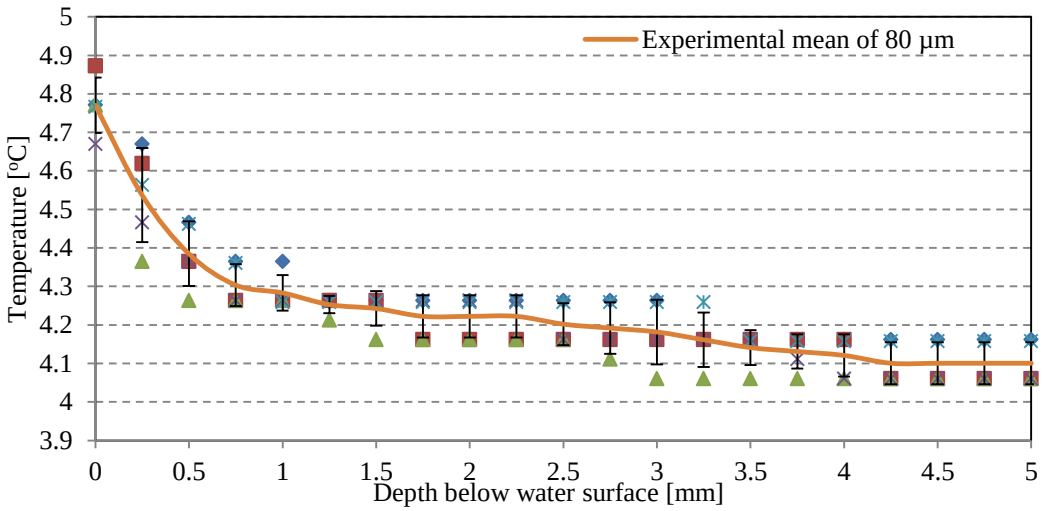

Fig. 5.4: Experimental results of water temperature distribution inside the copper block for the thermocouple size 80µm. Error bars are within ± one standard deviation.

section 5.3.5.1). The possible reason for that are: for each run, the possibility of getting the same starting point for the thermocouple 80µm is lower (in comparison with

315µm) when the thermocouple probe touches water surface. Furthermore, the thermocouple is supposed to measure the temperature distribution along the middle line through the plastic chamber or the copper block. Therefore, it was not possible to position the thermocouple in the same middle position during each experiment. Consequently, the error for each experimental run will be different. Secondly, the effect of surface tension on the thermocouple probe will vary the shape of water surface around the probe and therefore the heat transfer interaction with the thermocouple probe is different for each time.

Fig. 5.6 shows a comparison between the mean experimental measurements of the thermocouples, 80µm and 315µm, inside the water in the copper block. The 315µm thermocouple recorded a higher environmental heat impact at a depth near the water surface than that of the 80µm thermocouple. However, the heat impact effect of both the thermocouples decreased gradually until they were approximately equal at the bottom of the copper block.

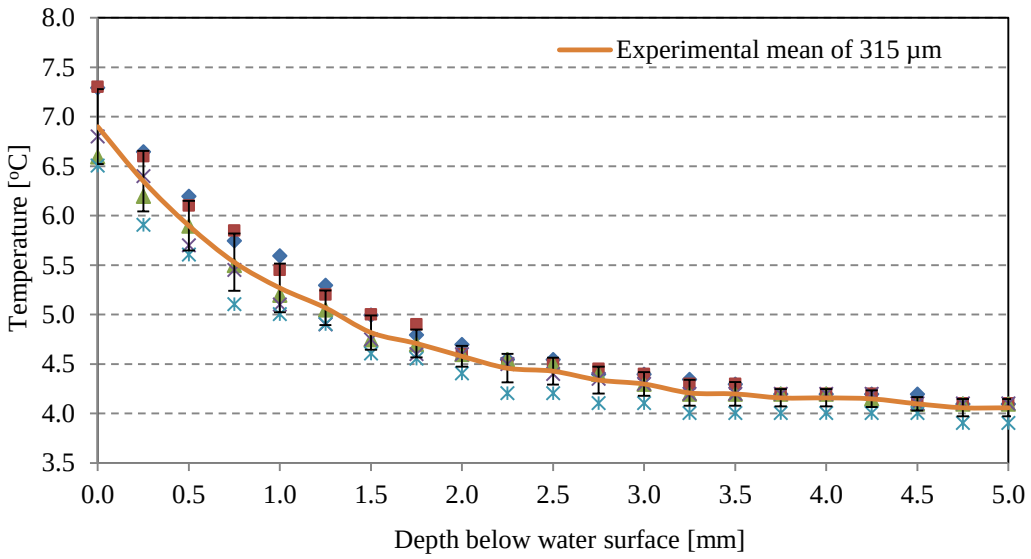

Fig. 5.5: Experimental results of water temperature distribution inside the copper block for the thermocouple size 315µm. Error bars are within ± one standard deviation.

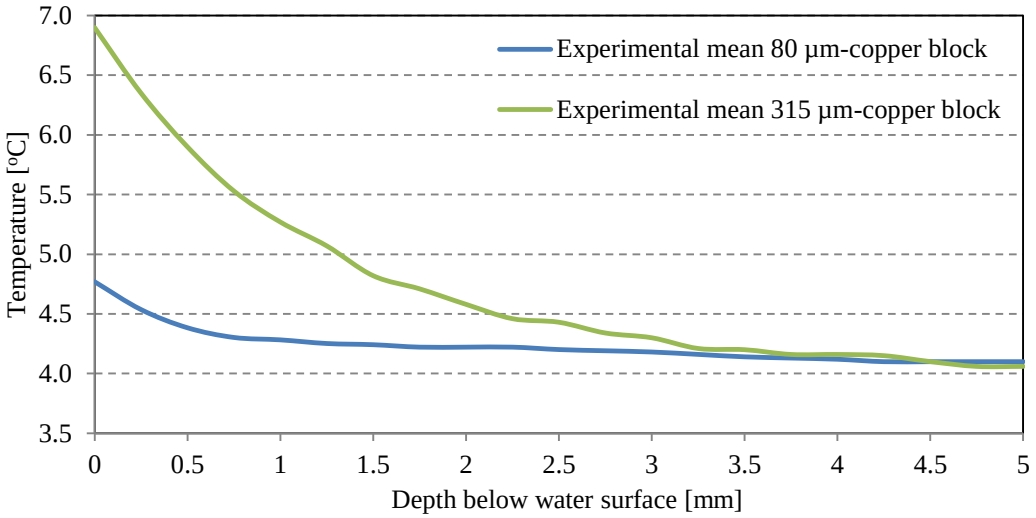

Fig. 5.6: Comparison between the mean experimental temperature of water inside the copper block for 80µm and 315µm.

5.1.5.2 Plastic insert experimental results

Fig. 5.7 and Fig. 5.8 show the experimental results of the water temperature inside the plastic insert measured by the thermocouple of sizes 80µm and 315µm respectively.

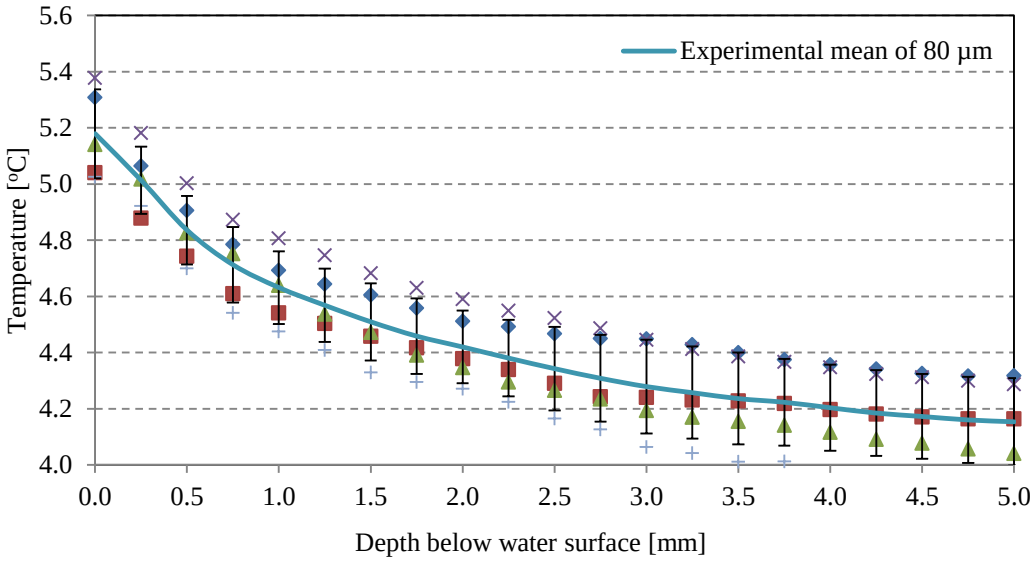

Fig. 5.7: Experimental results of water temperature distribution inside the plastic insert for the thermocouple size 80µm. Error bars are within ± one standard deviation.

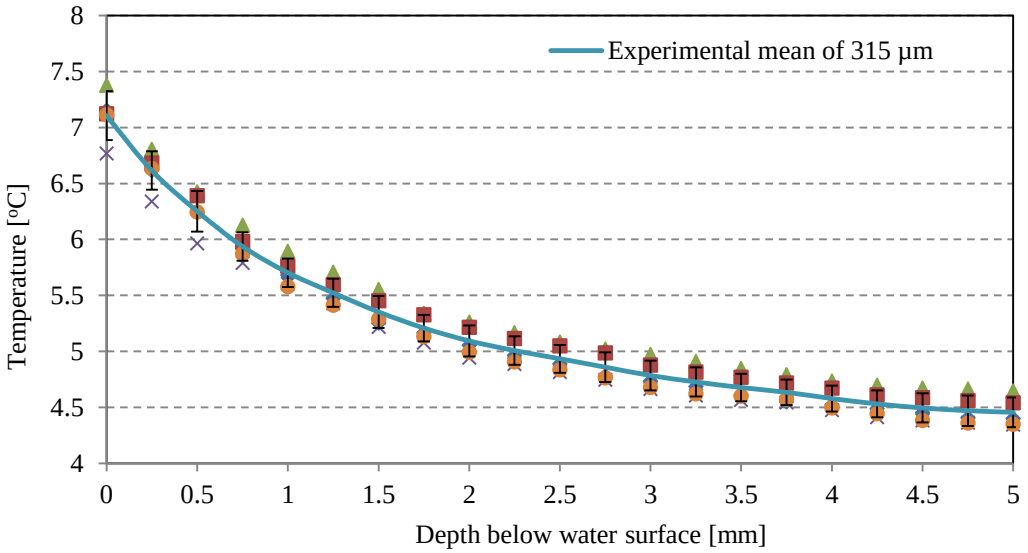

Fig. 5.8: Experimental results of water temperature distribution inside the plastic insert for the thermocouple size 315µm. Error bars are within ± one standard deviation.

Fig. 5.7 shows that the error bars are larger for the measurement of the thermocouple of the size 80µm. The possible reason for that are: for each run, there is no possibility of getting the same starting point when the thermocouple probe touches water surface (See section 5.1.4.1 for details).

Fig. 5.9 shows a comparison between the mean experimental measurements of the thermocouples, 80µm and 315µm, inside the water in the plastic insert. The 315µm thermocouple recorded a higher environmental heat impact at a depth near the water surface than that of the 80µm thermocouple. The heat impact effect of both the thermocouples decreased gradually and continued to the bottom surface of the plastic insert.

Fig. 5.10 shows a comparison between the mean data of the experimental measurements of both the copper-water and plastic-insert water models. The behaviour of the mean experimental results is similar for both sets at the points just below the water surface. However, this behaviour begins to differ at deeper positions.

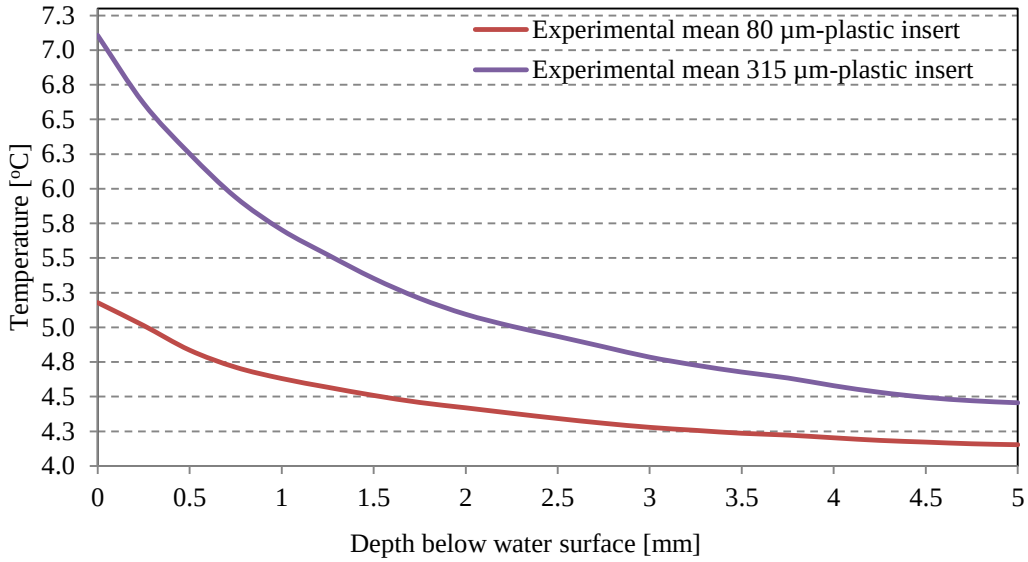

Fig. 5.9: Comparison between the experimental means of the water temperature distribution inside plastic insert for both sizes of thermocouples.

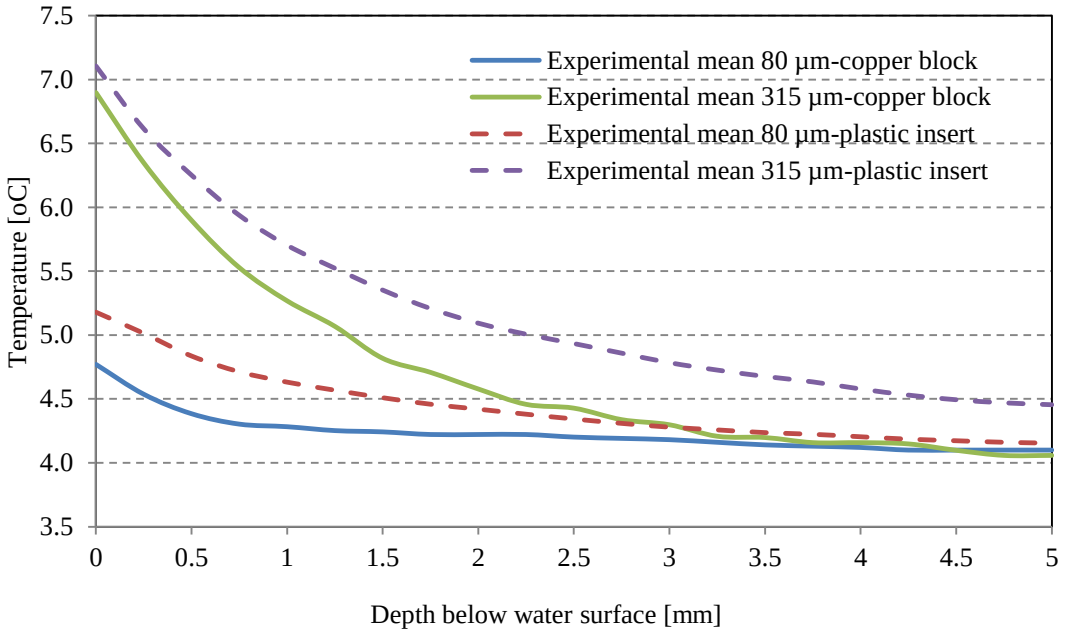

Fig. 5.10: Comparison between the experimental means of the water temperature distribution inside the copper block or plastic insert for both sizes of thermocouples.

The difference occurring in the results is due to the presence of the plastic insert, which introduces more thermal resistance between the copper block and the water inside the large well (See Fig. 5.2).

Water temperature near the copper block is approximately equal to the copper block temperature. Convection processes at this position with the wires can therefore eliminate the heating impact effect, regardless of the size of thermocouple. The energy balance of the thermocouple wires reveals that the heat transferred by convection to the wires from the outside environment was equal to the heat transferred to the water from the submerged part of the wires. Therefore, the heat impact effect of both the thermocouples was greater at the first few depths and gradually decreased at lower positions. This occurred due to the greater length of the wire within the water as the thermocouple moved downward. In addition, the length of the wires above the water surface was maintained at the required length at which the end temperature equalled that of the environment. The heating effect is approximately eliminated near the bottom of the copper block.

The effect of the thermal resistance, due to the presence of the plastic insert between the water inside the large well and the copper block, continues to the deeper positions in the plastic insert experiments. The heating impact effect therefore continues to the final position, particularly for the larger thermocouple. For example, at a depth of 3.5mm and for the copper block experiments the heating impact of both thermocouples is approximately eliminated and thus the thermocouple should measure the water temperature at this point. In the plastic insert experiments at the same depth, heating is available, particularly for the larger size of thermocouple.

5.2 Mathematical Modelling

Thermal analysis was conducted on a single chamber located in the first row. Free convection heat transfer was considered for the air gap(s), as well as for the water inside the well(s) (Fig. 5.2). The steady-state conditions governing differential equations for the flow and energy are written in section 3.1in Chapter 3.

For the natural convection, the driving force inside the TG40 system was the change in the density due to the temperature difference between the bottom and top surfaces of the system. Therefore, assuming *Boussinesq approximation* (for both air and water inside the chamber [112-114]), this force, acting only in the vertical direction, is included in the right-hand side of Eq.(3.4) (See section 3.1 in Chapter 3). Therefore, the body force term in Z-direction is written as [74]:

$$F_z = g\left[1-\beta\left(T-T_{inf}\right)\right] \tag{5.1}$$

where g [m/s^2] is the gravity acceleration and β [1/K] is the thermal expansion coefficient. The body forces in X- and Y-directions are assumed equal to zero (See section 3.1 in Chapter 3).

The air density change was calculated from [74]

$$\rho_{air} = \rho_o \left[1-\frac{T-T_{inf}}{T_{inf}}\right] \tag{5.2}$$

where ρ_{air} [kg/m^3] is the air density, ρ_o [kg/m^3]is the air reference density at 20^{o}C, T [K] is the temperature and T_{inf} [K] is the environment temperature. However, the water properties are calculated from Fig. 3.7-Fig. 3.9 (See section 3.3.3 in Chapter 3). The other properties of air and water are given in where H [m] is the height, v [m2/s] is the kinematic viscosity.

Table 5.2. The energy equation is identical to Eq.(3.5) (See section 3.1 in Chapter 3). The interface between air and water inside the chamber is considered to be stable and continuous boundary [112-115].

Laminar flow is considered in the simulation because the value of the *Grashof* number (*Gr*), Eq.(5.3); characterising the flow feature in the system becomes less than 10^9 for both air and water [74, 87]. For instance, with the wire length of 30 mm, which is the longest length of the thermocouple (Fig. 5.13), and with a temperature difference of $\Delta T = T - T_{inf} = 16^o$C, the *Grashof* number is calculated to be 64096.2 for air and is equal to 4087.44 for water (with height 5mm), (See where H [m] is the height, v [m2/s] is the kinematic viscosity.

Table 5.2 for air and water properties).

$$Gr=\frac{g\beta(T-T_{inf})H^3}{v^2} \tag{5.3}$$

where H [m] is the height, v [m^2/s] is the kinematic viscosity.

Table 5.2 Air and water properties at atmospheric pressure and 20°C [74].

Air		Water	
$v_a[m^2/s]$	15×10^{-6}	$v_w[m^2/s]$	1.004×10^{-6}
$\alpha_a[m^2/s]$	20.8×10^{-6}	$\alpha_w[m^2/s]$	0.142×10^{-6}
$k_a[W/mK]$	0.025	$k_w[W/mK]$	0.59
Pr_a	0.72	Pr_w	7.07
$\beta_a[1/K]$	3.403×10^{-3}	$\beta_w[1/K]$	2.1×10^{-4}
$\mu_a[kg/m.s]$	18.1×10^{-6}	$\mu_w[kg/m.s]$	10.02×10^{-4}
$C_{pa}[kJ/kg.K]$	1.006	$C_{pw}[kJ/kg.K]$	4.182

In a system of two immiscible fluids, when the system is heated from above the occurrence of anticonvection is possible (Welander[112]). However, the anticonvection phenomenon cannot occur in the air-water system inside the TG40 chamber. Welander [112] showed that for anticonvection to occur in the air-water system the ratio of the properties, $\mu_a\beta_aC_{pw}/\mu_w\beta_wC_{pa}$, should be greater than 9 or smaller than 1/9 where μ, β, and C_p are the dynamic viscosity, thermal expansion, and specific heat capacity respectively. However, in the TG40 system studied here the ratio $\mu_a\beta_aC_{pw}/\mu_w\beta_wC_{pa}$, using the air and water properties at 20°C, becomes 1.217, which is much lower than 9 and higher than 1/9. Therefore, a flat surface at the air-water interface is considered in the numerical simulation, which essentially ignores the effect of thermocapillary convection as unlikely to occur at the air-water interface inside the chamber [112, 114, 116].

5.3 Numerical analysis

The finite element method has been used as a numerical method, which is built on COMSOL Multiphysics software. Numerical analysis considers a half-model due to the symmetry in chamber geometry. Fig. 5.11 initially shows some simulation results of the temperature in the TG40 system with lids, which shows the half-geometry results.

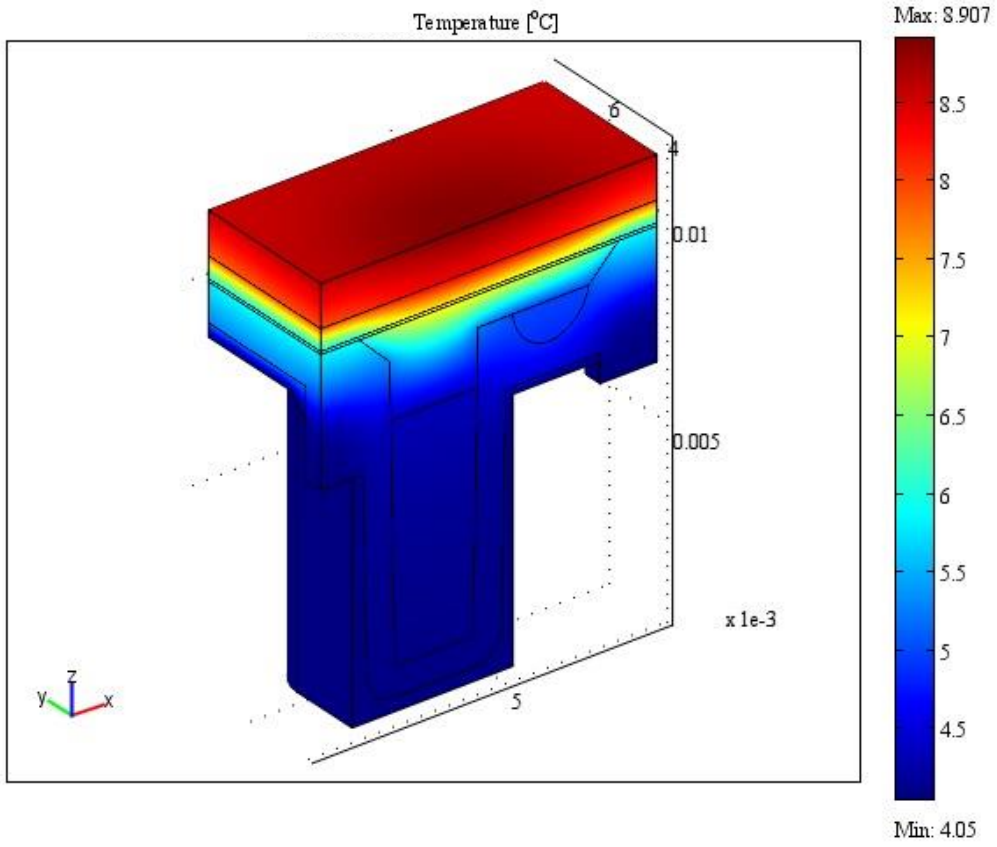

Fig. 5.11: 3D half geometry of the TG40 showing the simulated temperature results with lids.

The free convection boundary condition was applied at the upper surface of the first lid. The lower boundary condition represents the contact boundary between the air gap and the copper block, which is equal to 4.05°C (See Fig. 5.2 and section 5.3.5.1). Periodic and symmetrical boundary conditions are considered for the sides of the chamber and the cross-section boundaries respectively; see Fig. 5.16 for the details of the boundary conditions. The average environment temperature was 18°C, which is

higher than the copper block temperature. Fig. 5.11 shows that the temperature of the upper lid is higher than that of the base (copper block) of the chamber. The same reason explains the temperature inside the small well shown in Fig. 5.12, where the temperature is higher at the upper water surface in the well.

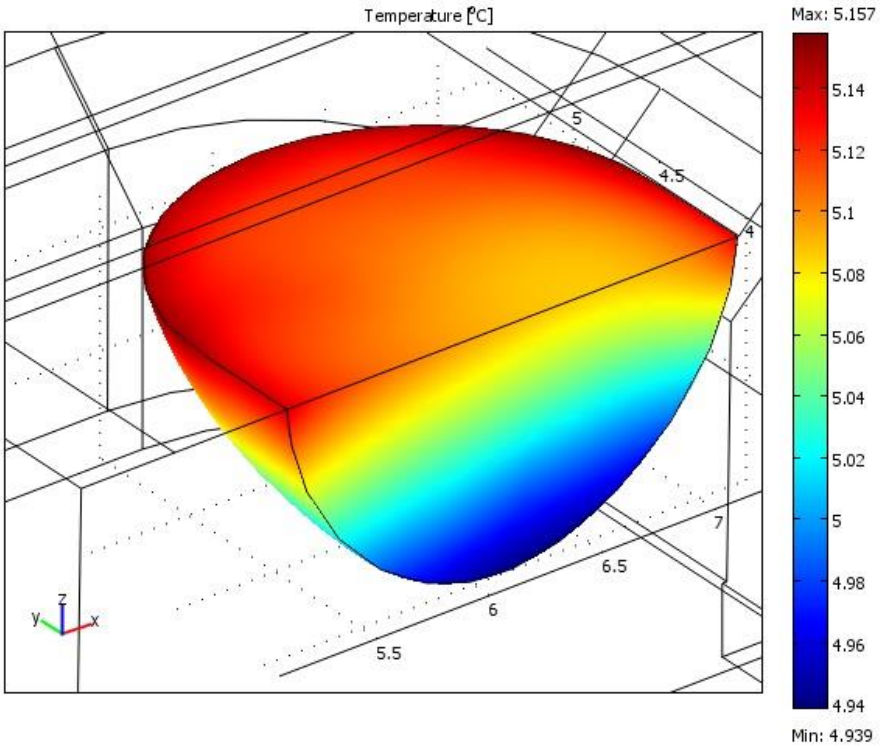

Fig. 5.12: Temperature variation inside the small well with lids.

Thermocouple wire made a heating impact on the large well temperature measurement during the experiment. Therefore, wires were treated as a very long fin and the temperature corresponding to the environmental temperature was determined [91]. The fin base temperature began with the water surface temperature in the large well, which was assumed to be equal to 4.05°C, and the room/environmental temperature was measured to be T_{inf} = 18°C. These results are presented in Fig. 5.13 for both thermocouples, with further details already given in Chapter 4.

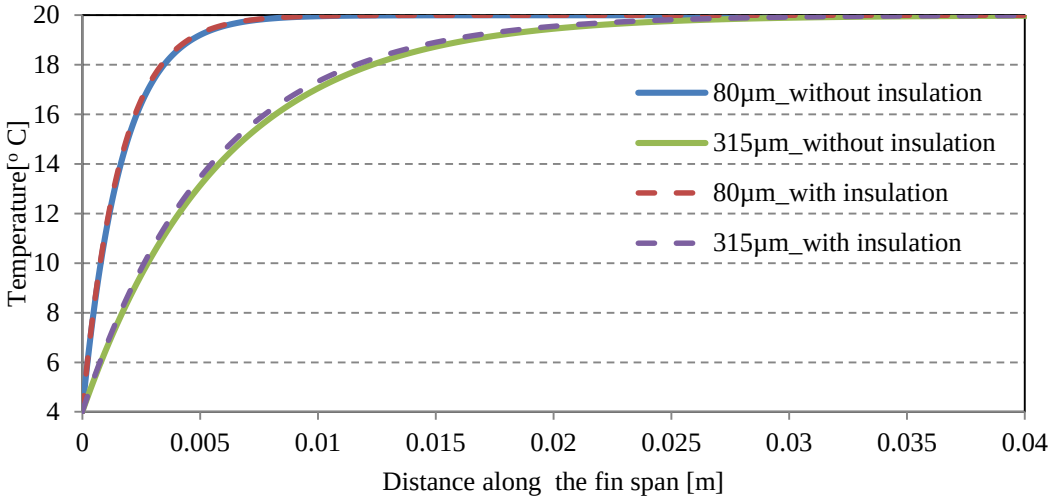

Fig. 5.13: Fin length required to reach the environmental temperature for the TG40 case.

Fig. 5.14 and Fig. 5.15 now demonstrate the numerical results of the impact of the thermocouple sizes, 80µm and 315µm, on the temperature distribution of the large well at a depth of 1.25 mm below the water surface.

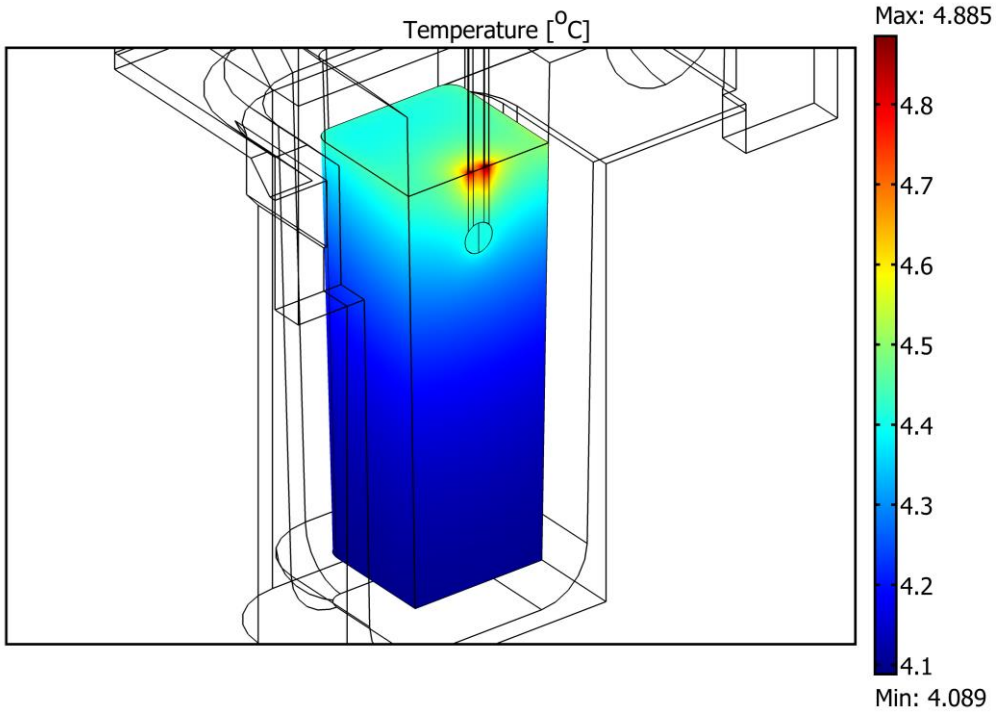

Fig. 5.14: Demonstration of the effect of the 80µm thermocouple on the water temperature inside the large well at1.25mm depth.

The results show that the heating impact was greater for the thermocouple with larger size (315µm), as the heat interaction area with the outside environment is larger. Consequently, the heat transfer by conduction through the wires to the large well is higher.

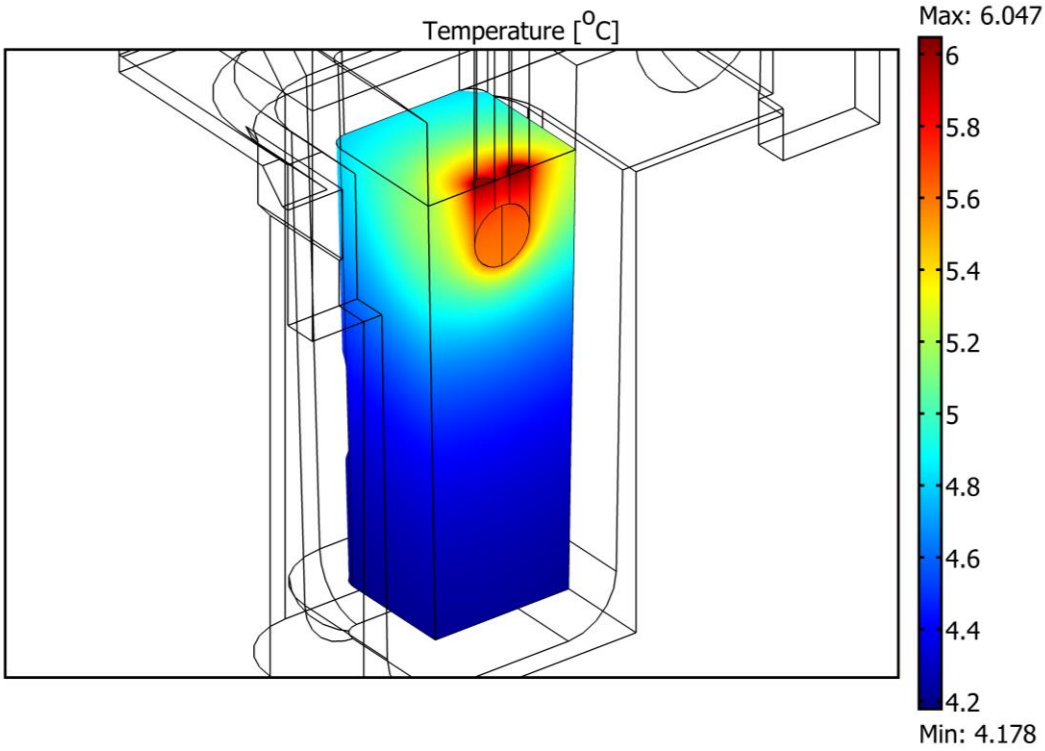

Fig. 5.15: Demonstration of the effect of 315µm thermocouple on the water temperature inside the large well for 1.25mm depth.

5.3.1 Full geometry simulation

In the numerical simulation, a half-geometry of the TG40 is considered due to the symmetry (as shown in Fig. 5.16), which represents a three-dimensional cross-section of a single chamber. As mentioned, the numerical analysis is performed for a single chamber at the middle position of the first row of the TG40 (See Fig. 5.1). The copper block will not be considered in the simulation as its temperature is constant and the temperature gradient across the block's wall is assumed to be very small (See Fig. 5.2). Therefore, the air gap between the copper block and the plastic insert is considered to be an individual subdomain. The contact boundary between the air gap and the copper block is set to a constant temperature (4.05°C), (See section 5.3.5.1).

Symmetry boundaries in the cross-section of the geometry are defined for the hydraulic and thermal simulations. Periodic boundary conditions are considered for the sides of the chamber that are connected to the other chambers in the same row. The upper surface of the second lid is subject to free convection at the atmosphere. The boundaries of the air gaps between the lids (opposite to the symmetry boundaries shown in Fig. 5.16 and next to the second row) are considered as open boundaries. The interface between air and water inside the chamber are considered to be continuous boundary [112, 113], (See section 5.2). The water height inside the large well has been discussed in section 5.3.2.1.

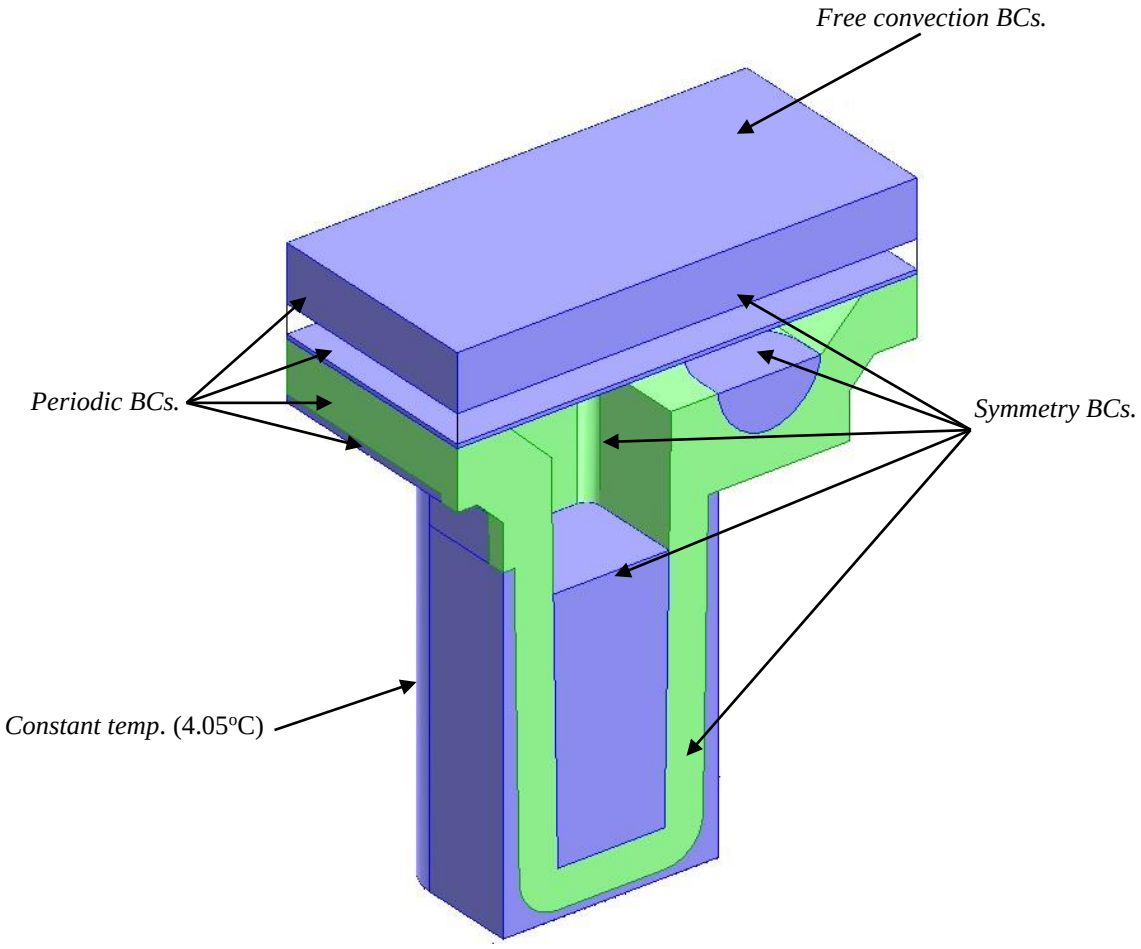

Fig. 5.16: 3D geometry of a single chamber with boundary conditions.

5.3.2 Simulation without the model lids

A simulation(s) without lids (See Fig. 5.2 and Fig. 5.16) and with inserting the thermocouple inside the water in the large well (or the water inside the copper block) has been considered in this section.

5.3.2.1 Water depth inside the large well

Several parameters affect the water depth inside the large well (or the copper block), and consequently the thermocouple zero position for the simulations without lids (See section 5.3.2.2). These are, for example, manufacturing tolerances in the plastic insert size and copper block, an increase in water height due to the thermocouple immersing, complex geometry of the water surfaces which are formed due to the surface tension between the water and plastic inserts (or the copper block) as well as between the thermocouple probe and water surface (See Fig. 5.17 and Fig. 5.18). Furthermore, due to the complex geometry of the water surface inside the large well (and copper block)

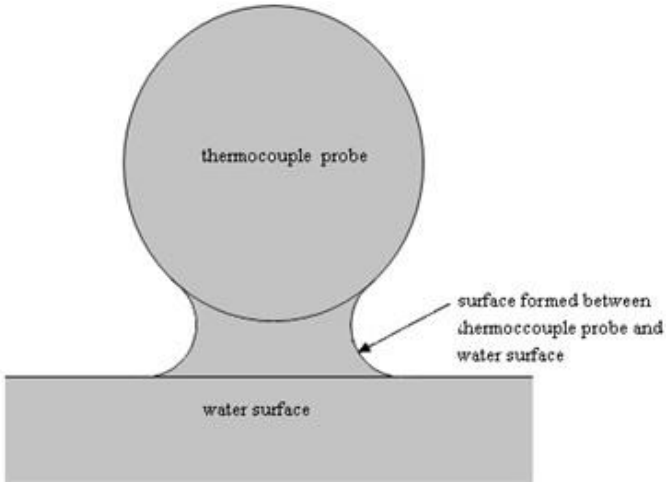

Fig. 5.17: Contact geometry between the water surface and thermocouple probe [117].

Fig. 5.18: Thermocouple probe touching the water surface inside the plastic insert.

and difficulty in predicting the shape of geometry, a flat surface is assumed in the numerical simulation, as shown in Fig. 5.19. Consequently, the three different surfaces were defined: a) calculated from the water volume that fills the large well; b) second curved surface formed due to surface tension; and c) virtual surface that has been adopted in the simulation, chosen to specify thermocouple zero position for starting simulation.

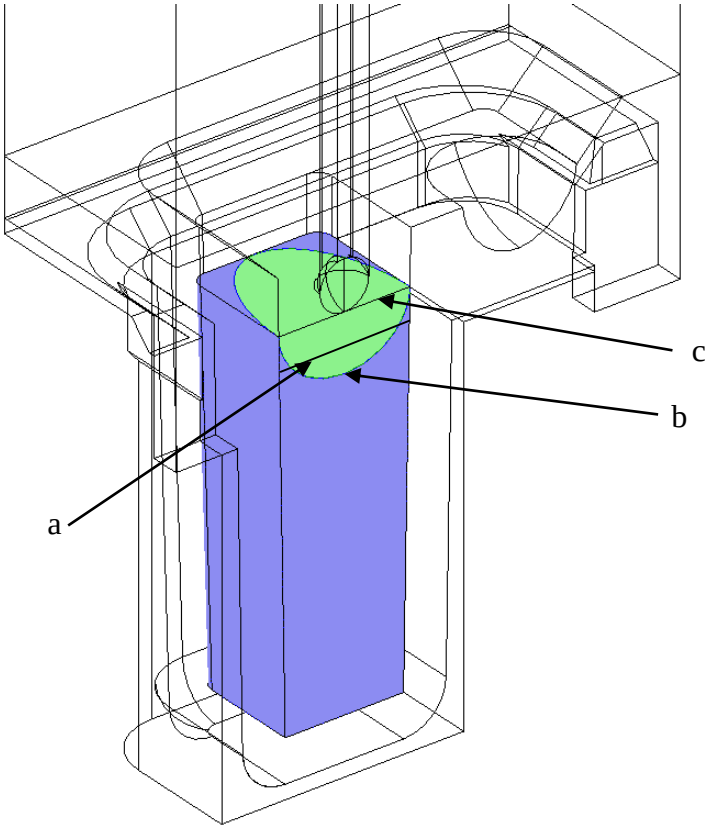

Fig. 5.19: Water surface(s) and thermocouple zero position: a) Primary chosen surface; b) Surface formed by the surface tension; c) Simulation virtual surface.

Three different water depths (6mm, 6.25mm, and 6.5mm) have been modelled in the numerical simulation of the plastic insert to include other effects, such as using different thermocouple sizes. There is no substantial difference between the three heights in comparison with experimental results. The model with the water depth of 6.25mm gives good agreement between the experimental and simulation results for both sizes of thermocouple (See Fig. 5.31 and Fig. 5.32 in section 5.3.5.2) . This value of calculated water height is not far from the measured height of 6mm (See section 0).

This value of the calculated water height (6.25mm) has been used for the full geometry and copper-water numerical simulations as well.

5.3.2.2 Thermocouple zero position

The thermocouple probe at the first point(s) was not totally submerged in the water during the measurement of the water temperature and, at the same time, part of it was still exposed to the outside environment. It is therefore difficult to exactly specify the length of the probe below the water, particularly considering the complex geometry of the water surface (See Fig. 5.17-Fig. 5.19 and section 5.3.2.1), because the thermocouple measures the air temperature just above the water surface which is higher than the water temperature. Consequently, the starting point(s) (or the zero position of the thermocouple probe) of the simulation was selected as the point at which the probe touched the water surface. Therefore, in the simulation the thermocouple probe measures the air temperature only, while this was not the case in reality since the probe was still positioned at the interface between the air and water. This may explain the jump found in the simulation data at the zero point(s) in Fig. 5.25-Fig. 5.26 and Fig. 5.31-Fig. 5.32, because the thermocouple measured the air temperature just above the water surface, which was higher than the water temperature.

5.3.2.3 Simulation with the plastic insert

The same boundary conditions have been applied to the chamber lower boundaries of the geometry, as explained in Fig. 5.16. However, the only difference here is that the lids have been removed and a thermocouple is inserted to measure the temperature inside the large well. Therefore, the upper surface of the plastic insert and each thermocouple wire are exposed to natural convection from the outside environment. Due to the complex geometry of the plastic insert upper surface, it was difficult to determine an accurate formula(s) of the heat transfer coefficients for all surfaces, which are required in the simulations. A virtual air subdomain is therefore added and extended vertically to the point at which the thermocouple wire end temperature is equal to the environmental temperature [75]. This additional subdomain implicitly calculates the heat transfer coefficients between the environment and thermocouple wires and the upper surface of the plastic insert (See Fig. 5.20 and Fig. 5.21).

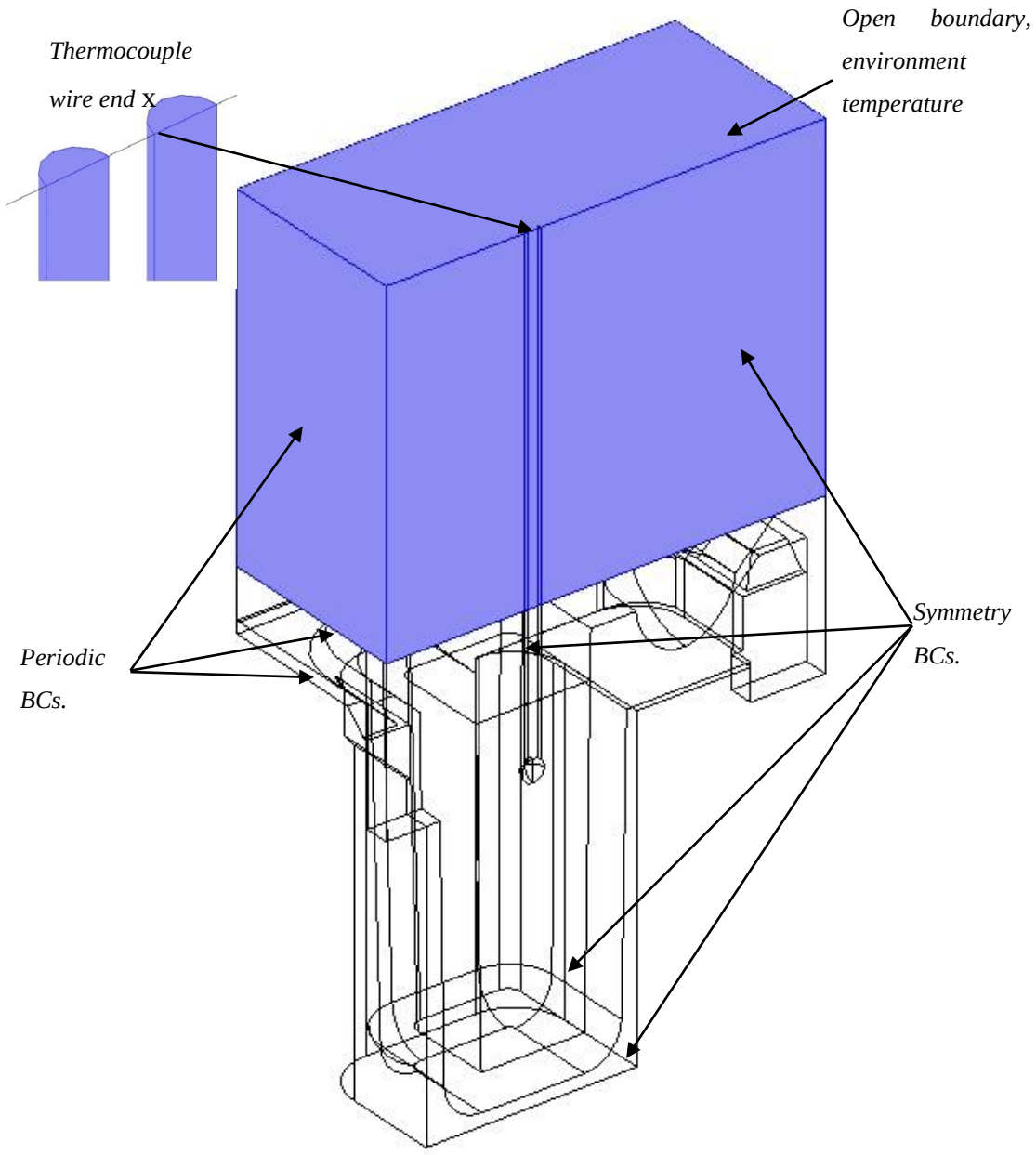

Fig. 5.20: 3D geometry of TG40 chamber with plastic insert and with a 80µm thermocouple inserted in large well.

The preliminary prediction of the air subdomain height is 10mm for the 80µm thermocouple; while it is 30 mm for the 315µm thermocouple (See Fig. 5.13); the numerical simulation for the three-dimensional model analysis gives wire lengths of 10mm and 20mm for the 80µm and 315µm thermocouples respectively. In addition, the upper surface of the virtual air subdomain, as in the previous case, is assumed to

be the open boundary condition and its temperature equal to that of the environment. Note that the effect of the thermocouple electrical insulation was neglected [118].

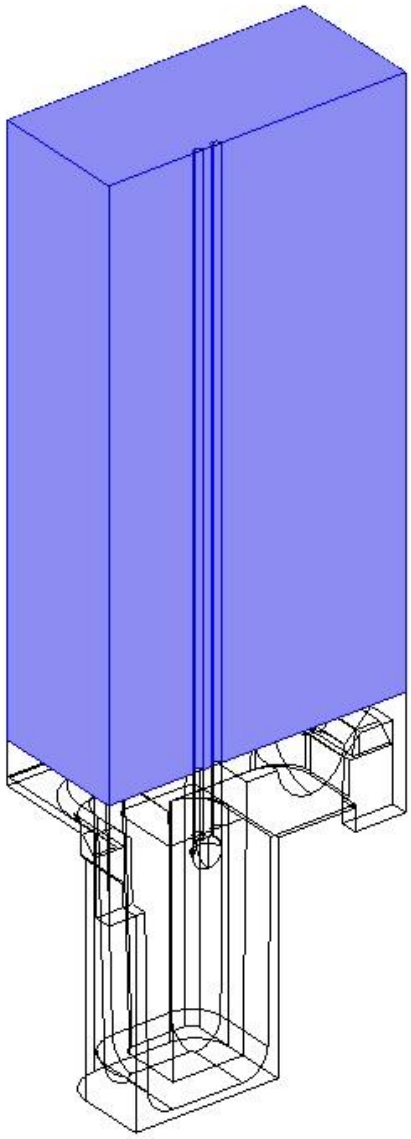

Fig. 5.21: 3D geometry of TG40 chamber with plastic insert and with a 315µm thermocouple inserted in large well.

5.3.2.4 Simulation without the plastic insert

Experiment and numerical simulations have been adopted for the copper block without the plastic insert to confirm the temperature of the block. Copper block temperature is the bottom boundary condition for numerical simulation (Fig. 5.16). Water height inside the copper block is therefore assumed to be equal to the calculated value

(6.25mm) in order to calculate its temperature. This assumption can be seen to be acceptable by observing results for the plastic insert, where the water height inside the large well is very close to the measured value (See Fig. 5.31 and Fig. 5.32 in section 5.3.5.2).

Simulation of the copper block with water follows the same procedure, with a virtual air subdomain added above the copper block and water. Water inside the copper block and the virtual air subdomain are included only in the simulation, and the contact boundary between the water and copper is set to 4.05ºC. Fig. 5.22 shows the three-dimensional simulation model for the measurement of the water temperature inside the copper block using thermocouple size 80µm. A similar model shown in Fig. 5.22 can be used to analyse the water temperature using thermocouple size 315µm except the air domain height will be larger (See Fig. 5.21).

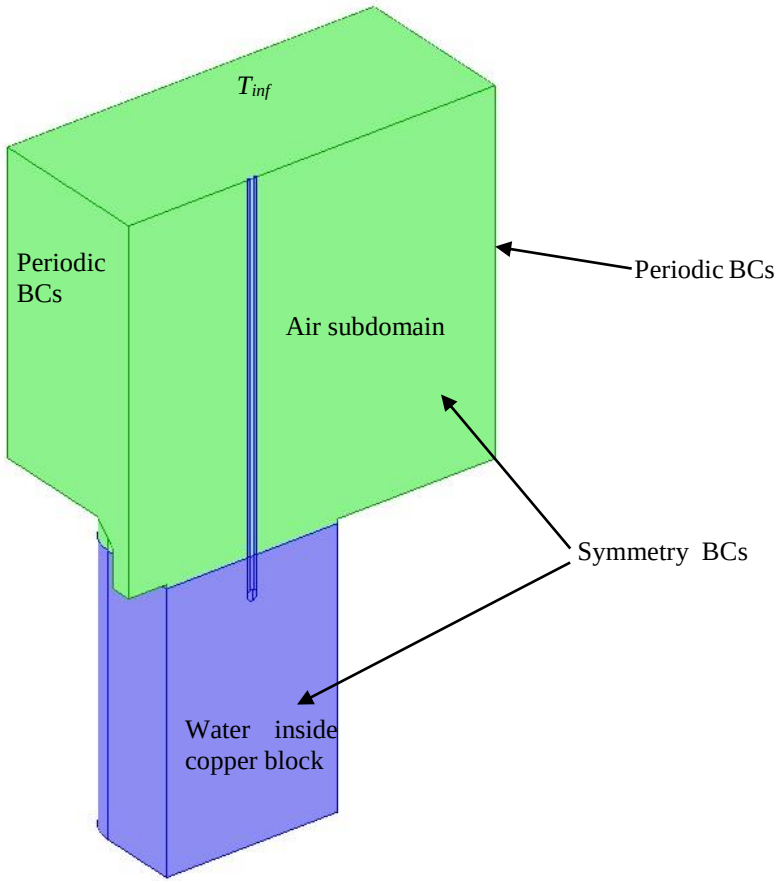

Fig. 5.22: 3D simulation model of the copper block with thermocouple inserted inside the water.

5.3.3 Simulation procedure and mesh resolution test

COMSOL Multiphysics software with finite element method was used to solve Eqs.(3.1)-(3.5), (See section 3.1 in Chapter 3). Due to a complex geometry, free meshing has been used with tetrahedral elements. Small geometry has been meshed with a fine mesh element size, particularly in and around the thermocouple wires and the probe (See Fig. 5.23 and Table 5.3). However, a massive increase in the number of mesh elements leads the solution to converge to a value higher than the specified convergence criterion (equal to 10^{-6}), i.e. the solution is trapped at a specific value and does not converge.

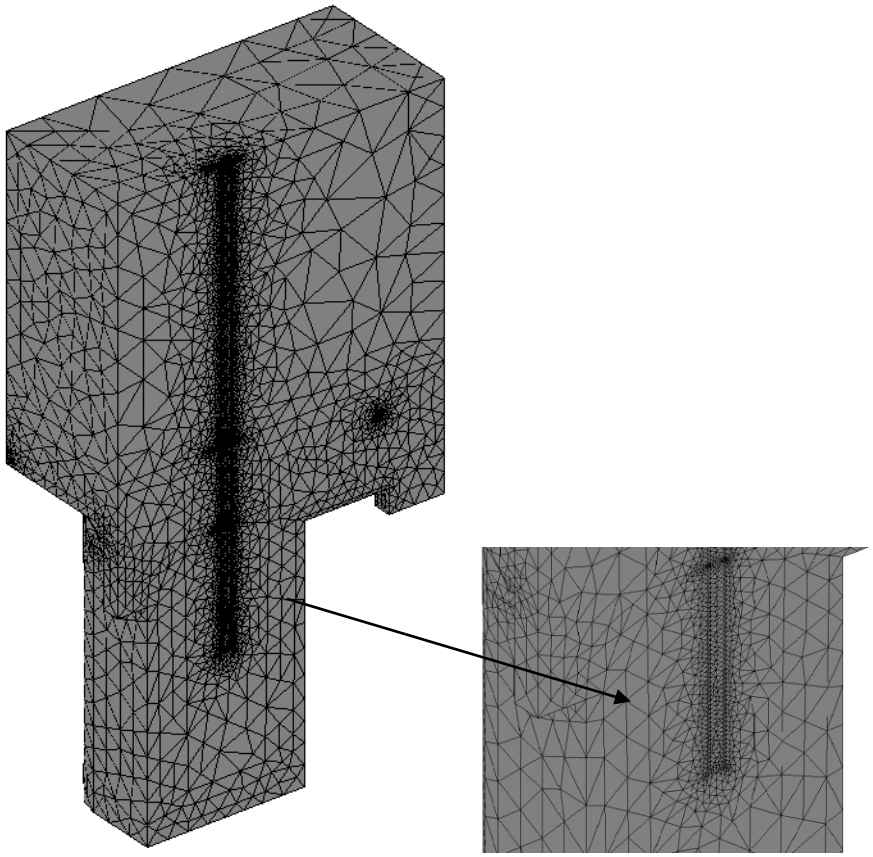

Fig. 5.23: 3D meshes of the chamber without lids with 80µm thermocouple.

An individual simulation was performed for each thermocouple position. Zero position of the thermocouple probe begins where the probe is in contact with the water surface (See Fig. 5.19). The thermocouple probe was then moved at 0.25mm step increments

below the water surface until a depth of 5mm was achieved. Therefore, there were a total of 20 simulation models for each case.

5.3.4 Mesh resolution test

Two models with water height of 6.25mm inside the plastic insert were selected to check the mesh independence in numerical solution. Thermocouple probe temperature was selected as a reference point for comparison between the solutions of different numbers of mesh elements.

Mesh dependence solution was checked using two models for water height 6.25 mm and thermocouple depth(s) position of 0.5mm and 1mm below water surface for 80µm and 315µm for respectively (See Table 5.3). The last mesh size was selected for this case, while for other positions of thermocouple the number of mesh elements increases automatically because the wire length increases in the model (See Fig. 5.24). Copper block temperature is equal to 4.05^{o}C for both models.

Table 5.3 Mesh dependent solution on the thermocouple probe temperature with the plastic insert.

No. of mesh elements	Probe temperature, 315µm size (at depth 1mm)	No. of mesh elements	Probe temperature, 80µm size (at depth 0.5mm)
64697	5.526	90139	4.407
76863	5.769	112232	4.4135
82141	5.7695	134240	4.4155

It was observed in Table 5.3 that there is a negligible change in probe temperature if the number of mesh elements is increased by more than 134240 and 82141 for the sizes of 80µm 315µm respectively. The number of mesh elements is increased when the thermocouple depth below water is increased, as shown in Fig. 5.24. Accordingly, thermocouple wire length inside the large well increases, and consequently the number of mesh elements should increase around the wires.

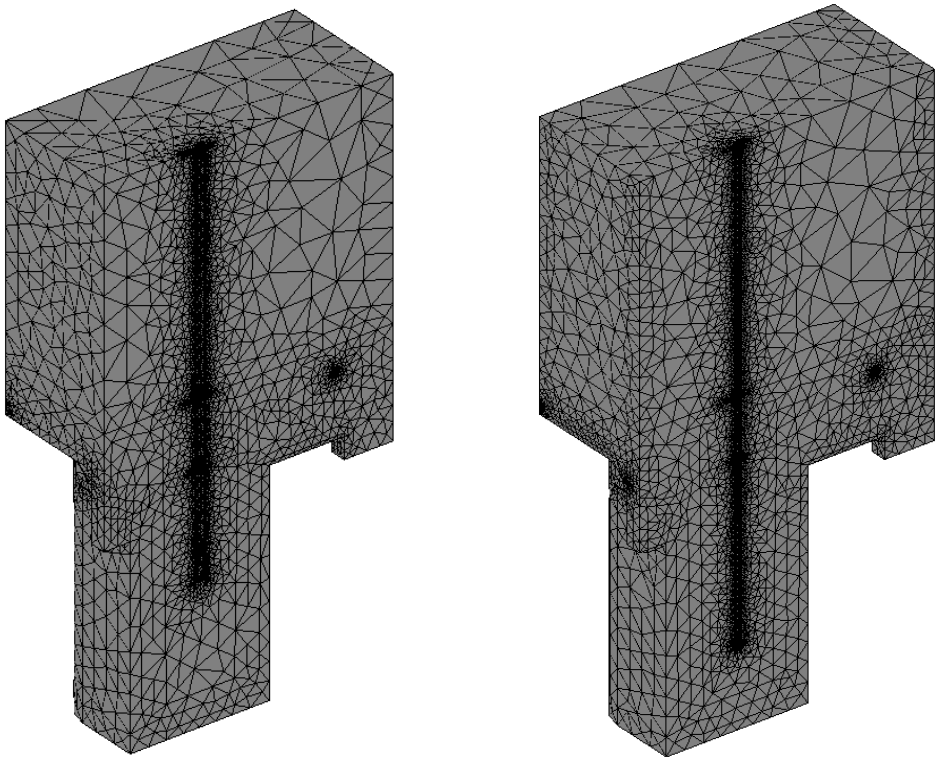

(a) 1mm depth position (b) 5mm depth position

Fig. 5.24: Comparison between number of mesh elements for two positions of thermocouple at depths 1mm and 5mm.

5.3.5 Numerical results and model validation

5.3.5.1 Copper block simulation results

Numerical simulation was performed with different values of copper block temperature for both sizes of thermocouple: 80μm and 315μm. Fig. 5.25 and Fig. 5.26 show a comparison between the experimental and simulation results of the temperature distribution inside the water in the copper block. The values of the copper block temperatures (4.05^{o}C and 4.1^{o}C) and (4^{o}C and 4.05^{o}C) give good agreement with the experimental data for the thermocouple sizes 80μm and 315μm respectively. Therefore, the value of the copper block temperature (4.05^{o}C) was adopted for the numerical analysis and during the experiments. The average environmental temperature was 18^{o}C.

Fig. 5.27 shows the deviation of the experimental results from the numerical results. Fig. 5.27 was produced by comparison the average of the experimental results with

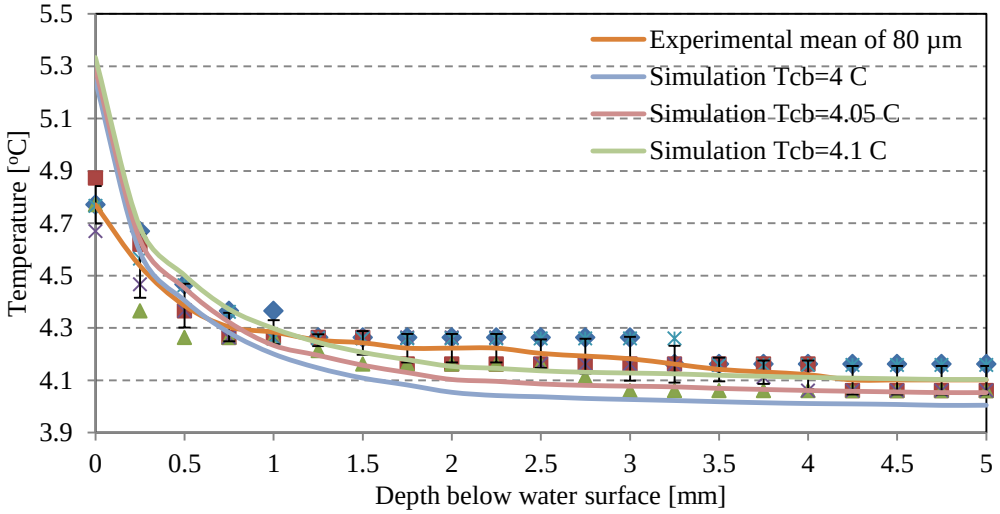

Fig. 5.25: Temperature distribution of water inside the copper block with different block temperature (T_{cb}) for the thermocouple size 80µm.

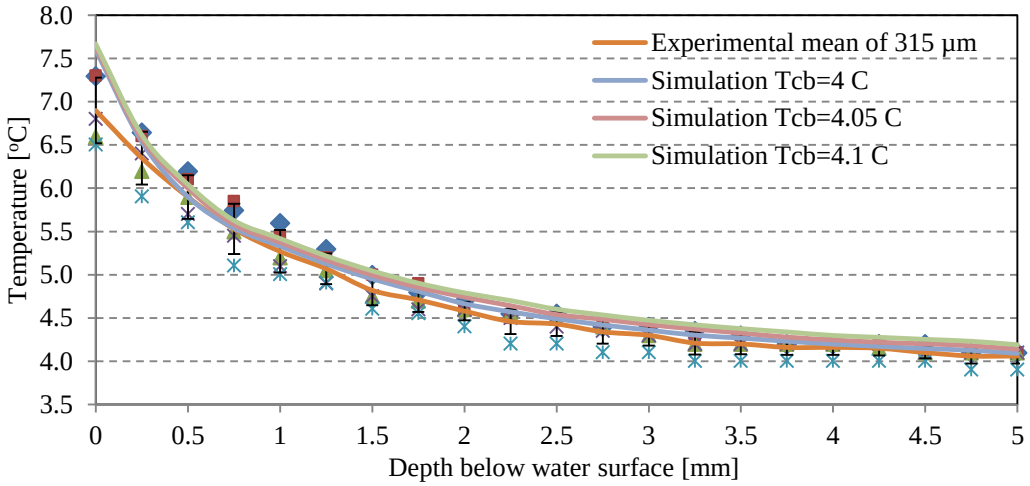

Fig. 5.26: Temperature distribution of water inside the copper block with different block temperature (T_{cb}) for the thermocouple size 315µm.

numerical analysis. The main uncertainty in the measurement process is specifying the accurate zero position of the thermocouple probe in each run. Therefore, each of the experiments has its own starting position which is different from the other run. This error will effect percentage deviation of the numerical results from the experimental results. Moreover, in the numerical simulation the assumption of a flat water surface in the copper block insert can lead to more deviation from the experiments. Fig. 5.27 shows that the deviation of numerical results of the size 315µm is larger than that of 80 µm. The explanation of that is the probe diameter of the thermocouple size 315µm

is larger than the size 80 µm (See Fig. 5.28). Therefore, the possibility of the error of specifying starting zero position of the measurement process is greater for the thermocouple size 315µm. Moreover, the assumption of spherical shape of the probe in the numerical analysis may lead to greater deviation of the numerical results from the experimental values while the actual shape of the probe is not totally spherical.

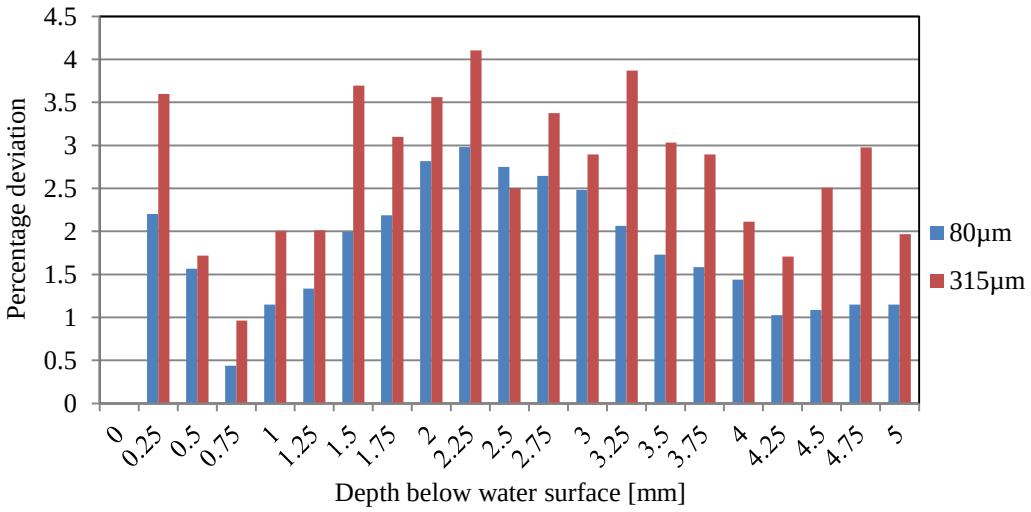

Fig. 5.27: Deviation of the copper block numerical results from the experimental results for both sizes of thermocouple 80µm and 315µm with copper block temperature equal to 4.05°C.

(a) 449µm (b) 860µm

Fig. 5.28: Thermocouple probe size shown in microscope pictures: a) 80µm, and c) 315µm.

Fig.5.29(a-b) shows a comparison between the means of the experimental results of the copper block (See Fig. 5.6) and simulation results of the same model without

thermocouple. It is clearly shown that the thermocouple of larger size has a higher heat impact.

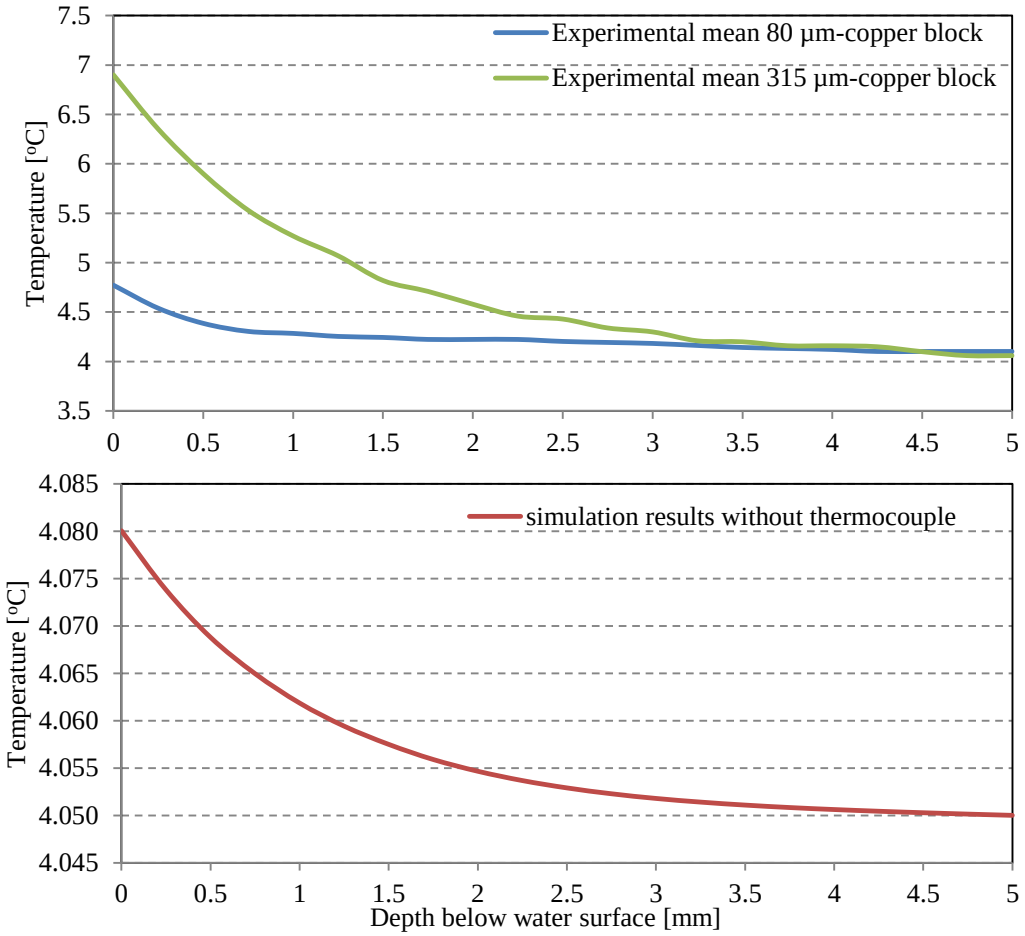

Fig.5.29: Comparison between: (a) the experimental means of the copper block-water system of the 80µm and 315µm thermocouples (See Fig. 5.6) with (b) simulation results of the same model without thermocouple.

Fig.5.30 shows the heating impact that both sizes of thermocouple have on the actual temperature measurement of the water in the copper block. The vertical axis presents the difference between the experimental mean and simulation data without the effect of thermocouple. It shows that there is a greater heating impact effect at the first points, but that this decreases at deeper points below the water surface. During the experiments, part of the thermocouple wires was submerged within the water, while the other part was exposed to free convection from the outside environment.

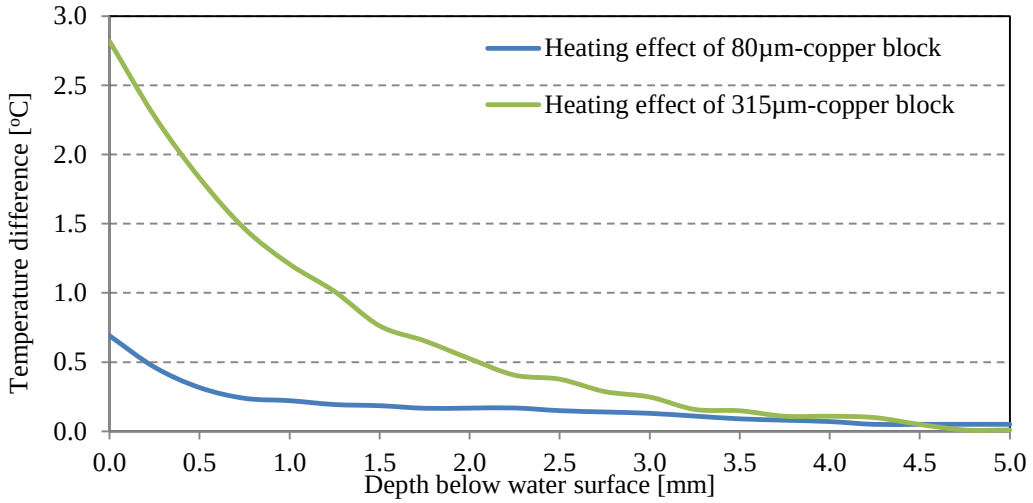

Fig.5.30: Comparison between heat impact of both sizes of thermocouple with copper block. The y-axis represents the difference between experimental mean results and simulation results without thermocouple.

5.3.5.2 Plastic insert simulation results

Three different heights were simulated (6mm, 6.25mm, and 6.5mm) for both sizes of thermocouple 80µm and 315µm, as shown in Fig. 5.31 and Fig. 5.32. There is no fundamental effect of the water height on the simulation results. Therefore, the depth of 6.25mm gives good agreement between the experimental and simulation results for

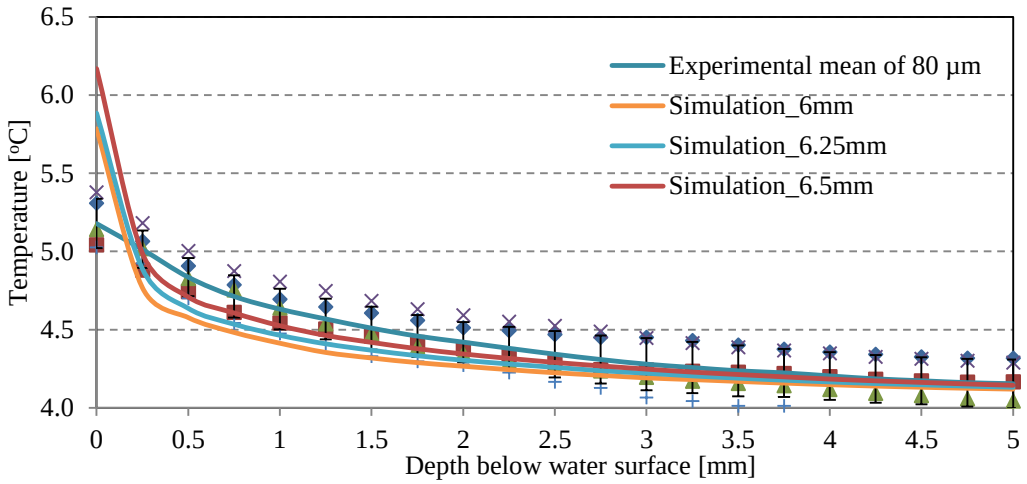

Fig. 5.31: Comparison between the experimental and simulation results with the plastic insert for different water heights inside the large well for the thermocouple size 80µm.

both thermocouples. This value was adopted for the numerical analysis and during the experiments.

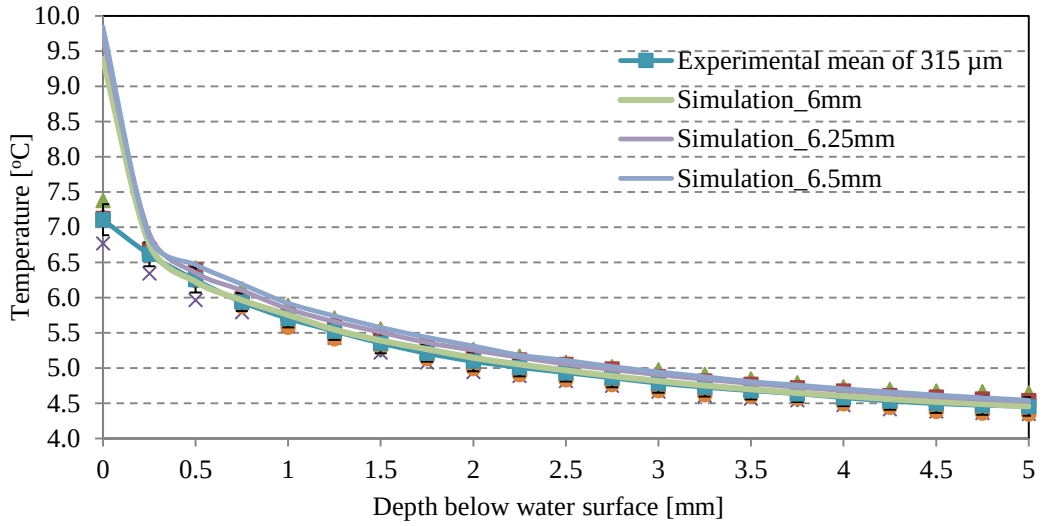

Fig. 5.32: Comparison between the experimental and simulation results with the plastic insert for different water heights inside the large well for the thermocouple size 315µm.

Fig. 5.33 the percentage deviation of the numerical results from the experimental

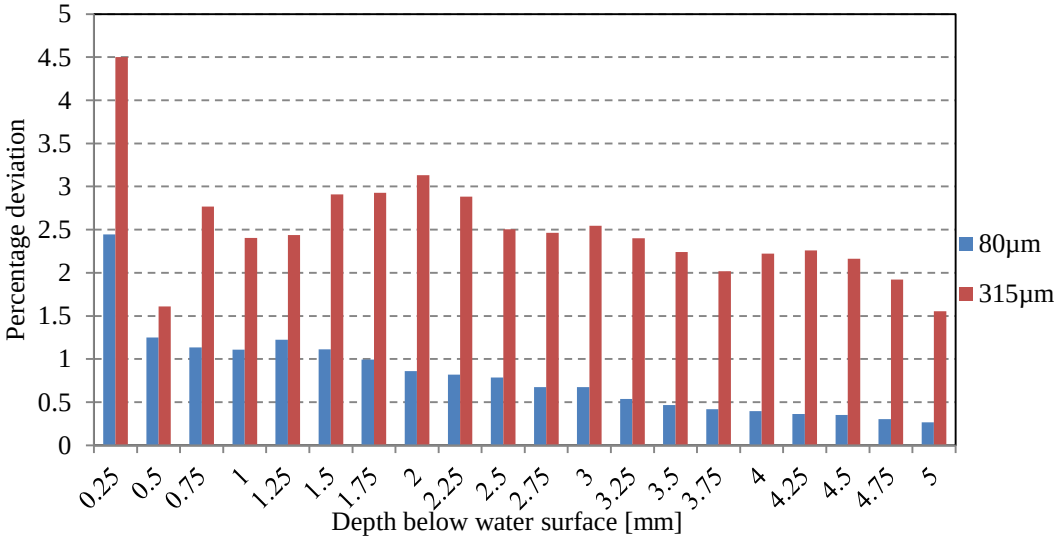

Fig. 5.33: Deviation of the plastic insert numerical results from the experimental results for both sizes of thermocouple 80µmand 80µm with copper block temperature equal to 4.05ºC.

values. The discussion of Fig. 5.27 in section 5.3.5.1 is valid for the Fig. 5.33.

Fig.5.34shows a comparison between the means of the experimental results of the plastic insert (See Fig. 5.9) and simulation results of the same model without thermocouple. It is clearly shown that the thermocouple of larger size has a higher heat impact.

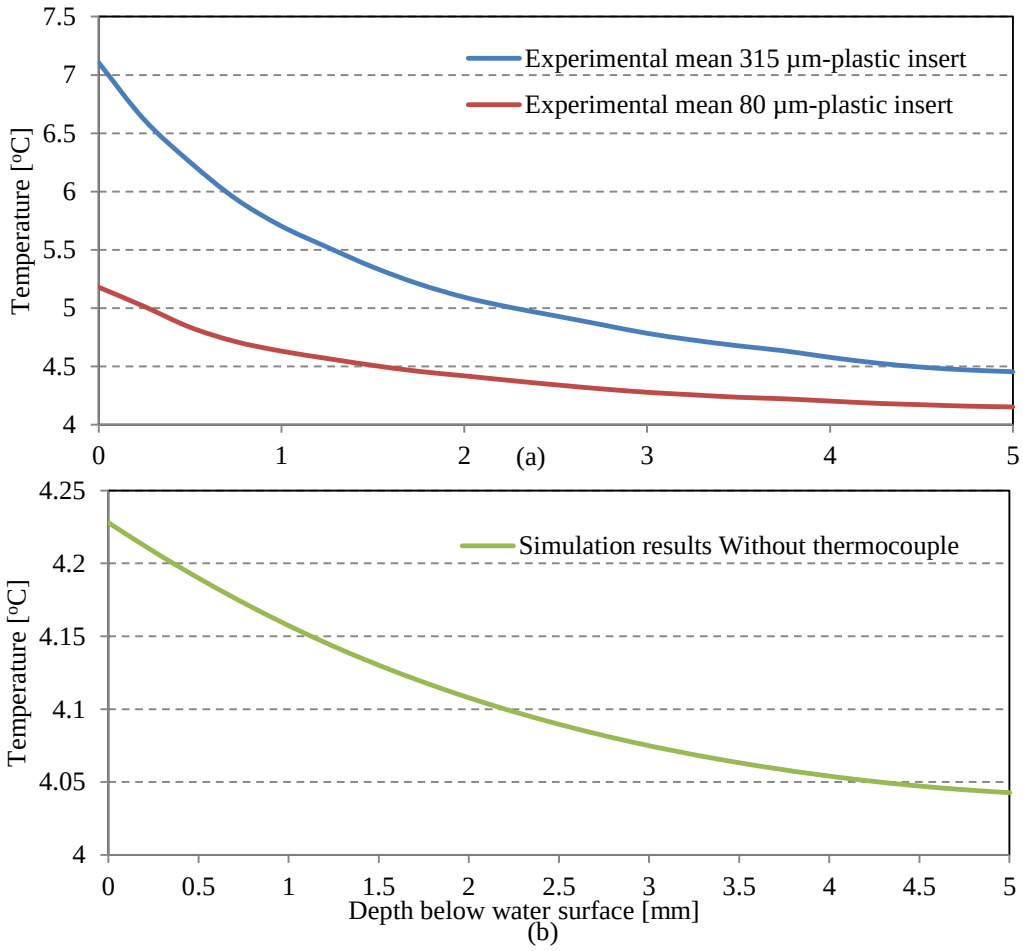

Fig.5.34: Comparison between: (a) the experimental means of the plastic insert system of the 80um and 315um thermocouples (See Fig. 5.9) with (b) simulation results of the same model without thermocouple.

Fig.5.35 demonstrates similar behaviour of the results in Fig.5.30 in section 5.3.5.1 except the effect of plastic insert appears near the bottom of the plastic insert where the heating impact is still dominant to the end. The presence of the plastic insert increases the thermal resistance between thermocouple probe and copper block which leads to more effect of the thermocouple wires conduction error.

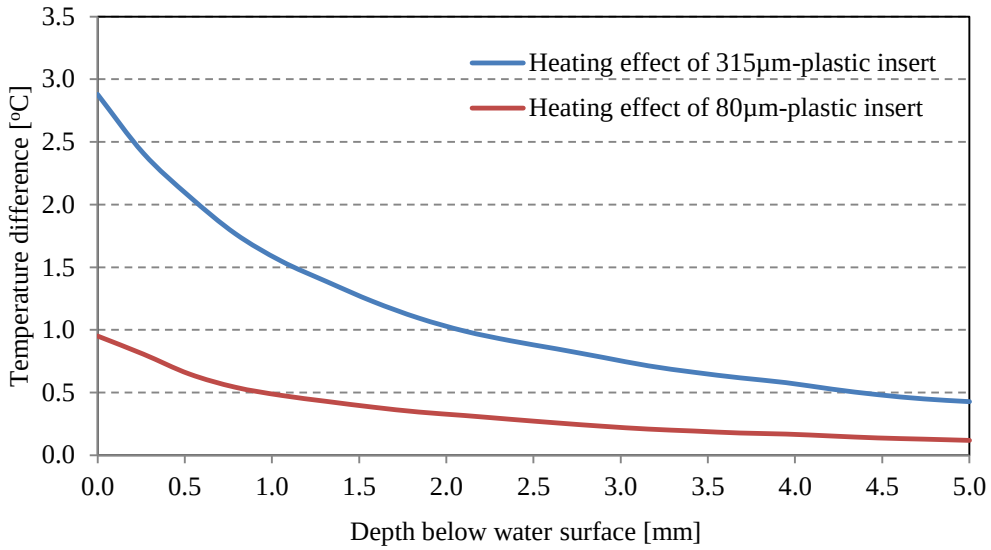

Fig.5.35: Comparison between heat impact of both sizes of thermocouple with plastic insert. The y-axis represents the difference between experimental mean results and simulation results without thermocouple.

5.3.6 Small well temperature distribution

According to the previous results presented earlier in Fig. 5.25-Fig. 5.26 and Fig. 5.31-Fig. 5.32, the simulation results alone can be used to predict the other required results for the TG40 cooling system, designed to keep a protein solution in the small well at a certain temperature (See Fig. 5.2). TG40 was designed to keep the temperature inside the small well uniform and close as much as possible to the copper block temperature. Two main parameters may affect the temperature of the small well: firstly, the water height inside the large well, and secondly the air gap between the plastic insert and copper block. Therefore, it is necessary to investigate the effect of these parameters and examine parameters which have greater effect on the temperature of the small well.

The existence of the air gap between the copper block and the plastic insert is due to the manufacturing tolerances of TG40 device, see Fig. 5.36. The increase in the air gap below the small well will enhance the thermal resistance between water inside the well and the copper block. Consequently, the cooling effect of the copper block on the water inside the well will be reduced and the temperature inside the small well is rising, see Fig. 5.37.

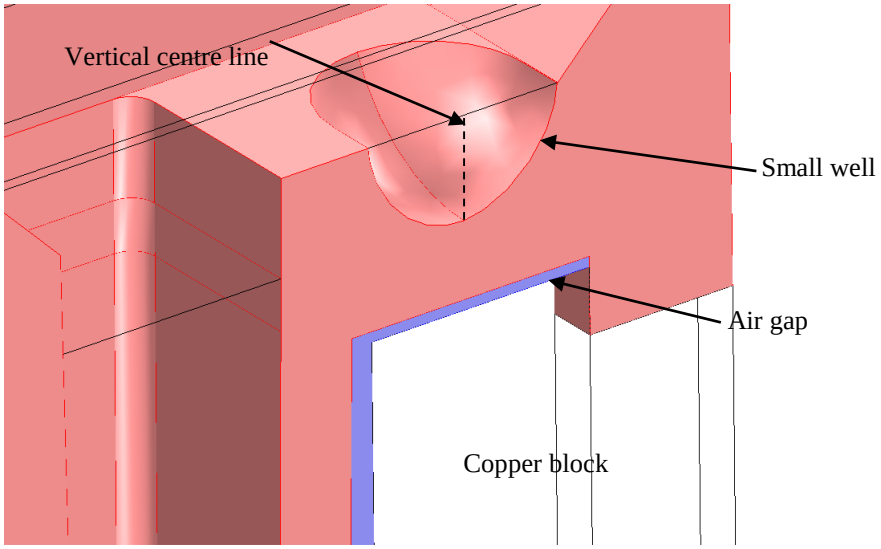

Fig. 5.36: 3D model of the small well in TG40 device and the position of the air gap.

Fig. 5.37 shows the numerical results and effects of increasing the air gap between the copper block and the plastic insert on the temperature distribution inside the small well. An increase in the air gap of 0-0.4 mm leads to a temperature difference of around 0.5°C. A zero gap, which can be considered as a reference point, means the bottom

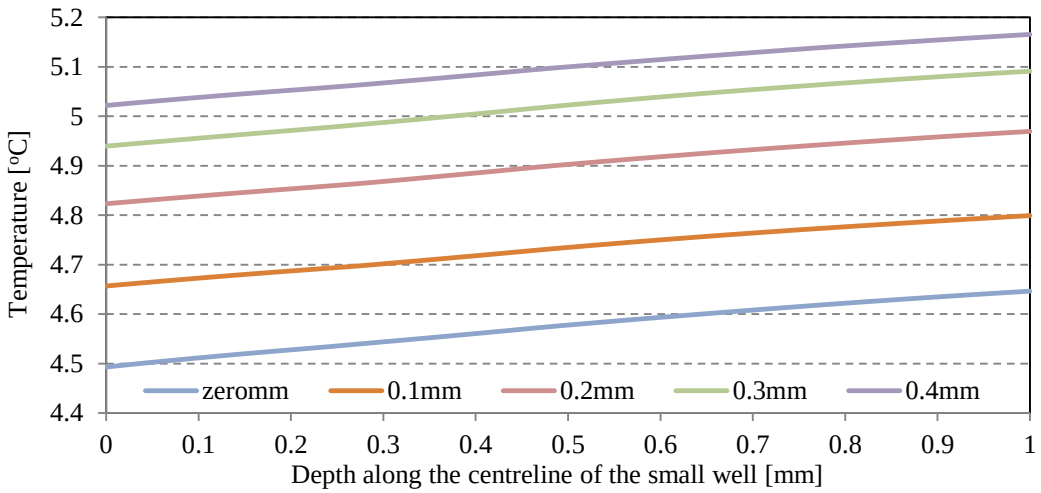

Fig. 5.37: Effect of varying the air gap on temperature distribution inside the small well. X-axis represents the distance along the centre line starting from zero mm (well bottom surface) to 1 mm (water surface in the well), see Fig. 5.36.

surface of the small well is in direct contact with the copper block and there is no air gap below the well. The increase in gap size therefore leads to an increase in thermal resistance between the well and the copper block. Consequently, the resistance to the cooling effect of the copper block will be greater and leads to a rise in the temperature of the small well.

An increase in the water height inside the large well has a small effect in comparison with that of the air gap between the plastic insert and copper block. Fig. 5.38 demonstrates that an increase in water height inside the large well has a small effect on temperature distribution inside the small well. Therefore, the increase in the air gap shown in Fig. 5.37 has a greater influence than that of the water height inside the large well.

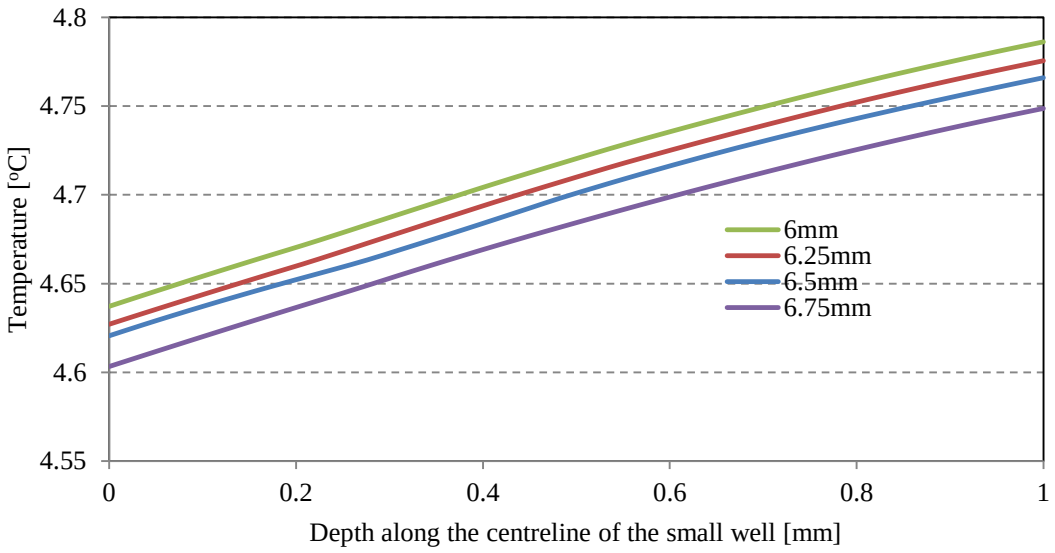

Fig. 5.38 Effect of variation the water height inside the large well on temperature distribution inside the small well. X-axis represents the distance along the centre line starting from well bottom surface to (water surface in the well), see Fig. 5.36.

5.4 Conclusions

Use of a thermocouple to measure the temperature of a small volume of liquid which is cooler than the environmental temperature causes a heating effect. In other words, the readings obtained from the thermocouple give an overestimation of the real

temperature of the liquid. The reading from the thermocouple therefore requires a correction to obtain a true value. The results showed that:

1. The heating effect of the thermocouple decreases measurements for at a greater depth, and this effect is eliminated when the thermocouple junction is close to the copper block.
2. The increase in the thermal resistance between the copper block and the thermocouple junction raises the heating effect of the thermocouple. This is clearly shown in Fig. 5.10, where the effect of the large size of thermocouple is greater than that of the smaller one.
3. The length of thermocouple wires exposed to the environment has no effect over a specific length where the wire end temperature is equal to that of the environment. But this critical length increases with an increase in thermocouple size.

These results are then used to relate experimental results with a FEM simulation of a system without inserted thermocouple. This simulation is employed to investigate the impact of various parameters on the TG40 performance, without the errors caused by temperature measurement tools. Therefore, the following have been concluded:

1. The resistance to the cooling effect of the copper block is enhanced when the air gap between copper block and plastic insert is increased. Consequently, the temperature inside the small well is raised.
2. The increase in the water height inside the large well has negligible effect on the temperature of the small well.

Chapter 6
Liquid Cooling of Non-Uniform Heat Flux of Chip Circuit by Subchannels

Experimental and numerical analyses have been performed to study the effect of using subchannels to enhance heat transfer from the hotspot generated on a chip circuit by non-uniform heat flux. Two models of heat sink– with and without subchannels– were fabricated in order to investigate this effect.

The first model was manufactured with a parallel channel with the hotspot at the middle position of the channels. The second model was designed to extract more heat by dividing the main channels above the hotspot into two subchannels.

Heat was generated by using twelve microheaters made from thin platinum film. The heaters were divided into three sets with four microheaters for each. High voltage was supplied to the middle set of microheaters to generate a hotspot and lower voltage was applied to the upstream and downstream sets in order to generate a uniform heat flux.

Inlet and outlet manifolds have two inlet ports in order to minimise any potential mal-distribution of mass flow rate through the channels. The models were fed with filtered water from a large container through two plastic tubes.

According to the results and the conclusions of the Chapter 4 and Chapter 5, the attachment methods of the thermocouples in the present work have been chosen to minimise the impact of the thermocouple(s) on the temperature measurement. The thermocouples were fixed perpendicular to the surface in order to avoid a temperature gradient and then heat conduction along the wires. Consequently, the effect of the thermocouple will be reduced and the temperature measurement will be more accurate. Moreover, a thermal paste was added between the thermocouple probe and surface to improve thermal contact and the wires were wrapped by thermal insulation to prevent any thermal contact with the other surfaces. Therefore, three thermocouples were attached to the bottom surface of the inlet manifold and another three attached to the

outlet manifold to record surface temperature. The water inlet temperature was measured by immersing a thermocouple in a water container and two thermocouples were inserted into outlet ports to monitor outlet water temperature. Five different mass flow rates were generated under gravity by changing water container height.

Numerical modelling of the two models was carried out using commercial COMSOL Multiphysics software, based on finite element method as a numerical technique. The experimental results were compared with numerical results to validate the numerical model. A good agreement between the experimental and numerical results was achieved.

The results showed that adding subchannels improves the uniformity of temperature distribution and reduces the maximum temperature on the bottom surface. Moreover, thermal resistance was reduced but pumping power increased as a result of the presence of subchannels.

6.1 Experimental techniques

6.1.1 Model fabrication

Eleven channels were fabricated on a copper plate by using Datron CAT 3D-M6 with an accuracy of ±1μm. The properties of the copper are shown in Table 6.1. Two cooling devices were manufactured with and without subchannels as shown in Fig. 6.1. The dimensions of the cross-sectional area of the main channel(s) were 0.9mm×0.9mm while the subchannel dimensions were 0.3mm×0.9mm with wall thickness of 0.3mm for both.

The total length of the channels was 12mm for both models with subchannels of length 4mm added to each at the middle of the modified model, as seen in Fig. 6.1, in order to extract the heat flux generated on the hotspot. Inlet and outlet manifold length was 4mm and width was 12.9mm which was equal to the width of the channels section. The total model dimension was 22.6mm×15.5mm×1.5mm while the channels section area was 12mm×12.9mm. Model thickness was 1.5mm including the channel height of 0.9mm and the base thickness of 0.6mm.

Table 6.1 Copper properties [87].

Density [kg/m^3]	8933
Specific heat capacity [J/kg K]	385
Thermal conductivity [W/m K]	401

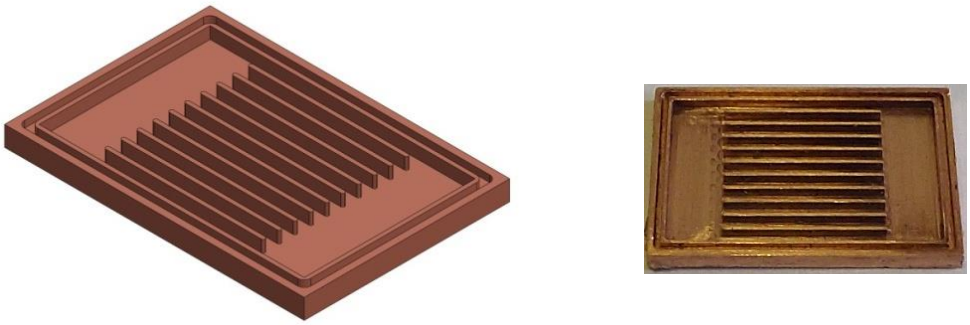

(a) without subchannels

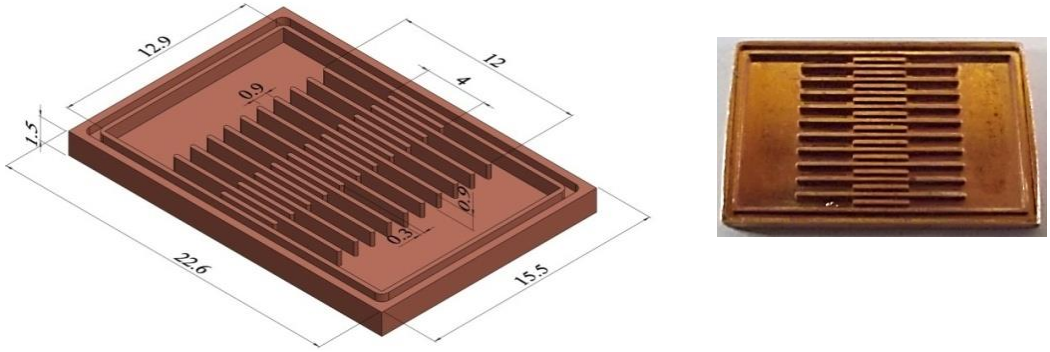

(b) with subchannels

Fig. 6.1: Models of microchannels: (a) without and with subchannels, all dimensions are in mm.

The lid of the cooling device was fabricated from polycarbonate material [119] with two inlet and outlet ports in order to minimise potential mal-distribution of the mass flow rate through the channels as shown in Fig. 6.2. The design of the lid gives flexibility to choose any ports as inlet or outlet. The copper channels and the lid were aligned to make a groove around the channel frame perimeter with a trace on the bottom surface of the lid with height and width of 0.5mm each as shown in Fig. 6.1 and Fig. 6.2. Special epoxy with thermal conductivity of 0.2 [W/(m K)] (LOCTITE® 5145™ [120]) was used to glue the copper plate and the lid together. Water with

filtered to remove particles down to 0.2µm [121] was fed to the models through two stainless steel small pipes which were inserted into the inlet holes. Moreover, outlet water flowed out of the model through outlet stainless pipes (See Fig. 6.2). Transparent plastic tubes were used to provide and collect water to and from the model(s) respectively (See ref.[122] for the full tube specifications).

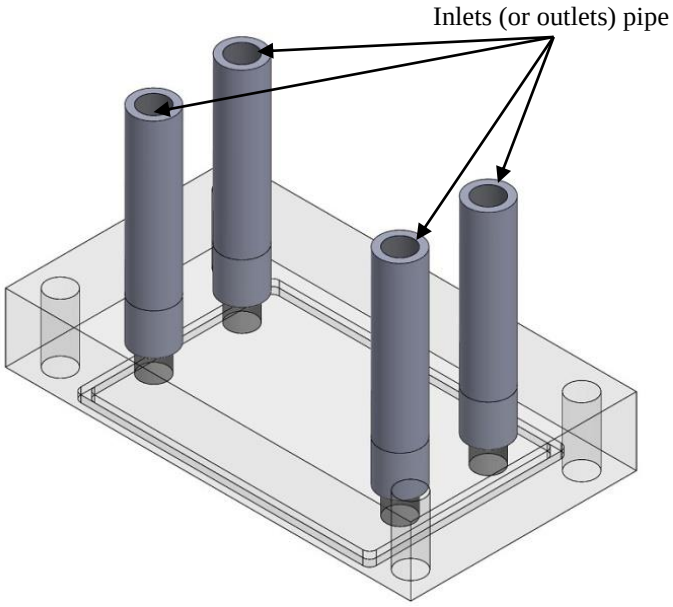

Fig. 6.2 Lid of the model has been fabricated with two inlets and two outlets. Lid symmetry allows the choice of any ports as inlet or outlet.

Twelve microheaters (Pt 6.8 M 1020 [123]) were used to generate the uniform and hotspot heat fluxes. The nominal resistance of each microheater was 6.8 Ohm at 0^{o}C which ensured a maximum current of 2A within the working temperature range from -40^{o}C to +500^{o}C. The dimension of a single microheater is shown in Fig. 6.3. These microheaters were soldered to PCB (See ref [124] for full specifications of this PCB)

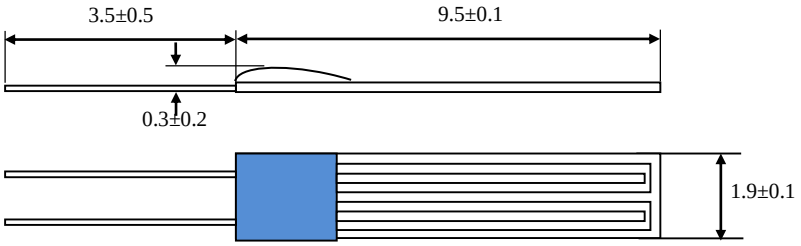

Fig. 6.3: Dimensions of single Pt6.8 microheaters. All dimensions in millimetres.

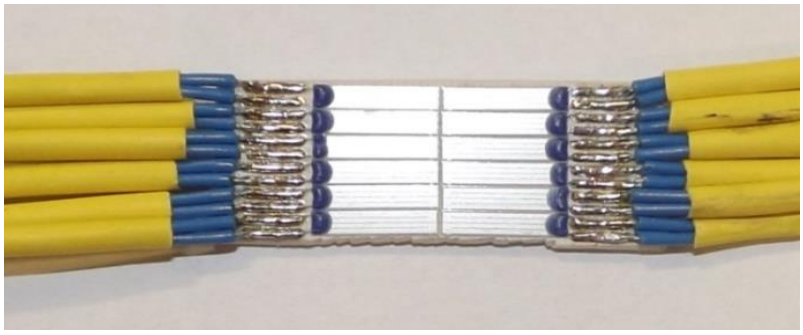

Fig. 6.4: Twelve microheaters circuit welded on PCB board with the wiring.

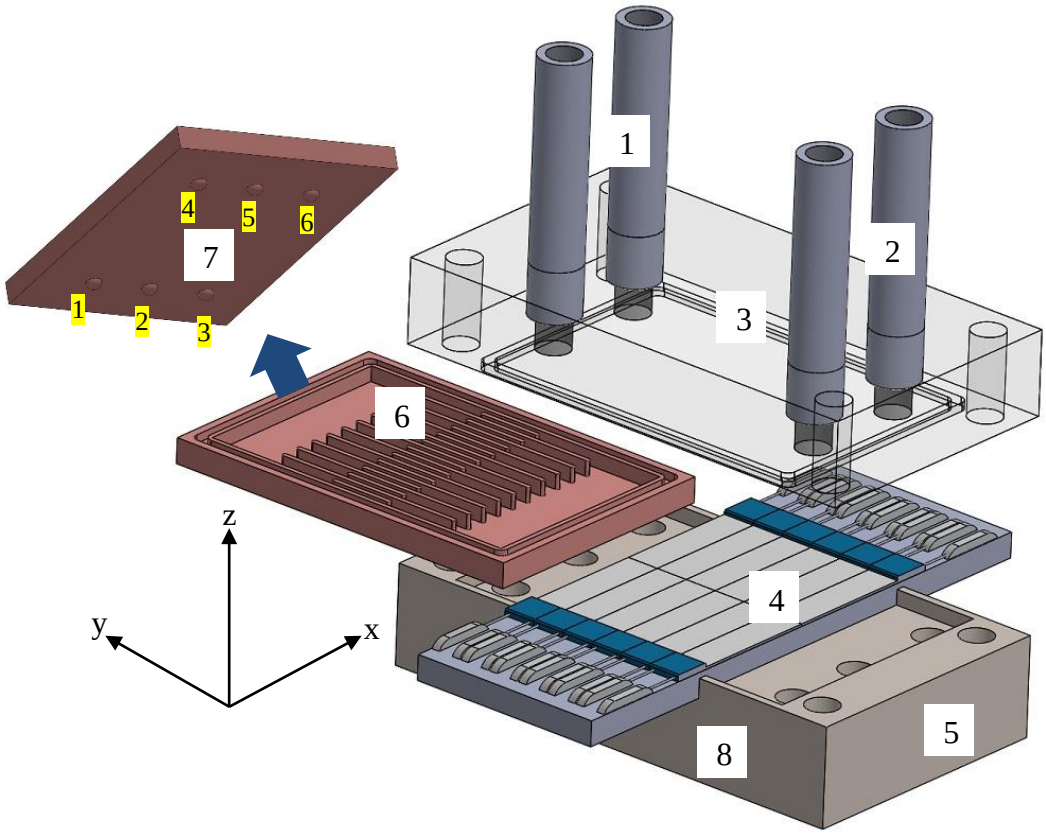

Fig. 6.5: Full geometry of the channels with subchannels: 1) and 2) inlet (or outlet ports), 3) lid, 4) microheaters and PCB, 5) base made of ceramic, 6) copper channels, 7) positions of the thermocouples on the back of the channels, and (8) ceramics base.

(See Fig. 6.4). High voltage was supplied to the middle heaters to generate a hotspot while a lower voltage was supplied to the off-centre heaters. A small quantity of thermal paste [125] was added between the channel copper plate and the microheaters

to improve thermal contact. The lid and the ceramics base were drilled with four holes of size 2mm in order to join all the parts with M2 screws (See Fig. 6.5). The base material was made from machinable ceramic [126].

6.1.2 Thermocouple attachment methods

The results of Chapter 4 Chapter 5 afforded deep understanding of the effect of thermocouple's interaction with a system on the temperature measurement. The conclusions recommended that the thermocouple wires and the probe should be in the same isothermal plane. Consequently, the temperature gradient along the wires will be avoided and then the impact of the thermocouple on the temperature measurement is eliminated. Furthermore, it was recommended in Chapter 4 that the thermal contact resistance between thermocouple probe and the measured surface added an additional obstacle on accurate temperature measurement.

Therefore, in the present work, the locations of thermocouples were selected to be perpendicular to the bottom surfaces of the inlet and outlet manifolds (See Fig. 6.5 and Fig. 6.6). Those locations were chosen in order to avoid passing thermocouple wires through a variable temperature medium and to minimize effect of the conduction through the wires. Thermocouple wires were passed through the holes in the ceramics base and then pushed through the thermal insulation material to prevent any contact between the wires and the other surfaces (e.g. ceramics base) as shown in Fig. 6.5, Fig. 6.7 and Fig. 6.9 [118]. A small drop of thermal paste [125] was added between the thermocouple probe and copper surface to improve heat transfer and also to minimise thermal contact resistance. The positions of each thermocouple are shown in Fig. 6.6(b).

Alternatively, direct measurement of surface temperature on the hotpot and uniform heat fluxes needed to glue the thermocouple to the back surface of the channel section or push through thermocouple wires inside a hole in the copper plate over the microheaters (See Fig. 6.5 and section 1.1 in Chapter 1). Surface temperature distribution under the channels will not be uniform (See section 6.4). Therefore, if this method was chosen to measure the temperature, conduction heat transfer may take place through the wires and cause measurement error [118]. The presence of

thermocouple wires works as an obstacle between the microheaters and channels and change heat flux distribution under the channels. Consequently, heat supplied by the microheaters to the area of the channel surface above the thermocouple wire will be less than the neighbours. Then heat flux distribution to channels will be altered.

Six thermocouples of type K of size 200µm (See Table 4.1 in section 4.1.2 in Chapter 4 for thermocouple materials properties) each were glued with epoxy (LOCTITE® 5145™) [120] to the bottom surface of the inlet and outlet manifolds at six positions to measure the temperature (See Fig. 6.5 and Fig. 6.6). Each thermocouple was held

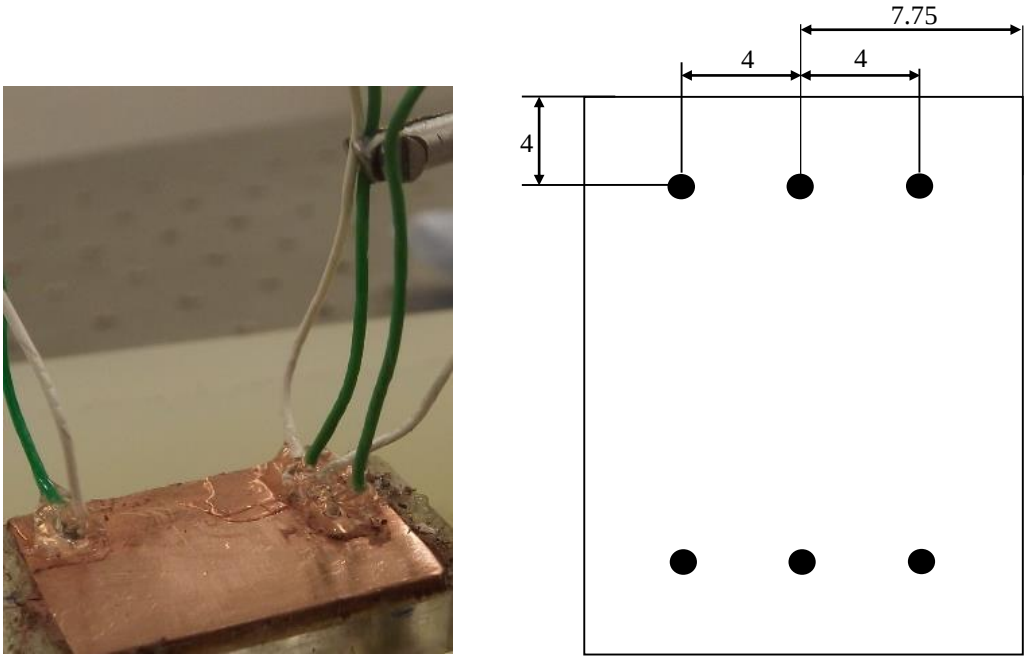

(a) (b)

Fig. 6.6: (a) Attachment method of thermocouples at the back of the channels, (b) positions of the thermocouples at the back surface of the manifolds, all dimensions are in mm.

by a micrometer for at least 24hrs to get a full strength of the epoxy. The extra epoxy-shown in Fig. 6.6(a) -was removed in order to fit the microheaters at the back of the channels. It should be mentioned that adding a large quantity of epoxy to glue the thermocouple will have confined pockets of air and make the thermocouple probe move and this may measure a different temperature.

Another two thermocouples of type K of size 200µm were inserted into the plastic tube close to outlet ports to measure water temperature. The inlet water temperature was measured by immersing thermocouple type K of size 200µm the water container.

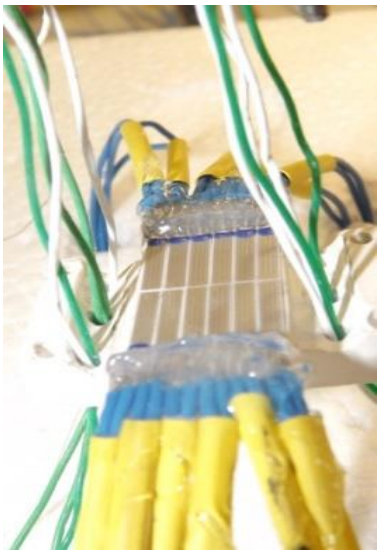

Fig. 6.7: Position of microheaters and thermocouples on the ceramic base.

6.1.3 Experimental set-up

Filtered water was used as a working fluid supplied from a 7-litre water container with a large surface area (30cm×30cm). Different levels of the container were chosen to generate various flow rates under gravity action [127]. Two 20ml syringes were

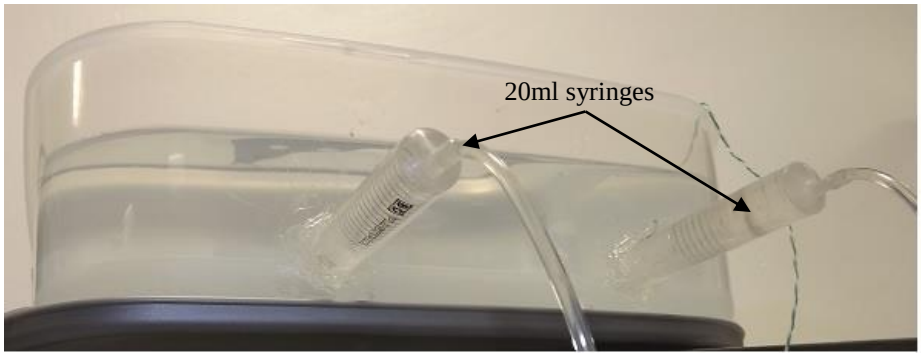

Fig. 6.8: Water container with two 20ml syringes were connected to plastic tubes to supply water to the model.

connected to the container to supply water to the model through two plastic tubes as shown in Fig. 6.8. The other terminals of the plastic tube were fitted to the model inlet ports as shown in Fig. 6.9.

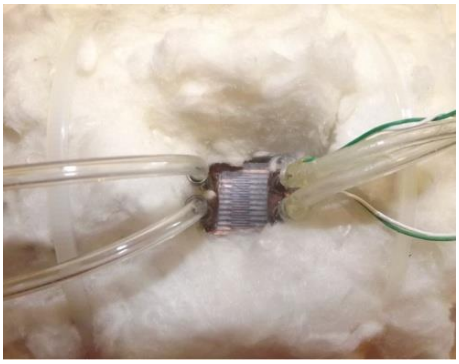

Fig. 6.9: Wrapping all the model parts with an external thermal insulation for the whole system to minimise heat losses.

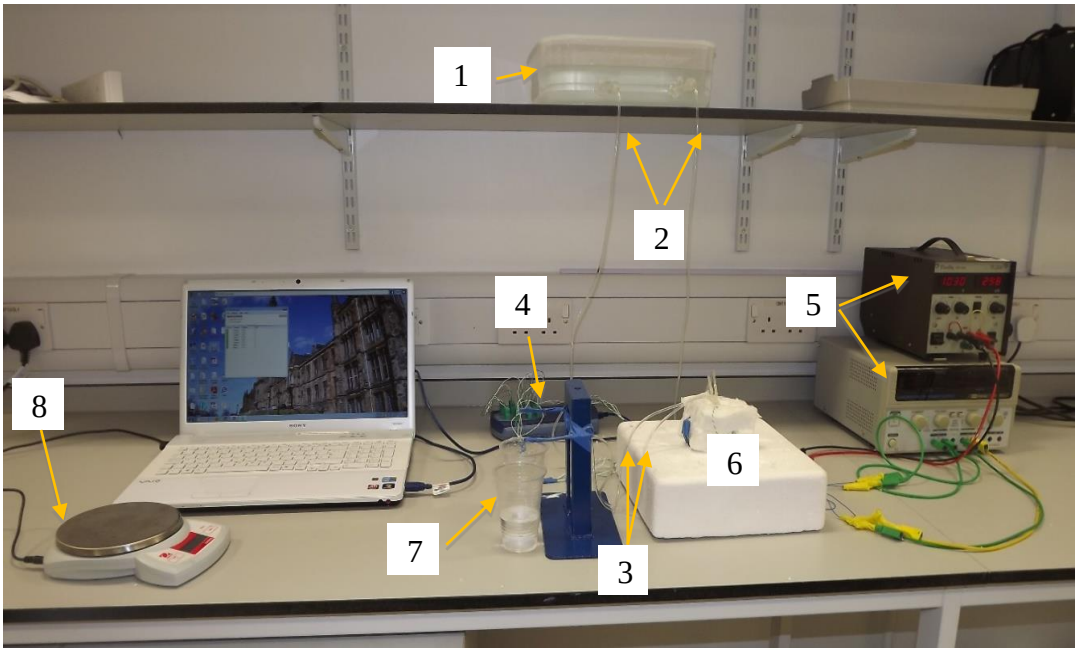

Fig. 6.10: Experimental setup: 1) water container, 2) plastic tubes feed water to the cooling device, 3) plastic tubes collect water from the cooling device, 4) pico TC-08data logger, 5) power supplies, 6) cooling device, 7) water collection, 8) digital scale.

Two another plastic tubes were connected to the outlet ports to collect water into the outlet containers as shown in Fig. 6.9 and Fig. 6.10. The outer and inlet diameter of the plastic tube were 3mm and 1.65mm respectively and the other specifications can

be found in Tygon® tubing Formulations [122]. The device was wrapped with an additional thermal insulation to minimise heat losses as shown in Fig. 6.9.

Each four set of heaters was connected in series to a single power supply to generate the required heat flux as shown in Fig. 6.11. Each set of H1 to H6 represented two

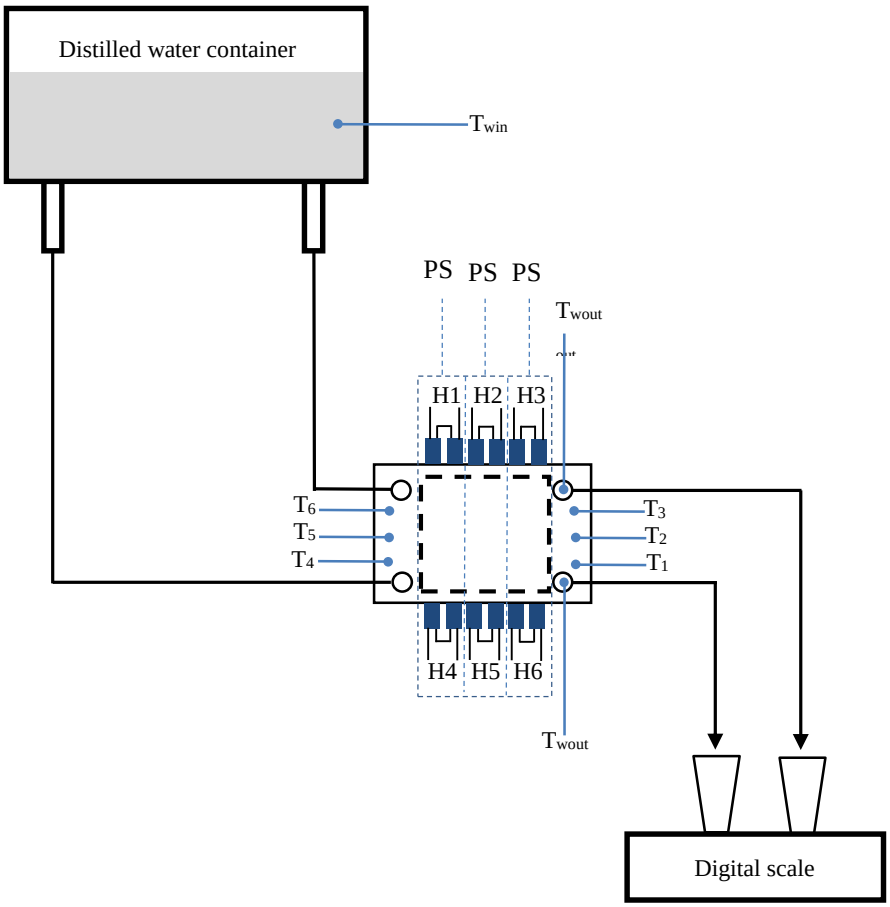

Fig. 6.11; Schematic diagram of the experimental setup H1to H6 representing two heaters connected in series. Sets H1 & H4, H2 & H5 and H3 & H6 are connected in series.

microheaters which were connected in series. Each set of H1& H4, H2 & H5 and H3 & H6 was linked in series and was provided by voltage from a single power supply. Uniform heat flux was generated by applying lower voltage to the micro-heater sets of H1 and H4, and H2 and H5, while a higher voltage is supplied to the set of H3 and H6 to generate the hotspot at the middle position of the channels. Thermocouples were connected to a laptop through a Pico data logger TC08 to record the readings. The

characteristics of the TC08 data acquisition system and the method of avoiding noise effect on temperature measurement can be found in section 4.1.2 in Chapter 4. Water inlet temperature was measured with a thermocouple type K which was connected to a 2000T thermocouple thermometer type K which is manufactured by digitron [128]. The calibration process of thermocouples was performed in comparison with freezing and boiling points of water (See section 4.1.3 in Chapter 4).

Two power supplies were used to provide the required voltage: the first was a GPS-3303 series power supply with two channels of voltage range 0-30V and current 0-3A with accuracy of 0.01%+3mV manufactured by GW Instek [129]. The second power supply was a single channel device model PL154 manufactured by Thurlby Thandar Instruments with an accuracy of 0.1% for voltage and 0.3% for current [130] (See Fig. 6.10). A digital scale was used to weigh the collected water during the experiments as shown in Fig. 6.10 and Fig. 6.11.

6.1.4 Experimental methodology and steps

Experiments were performed inside a temperature controlled room for different pressure heads (25cm, 38cm, 47cm, 61cm, and 79cm). A water container was chosen with a large surface area in order to ensure that there was a negligible change in water height during the experiments. The following steps were followed during each run and for each pressure head:

1. Filling the container with the proper amount of filtered water above the required level by five millimetres. Gravity effect more stable in producing a continuous flow rate [127].
2. Set the room temperature for the required temperature (21^{o}C).
3. The model and water were left for enough time to get thermal equilibrium for each part of the model before starting each run of the experiment.
4. Plug-in thermocouples to TC08 which should be connected to the laptop recorded thermocouple readings to monitor thermocouple temperature. The other thermocouple was plugged into a 2000T thermometer to measure inlet water temperature.

5. Leaving the water flow through the model before switching on the power supplies in order to avoid the quick rise of temperature and potential damage to the system.
6. Switch on the power supply(s) and adjust the voltage and the current for each set of the microheaters. A Higher voltage was applied to the central set of the microheaters H2&H5 (See Fig. 6.11) to produce 11.3W as a hotspot heating power while 3W was supplied to each off-centre sets (H1&H4 and H1&H4) to generate the uniform heat flux. Experimental working conditions will be different for each mass flow rate. Therefore, readjust the voltage and the current to generate approximately the same power supply for each microheaters set and for each run.
7. Leaving the water flow through the model until the water surface in the container reached the required level. Moreover, monitoring thermocouple readings ensured that the steady-state was achieved. Two important steps are performed here: firstly, the system is at the steady state, and secondly, the thermocouple readings recorded when the required pressure head was obtained.
8. Start to record thermocouple readings for five minutes.
9. Switch off power supplies and then stop water flow.
10. Change the water level by changing position of the water container and repeat steps 1-9 for the next mass flow rate.
11. Repeat steps 1-10 for five times in order to ensure the repeatability of the experiments results.

6.2 Experimental results and discussion

The results in this section (and in the numerical analysis section 6.4) were drawn with respect to Reynolds number (*Re*) based on the hydraulic diameter of the main for both models without and with subchannels. Therefore, *Re* was calculated from

$$Re=\frac{\rho\, U_m D_{channel}}{\mu} \tag{6.1}$$

where U_m [m/s] represents the inlet average velocity to the channel and $D_{channel}$ [m] is the hydraulic diameter of the main channel(s). U_m and $D_{channel}$ were calculated for a single channel from

$$U_m = \frac{1}{n}\left[\frac{m_{total}}{\rho\, A_{channel}}\right] \tag{6.2}$$

where n is total number of channels, m_{total} [kg/s] total inlet mass flow rate to the ehat sink and $A_{channel}$ [m^2] is cross-sectional area of the channel.

And

$$D_{channels} = \frac{4 \times A_{channel}}{channel\ perimeter} \tag{6.3}$$

6.2.1 Power supply and heat losses

During the experiments power was supplied for the twelve microheaters which were connected in series into three groups, (See Fig. 6.11). The fluctuation in total power supply to the microheaters is demonstrated in Fig. 6.12 and Fig. 6.13.

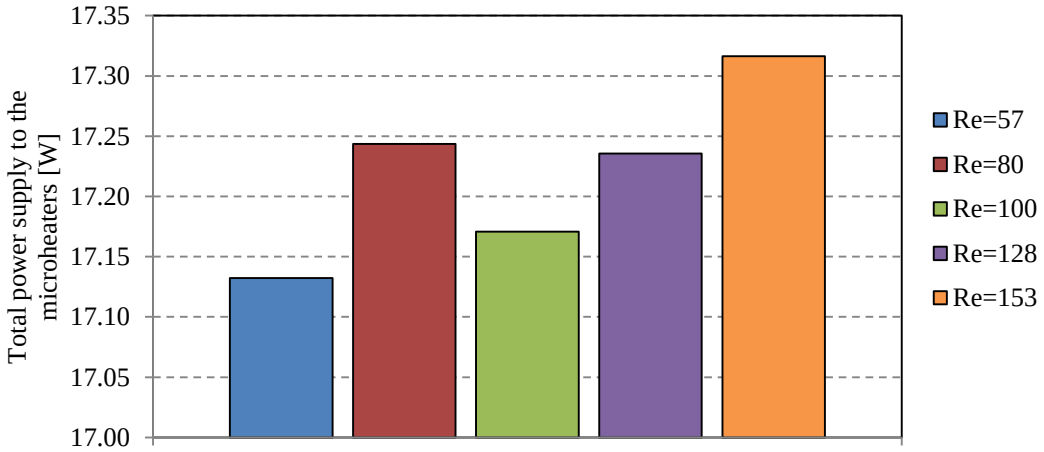

Fig. 6.12: Total power supplied to the twelve microheaters at different Reynolds number for the model **without** subchannels.

Fig. 6.12 and Fig. 6.13 show that the deviation in maximum power supply was about 0.15W for both models. Microheaters were made from thin platinum film (Pt 6.8 M 1020 [123]) and their resistance was temperature dependent [131], so the model bottom surface temperature varies according to the change in pressure and mass flow rate. Therefore, voltage supplied to the central set of the microheater should be adjusted to attain the required power supply for each run of the experiments. Since the

adjustment process cannot ensure exactly the same voltage and current on each run, there is a little change in voltage and current supplied to the models.

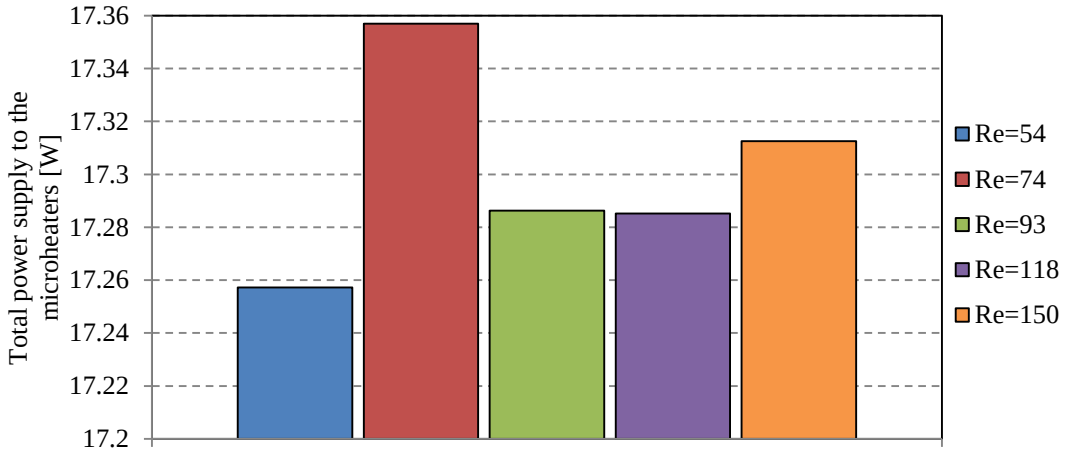

Fig. 6.13: Total power supplied to the twelve microheaters at different Reynolds number for the model **with** subchannels.

Heat losses from the model(s) were calculated by comparing heat transfer to water with heat supplied by the microheaters as shown in Fig. 6.14 and Fig. 6.15. Heat transferred to the water and power supplied by microheaters was calculated from [132]

$$\dot{Q}=\dot{m}_w Cp_w(T_{wout}-T_{win}) \tag{6.4}$$

where $\dot{Q}$ [J/s], $\dot{m}_w$ [kg/s], Cp_w [J/kg K], T_{wout} [K], and T_{win} [K] are heat extracted by the water, water mass flow rate, water heat capacity, water outlet temperature, and water inlet temperature, respectively. Power supply to microheaters is calculated from;

$$P=IV \tag{6.5}$$

where P [W], I [A], and V [V] are power supply, current, and voltage respectively.

Heat lost by conduction occurred through the wires that came out of the model(s) to connect the microheaters to the power supplies. The other possible source of heat loss was through stainless tubes which were fitted to the inlet and outlet ports. The maximum average heat loss was about 5% from each model which is also shown in Fig. 6.14 and Fig. 6.15.

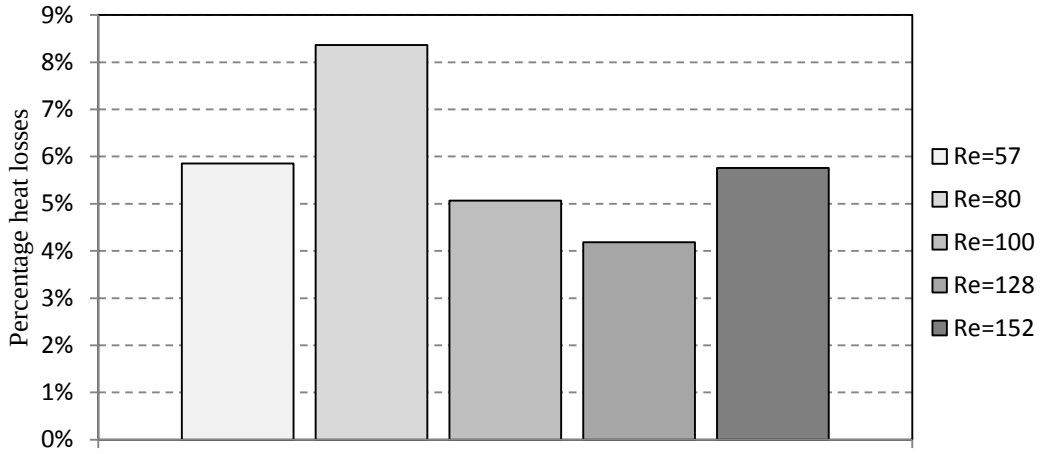

Fig. 6.14: Percentage deviation of heat losses from the model **without** subchannels at different Reynolds number.

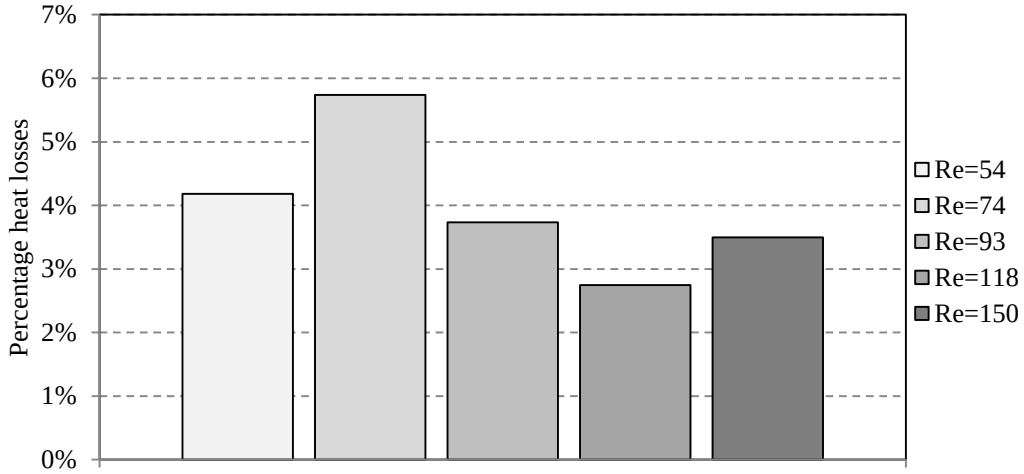

Fig. 6.15: Percentage deviation of heat losses from the model **with** subchannels at different Reynolds number.

6.2.2 Thermocouples results

Fig. 6.16[5] shows a comparison between the experimental readings of the thermocouples (*Thermocouple 1*, *Thermocouple 2* and *Thermocouple 3*) which were attached to the bottom surface of the outlet manifold for both the models with and

[5] Ie should mention here that Fig. 6.16 and Fig. 6.17 represent a comparison between the means of the experimental results for both systems and the other experimental runs were omitted from the figures to avoid the overlapping. Full experimental results are shown in Fig. 6.28, Fig. 6.29, Fig. 6.31, and Fig. 6.32 where the experimental and numerical results are compared.

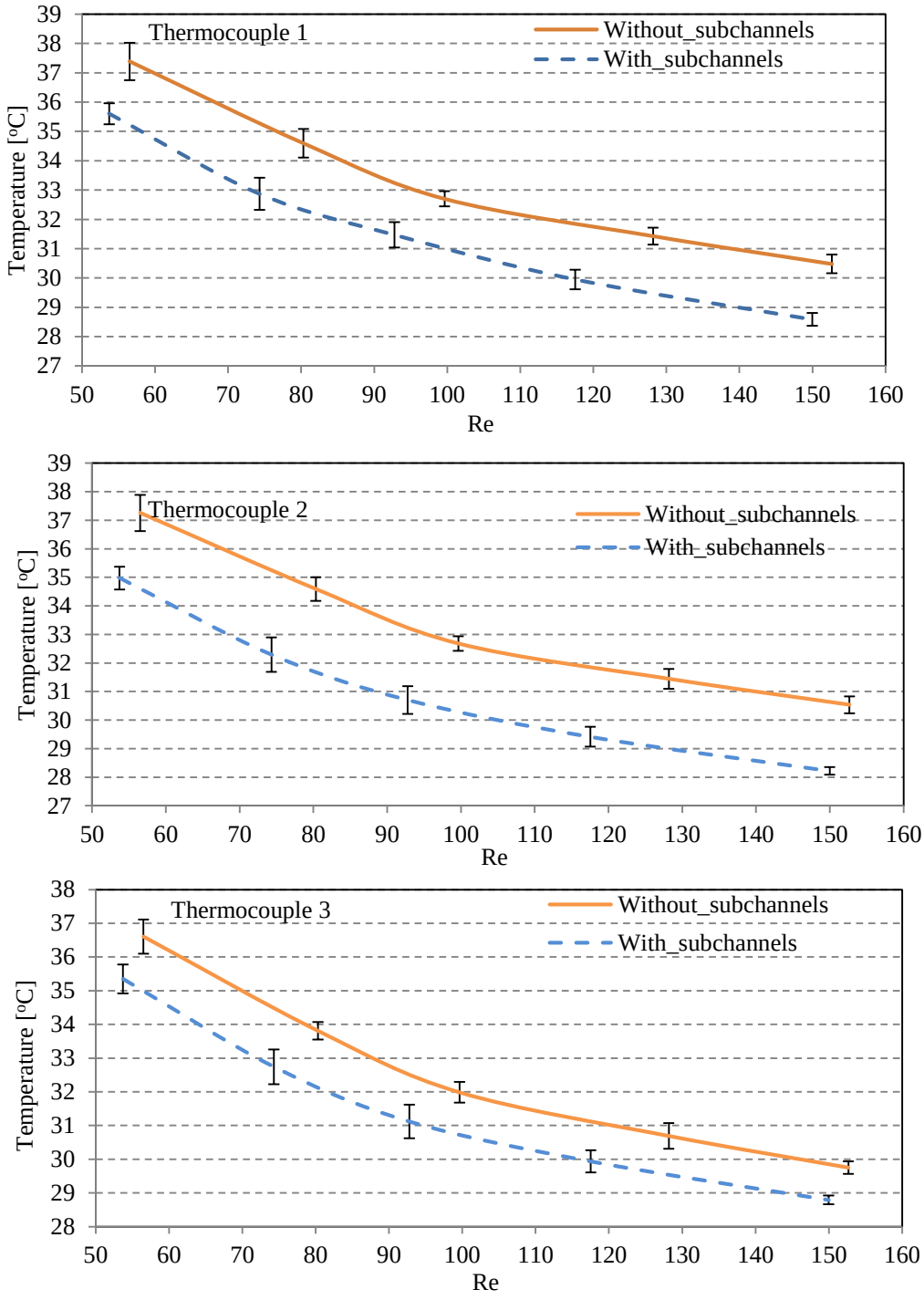

Fig. 6.16 Comparison of the experimental results the models **with** and **without** subchannels for *Thermocouple1, Thermocouple 2 and Thermocouple 3* attached to the bottom surface of the **outlet** manifold. Error bars are within the range ± one standard deviation.

without subchannels. The channel's width above the hotspot was reduced to one-third of the main channels (See section 6.1.1). Consequently, the solid-liquid interaction area increased, and the flow was accelerated at the entrance as a result of the contraction at the subchannels. Therefore, more energy was extracted from the hotspot by the water liquid, leading to a drop in surface temperature. This reduction in temperature could be detected by the thermocouples attached on the bottom surface of the outlet manifold.

The hotspot has a negligible effect on the readings of thermocouples attached to the inlet manifold (See Fig. 6.17). Moreover, the only expected effect on the thermocouple(s) reading came from the conduction through the base of the inlet manifold.

Thermocouple 5 measurement showed a lower temperature for the model with subchannels. The two inlet ports located at an equal distance from middle line of the inlet manifold (See Fig. 6.5) caused more mixing at the middle position of manifold for the model with subchannels, see Fig. 6.18 and Fig. 6.19. Fig. 6.18 and Fig. 6.19 show the mixing of two streams coming from inlet ports at the middle line of the inlet manifold of the models with and without subchannels where *Thermocouple 5* is located.

They show that two streams of liquid met at the middle line while the flow in front of the manifold inlet(s) went directly to the channels. It is also shown that the velocity at middle line for the model without subchannels is higher than the other model. The presence of the subchannels caused more pressure drop and retarded the flow.

The other thermocouples (*Thermocouple 4* and *Thermocouple 6*) had approximately the same reading for both models because they were located near the inlet ports and the effect of inlet velocity boundary conditions was more dominant than the mixing process.

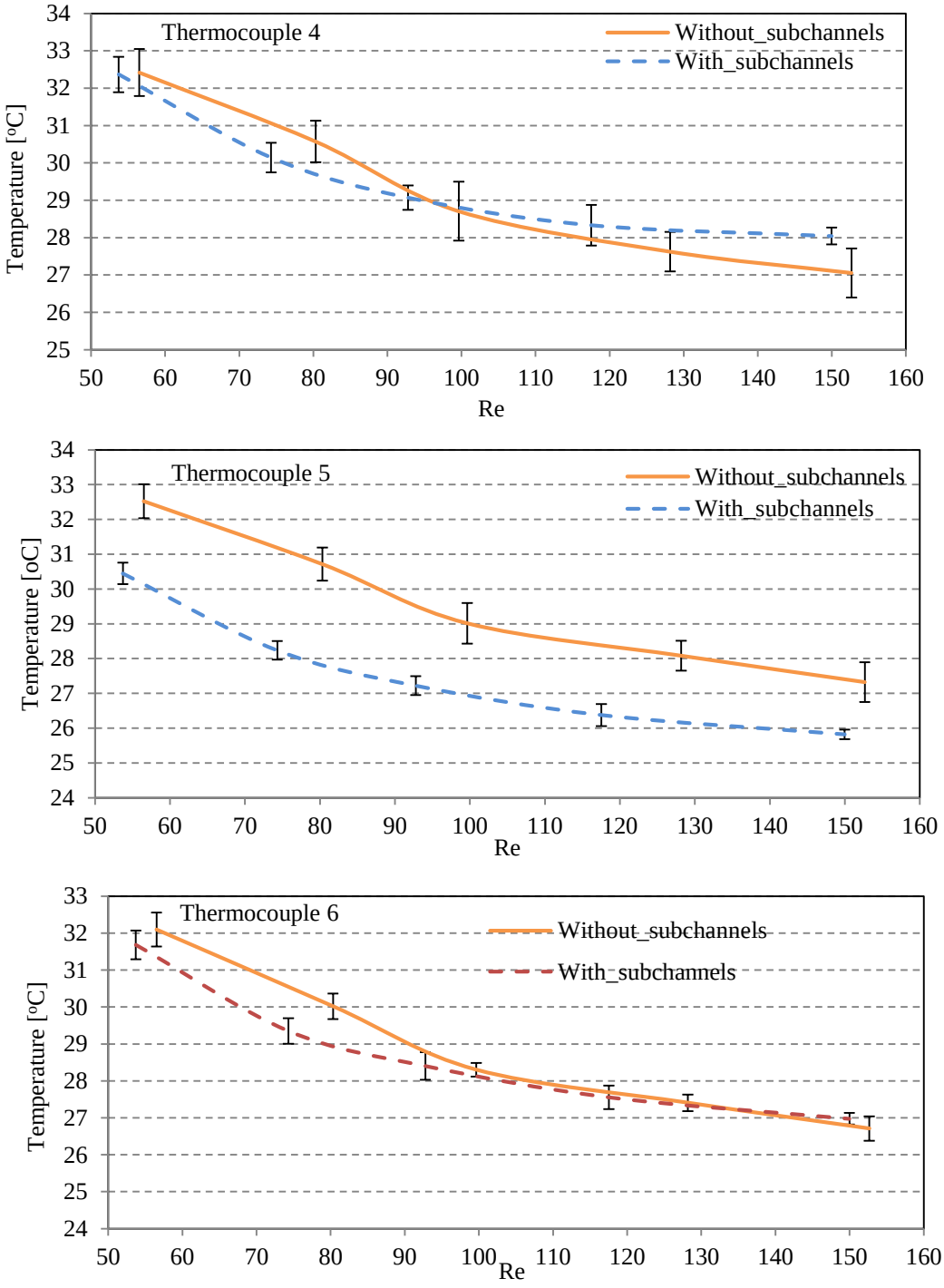

Fig. 6.17: Comparison of the experimental results the models **with** and **without** subchannels for *Thermocouple 4*, *Thermocouple 5 and Thermocouple 6* attached to bottom surface of the **inlet** manifold. Error bars are within the range ± one standard deviation.

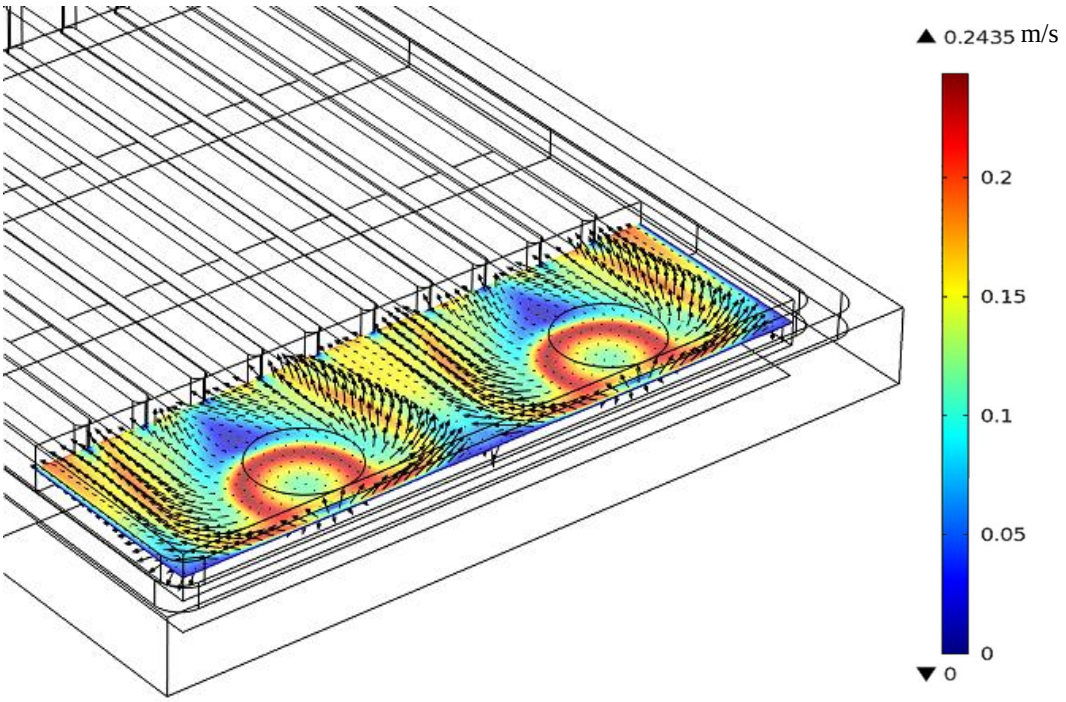

Fig. 6.18.Velocity distribution and direction at inlet manifold for the model **without** subchannels for the pressure head 75cm.

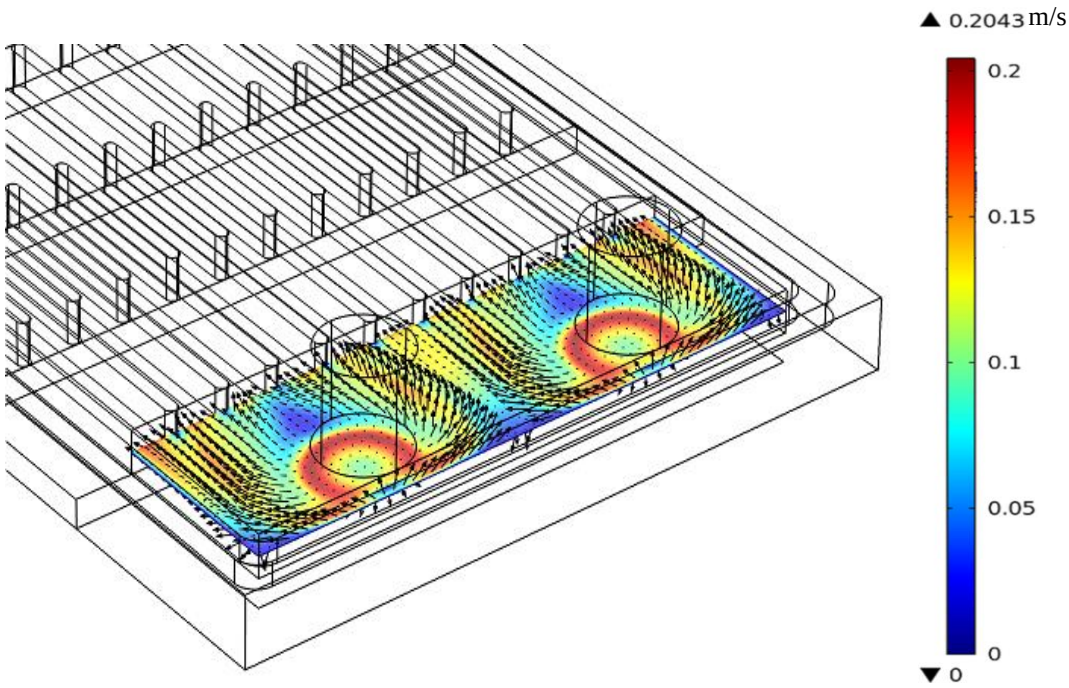

Fig. 6.19. Velocity distribution and direction at inlet manifold for the model **with** subchannels for the pressure head 75cm.

Fig. 6.20 shows a comparison between the averaged measured temperature of the outlet water for both models. A high heat transfer rate to water occurs at subchannels, therefore, the outlet water temperature reading shows a higher value for the model with subchannels.

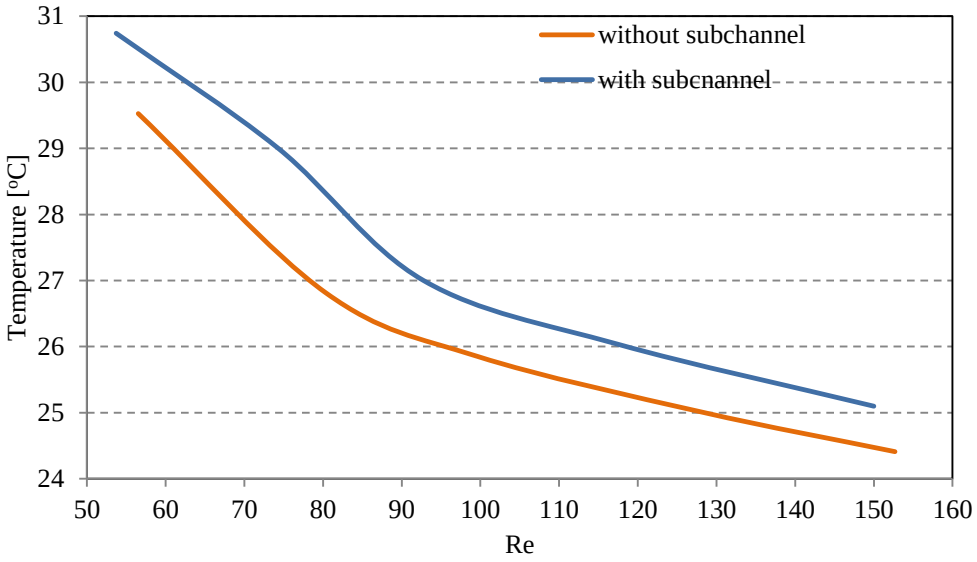

Fig. 6.20 Comparison of the water outlet temperature between the models **with** and **without** subchannels at different Reynolds number.

6.3 Mathematical modelling

Steady-state conditions, single-phase and laminar flows were considered for the liquid flowing through the microchannels. The governing differential Eqs.(3.1)-(3.5) (See section 3.1 in Chapter 3) describe the hydraulic and thermal behaviour but omit the body force term.

Two inlet velocity boundary conditions were investigated with a *uniform* inlet velocity, as well as with a *fully developed* inlet velocity [74] (See sections 3.3.1 and 3.3.2 in Chapter 3).

$$V_{in}=2V_{avg}\left(1-\frac{r^2}{R^2}\right) \tag{6.6}$$

Where V_{avg} average inelt velocity [m/s], $D_h=2R$ *hydraulic diameter[m]*. At the outlet boundary, atmospheric pressure is set equal to

$$p=0 \tag{6.7}$$

Thermal boundary conditions: Constant inlet temperature, Convective heat flux outlet boundary condition(s) and hotspot and uniform heat fluxes were applied at the middle and off-middle positions respectively.

6.4 Numerical analysis

The following assumptions were made in the numerical simulations in comparison with the actual cooling device(s) presented in Fig. 6.5 and Fig. 6.21

1. The effect of heat transfer through the lid was ignored to simplify the computational model and also to save computation time as shown in Fig. 6.21.

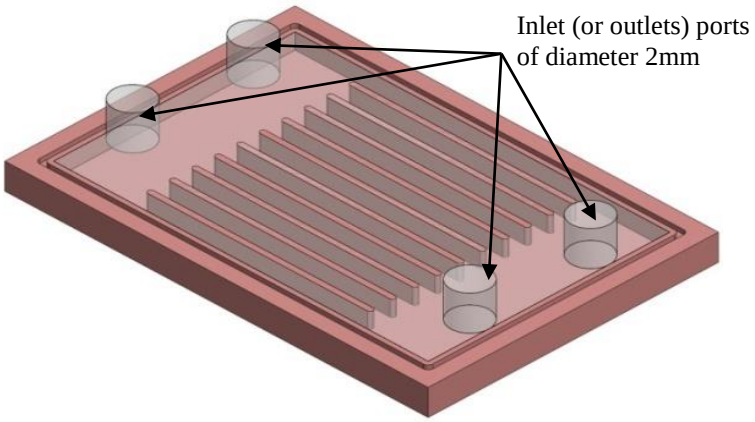

(a) Micro-channels without subchannels

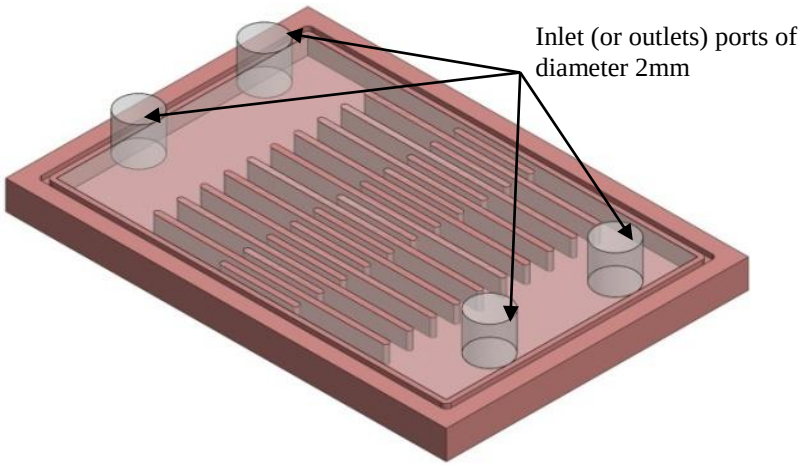

(b) Micro-channels with subchannels

Fig. 6.21 3D computational domain for both models **with** (a) and without (b) subchannels.

This assumption implied that the boundary condition of top surface was considered to be adiabatic because of the lid's low thermal conductivity.

2. The numerical model assumed that the channel cross-section was to be a right-angled rectangular shape, whereas, the actual geometry may have some deviation from a rectangular shape, (See Fig. 6.22).

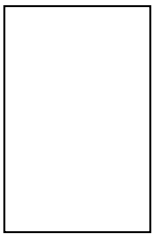

(a) right angle cross-section

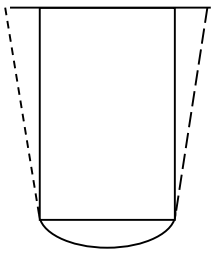

(a) deviation from right angle cross-section

Fig. 6.22 Deviation of channel cross-sectional area from right angle rectangular shape.

3. Model(s) internal surfaces were assumed to be smooth.
4. The mass flow rate distribution through the inlet ports was assumed to be equal. Therefore, an average velocity was calculated based on the total mass flow rate through both inlet ports.
5. The heat generated from each individual microheater was assumed to be uniform over the single heater and over all the heaters.
6. The heat lost from the system was calculated by measuring water outlet and inlet temperature and comparing it with heat supplied by the micro-heaters. The percentage average loss was assumed to be equal for each single micro-heater.
7. Microheaters were supposed to be in perfect contact with the back surface of the channel copper plate.
8. Differential pressure was assumed to be the same across both cooling devices. This assumption can be evaluated as follows: Steady state energy equation for the model including the tubes and model(s) is written [133]

$$\frac{p_1}{\rho g}+\frac{v_1^2}{2g}+z_1=\left(\frac{p_2}{\rho g}+\frac{v_2^2}{2g}+z_2\right)+h_f+h_k+h_m \tag{6.8}$$

where p, v and z are pressure, velocity and height respectively. Subscript 1 and 2 refer to the water surface level in the container and the exit from model respectively. h_f, h_k and h_m are head losses due friction, losses as a result of fittings and losses through cooling device(s) respectively.

Applying Eq.(6.8) for both models with and without subchannels

$$\left[z_1 = \left(\frac{v_2^2}{2g} + z_2\right) + h_{total}\right]_{m1} \tag{6.9}$$

$$\left[z_1 = \left(\frac{v_2^2}{2g} + z_2\right) + h_{total}\right]_{m2} \tag{6.10}$$

where $p_1 = p_2$ because the pressure on the water surface in the container and at exit from the model(s) is equal to atmospheric pressure. Assuming $v_1 \cong 0$ comparison with exit velocity v_2. $h_{total} = h_f + h_k + h_m$, $m1$ and $m2$ for model with and without subchannels respectively. The difference in total losses between two models for each pressure head can be expressed in the difference between Eq.(6.9) and (6.10):

$$h_{total\,m1} - h_{total\,m2} = \left(\frac{v_2^2}{2g}\right)_{m2} - \left(\frac{v_2^2}{2g}\right)_{m1} \tag{6.11}$$

The variation of mass flow rate through each model and tubes for different pressure head is shown in Fig. 6.23.

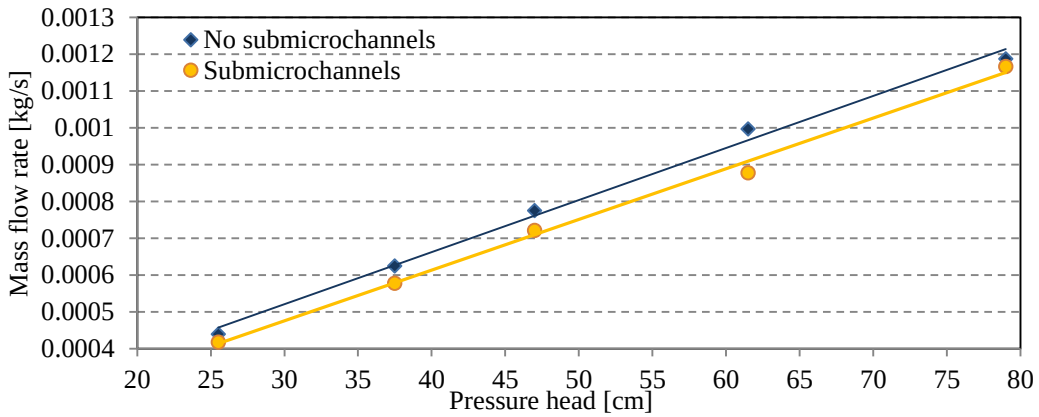

Fig. 6.23: Variation of mass flow rate with pressure head for the model **with** subchannels and **without** subchannels.

It reveals that there is no major difference in mass flow rates between two models. It is necessary to calculate v_2 form Fig. 6.23 for plastic tube diameter 1.65mm in order to calculate the pressure drop difference between the models as shown in Fig. 6.24. Consequently, it is possible to assume the pressure drop across each model is approximately the same.

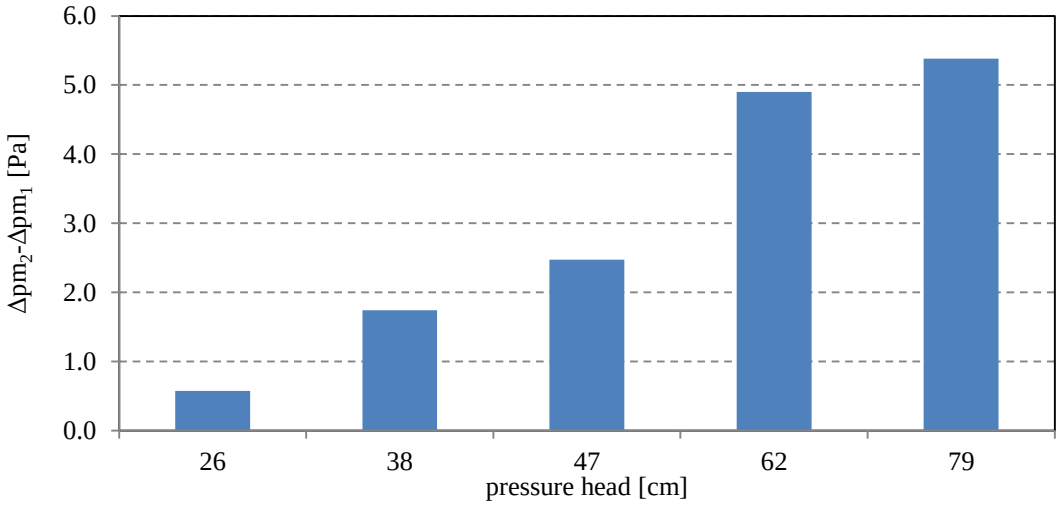

Fig. 6.24: Difference between pressure losses for both models for different pressure heads.

6.4.1 Boundary conditions and water properties

An average inlet velocity was adopted from experimental results as listed in Table 6.2. Heat fluxes were applied in an area of the size of 12mm×15.5mm where the area of hotspot and uniform heat which fluxed at upstream and downstream was each 4mm×15.5mm. The effective area of each micro-heater, excluding the blue part (micro-heater wiring), was equal to 2mm×8mm (See Fig. 6.3). The average effective length of 8mm was chosen for all microheaters. The average power provided to the middle sets of microheaters (H2 and H5) was 11.25W while it was 3W for each off-middle sets (H1and H4) or (H3 and H6). Therefore, heat flux calculation included the effect of heat losses but the other surfaces were assumed to be adiabatic. Applied heat fluxes are shown in

Table 6.3.Water was chosen as the working liquid where its properties were temperature dependent. The variation of water properties are shown in Fig. 3.7-Fig. 3.9 (See section 3.3.3 in Chapter 3).

Table 6.2 Average inlet velocity boundary conditions at different pressure heads.

	Without subchannels	With subchannels
Height [cm]	V_{in} [m/s]	V_{in} [m/s]
26	0.077	0.06
39	0.11	0.084
47	0.14	0.1
62	0.176	0.132
79	0.2	0.17

Table 6.3 Thermal inlet boundary conditions.

Inlet temperature [^{o}C]	21
Uniform heat flux [W/m^2]	4.45×10^4
Hotspot heat flux [W/m^2]	16.7×10^4

6.4.2 Meshing process and mesh dependency test

A free meshing process with tetrahedral mesh elements was chosen because of the irregular geometry of the model. The number of elements was increased at the entrance to the channels and on the interaction surface in order to capture flow conditions at these locations. COMSOL Multiphysics provides a tool which is called mesh quality (See section 3.4.1.1 Chapter 3) to ensure that meshing process does not affect the solution (See Fig. 6.25) [75].

A mesh independent solution for both models was investigated for the highest pressure head of 79cm which gave the flow Reynolds number (*Re*) of 150 and 152 for the models with subchannels and without subchannels respectively. To assess the mesh resolution on the numerical solutions, velocity and pressure results are shown in Fig. 6.26 and Fig. 6.27 have been taken along the centreline of the middle channel and bottom surface temperature at the middle position of the surface. Fig. 6.26(a-c) show that the number of three mesh element sets 1300422, 1551830, and 1737391 were examined for the model without subchannels.

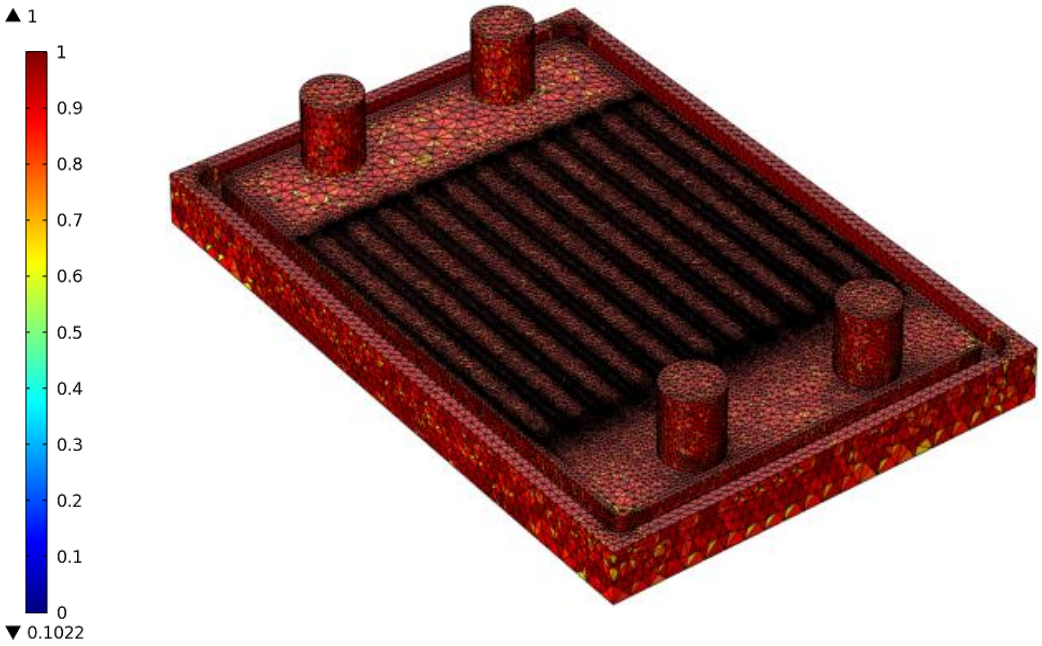

(a) model without subchannels

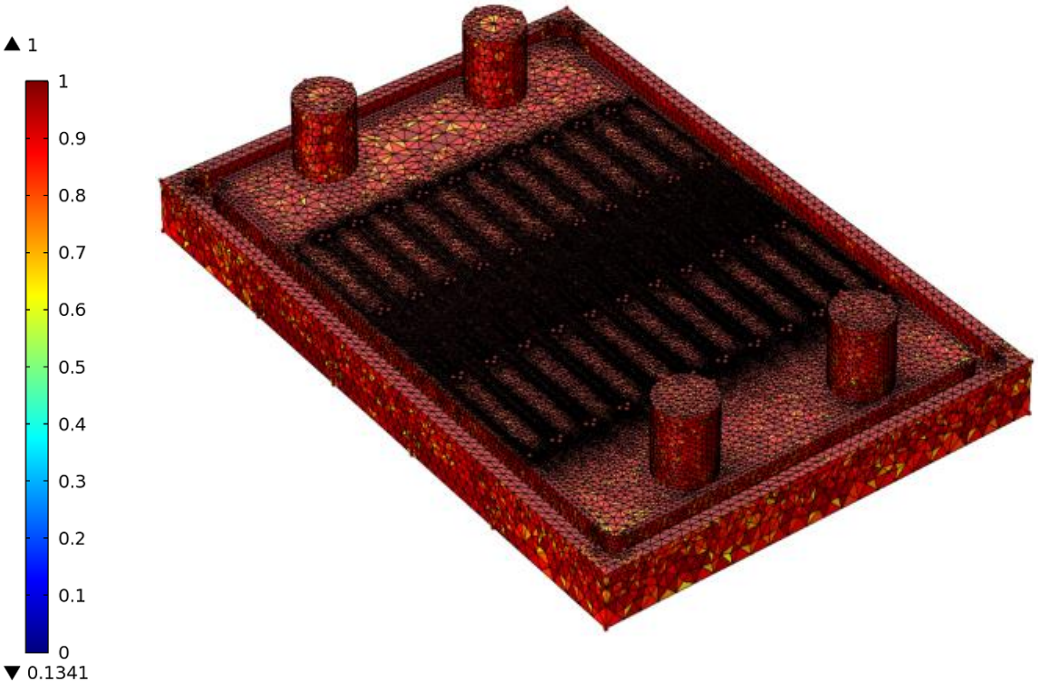

(a) model with subchannels

Fig. 6.25 Mesh elements quality for numerical analysis for both models **without** (a) and **with** (b) subchannels.

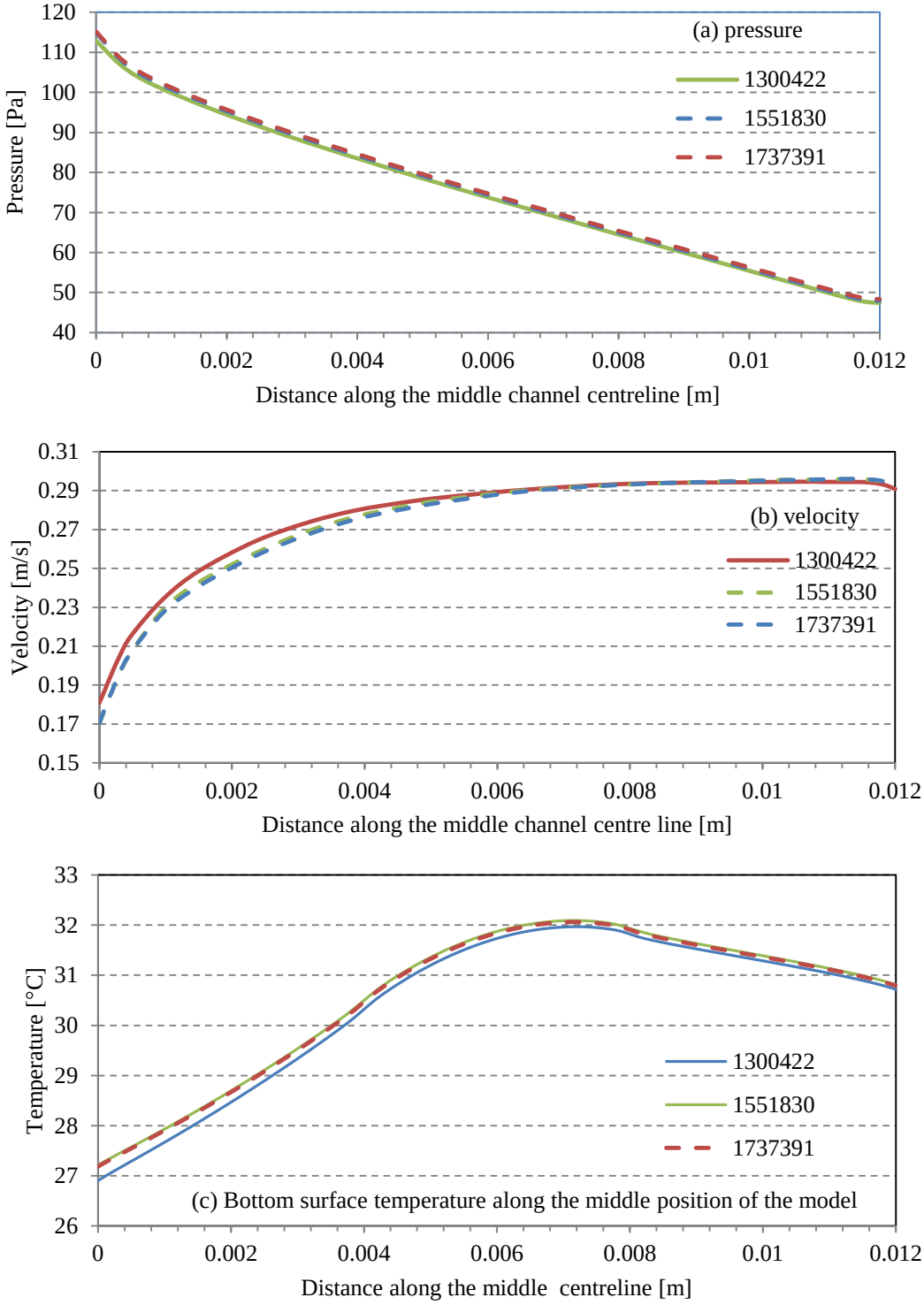

Fig. 6.26 Numerical solutions at different mesh resolutions of the model **without** subchannels for *Re*=152: (a) pressure, (b) velocity along the centre line of the middle channel and (c) Bottom surface temperature along the middle position of the model.

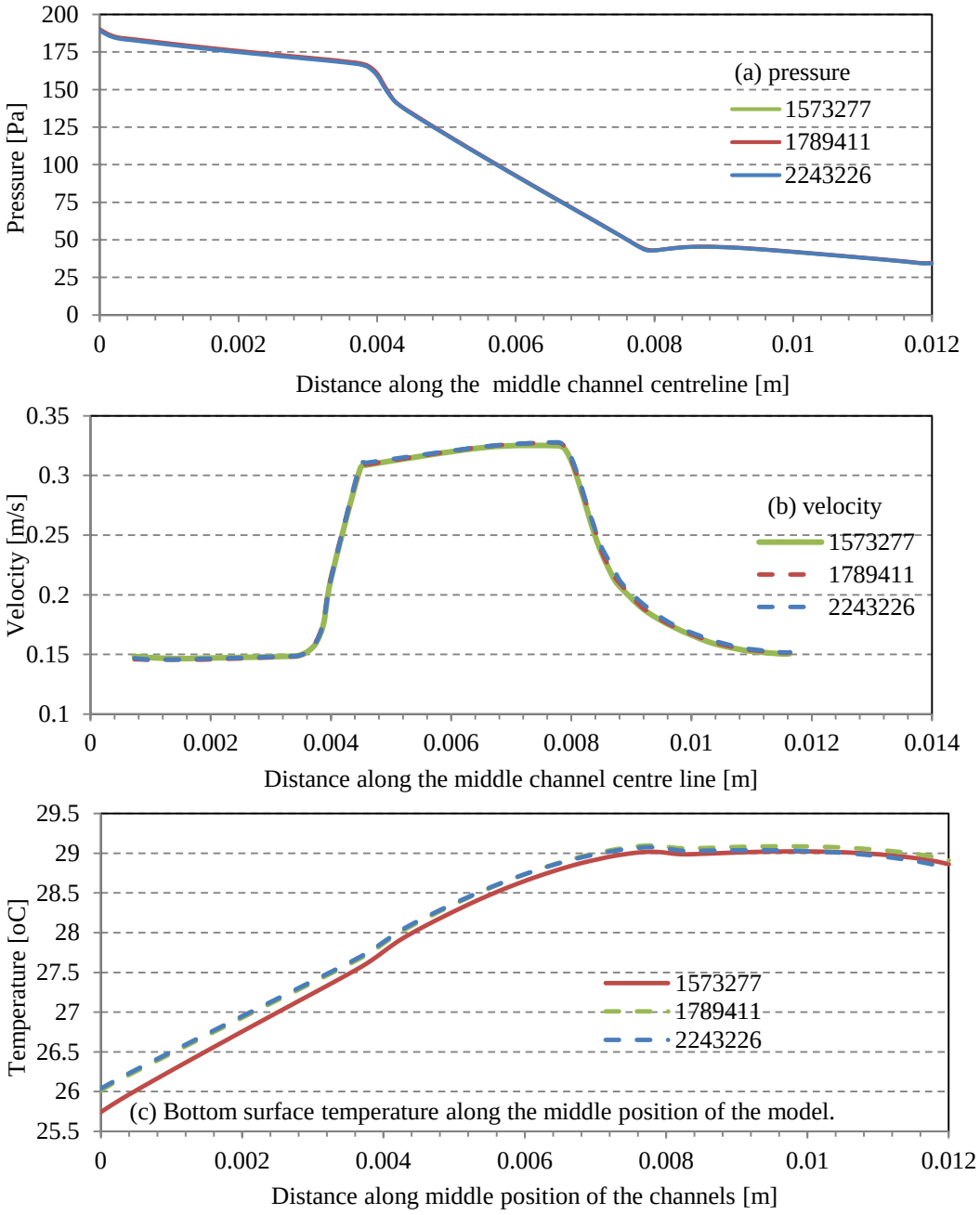

Fig. 6.27 Numerical solutions at different mesh resolutions of the model **with** subchannels for *Re*=150: (a) pressure, (b) velocity along the centre line of the middle channel, and (c) bottom surface temperature along the middle position of the model.

Fig. 6.26a shows a negligible change in pressure results shown for three sets of mesh elements, whereas, mesh independent solution was obtained for both velocity and temperature distribution when a number of mesh elements was equal to 173739 as shown in Fig. 6.26(b-c). Therefore, the solution of number of elements 173739 was

chosen for subsequent numerical analysis. The same trend is shown for the model with subchannels and the solution of mesh elements 2243226 was adopted as mesh independent solution as shown in Fig. 6.27(a-c).

6.4.3 Model validation

The following was taken into consideration when the numerical results were discussed:

1- The contact area of the thermocouple with surface in numerical analysis was assumed as square with a side length that equalled the probe diameter, while the actual contact area depends on the spherical shape of the probe (See Chapter 4). Therefore, the calculated surface temperature from the numerical simulations represented an average temperature taken at multiple points on the square surface area.

2- The thermocouple measures the temperature of the surface by comparing the probe temperature with a reference junction. The position of the effective junction of the thermocouple probe may be found inside the sphere of a thermocouple probe. During the experiments when the thermocouple probe touched the surface the effective junction in the probe may not have been in contact with the surface. Therefore, the thermocouple measures the temperature of the effective junction but not the surface, which gives a different reading than was expected from the numerical simulations (See Chapter 4).

3- Thermal paste is added to the tip of the thermocouple probe to improve heat transfer to the surface. Therefore, a perfect contact between the probe and the surface was assumed.

4- Actual surface roughness of the cooling device(s) causes more circulation and increases heat transfer rate. Therefore, the thermocouple gave a lower temperature reading than the numerical result where the effect of surface roughness was not considered.

6.4.3.1 Manifold bottom surface temperature results

A. *Model without subchannels*

Fig. 6.28 shows a comparison between the experimental and numerical results of temperature for the three thermocouples (*Thermocouple 1*, *Thermocouple 2*, and

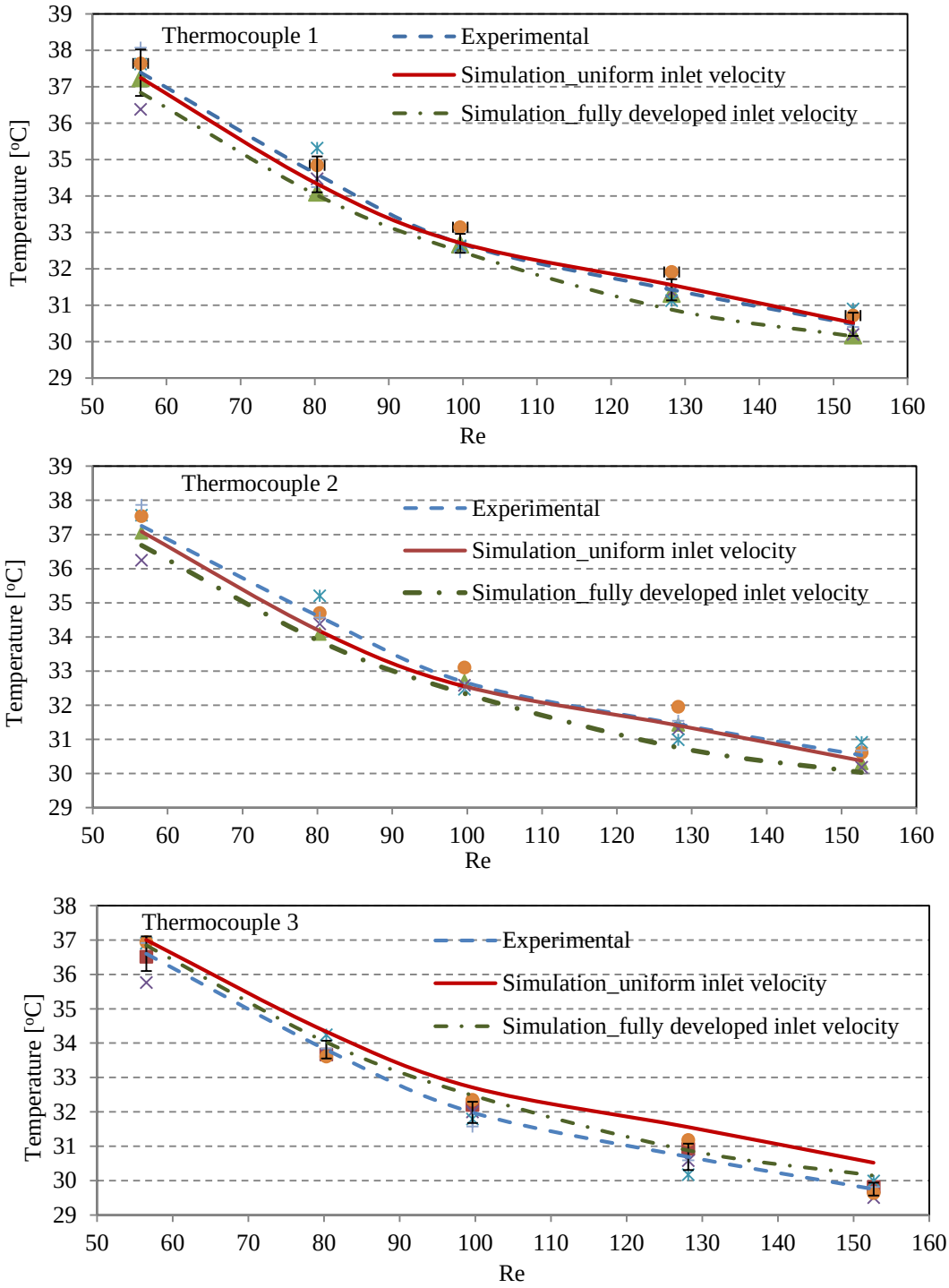

Fig. 6.28 Comparison between the experimental and simulation results of the model **without** subchannels of *Thermocouple 1, Thermocouple 2, and Thermocouple3* attached to the outlet manifold. Error bars are within the range ± one standard deviation.

Thermocouple 3) which were attached to the bottom surface of the outlet manifold. The numerical results showed agreement with the experimental results for both the inlet boundary conditions (uniform and fully developed velocity) except for a little deviation for *Thermocouple 3* for the uniform boundary conditions. *Thermocouple 3* gave a lower temperature reading because the contact area in the numerical simulation was considered to be smaller than the actual contact area or, as happened, an active junction was not in contact with surface.

Another comparison between the experimental and numerical results for the thermocouples (*Thermocouple 4*, *Thermocouple 5* and *Thermocouple 6*) which were attached to the bottom surface of the inlet manifold is shown in Fig. 6.29. There is also agreement but *Thermocouple 5* shows a little deviation from the experimental data for the boundary conditions of fully developed inlet velocity. *Thermocouple 5* is located at the middle line between the inlet ports where the two inlet streams are mixed. Assuming fully developed flow as a boundary conditions for the numerical method might under predict the temperature value because of the mixing condition at the middle positions between the two inlet ports. Consequently, numerical results gave a lower temperature for the thermocouple 5. Fig. 6.28 and Fig. 6.29 show that there is no major difference in the numerical results between the boundary conditions of uniform and fully developed inlet velocity. The flow entered through inlet ports and deviated by 90^{o} and was then redistributed through the inlet manifold. Consequently, the inlet velocity boundary condition was invalidated when the flow left the inlet ports and entered the channels. The uniform inlet velocity was closer to the actual case than the fully developed boundary because the plastic tube was bent before connecting to the inlet ports.

During the experiments water was supplied from a container to the cooling device(s) through two plastic tubes (See Fig. 6.10). The water container position was located higher than the model to generate different mass flow rates under the effect of gravity. Five different heights for water container were chosen using the lengths of tubes. The length of the tubes was enough to generate a fully developed flow at the inlet to the model(s). However the plastic tubes were bent before being connected to the model.

A separation and secondary flow occurs when the liquid passing through the bent and therefore the fully developed flow condition was invalidated.

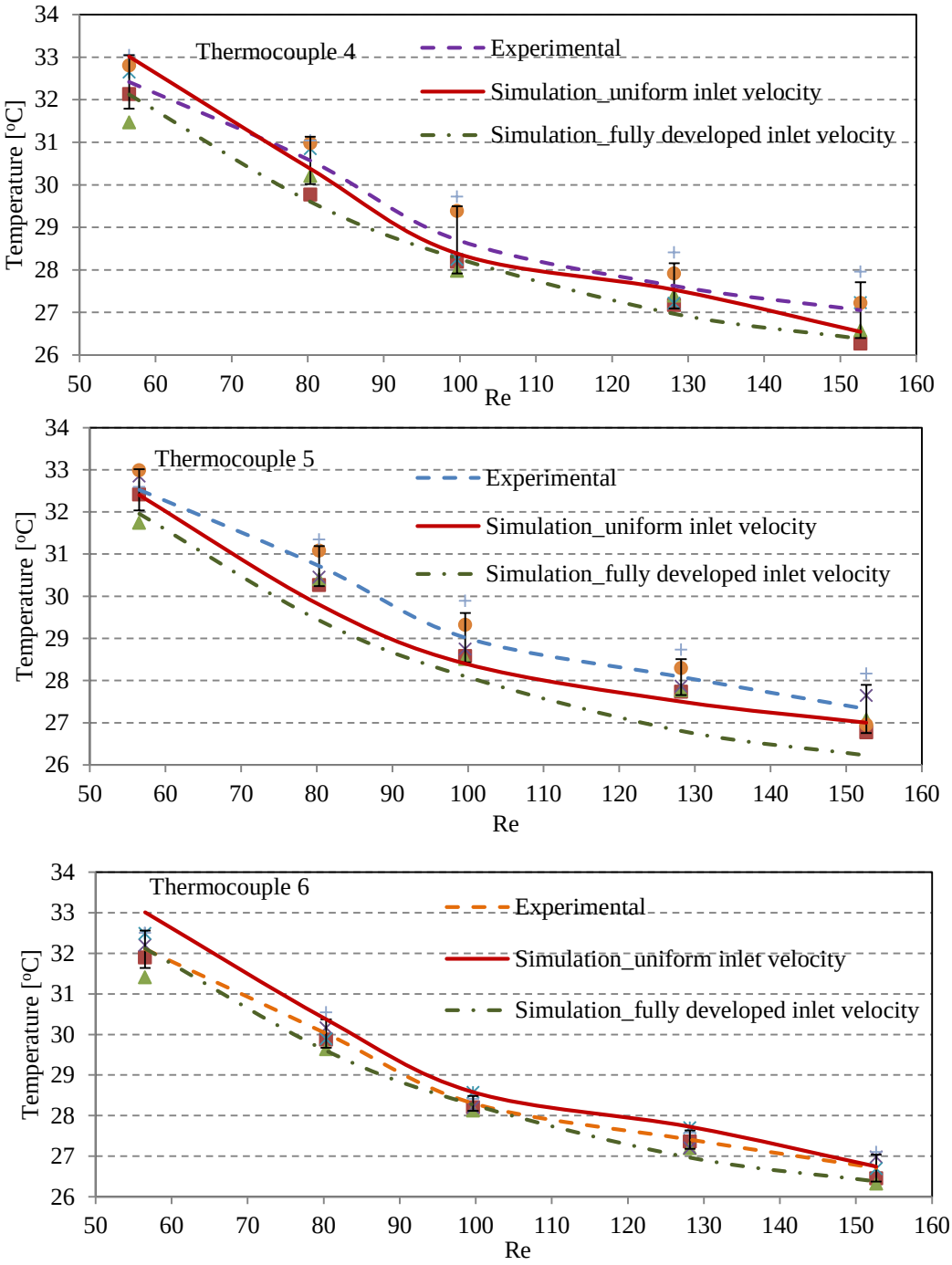

Fig. 6.29 Comparison between the experimental and simulation results of the model **without** subchannels for Thermocouple 4, Thermocouple 5 and Thermocouple 6 attached to the outlet manifold. Error bars are within the range ± one standard deviation.

Consequently, fully developed flow conditions at inlet to the model ports were invalidated because of the effect of the bends in the tubes. Moreover, the inner tube diameter was less than the model's inlet ports which would change the inlet flow conditions for the model. However, two inlet boundary conditions were investigated for the numerical analysis.

Fig. 6.30 shows the percentage deviations of the experimental data of the thermocouples' reading in comparison with the numerical results of a uniform inlet velocity boundary condition.

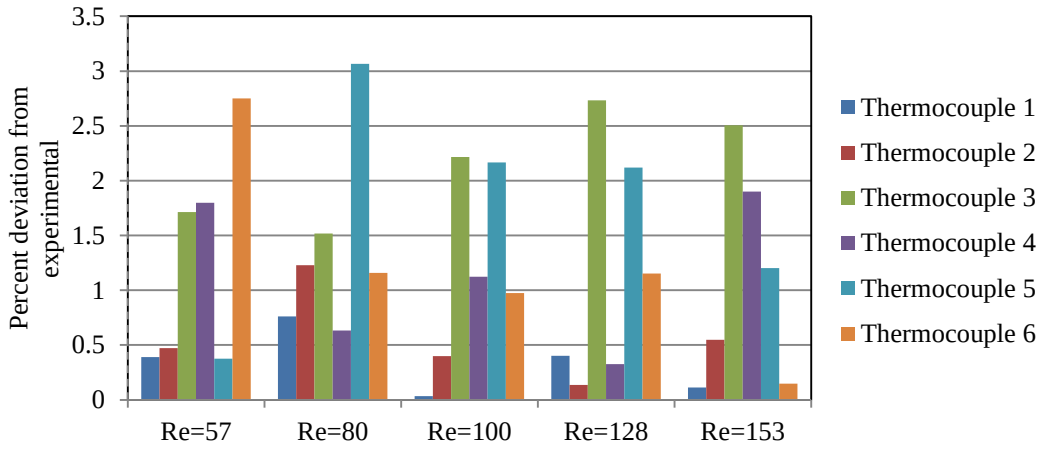

Fig. 6.30: Percentage deviation of thermocouple readings from the experimental data for various Reynolds number for the model **without** subchannels.

Fig. 6.30 shows that each thermocouple had a different percentage error for each pressure head. Each thermocouple measured temperature at different locations (See Fig. 6.5 and Fig. 6.6). Furthermore, the contact area between probe and the surface was different for each thermocouple which altered the thermal contact resistance (See Chapter 4). Moreover, each thermocouple measured a different temperature for each pressure head because of the various experimental conditions. Accordingly, it is possible to see a different percentage error for each thermocouple.

B. *Model with subchannels*

A good agreement was obtained for the readings of *Thermocouple 1*, *Thermocouple 2* and *Thermocouple 3* in comparison with experimental results for both inlet velocity conditions as shown in Fig. 6.31.

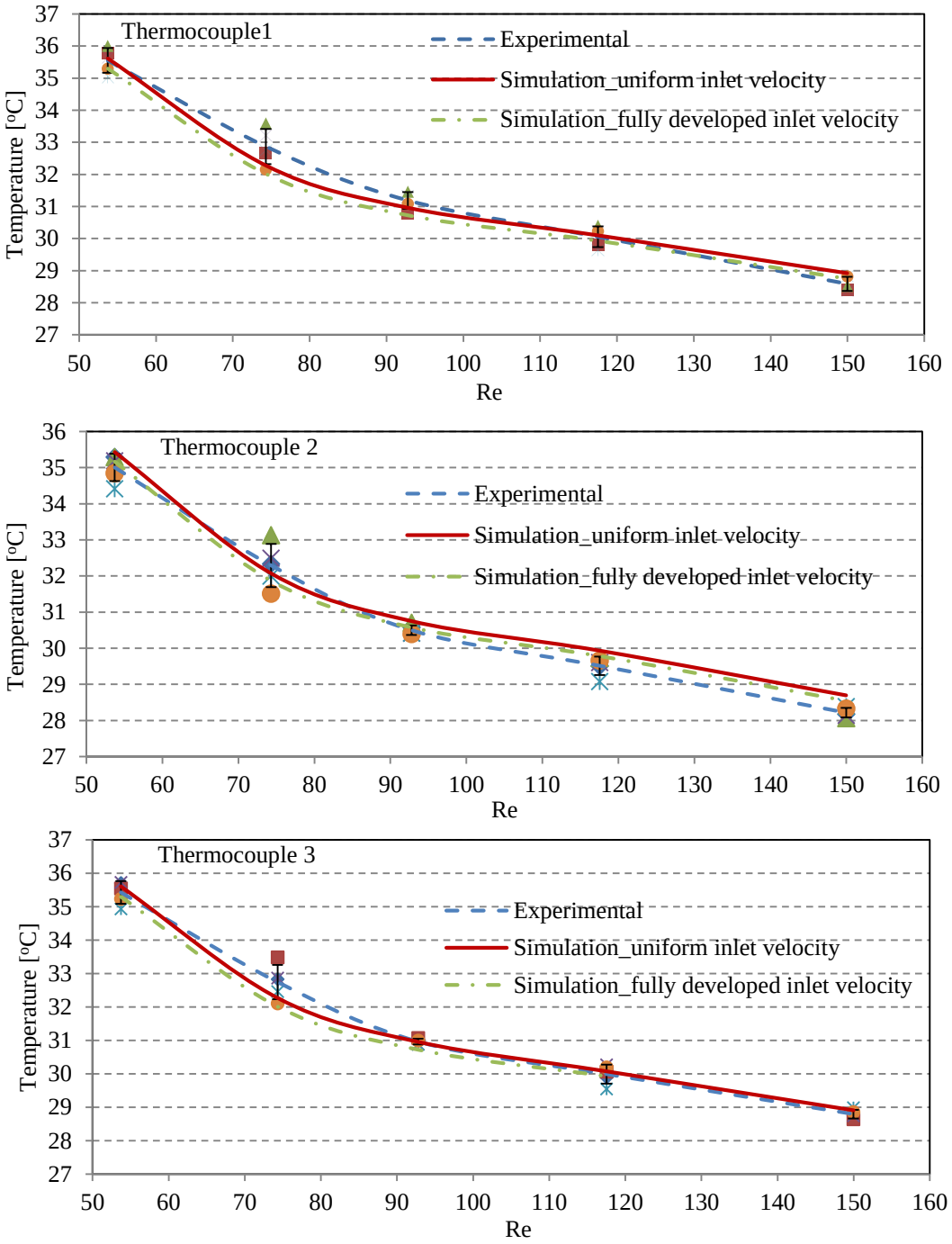

Fig. 6.31: Comparison between the experimental and simulation results of the model **with** subchannels of *Thermocouple 1*, *Thermocouple 2* and *Thermocouple 3* attached to the outlet manifold. Error bars are within the range ± one standard deviation.

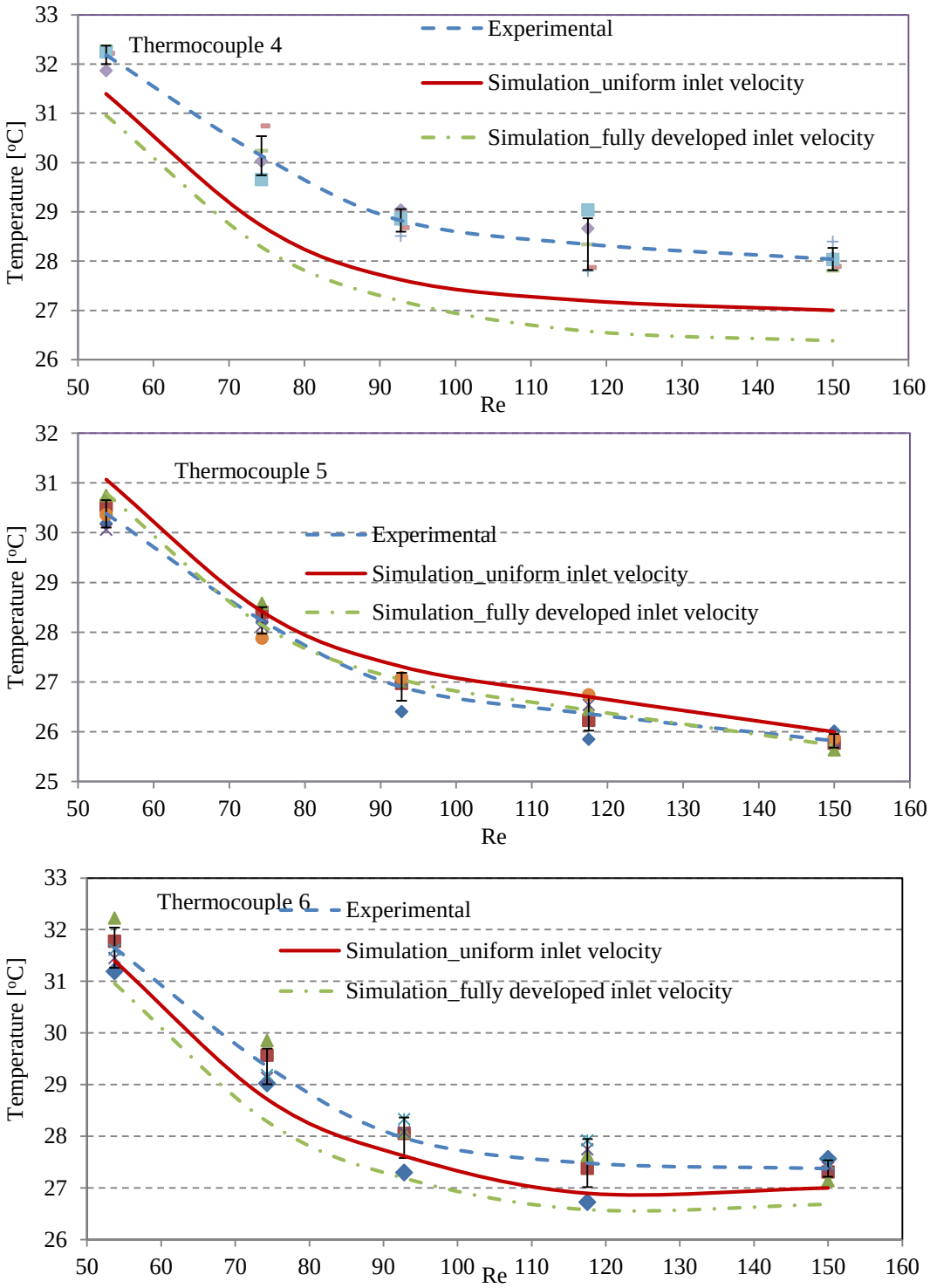

Fig. 6.32 Comparison between the experimental and simulation results of the model **with** subchannels of *Thermocouple 4*, *Thermocouple 5*, and *Thermocouple 6* attached to the inlet manifold. Error bars are within the range ± one standard deviation.

Another approval of numerical results was achieved for *Thermocouple 4*, *Thermocouple 5* and *Thermocouple 6* in comparison with experiments data (See Fig. 6.32) other than a small deviation in the numerical data of *Thermocouple 4* in comparison experiments results.

Fig. 6.33 shows the percentage deviation of numerical results in comparison with the experimental data of a uniform inlet velocity boundary condition. It was mentioned previously that many parameters have an effect on thermocouple readings such as: probe contact area, position of thermocouple and experiment operating conditions. Accordingly, the size of the error bars in Fig. 6.33 was different for each thermocouple and pressure head. *Thermocouple 4* shows a maximum deviation (5%) in comparison with the other thermocouples.

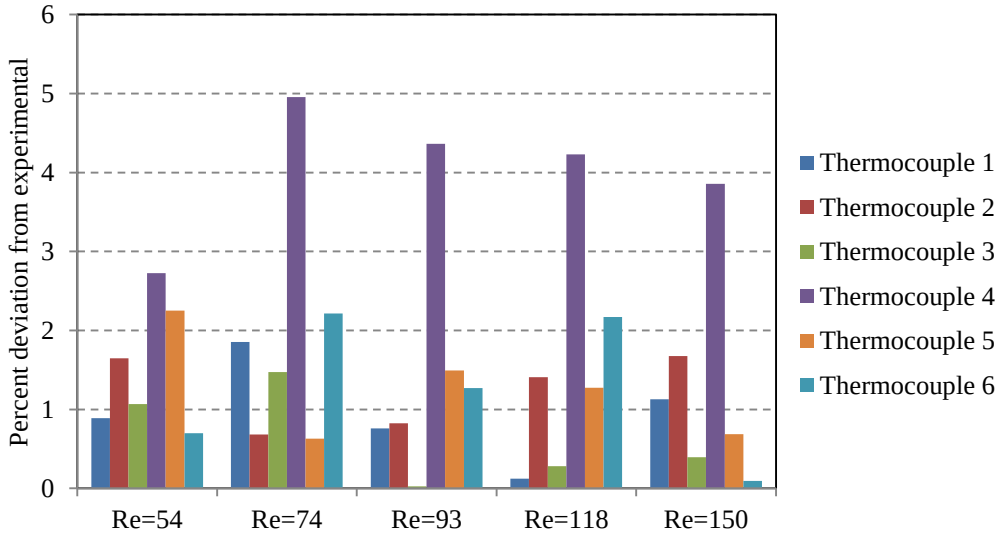

Fig. 6.33 Percentage deviation of thermocouples readings from experimental data for different pressure head for the model **with** subchannels.

It was found that during the attachment of thermocouple to the surface, a small pocket of air was trapped between the glue and the surface. Therefore, this gap allowed the probe to move nearer to the microheaters and that caused a higher surface measurement than expected. Moreover, if there is not a good contact between the microheaters and the bottom surface of copper channels at any point this may lead to

a higher reading for any thermocouple near that point. Consequently, this may cause a deviation in *Thermocouple 4* reading.

6.4.3.2 Water outlet temperature

Two type K thermocouples were inserted inside the plastic tubes close to the outlet ports to measure water temperature. Thermocouple wires were insulated from the outside environment to avoid any measurement being affected by conduction through the wires [118]. The numerical model can be validated by comparing the water outlet temperature for both models with experimental results as shown in Fig. 6.34 and Fig. 6.35 respectively.

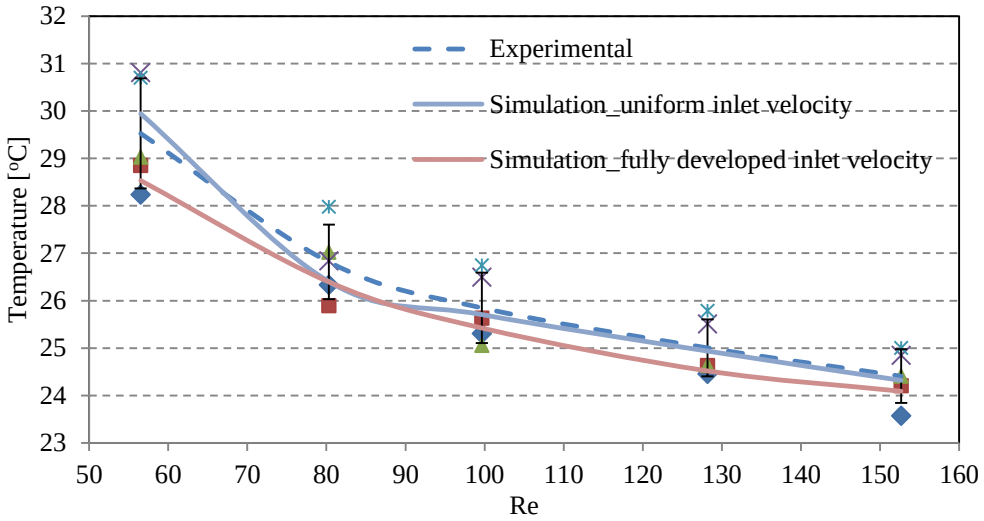

Fig. 6.34: Comparison between the experimental and simulation results of the water outlet temperature for the model **without** subchannels. Error bars are within the range ± one standard deviation.

A good agreement with the experimental results further confirmed the validity of the numerical model. The presence of the thermocouple junction may cause some flow disturbances over the probe and may alter the reading(s). During the experiment(s) flow behaviour around the probe may change and lead to a small difference in temperature reading. Therefore, the error bars were slightly larger because of the variable flow behaviour around the probe which was inserted at the exit from the model in a plastic tube.

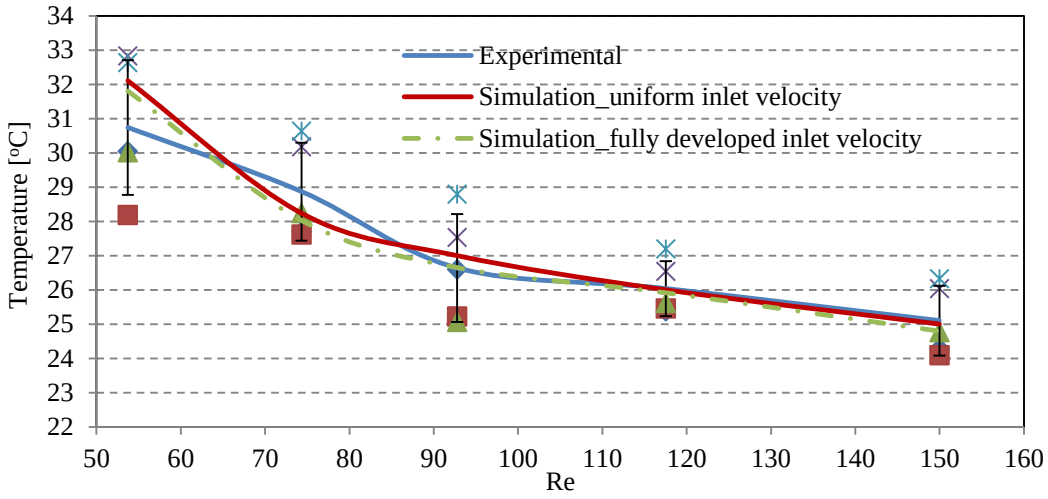

Fig. 6.35: Comparison between the experimental and simulation results of the water outlet temperature for the model **with** subchannels. Error bars are within the range ± one standard deviation.

6.4.4 Analysis of numerical results

6.4.4.1 Channel bottom surface temperature

Fig. 6.36 shows numerical results of the bottom surface temperature of the channels along the full model. It shows that the maximum temperature occurs downstream of the hotspot. Thermal and hydraulic boundary layers were re-created at the entrance to subchannels because of the presence of an obstacle (subchannels) in the flow direction.

The thickness of the thermal boundary layer increased towards the end of the subchannels. Consequently, the heat transfer rate was increased upstream and gradually decreased downstream through the subchannels (See section 6.4.4.3). The same behaviour was applicable for the model without subchannels except the maximum temperature occurred earlier. A comparison between Fig. 6.36 and Fig. 6.37 revealed that the maximum temperature occurred for the axial position approximately at 7.5cm for the model **without** subchannels and at 8cm for the model **with** subchannels.

Fig. 6.37 shows a comparison between the average surface temperatures along the axial location of the channels for both the models. Adding subchannels led to a reduction in the maximum surface temperature from 32.5ºC to 29ºC. Furthermore,

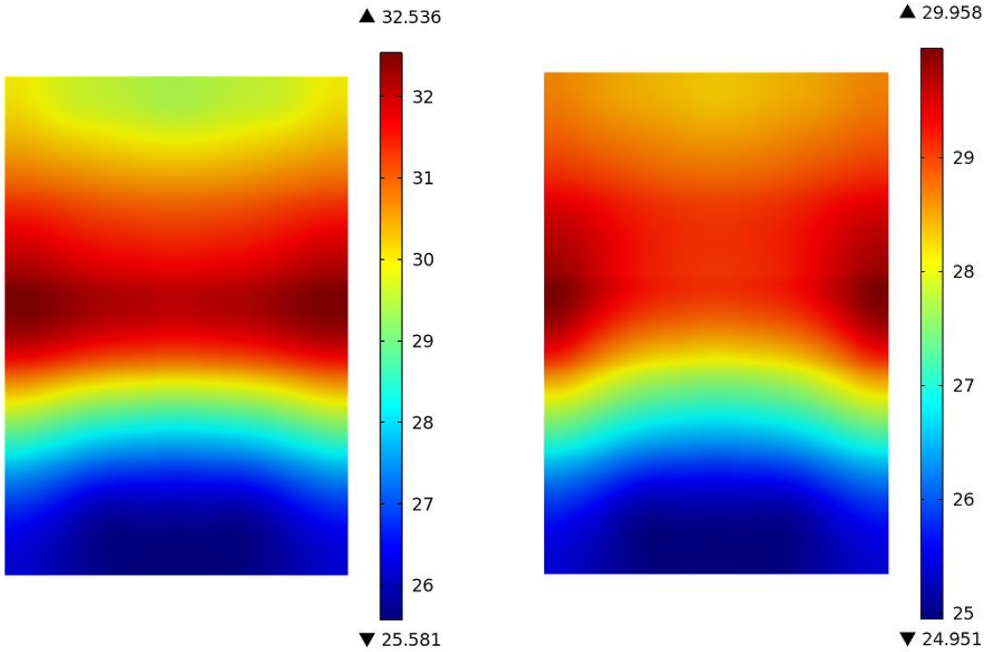

(a) without subchannels (b) with subchannels

Fig. 6.36 Temperature of the bottom surface under the copper plate for both models at the highest pressure head (79cm).

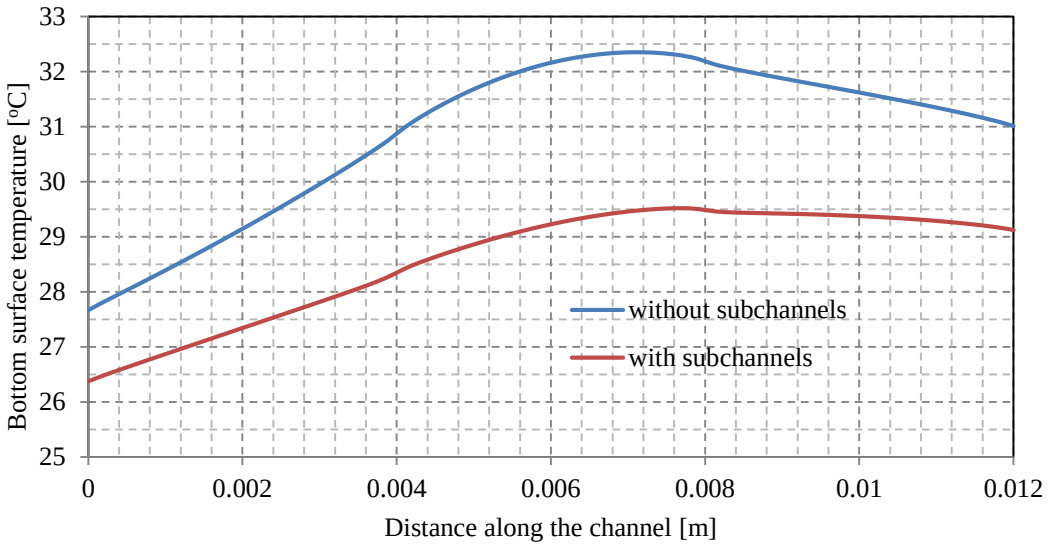

Fig. 6.37 Variation of the average bottom surface temperature of the channels along the centre line for both the models **with** and **without** subchannels of the highest pressure head (79cm).

temperature uniformity was improved by reducing the difference between maximum and minimum temperatures from ~5°C (without subchannels) to ~2.5°C (with subchannels).

Results of the highest pressure head (79cm) were considered for comparison between the two models because it gave the highest mass flow rate. Therefore, the effect of any change in flow direction or obstruction would be obvious. Consequently, the impact of subchannels on the flow behaviour is greater for higher mass flow rate.

Fig. 6.38 shows a comparison of maximum surface temperature between models with

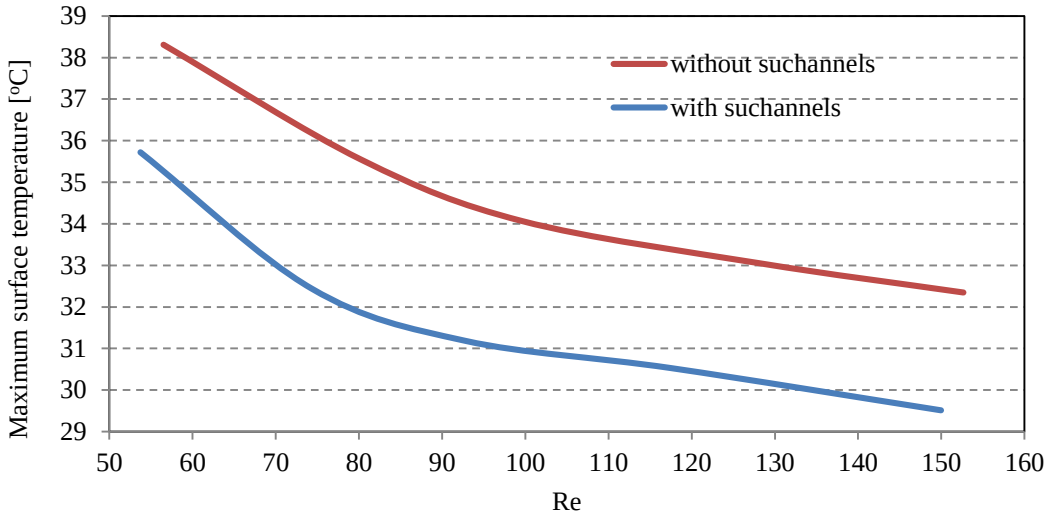

Fig. 6.38 Variation of the maximum bottom surface temperature with Re for both the models **with** and **without** subchannels.

an increase in *Re*. The increase in *Re* means more mass flow rate comes into the model(s) and therefore heat transfer increase. Fig. 6.38 shows that the increase in the mass flow rate augmented the heat transfer rate through both models. Because the liquid-solid interaction area in the model with subchannels was larger, there was more heat extraction above the hotspot and lower temperature of the channels bottom surface.

6.4.4.2 Bulk temperature

The main objective of the current work was to increase the total amount of energy transfer above the hotpot area by adding subchannels to increase solid-liquid interaction area. The increase in energy transferred to liquid water can be detected by computing fluid bulk temperature [91]. Bulk temperature was calculated at any axial location along the middle channel from Eq.(3.39) (See 3.4.2.1 in Chapter 3).

$$T_{b,avg} = \frac{\int \rho T u dA}{\int \rho u dA} \tag{3.39}$$

The numerator of Eq. (3.39) represents the total energy carried by the liquid while the dominator calculates the total mass flow rate through a cross-sectional area along the axial distance of the channels. Comparison between the results presented in Fig. 6.39 and Fig. 6.40 shows that adding of micro-channels leads to an increase in the energy transfer to the liquid water.

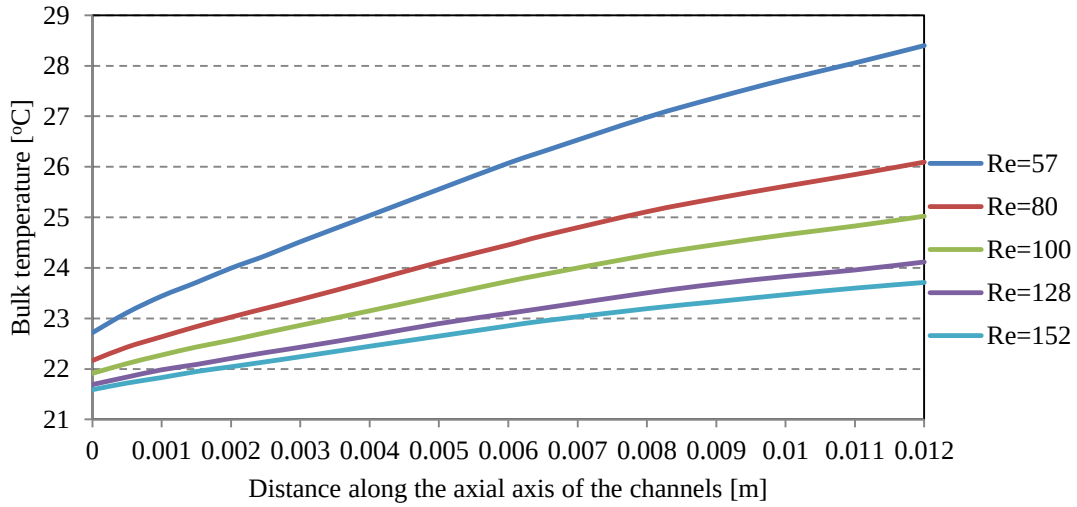

Fig. 6.39: Fluid bulk temperature for different pressure heads for the model **without** subchannels.

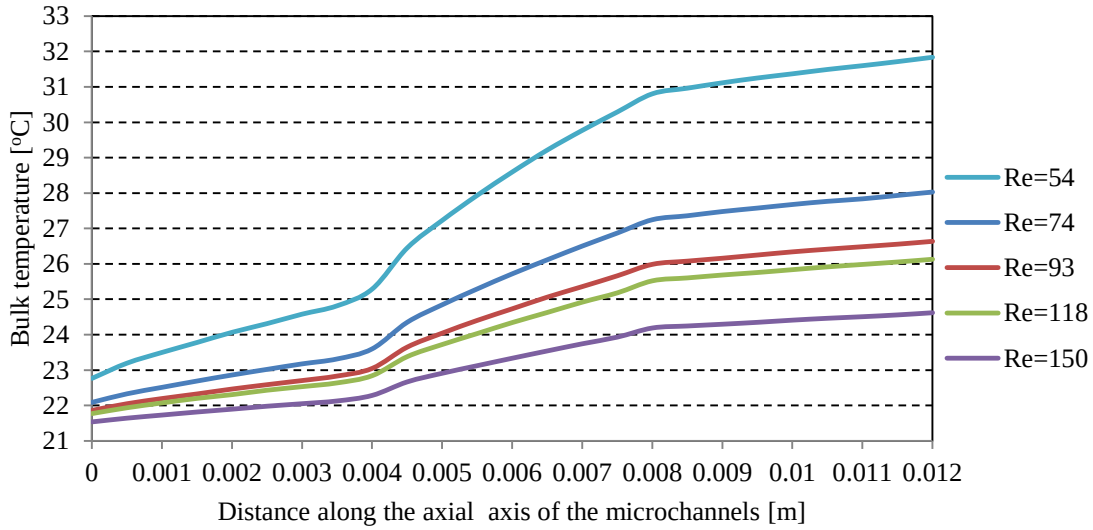

Fig. 6.40: Fluid bulk temperature for different pressure heads for the model **with** subchannels.

Bulk temperature also increases when the flow comes in contact with subchannels as a result of the increase in the solid-liquid heat transfer area. Consequently, this enhanced the heat transfer process and improved the system performance above the hotspot by reducing the channels' surface temperature as shown in Fig. 6.36 and Fig. 6.37.

Fig. 6.41(a-b) shows the velocity and temperature distribution at a plane across the middle height of the channels for the model without subchannels. Fluid at the channel inlet started to interact with the walls and developed hydraulic and thermal boundary layers.

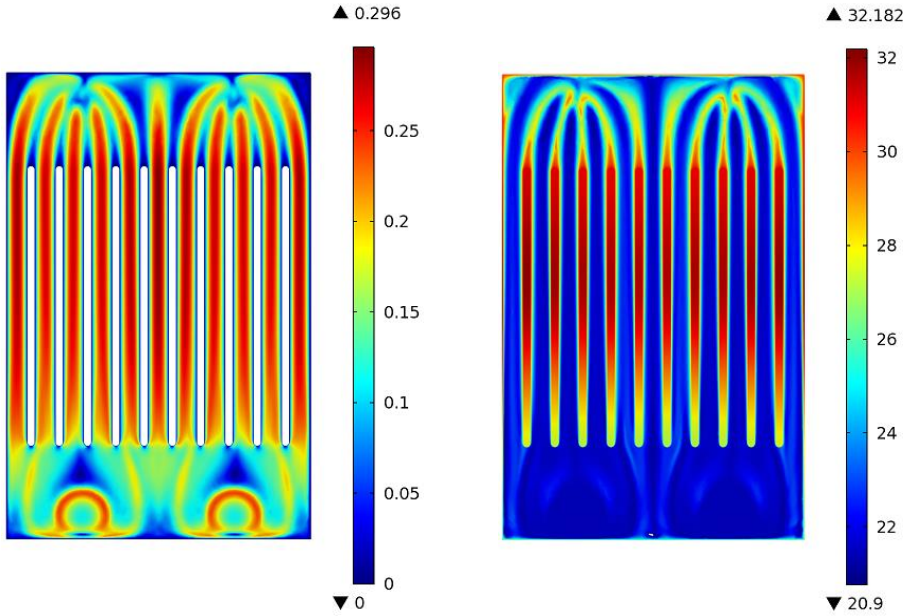

(a) velocity (b) temperature

Fig. 6.41Velocity and temperature distribution at the channels'middle height for the model **without** subchannels.

Fig. 6.41b shows that a thin layer of liquid was affected by the heat transfer from the channel walls while the temperature of the rest of the liquid had an approximate constant temperature. The fluid boundary layer developed at the channel inlet which led to a sharp increase in velocity and then a nearly fully developed flow was attained downstream of the channel as shown in Fig. 6.26b. Therefore, the velocity effect was dominant in the calculation of the bulk temperature from Eq. (3.39) and a linear increase was obtained as shown in Fig. 6.39.

A different behaviour for the system with subchannels was shown in Fig. 6.42. The flow before reaching subchannels had a similar behaviour to the model without subchannels (See Fig. 6.41 and Fig. 6.42). The rapid increase in flow velocity through the subchannels was due to an area reduction (See Fig. 6.42). The effects of the presence of the subchannels accelerated the flow and increased the heat transfer area (See Fig. 6.27b and Fig. 6.42). Consequently, energy transfer to the liquid was improved which could be detected by the jump in bulk temperature, (See Fig. 6.40). Moreover, model with subchannels shows better thermal performance due to lower temperature obtained as shown in Fig. 6.41b and Fig. 6.42b.

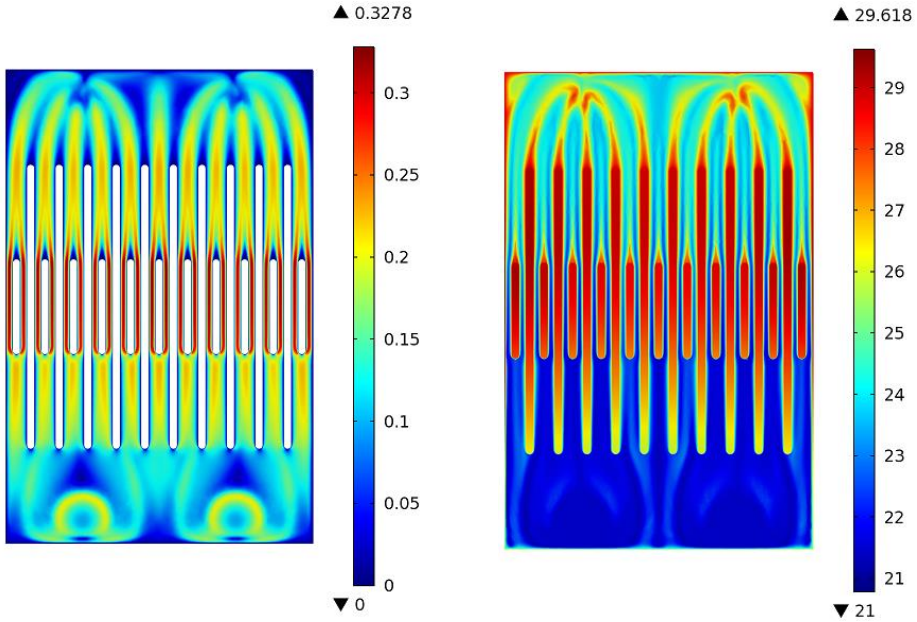

(a) velocity (b) temperature

Fig. 6.42: Velocity and temperature distribution at the channels' middle height for the model **with** subchannels.

6.4.4.3 Nusselt number

Nusselt number *Nu* is a dimensionless number which relates the rate of convection-conduction heat rate normal to the liquid-solid interaction surface [87]. Therefore, Nusselt number gives a deep understanding of the effect subchannels have on the system thermal performance. *Nu* is calculated from Eq.(3.40) [90] (See section 3.4.2.1 in Chapter 3).

$$Nu = \frac{D_h}{k_f} \frac{q''}{T_{w,avg} - T_{b,avg}} \tag{3.40}$$

where $T_{b,avg}$ is calculated from Eq.(3.39) and $T_{w,avg}$ is calculated from Eq.(3.38) (See section 3.4.2.1 in Chapter 3).

$$T_{w,avg} = \frac{1}{L} \int_L T_w dl \tag{3.38}$$

where L represents the perimeter length of the surface at a specific location along the middle channel's axial axis. The middle channel was chosen to calculate *Nu* for comparison to save computational time. Fig. 6.43 shows the variation of the *Nu* number along the channel axis for the model without subchannels. The developed thermal boundary layer is thin at the channel inlet which means that a high transfer rate was taking place. Consequently, there was a sharp increase in *Nu* at the channel entrance as shown in Fig. 6.43. Thereafter, a gradual drop was predicted in *Nu* because of the effect of developing a thermal boundary layer. The hotspot caused a small variation in the value of *Nu* at the middle of the channels as also shown in Fig. 6.43.

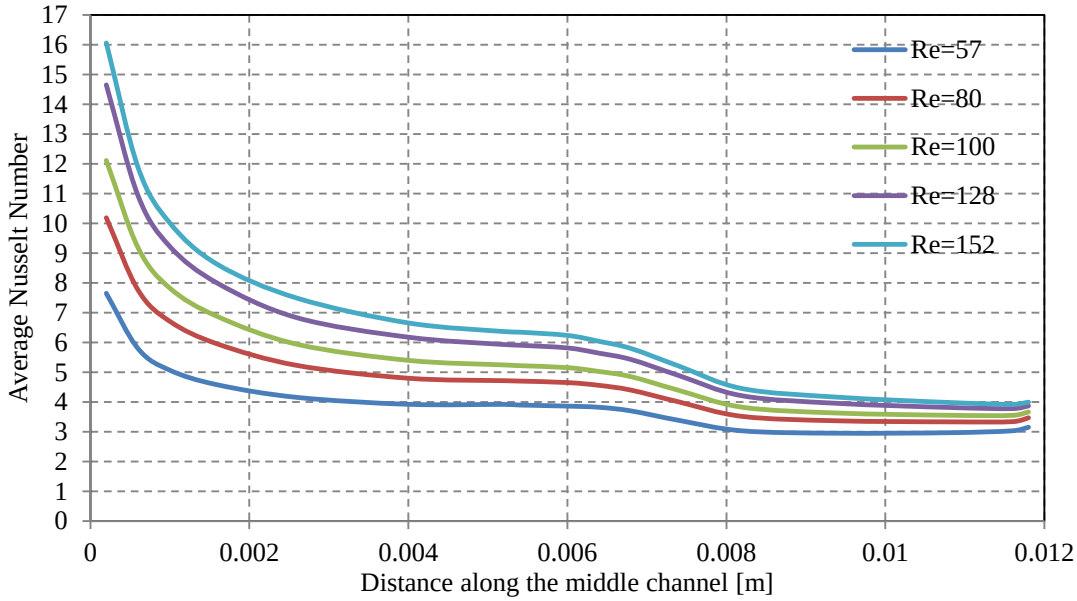

Fig. 6.43: Nusselt number variation along the middle channel for the model **without** subchannels for different Reynolds number.

A different behaviour of *Nu* was predicted for the model with subchannels as shown in Fig. 6.44. Three distinct behaviours of *Nu* are seen in the upstream, middle and downstream of the channels. The entrance effect is also obvious on the *Nu* value(s) and then the gradual drop as a result of the effect of developing boundary layers, as previously mentioned.

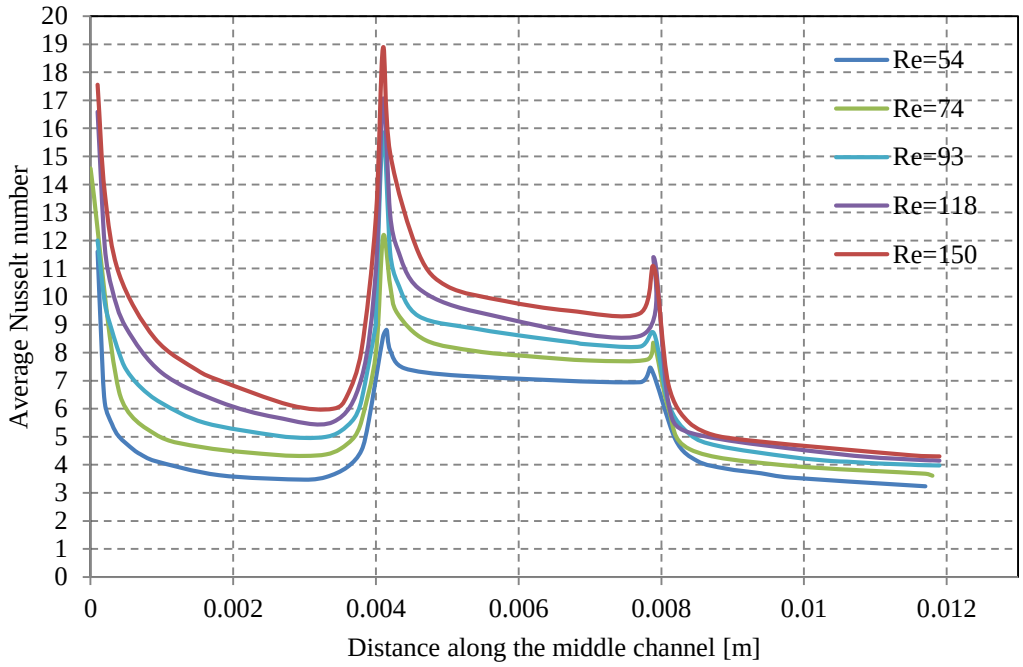

Fig. 6.44: Nusselt number variation along the middle channel for the model **with** subchannels different Reynolds number.

Subchannels above the hotspot enhance the heat transfer rate due to the increase in solid-liquid interaction. Moreover, thermal boundary layer(s) on the main were broken when the flow reached the subchannels. Therefore, new thermal and hydraulic boundary layers were started to create an entrance to the subchannels. Therefore, a sharp jump in *Nu* value(s) was obtained at the subchannels' inlet (See Fig. 6.44). A small jump in *Nu* at the exit of the subchannels was a result of the circulation and there was then a sharp drop in *Nu* at inlet to downstream subchannels, (See Fig. 6.44). A comparison between Fig. 6.43 and Fig. 6.44 shows that the performance of the model with subchannels has been improved.

6.4.4.4 Pumping power and thermal resistance

Pumping power (Po) was calculated from Eq. (6.12) [134]

$$Po=\Delta p*\dot{V} \tag{6.12}$$

where Δp [kPa] is pressure, $\dot{V}$ is the volume flow rate. The pumping power calculation depends on the numerical data of the pressure.

Thermal resistance was calculated from Eq.(6.13) [134]

$$R_{th}=\frac{\Delta T_{max}}{q_1''\times A_{uniform}+q_2''\times A_{spot}} \tag{6.13}$$

where $\Delta T_{max}=T_{s,max.}-T_{win}$, $T_{s,max.}$ maximum surface temperature [ºC] and T_{win} [ºC] water inlet temperature, q_1'' and q_2'' uniform and hotspot heat fluxes [W/m^2] respectively, $A_{uniform}$ and A_{spot} uniform and hotspot heat flux surface area [m^2] respectively.

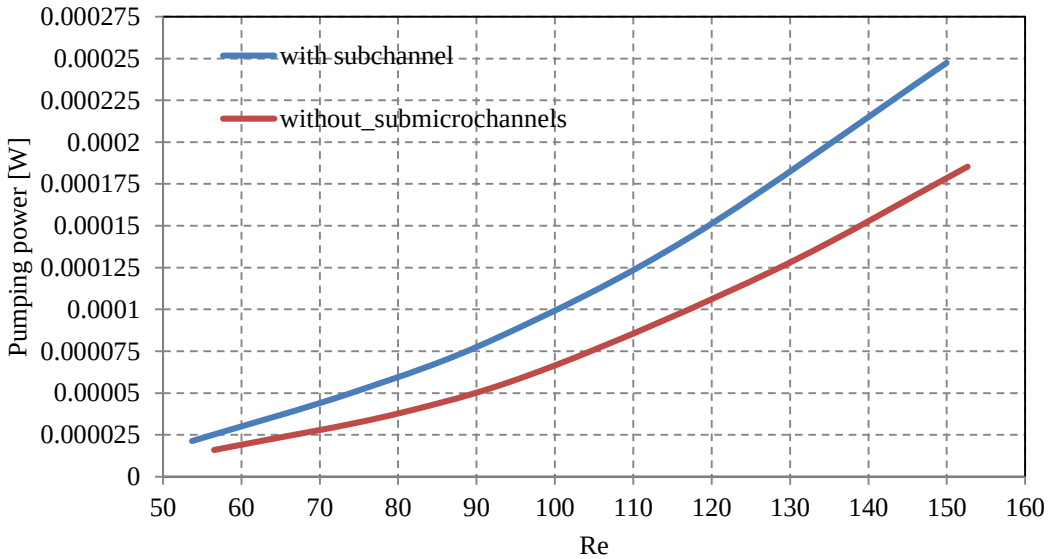

Fig. 6.45 Comparison of pumping power for both models **with** and **without** subchannels.

Pumping power rises are a result of the increase in the pressure drop in the presence of subchannels (See Fig. 6.45). The inserting of the subchannels in the middle of the main channels creates an obstacle to the fluid flow and then a circulation will be

generated at entrance to the subchannels. Moreover, the reduction in channel(s) cross-sectional area to one-third of the main channel area led to an increase in the pressure drop and higher pumping power will be required. The effect of the subchannels will be more complex with the increase in the mass flow rate and therefore higher pressure drop and pumping power were made as shown in Fig. 6.45.

The thermal resistance decreases following the drop in the maximum surface temperature for the model with subchannels, (See Fig. 6.36-Fig. 6.38 and Fig. 6.46). Eq.(6.14) and (6.15) are the best fit equation which can describe the variation with thermal resistance with *Re*.

For the model without subchannels thermal resistance can be written as

$$R_{th,No} = 6.23Re^{-0.425} \tag{6.14}$$

and for the model with subchannels

$$R_{th,with} = 6.51Re^{-0.5} \tag{6.15}$$

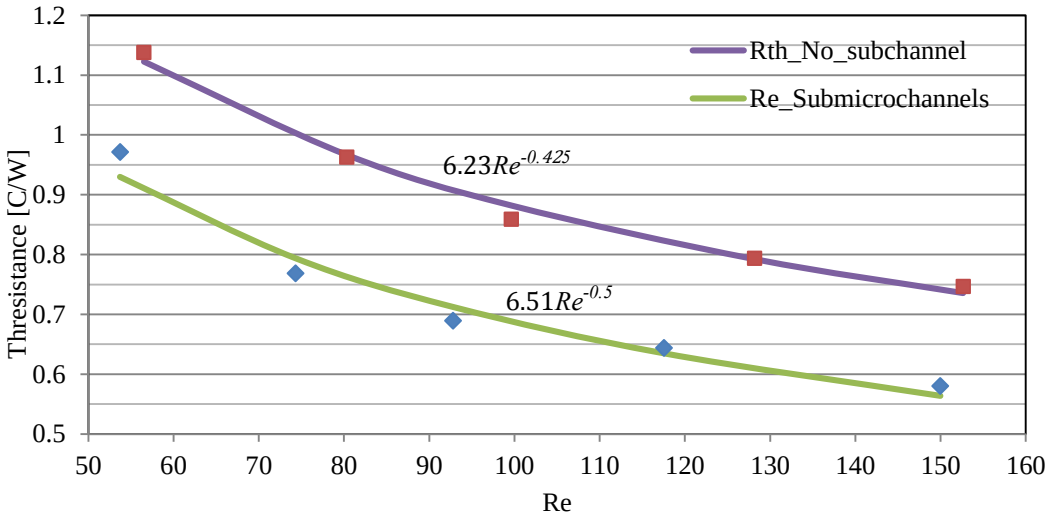

Fig. 6.46: Comparison of the thermal resistance with *Re* for the models **with** and **without** subchannels.

6.5 Conclusions

The effect of adding subchannels above the hotspot has been studied experimentally and numerically. A model consisting of eleven channels made from copper with a hotspot in the middle was investigated. The objective of adding subchannels was to reduce the maximum surface temperature and improve temperature uniformity. Model(s) of two inlets and outlets ports were fabricated in order to obtain approximately a uniform mass flow rate distribution through channels. A good agreement between the numerical and experimental results has been obtained. Therefore, the following conclusions were reached:

1. The increase in the fluid-liquid surface by adding subchannels reduced the maximum model bottom surface temperature.
2. The maximum surface temperature occurred upstream of the subchannels section because of the flow direction.
3. The surface temperature distribution was improved for the model with subchannels in comparison with that without subchannels. Consequently, the difference in the temperature along the surface was reduced.
4. There was a drop in maximum surface temperature with an increase in *Re* for both models.
5. The model with subchannels had a lower thermal resistance in comparison with the other model.
6. The pumping power was increased as a result of the addition of the subchannels.
7. The advantage of present device is that we can use the same parallel channels with a simple change in design by adding subchannels above the hotspot to reduce the channels widths. The subchannels can be added wherever the hotspot is available and no need to change the design of the other part of the channels.
8. In the present design, the main channel(s) was divided into two subchannels by inserting a fin above the hotspot. Moreover, the main channels can be divided into more than two subchannels depends on how much is the density of the heat flux on the hotspot. The main limitation is availability of the fabrication facility which can produce the smallest channel width.
9. The disadvantage is the main subchannels width(s) is confined by the main channel width. Consequently, the design can be improved by splitting into the main

channels and subchannels to control the width(s) according to density of the heat flux as suggested by numerical analysis of Li [16]. But this design increases the complexity and consequently the pumping power.

Chapter 7
Conclusions and Recommendations for Future Work

In this chapter, the overall conclusions are summarised based on the results presented in the thesis and some recommendations for the future work are suggested.

7.1 Conclusions

It was reported that during the measurement process, when the thermocouple junction is in contact with measured medium while the wires are extended and connected to measurement device to record the temperature, error occurs when the measured temperature by the junction is different than that of the wires. Consequently, the heat conducted through the probe, the wires to (or from) the measured medium and the thermocouple disturbs temperature which is different than expected. Therefore, this error should be considered and included in the measurement process.

In Chapter 40, the cooling and heating effects of different stripped lengths of the thermocouple electrical insulation for different wires sizes (80µm and 200µm) on the surface temperature measurement have been investigated. The surface temperature range was (4^oC-35^oC) while the wires were extended vertically and exposed to free convection from outside environment of temperature 13^oC. A good agreement between analytical, numerical and experimental results has been achieved. The following have been concluded:

- Stripping different lengths (0mm, 5mm, 10mm, 15, and 20mm) of insulation has a negligible effect on the surface temperature measurement within the measured range and is independent of thermocouple size.
- There is no specific critical diameter of the thermocouple wire(s) over which heat transfer to the wires decreases.
- The effect of the thermocouple electrical insulation is negligible if the experimental error in temperature measurement is higher than the impact of using the thermocouple (with or without insulation).

- The effect of the thermocouple electrical insulation can be considered when the surface temperature reaches 800°C for 80μm thermocouples and 250°C for 200μm thermocouples.

In Chapter 5, heating impact of different thermocouple sizes 80μm and 315μm on small volume of cold water have been analysed both experimentally and numerically. The water was in a small chamber of plastic insert which was cooling by a copper block inside a thermostatically controlled system. The copper block temperature was equal 4.05°C while the thermocouple wires were extended vertically and exposed to free convection to the outside environment of temperature 18°C. A good agreement between experimental and numerical analyses has been obtained. The following were concluded:

1. The heating effect of the thermocouple is eliminated when the thermocouple junction is close to the copper block. Moreover, this effect is increased when the thermal resistance between the copper block and the thermocouple junction rises due to the presence of the plastic insert.
2. The length of thermocouple wires exposed to the environment increases with an increase in thermocouple size while wire has no effect over a specific length where the wire end temperature is equal to that of the environment.

The cooling of hotspot generated due to non-uniform heat fluxes dissipation above a chip circuit have been investigated experimentally and numerically. The increase of the solid-liquid interaction area reducing the effect of the hotspot(s) has been studied. Different designs are available for enhancing the heat transfer rate and improving the thermal performance of the cooling devices.

In Chapter 6, two heat sinks have been designed and fabricated: the first device has been fabricated with parallel channels only while the second one was designed to extract the high heat fluxes by dividing the main channels above the hotspot(s) into two subchannels. The inlet and outlet manifolds were fabricated with two ports in order to minimise the mal-distribution of the flow rate through the channels. The analysis was limited to a laminar single-phase flow with water as a cooling liquid. The following have been found:

1. The addition of the subchannels leads to a reduction the maximum bottom surface temperature and improves the temperature uniformity. Furthermore, thermal resistance is decreased for the cooling device with subchannels.
2. The present design can be improved by increasing the density of the fins above the hotspot(s) or adding the fins wherever the hotspot(s) is available above chip circuit without any essential changes in the heat sink design.
3. The increase in the Reynolds number minimises the surface temperature for both heat sinks.
4. The heat sink with subchannels requires more pumping power in comparison with the one without subchannels.

7.2 Recommendations for future work

The present investigation of the cooling and heating effects of the thermocouple electrical insulation on surface temperature measurement in Chapter 4 was limited to a specific surface temperature range (4^{o}C-35^{o}C). Moreover, in Chapter 5, the heating impact of different thermocouple sizes on small volume of cold was only studied. Consequently, and according to the conclusions the following recommendations were suggested for the future work:

1. Experimental work is recommended to study the effect of the thermocouple electrical insulation for higher surface temperature.
2. Study the cooling effect of using thermocouple when the environment temperature is lower than the water temperature.

The study of using subchannels for cooling hotspot(s) above a chip circuit was conducted for water as a cooling liquid and a laminar single-phase flow. Therefore, the present work can be extended to include the followings:

1. The effect of turbulent can be investigated for both designs.
2. Two-phase flows can also be studied for the design with subchannels.

Appendix I: Publications

Journal paper

1. A. Y. Al Waaly, M. C. Paul and P. S. Dobson, Applied Thermal Engineering, "Effects of Thermocouple Electrical Insulation on the Measurement of Surface Temperature", 2015, vol. 89, pp. 421-431, DOI: 10.1016/j.applthermaleng.2015.06.020.

Conference paper

1- A. Y. Al Waaly, M. C. Paul and P. S. Dobson, "Effects of Thermocouple Electrical Insulation on the Measurement of Surface Temperature", 13th UK Heat Transfer Conference (UKHTC2013) 2nd – 3rd September 2013, Imperial College, London, United Kingdom.

2- A. Y. Al Waaly, M. C. Paul and P. S. Dobson, "Liquid Cooling of Non-Uniform Heat flux of Chip Circuit by Submicrochannels", International Conference On Advances in Civil, Structural and Mechanical Engineering – CSM, June 01-02, University of Westminster, London, United Kingdom.

Posters presentation

1- 24th Scottish Fluid Mechanics Meeting, 25th May 2011, Strathclyde University, Glasgow.

2-Iraqi Cultural Attache Conefernce For Engineers, 1-2/10/2011 Iraqi Cultural Attache, London, United Kingdom.

3- 25th Scottish Fluid Mechanics Meeting, 25th May 2011, Heriot Watt University, Edinburgh.

References

[1] X. Wei, "Stacked Microchannel Heat Sinks for Liquid Cooling Microelectronics Devices", PhD thesis, November 2004, Mechanical Engineering, Georgia Institute of Technology, DOI: hdl.handle.net/1853/4873.

[2] R. J. Moffat, Thermal Measurement in Electronics Cooling, "Uncertainty Analysis", 1997, Boca Raton, FL, CRC Press, pp. 45-80.

[3] B.S. Singh and A. Dybbs, Journal of Heat Transfer, "Error in Temperature Measurements Due to Conduction Along the Sensor Leads", August 1976, vol. 98, no. 3, pp. 491-495, DOI: 10.1115/1.3450581.

[4] H. Shaukatullah and A. Claassen, Semiconductor Thermal Measurement and Management Symposium - Ninteenth Annual IEEE, "Effect of Thermocouple Wire Size and Attachment Method on Measurement of Thermal Characteristics of Electronic Packages", 2003, pp. 97-105, DOI: 10.1109/STHERM.2003.1194345.

[5] D. I. Li and M.A. Wells, Metallurgical and Materials Transactions B, "Effect of Subsurface Thermocouple Installation on the Discrepancy of the Measured Thermal History and Predicted Surface Heat Flux during a Quench Operation", June 2005, vol. 36B, no. 3, DOI: 10.1007/s11663-005-0064-6.

[6] Q. He, S. Smith and G. Xiong, Semiconductor Thermal Measurement and Management Symposium (SEMI-THERM) - 27th Annual IEEE, "Thermocouple Attachment Using Epoxy in Electronic System Thermal Measurements — A numerical Experiment", 20-24 March 2011, San Jose, CA, DOI: 10.1109/STHERM.2011.5767212.

[7] I. U. Perera, N. Narendran and Y. W. Liu, SPIE Proceedings 8835 - LED-based Illumination Systems, "Accurate Measurement of LED Lens Surface Temperature", September 2013, San Diego, CA, DOI: 10.1117/12.2023091.

[8] L. M. K. Boelter and R. W. Lockhart, NACA Technical Note 2427, "An Investigation of Aircraft Heaters: XXXV-Thermocouple Conduction Error Observed in Measuring Surface Temperatures", July 1951, National Advisory Committee for Aeronautics; Washington, DC, United States.

[9] M. H. Attia, A. Cameron and L. Kops, Journal of Manufacturing Science and Engineering, "Distortion in Thermal Field Around Inserted Thermocouples in

Experimental Interfacial Studies, Part 4: End Effect", February 2002, vol. 124 pp. 135-145 DOI: 10.1115/1.1419199.

[10] C. T. Kidd, ISA Transactions, "Thin-Skin Technique Heat-Transfer Measurement Errors Due to Heat Conduction into Thermocouple Wires", 1985 vol. 24, no. 2, pp. 1-9.

[11] M. Tarnopolsky and I. Seginer, Agricultural and Forest Meteorology, "Leaf Temperature Error from Heat Conduction Along Thermocouple Wires", March 1999, vol. 93, pp. 185-194, DOI: 10.1016/S0168-1923(98)00123-3.

[12] J. W. Woolley and K. A. Woodbury, Heat Transfer Engineering, "Thermocouple Data in the Inverse Heat Conduction Problem", October 2011, vol. 32, no. 9, DOI: 10.1080/01457632.2011.525468.

[13] T. C. Tszeng and V. Saraf, Transactions of ASME, "A study of Fin Effects in the Measurement of Temperature Using Surface-Mounted Thermocouples", October 2003, vol. 125, pp. 926-035.

[14] K. S. Kulkarni, S. Han and R. J. Goldstein, Heat and Mass Transfer, "Numerical Simulation of Thermal Boundary Layer Profile Measurement", August 2011, vol. 47, no. 8, pp. 869-877, DOI: 10.1007/s00231-011-0833-5.

[15] M. V. Heitor and A. L. N. Moreira, Progress in Energy and Combustion Science, "Thermocouples and Sample Probes for Combustion Studies", 1993, vol. 19, no. 3, pp. 259-278, DOI: 10.1016/0360-1285(93)90017-9.

[16] Y. Li, D. Guo and S. C. Yao, Journal of Electronic Packaging, "Thermal-Aware Microchannel Cooling of Multicore Processors: A Three-Stage Design Approach", June 2014, vol. 136, DOI: 10.1115/1.4027174.

[17] A. Chauhan, B. Sammakia, F. F. Afram, K. Ghose, G. R. Ahmed, and D. Agonafer, Proceedings of the ASME 2011 Pacific Rim Technical Conference & Exposition on Packaging and Integration of Electronic and Photonic Systems, "Single-Phase Liquid Cooling of A Quad-Core Processor", 2011, IPACK2011-52139, Portland, Oregon, USA ASME, DOI: 10.1115/IPACK2011-52139

[18] D. B. Tuckerman and R.F.W Pease, IEEE Electron Device Letters, "High-Performance Heat Sinking for VLSI", May 1981, vol. EDL-2, no. 5, DOI: 10.1109/EDL.1981.25367.

[19] M. C. Lu and C. C. Wang, IEEE Transactions on Components and Packaging Technologies, "Effect of the Inlet Location on the Performance of Parallel-Channel Cold-Plate", March 2006, vol. 29, no. 1, pp. 30-38, DOI: 10.1109/TCAPT.2005.850539.

[20] A. Chauhan, B. Sammakia, K. Ghose, G. R. Ahmed and D. Agonafer, 12th IEEE Intersociety Conference, Thermal and Thermomechanical Phenomena in Electronic Systems (ITherm), "Hot Spot Mitigation Using Single-Phase Microchannel Cooling For Microprocessors", 2-5 June 2010, Las Vegas, NV, DOI: 10.1109/ITHERM.2010.5501357.

[21] G. Hetsroni, A. Mosyak and Z. Segal, IEEE Transactions on Components and Packging Technologies, "Nonuniform Temperature Distribution in Electronic Devices Cooled by Flow in Parallel Microchannels", March 2001, vol. 24, no. 1, pp. 16 - 23, DOI: 10.1109/6144.910797.

[22] Y. Li, Y. Zhang and S. Yao, Proceedings of the ASME 2013 Heat Transfer Summer Conference HT2013, "Porous Media Thermal Modeling of an Elelctronic Chip with Non-Uniform Power Distribution and Cooled by Micro-Channels", 2013, HT2013-17184, Minneapolis, MN, USA, DOI: 10.1115/HT2013-17184.

[23] J. J. Liu, H. Zhang, S. C. Yao and Y. Li, Journal of Electronic Packaging, "Porous Media Modeling of Two-Phase Microchannel Cooling of Electronic Chips With Nonuniform Power Distribution", 2014, vol. 136, pp. 021008-1-021008-9, DOI: 10.1115/1.4027420.

[24] V. Sahu, Y. K. Joshi and A. G. Fedorov, Nanoscale and Microscale Thermophysical Engineering, "Hybrid Solid State/Fluidic Cooling for Hot Spot Removal", August 2009, vol. 13, no. 3, pp. 135-150, DOI: 10.1080/15567260903058033.

[25] K. Yazawa, A. Ziabari, Y. R. Koh and A. Shakouri, Thermal and Thermomechanical Phenomena in Electronic Systems (ITherm), "Cooling Power Optimization for Hybrid Solid-State and Liquid Cooling in Integrated Circuit Chips with Hotsspots", 2012, San Diego, CA IEEE, pp. 99 - 106, DOI: 10.1109/ITHERM.2012.6231419.

[26] Centeo Bioscience, "Centeo's TG40", <http://www.centeo.com/products/tg-40>. Access Date: 01-08 2015

[27] W. D. Brewer, NASA Technical Note D-3812, "Effect of Thermocouple Wire Size and Configuration on Internal Temperature Measurements in a Charring Ablator", March 1967, Langley Research Center, Langley Station, Hampton, Va, Washington, D.C.

[28] M.B. Dow, NASA Technical Note D-2165, "Comparison of Measurements of Internal Temperatures in Ablation Material by Various Thermocouple Configurations", November 1964, Washington, D.C.

[29] S. J. Bartkus, R. A. Dulinskas, R. Skema and V. Lapo, Heat Transfer-Soviet Research, "Errors of Temperature Measurement within a Body with Internal Heat Sources", May-June 1987, vol. 19, no. 3.

[30] W.A. Mohun, Canadian Journal of Research, "Precision of Heat Transfer Measurements With thermocouples-Insulation Error", 1948, vol. 26F, no. 12, pp. 565-583, DOI: 10.1139/cjr48f-054.

[31] T. C. Tszeng and G. F. Zhou, Journal of Heat Transfer, "A Dual-Scale Computational Method for Correcting Surface Temperature Measurement Errors", August 2004, vol. 126, no. 4, pp. 535-539, DOI: 10.1115/1.1773585.

[32] D. Roertson and G. Sterbutzel, IEEE Transaction on Industry and General Applications, "An Accurate Surface Temperature Measuing System", January 1970, vol. IGA-6, no. 1, pp. 43 - 47, DOI: 10.1109/TIGA.1970.4181127.

[33] Y. Rabin, Cry-Letters, "Uncertainty in Measurements of Fluid Temperature in Tubes", 1998, vol. 19, pp. 319-326.

[34] J.P. Hindmarsh, A.B. Russell and X.D. Chen, International Journal of Heat and Mass Transfer, "Experimental and Numerical Analysis of the Temperature Transition of a Suspended Freezing Water Droplet", MARCH 2003, vol. 46, no. 7, pp. 1199–1213, DOI: 10.1016/S0017-9310(02)00399-X.

[35] F. Xu and M. S. Gadala, Experimental Heat Transfer, "Investigation of Error Sources in Temperature Measurement Using Thermocouple in Water Impingement Cooling", 2005, vol. 18, no. 3, pp. 153-177, DOI: 10.1080/08916150590953388.

[36] G. Fang and C. A. Ward, Physical Review Review E, "Temperature Measured Close to the Interface of an Evaporating Liquid", January 1999, vol. 59, no. 1, DOI: 10.1103/PhysRevE.59.417.

[37] C. J. Kobus, Reiview of Scientific Instruments, "True Fluid Temperature Reconstruction Compensation for Conduction Error in the Temperature Measurement of Steady Fluid Flows", March 2006, vol. 77, no. 3, DOI: 10.1063/1.2186211.

[38] J. Li and G. P. Peterson, International Journal of Heat and Mass Transfer, "3-Dimensional Numerical Optimization of Silicon-Based High Perfomance Parallel Microchannel Heat Sink with Liquid Flow", July 2007, vol. 50, no. 15–16, pp. 2895-2904, DOI: 10.1016/j.ijheatmasstransfer.2007.01.019.

[39] J. Li, G. P. Peterson and P. Cheng, International Journal of Heat and Mass Transfer, "Three-Diensional Analysis of heat Transfer in a Micro-Heat Sink Single Phase Flow", September 2004, vol. 47, no. 19-20, pp. 4215-4231, DOI: 10.1016/j.ijheatmasstransfer.2004.04.018.

[40] Y. Zhang, Y. Li, X Li and S. Yao, Proceedings of the ASME 2013 Heat Transfer Summer Conference HT2013, "Strip-And-Zone Micro-Channel Liquid Cooling of Integrated Circuits Chips with Non-Uniform Power Distribution", July 14-19 2013, Minneapolis, MN, USA, DOI: 10.1115/HT2013-17311.

[41] J. M. Koo, L. Jiang, A. Bari, L. Zhang, E. Wang, T. W. Kenny, J. G. Santiago, and K. E. Goodson, 8th Intersociety Conference on Thermal and Thermommechanical phenomena in Electronic Systems, "Convective Boiling in Microchannel Heat Sinks with Spatially-Varying Heat Generation", 2002, IEEE, DOI: 10.1109/ITHERM.2002.1012477.

[42] J. M. Koo, S. Im, E. S. Cho, R. S. Prasher, E. Wang, L. Jiang, A. Bari, D. Campion, D. Fogg, M. S. Kim, T. W. kenny, J. G. Santiago, and K. E. Goodson, ASME 2002 International Mechanical Engineering Congress and Exposition, "VLSI Hopspot Cooling Using Two-Phase Microchannel Convection", November 17–22 2002, IMECE2002-39585, New Orleans, Louisiana, DOI: 10.1115/IMECE2002-39585.

[43] C. E. Seok, K. J. Mo, J. Linan, R.S. Prasher, K. M. Soo, J. G. Santiago, T. W. Kenny, and K. E. Goodson, Semiconductor Thermal Measurement and Management Symposium, 2003. Ninteenth Annual IEEE, "Experimental Study on Two-Phase Heat Transfer in Microchannel Heat Sinks with Hotspots", 11-13 March 2003, Ninteenth Annual IEEE, DOI: 10.1109/STHERM.2003.1194369.

[44] E. S. Cho, J. W. Choi, J. S. Yoon and M. S. Kim, International Journal of Heat and Mass Transfer, "Experimental Study on Microchannel Heat Sinks Considering Mass Flow Distribution with Non-Uniform Heat Flux Conditions", 2010, vol. 53, no. 9-10, pp. 2159–2168, DOI: 10.1016/j.ijheatmasstransfer.2009.12.026.

[45] R. Flynn, C. H. Cheng and K. Goodson, ASME 2007 InterPACK Conference, "Decoupled Thermal and Fluidic Effects on Hotspot Cooling in a Boiling Flow Microchannel Heat Sink", July 8–12 2007, IPACK2007-33484, Vancouver, British Columbia, Canada, DOI: 10.1115/IPACK2007-33484.

[46] S. N. Ritchey, J. A. Weibel and S V. Garimella, International Journal of Micro-Nano Scale Transport, "Effects of Non-Uniform Heating on the Location and Magnitude of Critical Heat Flux in a Microchannel Heat Sink", March 2015, vol. 5, no. 3, pp. 95-108, DOI: http://dx.doi.org/10.1260/1759-3093.5.3.95.

[47] R. S. Prasher, J. Dirner, J. Y. Chang, A. Myers, D. Chau, S. Prstic, and D. He, ASME 2005 Pacific Rim Technical Conference and Exhibition on Integration and Packaging of MEMS, NEMS, and Electronic Systems "Effect of Localized Hotspot on the Thermal Performance of Two-Phase Microchannel Heat Exchanger", 2005, IPACK2005-73087, San Francisco, California, USA, DOI: 10.1115/IPACK2005-73087.

[48] T. Alam, P. S. Lee, C. R. Yap and L. Jin, Electronics Packaging Technology Conference (EPTC), 2011 IEEE 13th, "Experimental Investigation of Microgap Cooling Technology for Minimizing Temperature Gradient and Mitigating Hotspots in Electronic Devices", 7-9 December 2011, Singapore IEEE, DOI: 10.1109/EPTC.2011.6184478.

[49] E. Costa-Patry, S. Nebuloni, J. Olivier and J. R. Thome, Components, Packaging and Manufacturing Technology, IEEE Transactions "On-Chip Two-

Phase Cooling With Refrigerant 85um -Wide Multi-Microchannel Evaporator Under Hot-Spot Conditions", 29 November 2011, vol. 2, no. 2, pp. 311 - 320, DOI: 10.1109/TCPMT.2011.2173572.

[50] E. S. Cho, J. W. Choi, J. S. Yoon and M. S. Kim, International Journal of Heat and Mass Transfer "Modeling and Simulation on the Mass Flow Distribution in Microchannel Heat Sinks with Non-Uniform Heat Flux Conditions", 2010, vol. 53, no. 7-8, pp. 1341–1348, DOI: 10.1016/j.ijheatmasstransfer.2009.12.025.

[51] P. Smakulski, Archives of Thermodynamics, "Method of High Heat Flux Removal by Usage of Liquid Spray Cooling", 2013, vol. 34, no. 3, pp. 173–184, DOI: 10.2478/aoter-2013-0023.

[52] C. L. Tilton, D. E Tilton, T. D. Weir, T. Cader and P. A. Knight, Publication, P.A., "Hotspot Spray Cooling", 2005, US 2005/0183844 A1, United States.

[53] P. G. Hegde and K.N. Seetharamu, Electronic Manufacturing Technology Symposium (IEMT), 2008 33rd IEEE/CPMT International, "Effects of Non-Uniform Base Heating in Multi Stack Microchannel Heat Sinks Used for Cooling High Heat Flux Electronic Chips and Devices", 4-6 November 2008, Penang, DOI: 10.1109/IEMT.2008.5507856.

[54] G. Xie, S. Li, B. Sunden and W. Zhang, International Journal for Numerical Methods in Heat & Fluid Flow, "Computational Fluid Dynamics for Thermal Perfomance of a Water-Cooled minichannel Heat Sink with Different Chip Arrangements", 2014, vol. 24, no. 4, pp. 797 - 810, DOI: dx.doi.org/10.1108/HFF-01-2013-0013.

[55] L. Biswal, S. Chakraborty and S.K. Som, IEEE Transactions on Components and Packaging Technologies, "Design and Optimization of Single-Phase Liquid Cooled Microchannel Heat Sink", 04 December 2009, vol. 32, no. 4, pp. 876-886, DOI: 10.1109/TCAPT.2009.2025598.

[56] Ling Ling, "Numerical Investigation of the Cooling Performance of Microchannel Heat Sinks Under Uniform and Non-Uniform Heating Conditions", Degree of Master of Applied Science, March 2012, Mechanical and Industrial Engineering, Concordia University.

[57] C. K. Liu, S. J. Yang, Y. L. Chao, K. Y. Liou and C. C. Wang, International Communications in Heat and Mass Transfer, "Effect of Non-Uniform heating on the Performance of the Microchannel Heat Sinks", 2013, vol. 43, pp. 57-62.

[58] S. A. Jajja, W. Ali, H. M. Ali and A. M. Ali, Applied Thermal Engineering, "Water Cooled Minichannel Heat Sinks for Microprocessor Cooling: Effect of Fin Spacing", March 2014, vol. 64, no. 1-2, pp. 76-82, DOI: 10.1016/j.applthermaleng.2013.12.007.

[59] J. Barrau, D. Chemisana, J. Rosell, L. Tadrist and M. Ibanez, Applied Thermal Engineering, "An Experimental Study of a New Hybrid Jet Imoingment / Micro-Channel Cooling Scheme", October 2010, vol. 30, no. 14-15, pp. 2058-2066, DOI: 10.1016/j.applthermaleng.2010.05.013.

[60] S. Riera, J. Barrau, M. Omri, L. G. Frechette and J. I. Rosell, Applied Thermal Engineering, "Stepwise Varying Width Microchannels Cooling Device for Uniform Wall Temperature: Experimental and Numerical Study", March 2015, vol. 78, pp. 30-38, DOI: 10.1016/j.applthermaleng.2014.12.012.

[61] R. Prasher and J. Y. Chang, Proceedings of the Sixth International ASME Conference on Nanochannels, Microchannels and Minichannels, ICNMM2008, "Cooling of Electronic Chips Using Microchannel and Micro-Pin Heat Exchangers", June 23-25 2008, Darmstadt, Germany, DOI: 10.1115/ICNMM2008-62384.

[62] Z. Minliang, W. Xiaojing, L. Hongjun and W. Guoliang, International Conference on Electronic Packaging Technology and High Density Packaging ICEPT-HDP 2008, "Numerical Simulation of the Micro-Channel Heat Sink on Non-Uniform Heat Source", 28-31 July 2008, Shanghai IEEE, DOI: 10.1109/ICEPT.2008.4606946.

[63] X. Wang, W. Zhang, H. Liu, L. Chen and Z. Li, International Conference on Electronic Packaging Technology and High Density Packagning ICEPT-HDP09, "Numerical Simulation on Variable Width Multi-Channels Heat Sinks with Non-Uniform Heat Source", 10-13 August 2009, Beijing IEEE, DOI: 10.1109/ICEPT.2009.5270609.

[64] G. Türkakar and T. O. Özyurt, International Journal of Thermal Sciences, "Dimensional Optimization of Microchannel Heat Sinks with Multiple Heat Sources", December 2012, vol. 62, pp. 85-92, DOI: 10.1016/j.ijthermalsci.2011.12.015.

[65] C. S. Sharma, M. K. Tiwari, S. Zimmermann, T. Brunschwiler, G. Schlottig, B. Michel, and D. Poulikakos, Applied Energy, "Energy Efficient Hotspot-Targeted Embedded Liquid Cooling of Electronics", 15 January 2015, vol. 138, pp. 414–422, DOI: 10.1016/j.apenergy.2014.10.068.

[66] C. S. Sharma, G. Schlottig, T. Brunschwiler, M. K. Tiwari, B. Michel, and D. Poulikakos, International Journal of Heat and Mass Transfer, "A Novel Method of Energy Efficient Hotspot-Targeted Embedded Liquid Cooling for Electronics: An experimental Study", 2015, vol. 88, pp. 684–694, DOI: 10.1016/j.ijheatmasstransfer.2015.04.047.

[67] R. Dias and L. Skoglund, Publication, P.A., "Variable Depth Microchannels", 27 March 2008, Publication No.:US 2008/0073061 A1, Application No.:11/528,773, United States.

[68] Y. J. Lee, P. S. Lee and S. k. Chou, International Mechanical Engineering Congress & Exposition IMECE2010, "Hot Spot Mitigating Oblique Finned Microchannel Heat Sink", November 12-18 2010, Vancouver, British Columbia, Canada IEEE, DOI: 10.1109/TCPMT.2013.2244164.

[69] Y. J. Lee, P. S. Lee and S. K. Chou, IEEE Transaction on Components, Packaging and Manfacturing Technology, "Hotspot Mitigating with Obliquely Finned Microchannel Heat Sink-An Experimental Study", 22 February 2013, vol. 3, no. 8, pp. 1332-1341, DOI: 10.1109/TCPMT.2013.2244164.

[70] T. T. Lee, IEEE Transactions on Components and Packaging Technologies, "Design Optimization of an Integrated_Cooled IGBT Power Module Using CFD Technique", March 2000, vol., pp. 337-342, DOI: 10.1109/6144.833042.

[71] K. Goodson, T. Kenny, P. Zhou, Upadhya, M. Munch, M. McMaster, and J. Horn, United States Patent, No. US 7,104,312, B2, "Method and Apparatus for Achieving Temperature Uniformity and Hot Spot Cooling in a Heat Producing Device", September 12 2006, vol.

[72] Y. Fan and I. Hassan, ASME 2011 9th International Conference on Nanochannels, Microchannels, and Minichannels, "Numerical Simulation of a Novel Jet-Impingement Micro Heat Sink with Cross Flow Under Non-Uniform Heating Condition", June 19-22 2011, Edmonton, Alberta, Canada Proceedings of the ASME, DOI: 10.1115/ICNMM2011-58002.

[73] S. XU, W. Wang, Z. GUO, X. Hu and W. GUO, "A Multi-Channel Cooling System for Multiple Heat Source", <http://www.doiserbia.nb.rs/Article.aspx?id=0354-98361400123X#.VPGc7_msVps>. Access Date: 28/02/2015 2015

[74] Aderian Bejan, "Convection Heat Transfer", 1995, 2nd ed., John Wiley & Sons, Incorporated.

[75] COMSOL AB, "COMSOL Multiphysics Modeling Guide / v3.5a", 1998-2008.

[76] O. C. Zeinkiewicz, R. L. Taylor and J. Z. Zhu, "The Finite Element Method: Its Basis and Fundamentals", 2013, 7th edition, Elsevier Ltd, DOI: 10.1016/B978-1-85617-633-0.00021-6.

[77] R.W. Lewis, P. Nithiarasu and K.N. Seetharamu, "Fundamentals of the Finite Element Method for Heat and Fluid Flow", 2004, John Wiley & Sons Ltd,, DOI: 10.1002/0470014164.

[78] E. Madenci and I. Guven, "The Finite Element Method and Applications in Engineering Using ANSYS®", 2006, 2nd edition, Springer International Publishing, DOI: 10.1007/978-1-4899-7550-8.

[79] M. G. Larson and F. Bengzon, "The Finite Element Method: Theory, Implementation, and Applications", 2013, Springer-Verlag Berlin Heidelberg DOI: 10.1007/978-3-642-33287-6.

[80] R. W. Lewis, K. Morgan, H. R. Thomas and K. N. Seetharamu, "The Finite Element Method in Heat Transfer Analysis", 1996, John Wiley & Sons Ltd.

[81] COMSOL AB., "COMSOL Multiphysics Reference Guide / v3.5a", 1998-2008.

[82] M. Tanaka, G. Girard, R. Davis, A. Peuto and N. Bignell, Metrologia, "Recommended Table for the Density of Water Between 0 C and 40 C Based on Recent Experimental Reports", 2001, vol. 38, pp. 301-309, DOI: 10.1088/0026-1394/38/4/3.

[83] M. L. V. Ramires, C. A. Nieto de Castro, Y. Nagasaka, A. Nagashima, M. J. Assael., and W. A. Wakeham, Journal of Physical and Chemical Reference Data, "Standard Reference Data for the Thermal Conductivity of Water", 1995, vol. 24, pp. 1377-1381, DOI: 10.1063/1.555963.

[84] J. Kestin, M. Sokolov and W. A. Wakeham, Journal of Physical and Chemical Reference Data, "Viscosity of Liquid Water in the Range −8 °C to 150 °C", 1978, vol. 7, no. 3, pp. 941-948, DOI: dx.doi.org/10.1063/1.555581.

[85] COMSOL AB, "Comsol Multiphysics User's Guide", 1998-2008.

[86] C. J. Glassbrenner and G. Slack, Physical Review, "Thermal Conductivity of Silicon and Germanium from 3K to the Melting Point", 1964, vol. 134, no. 4A, DOI: dx.doi.org/10.1103/PhysRev.134.A1058.

[87] F. P. Incropera, D. P. Dewitt, T. L. Bergman and A. S. Lavine, "Fundamentals of Heat and Mass Transfer", 2007, Sixth, Jhon Wiley & Sons, Inc.

[88] M. K. Parsa and F. Hormozi, Journal of Micromechanics and Microengineering, "Experimental and CFD Modeling of Fluid Mixing in Sinusoidal Microchannels with Different Phase Shift between Side Walls", 2014, vol. 24, no. 6, DOI: 10.1088/0960-1317/24/6/065018.

[89] A. Adrover and A. Pedacchia, International Journal of Heat and Mass Transfer, "Mass / Heat Transfer Through Laminar Boundary Layer in Axisymmetric Microchannels with Nonuniform Cross Section and Fixed Wall Concentration / Temperature", January 2014, vol. 68, pp. 21-28, DOI: 10.1016/j.ijheatmasstransfer.2013.08.101.

[90] W. Qu and I. Mudawar, International Journal of Heat and Mass Transfer, "Analysis of Three-Dimensional Heat Transfer in Micro-Channel Heat Sinks", September 2002, vol. 42, no. 19, pp. 3973-3985, DOI: 10.1016/S0017-9310(02)00101-1.

[91] J.P. Holman, "Heat transfer", 1987, 6th ed., McGraw-Hill.

[92] S.B. Riffat and X. Ma, Applied Thermal Engineering, "Thermoelectrics: a Review of Present and Potential Applications", June 2003, vol. 23, no. 8, pp. 913-935, DOI: 10.1016/S1359-4311(03)00012-7.

[93] American Society for Testing Materials, "Manual on the Use of Thermocouples in Temperature Measurement", 1993, 4th ed.

[94] K.M.B. Jansen, International Journal of Heat and Mass Transfer, "Heat Transfer in Injection Moulding Systems with Insulation Layers and Heating Elements", January 1995, vol. 38, no. 2, pp. 309-316, DOI: 10.1016/0017-9310(95)90021-7.

[95] M. D. Lechner, Springer Handbook of Condensed Matter and Materials Data, "Polymers", 2005, Springer Berlin Heidelberg, Part3, pp. 477-522, DOI: 10.1007/978-3-540-30437-1.

[96] k. Mollmann and M. Vollmer, European Journal of Physics, "Infrared Thermal Imaging as a Tool in University Physics Education", April 2007, vol. 28, no. 3, pp. S37-S50, DOI: 10.1088/0143-0807/28/3/S04.

[97] D. R. Lide, "CRC Handbook of Chemistry and Physics", Internet Version 2005, CRC Press, Boca, Raton, FL, 2005: http://www.hbcpnetbase.com,

[98] Pico Technical Support, "Noise rejection / Request Ticket Number: TS00065500", Access Date: 13/10/2014 2014

[99] Pico Technology Limited, "TC-08 User's Guide Thermocouple Logger", 2005-7.

[100] H. W. Coleman and W. G. Steele, "Experimentation and Uncertainty Analysis for Engineers", 1999, 2nd edition, John Wiley & Sons, Incorporation.

[101] R. J. Moffat, Transactions of the ASME "Contributions to the Theory of Single-Sample Uncertainty Analysis", JUNE 1982, vol. 104, pp. 250-258.

[102] R.J. Moffat, Proceedings of the 5th annual ISA test measurement symposium, "Temperature Measurement in Solids", October 28-31 1968, No. 68-514, New York.

[103] M. H. Attia and L. Kops, International Journal of Advanced Manufacturing Technolology, "Thermometric Design Considerations for Temperature Monitoring in Machine Tools and CMM Structures", 1993, vol. 8, no. 5, pp. 311-319, DOI: 10.1007/BF01783615.

[104] L. Thiery, S. Toullier, D. Teyssieux and D. Briand, Journal of Heat Transfer, "Thermal Contact Calibration between a Thermocouple Probe and a Microplate", September 2008, vol. 130, no. 9, DOI: 10.1115/1.2943306.

[105] B. Kundu and A. Aziz, Journal of Heat Transfer, "Performance of a Convectively Heated Rectangular Fin With a Step Change in Cross-Sectional

Area and Losing Heat by Simultaneous Convection and Radiation (Step Fins Under Radiation Environment)", October 2010, vol. 132, no. 10, DOI: 10.1115/1.4001928.

[106] C. Arslanturk, Journal of Thermal Science and Technology, "Optimization of Straight Fins with A step Change in Thickness and Variable Thermal Conductivity by Homotopy Perturbation Method", 2010, vol. 30, no. 2, pp. 09-19.

[107] Comsol AB, "Heat Transfer Model Library", 2008, Comsol Multiphysics.

[108] H. Celanese G. Khanarian, Optical Engineering, "Optical properties of cyclic olefin copolymers", June 2001, vol. 40, no. 6, pp. 1024–1029 DOI: 10.1117/1.1369411.

[109] M. Sahli, J-C Gelin and T. Barrière, Int J Mater Form "Numerical Modelling of the Polymers Replication in Micro-Cavities by the Roll Embossing Process", 2010, vol. 3, no. 1, pp. 607– 610, DOI: 10.1007/s12289-010-0843-8.

[110] C. V. Y. Chong, "Properties of Materials", 1977, Macdonald and Evans, The M. & E. handbook series.

[111] Y. Agar and T. Uno, Journal of Applied Polymer Science, "Estimation on Thermal Conductivities of Filled Polymers", November 1986, vol. 32, no. 7, pp. 5705-5712 DOI: 10.1002/app.1986.070320702.

[112] P. Welander, Tellus, "Convective Instability in Two-Layer fluid Heated Uniformaly from Above", August 1964, vol. 16, no. 3, DOI: 10.1111/j.2153-3490.1964.tb00171.x.

[113] G. Z. Gershuni and E. M. Zhukhovitskii, Fluid Dynamics, (Originally published in Russian in Izv. Akad. Nauk SSSR, Mekh. Zhidk. Gaza 6, 28–34), "Instability of a System of Horizental Layers of Immiscible Fluids Heated From Above", 1981, vol. 15, no. 6, pp. 816-822, DOI: 10.1007/BF01096629.

[114] A. A. Gubaidullin, "Natural Convection Heat Transfer in Two-Fluid Stratifed Pools with Internal Heat Sources", Doctoral Thesis, January 21 2002, Royal Institute Of Technology Stockholm, Sweden.

[115] M. Bargach and P. Vasseur, Numerical Heat Transfer, Part A:Applications, "Natural Convection in Shallow Cavity Containing two Superimposed Layers

of immiscible Liquids", 1993, vol. 24, no. 3, pp. 357-373, DOI: 10.1080/10407789308902626.

[116] L. Kh Ingel, Uspekhi Fizicheskikh, Russian Academy of Sciences, Physics-Uspekhi, "Anticonvection", 1997, vol. 40, no. 7, pp. 741-745, DOI: 10.1070/PU1997v040n07ABEH000256.

[117] J. N. Israelachvili, Intermolecular and Surface Forces, "Adhesion and Wetting Phenomena", 2011, Academic Press, pp. 415–467, DOI: 10.1016/B978-0-12-375182-9.10017-X.

[118] A. A. Y. Al Waaly, M. C. Paul and P. S. Dobson, Applied Thermal Engineering, "Effects of Thermocouple Electrical Insulation on the Measurement of Surface Temperature", 2015, vol. 89, pp. 421-431, DOI: 10.1016/j.applthermaleng.2015.06.020.

[119] Sabic Innovative Plastics, "Lexan sheet of number 9030", <https://sfs.sabic.eu/wp-content/uploads/resource_pdf/1345453948-48623687-Technical-Manual-Coated-Uncoated-Sheet.pdf>. Access Date: 05th April 2015

[120] Henkel Corporation, " Adhesive Epoxy LOCTITE® SI 5145™", <http://www.henkelna.com/about-henkel/product-search-1554.htm?nodeid=8797879926785>. Access Date: 17th April 2015

[121] ELGA LabWater, "PURELAB® Option-S/R 7/15", <http://www.elgalabwater.com/purelab-option-s-r-7-15-en>. Access Date: 16th April 2015

[122] Performance Plastics Corporation Saint-Goban, "Comprehensive Guide to Tygon® tubing Formulations", 2006,

[123] HERAEUS, "Pt 6,8 M1020, order number 32208172", <http://heraeus-sensor-technology.com/en/produkte_1/sensormodule/sensor_module.aspx>. Access Date: 06-04-2015 2015

[124] Mega Electronics Limited, "Fotoboard-Pre-Sensitised Copper Board", <http://www.megauk.com/>. Access Date: 18th April 2015

[125] Electrolube/ The solution People, "HTC, non-silicone thermal paste heat transfer compound, REF:HTC02S ", <www.electrolube.com >. Access Date: 6th April 2015

[126] CORNING, "Machinable Glass Ceramic-Macor", <http://www.corning.com/specialtymaterials/advanced_optics/specialty_glass_ceramics/products/macor/index.aspx>. Access Date: 16th of April 2015

[127] R. A. Hart and A.K. da Silva, International Journal of Heat and Mass Transfer "Experimental Thermal–Hydraulic Evaluation of Constructal Microfluidic Structures under Fully Constrained Conditions", July 2011, vol. 54, no. 15-16, pp. 3661–3671, DOI: 10.1016/j.ijheatmasstransfer.2011.02.063.

[128] digitron of a brand of electron technology, "http://www.digitron.com/", Access Date: 13th of April 2015

[129] GW Instek, "Linear DC power supplies, GPS-x303 Series", <http://www.gwinstek.com.tw/en/product/productdetail.aspx?pid=38&mid=53&id=131>. Access Date: 17th April 2015

[130] Rs Components, "Aim-TTi PL154 Bench Power Supply", <http://uk.rs-online.com/web/p/bench-power-supplies/0218829/>. Access Date: 17th April 2015

[131] British Standard Instituation (BSI), "Industrial Platinum Resistance Thermometers and Platinum Temperature Snesors", September 2009, IEC 60751:2008.

[132] I.K. Karathanassis, E. Papanicolaou, V. Belessiotis and G.C. Bergeles, International Journal of Heat and Mass Transfer, "Experimental and Numerical Evaluation of an Elongated Plate-Fin Heat Sink with Three Sections of stepwise Varying Channel Width", 2015, vol. 84 pp. 16–34, DOI: 10.1016/j.ijheatmasstransfer.2014.12.013.

[133] F. M. White, "Fluid Mechanics", 1979, International Student Edition, McGraw-Hill Kogakusha, LTD.

[134] D. Liu and S. V. Garimella, International Journal for Numerical Methods in Heat & Fluid Flow, "Analysis and Optimization of the Thermal Performance of Microchannel Heat Sinks", 2005, vol. 15, no. 1, pp. 7-26, DOI: 10.1108/09615530510571921.